
THE UNIVERSITY *of* EDINBURGH


# Uncertainty quantification in wavefield interferometry

Daniella Ayala-Garcia

A thesis presented for the degree of
Doctor of Philosophy

School of Mathematics
University of Edinburgh
2021

# Declaration

I declare that this thesis has been composed solely by myself and that the work presented is my own, except where otherwise explicitly stated in the text, and that it has not been submitted either in whole or in part for any other degree or professional qualification.

Parts of this work have been published in Ayala-Garcia et al. (2021).

*Daniella Ayala-Garcia*
*September 2021*

# Lay Summary

Just as doctors use X-rays to look inside living tissue, geophysicists can use seismic waves to scan geological formations beneath the Earth's surface that are too inaccessible to be studied directly. The speed of these waves changes when traversing different kinds of materials in the Earth's crust, the same way that X-rays change speed when travelling through different tissues inside the human body. These changes help create images of our body in the case of X-rays, and images of the Earth's subsurface in the case of seismic waves. There are many kinds of sources for waves travelling across the Earth, ranging from earthquakes to ocean noise to urban noise, and these waves are usually recorded on the surface using sensors known as geophones. Unfortunately, unlike an X-ray machine that emits X-rays on demand, the Earth does not produce seismic energy whenever geoscientists need it, posing significant challenges for creating images of the Earth's subsurface. However, a recent technique known as wavefield interferometry allows geoscientists to create virtual sources at times and locations where no sources were originally physically recorded. Wavefield interferometry is in fact so powerful that it can even take advantage of ambient noise, previously considered a nuisance and discarded, to create these virtual sources. This technique has greatly advanced our ability to image the Earth's subsurface and has many industrial and environmental applications, at scales ranging from the local regions to entire continents.

Wavefield interferometry works by taking seismic recordings from pairs of sensors and processing them using certain mathematical operations that effectively turn one of the sensors into a "virtual" source. However, the mathematical theory that makes wavefield interferometry work requires very idealised conditions that are not often found in practice. Therefore, practical studies of wavefield interferometry often need to make a series of assumptions and simplifications in order to be able to apply this mathematical machinery. Whenever these assumptions are not satisfied, or approximations are made, there is potential for error and uncertainty in the final result. In the case of wavefield interferometry, it can ultimately affect our understanding of sub-surface Earth structures. In this thesis, we study and quantify

uncertainty in interferometric estimates as a consequence of errors introduced by violating some important assumptions of the mathematical theory and by making approximations commonly used in wavefield interferometry. We derive bounds for these errors, which can be a useful tool for geoscientists to estimate the uncertainty in their practical applications, and propose some strategies to mitigate this uncertainty.

# Abstract

It is a well-established principle that cross-correlating wavefield observations at different receiver locations yields new responses that, under certain conditions, provide a useful estimate of the Green's function between the receiver locations. This principle, known as wavefield interferometry, is a powerful technique that transforms previously discarded data, such as background noise or earthquake codas (the multiply scattered tails of earthquake seismograms), into useful signals that allow us to remotely illuminate subsurface Earth structures.

The mathematical machinery that underlies wavefield interferometry assumes a number of ideal conditions that are not often found in practical settings. Furthermore, the original formulations are frequently simplified through a variety of approximations, in order to derive expressions that are more amenable to applications. These assumptions and approximations are frequently made in an ad-hoc fashion, without consideration of the errors thus introduced.

This thesis centres on the study of errors introduced by violating two important assumptions of wavefield interferometry. Namely, that the noise sources are statistically uncorrelated, and that their energy contributions are isotropic. Violating these conditions makes the Green's function and associated phases liable to estimation errors that so far have not been accounted for or corrected. We show that these errors are indeed significant for commonly used noise sources, and illustrate cases in which the errors completely obscure the phase one wishes to retrieve. Moreover, we consider the relevant case of the stationary phase approximation, widely invoked in interferometry theory and applications, and quantify mathematically the errors introduced both in an ideal setting and in the presence of correlated, anisotropic sources, applying and extending existing error quantification theory.

Throughout these settings, this thesis implements an appropriate geostatistical correlation model to investigate the effect that smoothness and long-range correlations have on the interferometric estimate, particularly its phase. Analytical expressions are given for the first and second moments of these errors, as well as deterministic error bounds and probability bounds on the uncertainty of these approximations. These results are given in terms of sta-

tistical parameters that can be empirically estimated in practice, and numerically explored.

Finally, this thesis contrasts the two main types of wavefield interferometry, active or controlled source interferometry and passive or ambient noise interferometry. The impact of violating the uncorrelatedness assumption is considered. This thesis proposes strategies to mitigate uncertainty in both settings, and in the case of ambient noise interferometry, the thesis presents a novel workflow that significantly mitigates errors introduced by the presence of statistical correlations in the sources. The methodology is general in the sense that it can be applied to noise with any degree of correlation, including completely uncorrelated sources. The methods are tested on synthetic data, illustrating significant improvement in the phase estimates in both settings. In all these cases we establish various bounds on the estimation error, and we analyse their significance and utility in real-life interferometric retrieval experiments.

# Acknowledgements

This research was funded by the Mexican Institute of Petroleum (IMP), thorough the programme Programa de Captación de Talento, Reclutamiento, Evaluación y Selección de Recursos Humanos (PCTRES), overseen by Dr. Leonid Shemeretov. I am grateful for the supervision of Dr. Michal Branicki and Prof. Andrew Curtis. For their guidance, patience and support through the completion my research, and for the long and useful discussions. Furthermore, I wish to thank my examiners, Dr. Ben Goddard and Prof. Kees Wapenaar, for their feedback and suggestions to improve this manuscript, and a truly insightful and enjoyable viva discussion. I would also like to mention the staff at the School of Mathematics, in particular Chris Jowett and Jill Douglas, whose kindness and support allowed me to focus on completing my research through the many challenges along the way.

Thank you Veronika for the dancing and the wine, and Ruth for all the tea and breakfast at dinnertime. Thank you Tim for your top-notch cooking and frank friendship, and Jenny for baking and giving us all a home on Wednesdays. Thank you Manuel for your constant company and compassion. I could not have been luckier in finding friendships like yours. Our times together kept me sane and laughing throughout these years. I also wish to thank my Rencounter family, especially Linn and Sarah, for helping me find my strength on and off the mats. Thank you for all the lockdown walks and the consensual fighting while I was completing this manuscript.

*Gracias Mariajose*. I can hardly put into words how thankful I am for the resilience of our bond through the mountains we have climbed together, and across the ocean between us. I am proud and grateful to call you my sister.

Thank you James, mi *compañero*, for your emotional, material and intellectual support these last three years. Thank you for reminding me to take breaks and making sure I ate dinner. Thank you for your unfaltering faith in me. I love you with all my heart. 🐰

# Contents

Chapter 1

# Introduction

The Earth's crust is constantly monitored across ecological and geological disciplines due to its importance to terrestrial life, for industrial applications and for advancing science. Given the inaccessibility of many of Earth's subsurface structures, remote sensing methods are commonly deployed in which physical energy fields are recorded on or below the Earth's surface, and are used to infer structure and properties of the subsurface. In particular, wavefield interferometry is a powerful technique which transforms previously discarded data, such as seismic energy from earthquakes or the background ambient noise field, into useful signals that remotely illuminate subsurface Earth structures (Campillo and Paul, 2003; Wapenaar and Fokkema, 2006; Curtis et al., 2006). The origin of wavefield interferometry can be traced back to the seminal work of Claerbout (1968), who showed that the reflection response of a horizontally layered medium could be estimated from the autocorrelation of its transmission response. Wavefield interferometry has since become a rapidly evolving field of research (Rickett and Claerbout, 1999; Weaver and Lobkis, 2001; Derode et al., 2003; Snieder, 2004; Sánchez-Sesma et al., 2006; Slob and Wapenaar, 2007), leading to fundamental advances in our ability to image the Earth's crust at global (Ruigrok et al., 2008; Nishida et al., 2009), regional (Shapiro et al., 2005; Nishida et al., 2008; Halliday et al., 2008a; Arroucau et al., 2010) and industrially relevant scales (Bakulin and Calvert, 2006; Bakulin et al., 2007; Halliday and Curtis, 2010).

In general, interferometric methods rely on cross-correlating (Wapenaar and Fokkema, 2006; Schuster et al., 2004; Wapenaar et al., 2010b; Snieder et al., 2009; Sánchez-Sesma et al., 2006), convolving (Slob and Wapenaar, 2007; Slob et al., 2007) or deconvolving (van Dalen et al., 2014; Ravasi et al., 2015; van Dalen et al., 2015) pairs of recorded signals in order to extract information about the medium. The goal is to estimate signals that were not physically recorded, but which would have been acquired if the receivers (Hong and Menke,

2006; Curtis et al., 2009) or sources (Campillo and Paul, 2003; Wapenaar, 2004; Wapenaar and Fokkema, 2006) had been deployed at different locations or at different times (Curtis and Halliday, 2010a; Curtis et al., 2012; Entwistle et al., 2015; Chen and Saygin, 2020). Theoretically, the response of a medium measured at a given location to an impulsive source at a different location is described by Green's functions associated with specific equations that describe the wave dynamics. The purpose of wavefield interferometry is usually to estimate various approximations to these Green's functions. A further distinction can be made between ambient noise interferometry, which uses passive wavefield measurements such as microseismic responses or urban-generated noise (Campillo and Paul, 2003; Shapiro and Campillo, 2004; Shapiro et al., 2005; Sabra et al., 2005b; Draganov et al., 2006; Behm and Snieder, 2013; Pinzon-Rincon et al., 2021), and active or controlled source interferometry, where recordings of the medium response to individual sources are available (Bakulin and Calvert, 2006; Slob et al., 2007; Wapenaar et al., 2010a; King et al., 2011b).

The theoretical assumptions that underpin many interferometric methods include that the recorded energy comes from sources that are distributed isotropically in space around the receivers, emitting energy with equal intensity, and that they are statistically uncorrelated. These assumptions are not always realistic in practical applications. The source distribution around the receivers is often insufficient (Harmon et al., 2010; Curtis and Halliday, 2010b), the noise sources are commonly correlated (van Dalen et al., 2014), and pragmatic approximations need to be made (Kimman and Trampert, 2010), all to the potential detriment of the Green's function estimate (Yao and Van Der Hilst, 2009).

In this introductory chapter, we describe the physical intuition behind wavefield interferometry in Section 1.1, followed by a brief presentation of the theoretical foundations of active source and passive noise wavefield interferometry in Section 1.2, highlighting explicit and implicit assumptions in the derivations. For reference throughout this work, the relevant Green's functions are briefly introduced in Section 1.2.6. Next, relevant geophysical applications and some of their limitations are discussed in Section 1.3. The main assumptions and approximations made in wavefield interferometry are summarised in Section 1.4, along with current approaches to mitigate their spurious effects and areas that remain unaddressed. Finally an outline of the thesis is given in Section 1.5, as a guide for the reader.

## 1.1 Physical intuition behind wavefield interferometry

It is a well-established principle that cross-correlating wavefield observations which are recorded at different receiver locations yields new seismic responses that, under certain conditions, provide a useful estimate of the Green's function of the wave equation. This

principle has been expressed in a variety of ways, often via acoustic representation theorems, and using either the convolution, deconvolution, or cross-correlation of the seismic traces. In this thesis, we focus on cross-correlational interferometry, which is a classical form of interferometry widely used in theory and practice (Wapenaar and Fokkema, 2006; Schuster, 2009; Fichtner et al., 2019).

Cross-correlational wavefield interferometry estimates properties of the Earth by analysing interference patterns of recorded wavefields (sometimes called *traces*). This analysis is conducted by cross-correlating and integrating (also known as *stacking*) wavefield traces in order to image Earth's subsurface structures, and is often referred to as Green's function *retrieval*. More precisely, for a homogeneous medium where waves travel at speed $c$, let $\hat{G}(\mathbf{x}, \mathbf{y}, k)$ denote the frequency response of the medium to a point source located at $\mathbf{y}$, measured at $\mathbf{x}$, where $k = \omega/c$ is the wavenumber corresponding to the angular frequency $\omega$. In this work, $c$ is assumed to be constant. This medium response, $\hat{G}(\mathbf{x}, \mathbf{y}, k)$ corresponds to the fundamental solution of the Helmholtz equation, discussed in Section 1.2.1. This thesis is concerned with the *interferometric estimate*, which is given for each wavenumber $k$ by

$$\hat{G}(\mathbf{x_A}, \mathbf{x_B}, k) - \hat{G}^*(\mathbf{x_A}, \mathbf{x_B}, k) \approx -2ik \oint_S \hat{G}(\mathbf{x_A}, \mathbf{x}, k)\hat{G}^*(\mathbf{x_B}, \mathbf{x}, k)d\mathbf{x}\,. \tag{1.1.1}$$

where $S$ is a boundary enclosing locations $\mathbf{x_A}$ and $\mathbf{x_B}$. While in general the speed $c$ at which waves travel through a medium is not constant, in this work we assume a constant medium speed $c$ so that the wavenumber $k = \omega/c$ is in this work simply a rescaling of the frequency $\omega$. Note that equation (1.1.1) is valid regardless of the choice of boundary $S$, as long as $S$ encloses both receivers and the radius of $S$ is sufficiently large with respect to the wavelength one wishes to observe. The requirements on the radius of $S$ is related to the Sommerfeld radiation condition and the wavelength, and this is discussed in detail in Section 1.2.2. and 1.2.3, When $\mathbf{x_A}$ and $\mathbf{x_B}$ are receivers, expression (1.1.1) is referred to as inter-receiver interferometry. The left hand side of (1.1.1) can be interpreted as the superposition of the Green's function between locations $\mathbf{x_A}$ and $\mathbf{x_B}$, $\hat{G}(\mathbf{x_A}, \mathbf{x_B}, k)$, and its time reverse $\hat{G}^*(\mathbf{x_A}, \mathbf{x_B}, k)$, since conjugation in the frequency domain corresponds to reversal in the time domain (see, e.g., Derode et al. (2003)). For a fixed location $\mathbf{x} \in S$, the integrand on the right hand side of (1.1.1) corresponds to the cross-correlation of the medium responses at $\mathbf{x_A}$ and $\mathbf{x_B}$ to a point source at $\mathbf{x}$. Integrating over $S$ corresponds to summing these cross-correlations over source locations. Thus, when $S$ is interpreted as a boundary of point sources, and $\mathbf{x_A}$ and $\mathbf{x_B}$ are a pair of receivers, expression (1.1.1) states that cross-correlating wavefields recorded at a pair of receivers and adding these cross-correlations comprises an approximation of the medium response at one of the receivers, had the other receiver been a

source. This situation is depicted in Figure 1.1, where the blue triangles represent a pair of receivers, surrounded by a boundary $S$ of point sources in orange. The medium's responses to each point source, recorded at each of the two receivers, are represented as grey dashed lines. The inter-receiver Green's function is shown in solid black. This is why wavefield

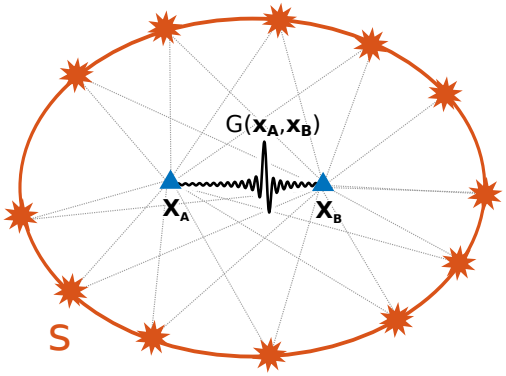


**Figure 1.1:** General layout of inter-receiver interferometry. The blue triangles represent receivers and the orange stars on the contour $S$ represent active sources. Traces (Green's functions) between the receivers and the sources are represented by grey dotted lines. The Green's function between $\mathbf{x_A}$ and $\mathbf{x_B}$ is illustrated in solid black.

interferometry in the formulation (1.1.1) is commonly referred to in literature as the "virtual source" method, as it remarkably allows for the estimation of the inter-receiver Green's function without the need to physically place a source at one of the receiver locations. The left hand side of equation (1.1.1) is known as the *homogeneous Green's function* for the receiver pair $\mathbf{x_A}$ and $\mathbf{x_B}$, denoted in this work as

$$\hat{G}_{\text{hom}}(\mathbf{x},\mathbf{y},k) := \hat{G}(\mathbf{x},\mathbf{y},k) - \hat{G}^*(\mathbf{x},\mathbf{y},k) = 2i\text{Im}\left\{\hat{G}(\mathbf{x},\mathbf{y},k)\right\}, \tag{1.1.2}$$

noting that in the formulation used here the homogeneous Green's function is a purely imaginary quantity. Figure 1.2 illustrates approximation (1.1.1), facilitating its intuitive interpretation. The left and right hand sides of (1.1.1) were simulated in a medium of speed $c = 1000$ m/s, for a horizontal pair of receivers 300 m away from each other and a circular point-source boundary of radius $r = 1000$ m, with a source spectrum between 0.1 and 40 Hz. The waveforms in the left panel of this figure correspond to the time domain representation of the integrand $\hat{G}(\mathbf{x_A},\mathbf{x},k)\hat{G}^*(\mathbf{x_B},\mathbf{x},k)$ for each source location $\mathbf{x}$ along a circular boundary $S$ using a standard parametrisation in radians ranging from $-pi/2$ to $3\pi/2$ (horizontal axis). The vertical axis corresponds to time. The cross-correlations $\hat{G}(\mathbf{x_A},\mathbf{x},k)\hat{G}^*(\mathbf{x_B},\mathbf{x},k)$ yield the phase difference (travel-time difference) of the signals arriving from $\mathbf{x}$ to $\mathbf{x_A}$ and $\mathbf{x_B}$, respectively (this travel time difference is negative for one half of the boundary). A distinct profile comprised of waveform arrivals at these travel-time differences can be plainly

appreciated in this panel. The right panel of the Figure shows the waveform that results

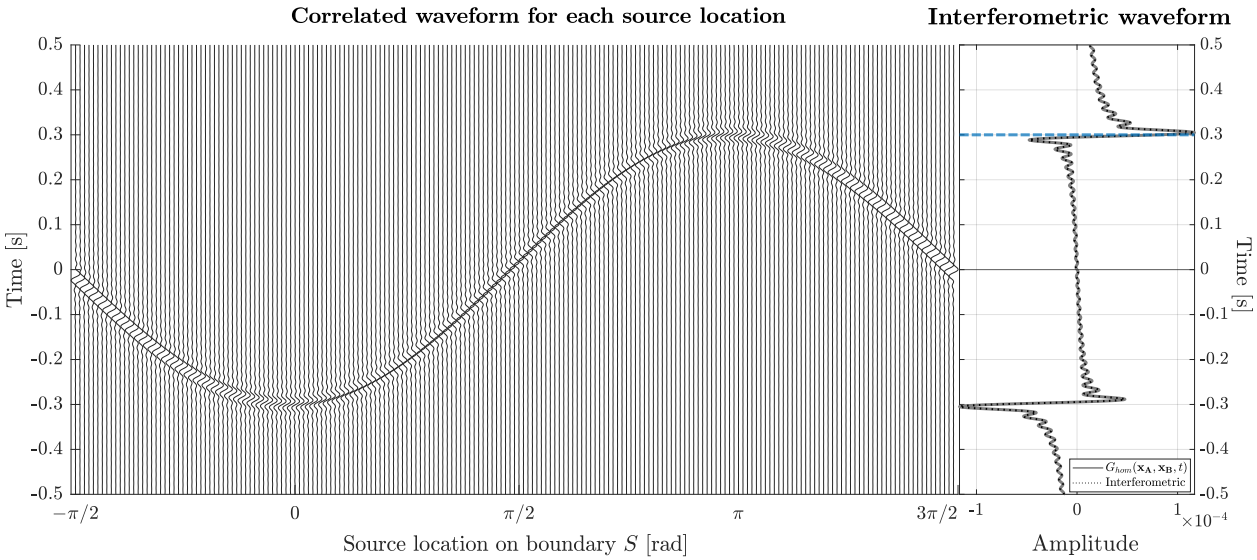


**Figure 1.2:** Illustration of the wavefield interferometry approximation (1.1.1). The time domain representation of the integrand of (1.1.1) (**left**) is shown for each source location, and the waveform resulting from the sum of these integrands (**right**) in solid grey. The right panel also shows the homogeneous Green's function (1.1.2) in black dashes, and the inter-receiver arrival time $t = |\mathbf{x_A} - \mathbf{x_B}|/c$ highlighted in blue dashes. The homogeneous Green's function and the inter-receiver estimate agree.

from stacking the traces from the left panel along all the source locations in solid gray, i.e. performing the integral in the right hand side of (1.1.1), as well as the homogeneous inter-receiver Green's function in the left hand side of (1.1.1) in black dashes, for comparison. These two waveforms are virtually indistinguishable, showcasing the effectiveness of the interferometric approximation. Note that the waveform in the right panel exhibits an arrival at $t = 0.3$ s, highlighted with blue dashes, consistent with the inter-receiver distance of 300 m and medium speed of $c = 1000$ m. There is a corresponding arrival at $t = -0.3$ s, in agreement with the superposition of the negative time-reverse of the inter-receiver Green's function in the right hand side of (1.1.1). Interestingly, we can see that when the cross-correlation waveforms from the right panel are added over the source locations, all the phase differences cancel out except for the regions around the stationary points of this profile, which correspond to the source locations along the axis through the inter-receiver pair (which was arranged horizontally in this example). This is in fact not a coincidence, but a consequence of the principle of stationary phase, which lies at the core of the physical interpretation of the interferometric equation (1.1.1). The stationary phase approximation and its use in wavefield interferometry is studied in Chapter 3.

Negative-time arrivals are generally referred to as *acausal* arrivals. They arise as a

consequence of the antisymmetric behaviour of the homogeneous Green's function (1.1.2), which includes the superposition of a time-reversed (complex-conjugated) copy of the inter-receiver Green's function. The homogeneous Green's function (1.1.2) arises quite naturally during the construction of interferometric representations, as will be seen in Section 1.2.3. The antisymmetric behaviour of the interferometric estimate is well known and commonly addressed in practice through various signal processing procedures, such as averaging the causal (positive-time) and acausal (negative-time) portions of the waveform (Bensen et al., 2007), or applying a Hilbert transform to the interferometric spectrum (Purves, 2014), thus deriving an estimate for the inter-receiver Green's function $\hat{G}(\mathbf{x_A}, \mathbf{x_B}, k)$ rather than its homogeneous version $\hat{G}_{\text{hom}}(\mathbf{x_A}, \mathbf{x_B}, k)$. The choice of post-processing is generally subjective and depends on the data available and the type of Green's function one wishes to estimate. In this work, the homogeneous Green's function (1.1.2) is used as the benchmark against which all approximations are compared, in order to maintain consistency with the mathematical derivations that lead to the approximation (1.1.1), and hence we do not consider processing procedures beyond the acquisition of the interferometric estimate of the homogeneous Green's function. Furthermore, for the sake of clarity, the term *acausal* is used throughout this work to refer to the negative-time but mathematically correct arrivals. On the other hand, as previously stated, the term *spurious* is used to refer to any events in the waveform that do not correspond to the correct inter-receiver arrival time $t = |\mathbf{x_A} - \mathbf{x_B}|/c$, causal or acausal.

In the following Section we present the analytical derivations and assumptions that lead to the interferometric approximation (1.1.1).

**Remark 1.1.1.** Different formulations of cross-correlational interferometry can be found across the literature. They only differ on whether there is a frequency factor in front of the integral, and whether the homogeneous Green's function retrieved is a sum rather than a difference as in (1.1.1). All of these formulations are correct and essentially equivalent (Wapenaar and Fokkema, 2006). When there is a frequency factor in front of the integral, as in (1.1.1), the point sources are physically interpreted as sources of volume injection *rate* (as opposed to volume injection, see for example Galetti et al. (2013)), recognising the product by a frequency as a differentiation in the time domain. When the homogeneous Green's function recovered is a sum rather than a difference, the resulting waveform is symmetric about the origin rather than the antisymmetric form shown in the right panel of Figure 1.2, and twice the real part of the inter-receiver Green's function is recovered as opposed to twice the imaginary part as in (1.1.2). The sign difference stems from the particular choice of construction of the representation theorems presented in Section 1.2.

Equation (1.1.1) is at the heart of interferometric applications, and the focus of this thesis. Its theoretical foundation lies on Green's function representation theorems, but a number of

assumptions and simplifications are necessary to arrive at the simplified formulation (1.1.1) from these general representations. In the following sections, we present the representation theorems and discuss these assumptions and simplifications.

## 1.2 Theoretical background

In this Section, we present the Green's function representation theorems that lead to the interferometric approximation (1.1.1). These theorems comprise the fundamental theoretical basis of wavefield interferometry (Schuster et al., 2004; Wapenaar and Fokkema, 2006). While these results have become standard in current interferometric literature, their proof is briefly presented here as it provides insight into the implicit assumptions in the formulation of wavefield interferometry. Since this thesis deals with estimation errors in (1.1.1), the approximations and assumptions required to arrive at (1.1.1) are highlighted, and discussed in further detail in Section 1.4.

Intuitively, a Green's function is the response of a linear differential operator to an impulse forcing, where the operator is defined on a domain with set boundary conditions. While commonly referred to as a function, it is in fact a Schwartz distribution. To be precise, if $\mathcal{L}$ is a linear differential operator, then the Green's function is a distributional solution to

$$\mathcal{L}\left[G(\mathbf{x},\mathbf{y})\right] = \delta(\mathbf{x}-\mathbf{y})\,, \qquad \delta \in \mathcal{D}(\mathbb{R}^n)$$

where $\mathcal{D}(\mathbb{R}^n)$ denotes the space of Schwartz distributions over $\mathbb{R}^n$, and the distribution $\delta$ is the Dirac delta, i.e. a distribution such that

$$\int_{\mathbb{R}^n} f(\mathbf{y})\delta(\mathbf{x}-\mathbf{y})d\mathbf{y} = f(\mathbf{x}) \qquad \forall\, f \in C_0^\infty(\mathbb{R}^n)\,, \tag{1.2.1}$$

where $C_0^\infty(\mathbb{R}^n)$ denotes the space of infinitely differentiable functions over $\mathbb{R}^n$ (i.e. a test function space). Equation (1.2.1) is sometimes referred to as the sifting property of the delta distribution. Because of its physical interpretation, the delta distribution is also known as a point or impulsive source. Uniqueness is usually established by boundary conditions or other physically imposed criteria. Green's functions are profoundly useful in finding more general responses to inhomogeneous linear operators, since due to the sifting property of the delta distribution, any forcing can be expressed as a superposition of point sources. Invoking the principle of superposition yields the property that the response of a linear differential operator to an arbitrary forcing can be found by convolving the Green's function with the forcing, as long as the Green's function is known.

This work is concerned with Green's functions as fundamental solutions of the Helmholtz equation in the distributional sense, i.e. for the Helmholz operator $\mathcal{L} = (\nabla^2_{\mathbf{x}} + k^2)$, the Helmholtz Green's function is defined as the solution to the equation

$$(\nabla^2_{\mathbf{x}} + k^2)\hat{G}(\mathbf{x}, \mathbf{y}, k) = \delta(\mathbf{x} - \mathbf{y})\,, \tag{1.2.2}$$

where $\delta$ is the distribution that satisfies the sifting property (1.2.1). In this work, we consider free-space Green's functions in one, two or three dimensions (see Section 1.2.6) where uniqueness is established by appropriate radiation conditions at infinity (Section 1.2.2).

Following the above discussion and intuitively speaking, if one knows the Helmholtz Green's function of a medium, one knows in theory how waves travel through the medium and in consequence a wealth of information about the medium itself (the Helmholtz operator being the frequency domain counterpart of the d'Alembert operator, i.e. the wave equation). Thus, it is no surprise that wavefield interferometry is centred on estimating Green's functions of the medium.

### 1.2.1 Interferometric representation theorem of the convolution type

Assume a two or three dimensional medium as depicted in Figure 1.1, where a pair of receivers have been placed at locations $\mathbf{x_A}$ and $\mathbf{x_B}$, and these receivers are surrounded by an arbitrary boundary of point sources $\mathbf{x} \in S$. Then we have the following result.

**Theorem 1.2.1** (Representation theorem of the convolution type, Schuster (2009))**.** *Let $\hat{G}(\mathbf{x}, \mathbf{y}, k)$ denote a fundamental solution to the Helmoltz equation for spatial locations $\mathbf{x}$ and $\mathbf{y}$ and a wavenumber $k$, as defined in (1.2.2). Then*

$$\begin{aligned}\hat{G}(\mathbf{x_B}, \mathbf{x_A}, k) - \hat{G}(\mathbf{x_A}, \mathbf{x_B}, k) = \oint_S \hat{G}(\mathbf{x}, \mathbf{x_A}, k)\, \partial\mathbf{n}_{\mathbf{x}} \hat{G}(\mathbf{x}, \mathbf{x_B}, k) \\ - \hat{G}(\mathbf{x}, \mathbf{x_B}, k)\, \partial\mathbf{n}_{\mathbf{x}} \hat{G}(\mathbf{x}, \mathbf{x_A}, k)\, d\mathbf{x},\end{aligned} \tag{1.2.3}$$

*where $\partial\mathbf{n}_{\mathbf{x}} = \mathbf{n}_{\mathbf{x}} \cdot \nabla_{\mathbf{x}}$, i.e. the derivative of with respect to the outward normal direction at point $\mathbf{x}$ on the boundary $S$.*

*Proof.* Consider the Helmholtz equations for the medium's response to a point source at $\mathbf{x}$, recorded respectively at locations $\mathbf{x_A}$ and $\mathbf{x_B}$ for a wavenumber $k$,

$$(\nabla^2_{\mathbf{x}} + k^2)\hat{G}(\mathbf{x}, \mathbf{x_A}, k) = -\delta(\mathbf{x} - \mathbf{x_A})\,, \tag{1.2.4}$$

$$(\nabla^2_{\mathbf{x}} + k^2)\hat{G}(\mathbf{x}, \mathbf{x_B}, k) = -\delta(\mathbf{x} - \mathbf{x_B})\,, \tag{1.2.5}$$

for the Dirac delta distribution $\delta(\mathbf{x}-\mathbf{y})$ defined in (1.2.1). Multiplying (1.2.4) by $\hat{G}(\mathbf{x}, \mathbf{x_B}, k)$, (1.2.5) by $\hat{G}(\mathbf{x}, \mathbf{x_A}, k)$, and subtracting the resulting expressions yields

$$\begin{aligned}\hat{G}(\mathbf{x}, \mathbf{x_B}, k)\nabla^2_{\mathbf{x}}\hat{G}(\mathbf{x}, \mathbf{x_A}, k) - \hat{G}(\mathbf{x}, \mathbf{x_A})\nabla^2_{\mathbf{x}}\hat{G}(\mathbf{x}, \mathbf{x_B}, k) = \\ \hat{G}(\mathbf{x}, \mathbf{x_A}, k)\delta(\mathbf{x} - \mathbf{x_B}) - \hat{G}(\mathbf{x}, \mathbf{x_B}, k)\delta(\mathbf{x} - \mathbf{x_A})\,.\end{aligned} \tag{1.2.6}$$

Using the product rule, the terms on the left hand side of this expression can be written as

$$\begin{aligned}\hat{G}(\mathbf{x}, \mathbf{x_B}, k)\nabla^2_{\mathbf{x}}\hat{G}(\mathbf{x}, \mathbf{x_A}) = \\ \nabla_{\mathbf{x}} \cdot \Big[\hat{G}(\mathbf{x}, \mathbf{x_B}, k)\nabla_{\mathbf{x}}\hat{G}(\mathbf{x}, \mathbf{x_A}, k)\Big] - \nabla_{\mathbf{x}}\hat{G}(\mathbf{x}, \mathbf{x_B}, k) \cdot \hat{G}(\mathbf{x}, \mathbf{x_A}, k)\,,\end{aligned}$$

and similarly for $\hat{G}(\mathbf{x}, \mathbf{x_A}, k)\nabla^2_{\mathbf{x}}\hat{G}(\mathbf{x}, \mathbf{x_B}, k)$,

$$\begin{aligned}\hat{G}(\mathbf{x}, \mathbf{x_A}, k)\nabla^2_{\mathbf{x}}\hat{G}(\mathbf{x}, \mathbf{x_B}) = \\ \nabla_{\mathbf{x}} \cdot \Big[\hat{G}(\mathbf{x}, \mathbf{x_A}, k)\nabla_{\mathbf{x}}\hat{G}(\mathbf{x}, \mathbf{x_B}, k)\Big] - \nabla_{\mathbf{x}}\hat{G}(\mathbf{x}, \mathbf{x_A}, k) \cdot \hat{G}^*(\mathbf{x}, \mathbf{x_B}, k)\,.\end{aligned}$$

Substituting these expressions into (1.2.6), and integrating over an arbitrary volume $V$ enclosing $\mathbf{x_A}$ and $\mathbf{x_B}$ we have

$$\begin{aligned}\int_V \nabla_{\mathbf{x}} \cdot \Big[\hat{G}(\mathbf{x}, \mathbf{x_B}, k)\nabla_{\mathbf{x}}\hat{G}(\mathbf{x}, \mathbf{x_A}, k)\Big] - \nabla_{\mathbf{x}} \cdot \Big[\hat{G}(\mathbf{x}, \mathbf{x_A}, k)\nabla_{\mathbf{x}}\hat{G}(\mathbf{x}, \mathbf{x_B}, k)\Big]\, d\mathbf{x} = \\ \hat{G}(\mathbf{x_A}, \mathbf{x_B}, k) - \hat{G}(\mathbf{x_B}, \mathbf{x_A}, k)\,.\end{aligned} \tag{1.2.7}$$

where the sifting property of the delta distribution has been used on the right hand side. Next, applying the divergence theorem we have

$$\int_V \nabla_{\mathbf{x}} \cdot \Big[\hat{G}(\mathbf{x}, \mathbf{x_B}, k)\nabla_{\mathbf{x}}\hat{G}(\mathbf{x}, \mathbf{x_A}, k)\Big] = \oint_S \hat{G}(\mathbf{x}, \mathbf{x_B}, k)\nabla_{\mathbf{x}}\hat{G}(\mathbf{x}, \mathbf{x_A}, k) \cdot \mathbf{n}_{\mathbf{x}}\, d\mathbf{x}\,,$$

where $S = \partial V$ and $\mathbf{n}_{\mathbf{x}}$ is the outward pointing unit vector normal to $S$ at $\mathbf{x}$, and similarly for the remaining term in the left hand side of (1.2.7), finally yielding

$$\hat{G}(\mathbf{x_B}, \mathbf{x_A}, k) - \hat{G}(\mathbf{x_A}, \mathbf{x_B}, k) = \oint_S \hat{G}(\mathbf{x}, \mathbf{x_A}, k)\, \partial\mathbf{n}_{\mathbf{x}}\hat{G}(\mathbf{x}, \mathbf{x_B}, k) - \hat{G}(\mathbf{x}, \mathbf{x_B}, k)\, \partial\mathbf{n}_{\mathbf{x}}\hat{G}(\mathbf{x}, \mathbf{x_A}, k)\, d\mathbf{x},$$

where $\partial\mathbf{n}_{\mathbf{x}} = \mathbf{n}_{\mathbf{x}} \cdot \nabla_{\mathbf{x}}$. □

Representation (1.2.3) is referred to as of the convolution type because the integrand in the right hand side is comprised of products in the frequency domain, corresponding to convolutions in the time domain. The terms of the form $\hat{G}(\mathbf{x}, \mathbf{x}', k)$ and $\partial \mathbf{n}_{\mathbf{x}} \hat{G}(\mathbf{x}, \mathbf{x}', k)$ represent respectively responses of the medium at a location $\mathbf{x}'$ to point sources (referred to as monopoles) and a derivative of this response (known as dipole sources). The main utility of the representation theorem of the convolution type in this work is that it leads to the well-known (Aki and Richards, 2002; Wapenaar and Fokkema, 2006; Schuster, 2009) source-receiver reciprocity relation

$$\hat{G}(\mathbf{x}, \mathbf{y}, k) = \hat{G}(\mathbf{y}, \mathbf{x}, k)\,. \tag{1.2.8}$$

This relationship states that the trace is the same even if we interchange the location of the source and the receiver. It is true in general for any type of medium velocity and for media with variable density (Aki and Richards, 2002). The reciprocity relation can be established from (1.2.3) making use of two intuitive and physically appropriate approximations: the Sommerfeld radiation condition and the far-field approximation. The latter are indispensable in establishing the interferometric approximation (1.1.1), and therefore we briefly present them below. We explain how they lead to the reciprocity relation (1.2.8), and most importantly we use them in the sequel to establish the connection between (1.1.1) and the second fundamental theorem of wavefield interferometry.

### 1.2.2 The Sommerfeld radiation condition and the far field approximation

To establish the reciprocity relation (1.2.8) note that an outgoing Green's function $\hat{G}$ satisfies the Sommerfeld radiation condition at infinity (Bleistein and Handelsman, 1986),

$$\left(\frac{\partial \hat{G}}{\partial r} - ik\hat{G}\right) \sim o\left(\frac{1}{r}\right) \text{ as } r \to \infty\,, \tag{1.2.9}$$

where $r$ is the distance between the source and the receiver, and order notation[1] is used. The Sommerfeld radiation condition derives from the physical principle that energy radiated from sources must scatter to infinity, and that no energy may be radiated from infinity into the field (Sommerfeld, 1949). It is imposed on the Helmholtz equation to ensure uniqueness of outgoing solutions in unbounded domains (Bleistein, 2012). It has the advantage of being

[1]This is standard little-o notation for asymptotic decay. Namely, given two functions $f(x)$ and $g(x)$, we say $f(x) \sim o(g(x))$ as $x \to \infty$ if $\lim_{x\to\infty} \dfrac{f(x)}{g(x)} = 0$.

consistent with physical intuition: for an observer sufficiently far away from any finite domain from which the wave originates, the finite domain in question shrinks to a point (relative in size to the scale of the range of the wave). Hence, for such an observer, the medium response corresponds to a point source, i.e. the solutions should behave as the Green's function in the far-field. To quantify the asymptotic regime in which this radiation condition should be valid, one must consider that the distance between the source and the observer (receiver) should be large relative to the wavelength. Hence, it is the product of the wavenumber $k$ (which corresponds to cycles per unit of distance) and the distance between the source and the receiver $r$ that should be large. This results in the appropriate non-dimensional quantity $kr$, and the requirement that $kr \gg 1$.

The reciprocity relation (1.2.8) follows from (1.2.3) by noting that the convolution representation theorem holds for an arbitrary boundary $S$. If in particular we take a boundary of radius $r$ such that $kr \gg 1$, we have that outgoing waves leave the boundary in an approximately perpendicular fashion, and hence the normal to $S$ coincides with the radial direction. In consequence, when the surface $S$ is sufficiently far from a receiver $\mathbf{x_R}$ we have

$$\partial \mathbf{n}_{\mathbf{x}} \hat{G}(\mathbf{x}, \mathbf{x_R}, k) \sim \frac{\partial}{\partial r} \hat{G}(\mathbf{x}, \mathbf{x_R}, k)\,. \tag{1.2.10}$$

Statements of the type (1.2.2) are known as far-field approximations, and they also hold under complex conjugation. Their impact on the interferometric approximation (1.1.1) is discussed later on. Using Sommerfeld's radiation condition (1.2.9) along with (1.2.2), we can assert that if $kr \gg 1$, then

$$\frac{\partial}{\partial r} \hat{G}(\mathbf{x}, \mathbf{x_R}, k) = ik\, \hat{G}(\mathbf{x}, \mathbf{x_R}, k) - \frac{1}{r} \hat{G}(\mathbf{x}, \mathbf{x_R}, k)\,,$$

Therefore

$$\partial \mathbf{n}_{\mathbf{x}} \hat{G}(\mathbf{x}, \mathbf{x_R}, k) \approx ik\, \hat{G}(\mathbf{x}, \mathbf{x_R}, k)\,. \tag{1.2.11}$$

Substituting approximations (1.2.11) into the representation theorem of the convolution type (1.2.3) for each receiver and simplifying yields relation (1.2.8). Source-receiver reciprocity is assumed throughout this work. We now present the second fundamental result of wavefield interferometry.

### 1.2.3 Interferometric representation theorem of the correlation type

Taking equation (1.2.4) in conjunction with the conjugate of (1.2.5), and following an entirely analogous procedure as in Theorem 1.2.1 yields after applying source-receiver reciprocity (1.2.8) the following

**Theorem 1.2.2** (Representation theorem of the correlation type, Wapenaar and Fokkema (2006))**.** *Let $\hat{G}(\mathbf{x}, \mathbf{y}, k)$ denote a fundamental solution to the Helmoltz equation for spatial locations $\mathbf{x}$ and $\mathbf{y}$ and a wavenumber $k$, as defined in (1.2.2). Then*

$$\hat{G}(\mathbf{x_A}, \mathbf{x_B}, k) - \hat{G}^*(\mathbf{x_A}, \mathbf{x_B}, k) = \oint_S \hat{G}(\mathbf{x_A}, \mathbf{x}, k)\partial\mathbf{n_x}\hat{G}^*(\mathbf{x_B}, \mathbf{x}, k) - \partial\mathbf{n_x}\hat{G}(\mathbf{x_A}, \mathbf{x}, k)\hat{G}^*(\mathbf{x}_B, \mathbf{x}, k)\, d\mathbf{x}\,. \tag{1.2.12}$$

The interferometric equation (1.2.12) can be interpreted as follows. The terms of the form $\hat{G}(\mathbf{x}, \mathbf{x}', k)$ and $\partial\mathbf{n_x}\hat{G}(\mathbf{x}, \mathbf{x_A}, k)$ represent respectively responses of the medium at a location $\mathbf{x}'$ to point sources (referred to as monopoles) and a derivative of this response (known as dipole sources) at a source location $\mathbf{x}$ on the boundary $S$. The products $\hat{G}(\mathbf{x}, \mathbf{x_A}, k)\, \partial\mathbf{n_x}\hat{G}^*(\mathbf{x}, \mathbf{x_B}, k)$ correspond in the time domain to the convolution of the waveform recorded at receiver $\mathbf{x_A}$ form that source with the time-reverse of the waveform recorded at $\mathbf{x_B}$ from the same source, i.e. a cross-correlation. Hence the right hand side of (1.2.12) can be interpreted as cross-correlating the monopole and dipole responses recorded at $\mathbf{x_A}$ and $\mathbf{x_B}$ for each point source $\mathbf{x}$, and then stacking (integrating) these cross-correlations along $S$. On the other hand, the left hand side is simply the homogeneous Green's function defined in (1.1.2) (the superposition of the inter-receiver Green's function and its negative time-reverse). This equation is exact in a lossless medium[2] (Wapenaar and Fokkema, 2006; Schuster, 2009) and the choice of $S$ is arbitrary as long as it encloses $\mathbf{x_A}$ and $\mathbf{x_B}$. While there are other ways of performing interferometry, such as deconvolution (Ravasi et al., 2015), these methods are closely mathematically related and each has its own drawbacks and advantages (see Wapenaar et al. (2011) for a systematic comparison of different methods). This work is concerned specifically with interferometry in its cross-correlational form, which remains a very widely used form of interferometry in both practice and theory. Representations (1.2.12) and (1.2.3) are standard results in wavefield interferometry and form the basis of this discipline. Proofs can be found in standard literature on interferometry, see for example Schuster (2009).

[2]Broadly speaking, a lossless medium is such that the energy of a propagating wave is not significantly lost as the wave travels through the medium. The amplitude of the wave is preserved. Otherwise, the medium is often referred to as *attenuative*.

**Remark 1.2.1.** Note that the representation theorems assume that recordings are available for each source location $\mathbf{x} \in S$ for an enclosing boundary $S$. Therefore, there is an implicit assumption that these source locations contribute equal energy to the integration and that they are isotropically distributed around the receivers. Furthermore, the use of wavefield interferometry in applications carries an implicit assumption that the sources of noise in real settings are point sources.

While having the exact representation (1.2.12) is in principle advantageous, this equation can be ill-suited for real world applications for a number of reasons. Note that the integrand requires the evaluation of two separate correlations. It also assumes that both monopole and dipole source recordings are available for every source location $\mathbf{x} \in S$, which is often not the case in practice (Schuster, 2009; Wapenaar and Fokkema, 2006). This motivates the simplification of (1.2.12) to the form (1.1.1), where the integrand involves only one cross-correlation of monopole recordings. In what follows, we summarise this simplification using the Sommerfeld radiation condition and the far-field approximation.

### 1.2.4 Simplification of the cross-correlation interferometric representation

Using the far-field approximation (1.2.2) and source-receiver reciprocity directly in the representation theorem of the correlation type (1.2.12) yields

$$\hat{G}_{\text{hom}}(\mathbf{x_A}, \mathbf{x_B}, k) \approx -2ik \oint_S \hat{G}(\mathbf{x_A}, \mathbf{x}, k)\hat{G}^*(\mathbf{x_B}, \mathbf{x}, k)\, d\mathbf{x}\,, \tag{1.2.13}$$

where $\hat{G}_{\text{hom}}(\mathbf{x_A}, \mathbf{x_B}, k)$ is the homogeneous inter-receiver Green's function defined in (1.1.2). The error introduced in this approximation through the far-field assumption can be estimated using (1.2.2) and (1.2.11) to derive, for example,

$$\partial\mathbf{n_x}\hat{G}(\mathbf{x}, \mathbf{x_A}, k) - ik\,\hat{G}(\mathbf{x}, \mathbf{x_A}, k) \approx -\frac{1}{r}\hat{G}(\mathbf{x}, \mathbf{x_A}, k)\,,$$

and similarly for $\mathbf{x_B}$. That is, the error incurred by using the monopole retrieval (1.2.13) to retrieve the homogeneous Green's function $\hat{G}_{\text{hom}}(\mathbf{x_B}, \mathbf{x_A}, k)$ is negligible in the far-field regime ($kr \gg 1$).

**Remark 1.2.2.** The far-field approximation applies only to Green's functions describing arrivals propagating in the same direction, which is not always the case in practice. Wapenaar and Fokkema (2006) show that the far-field approximation introduces spurious signals that arise from the interactions of incoming and outgoing monopole and dipole responses at the

boundary $S$. They argue that when the sources are sufficiently random, these spurious signals integrate incoherently and cancel out. Hence, there is an implicit assumption that the sources surrounding the receiver pair are statistically uncorrelated.

### 1.2.5 Passive noise interferometry

The theory presented so far assumes that the sources on the boundary $S$ are point sources for which individual medium responses can be measured at both receiver locations. In practice, recordings for individual active source locations are often not available. Hence, it becomes necessary and even desirable to rely on noise that is already present in the environment, commonly referred to as passive or ambient noise. When these noise sources are uncorrelated in the statistical sense, it has been shown that the homogeneous inter-receiver Green's function can still be estimated by taking an average of the cross-correlations over many recordings[3] (Weaver and Lobkis, 2001; Derode et al., 2003; Snieder, 2004; Wapenaar and Fokkema, 2006). To be precise, let $\hat{p}(\mathbf{x_R}, k)$ be a recording of ambient noise at a receiver location $\mathbf{x_R}$ that can be represented as

$$\hat{p}(\mathbf{x_R}, k) = \oint_S \hat{F}(\mathbf{x}', k)\hat{G}(\mathbf{x_R}, \mathbf{x}', k)d\mathbf{x}' \,,$$

where $\hat{F}(\mathbf{x}, \omega)$ characterizes the unknown source signature, i.e. the medium response is simply the convolution of the source term with the Green's function of the medium. Further assume that, on average, the source terms satisfy the statistical uncorrelatedness assumption

$$\mathbb{E}\left[\hat{F}(\mathbf{x}', k)\hat{F}(\mathbf{x}'', k)\right] \propto \delta(\mathbf{x}' - \mathbf{x}'')|\hat{s}(k)|^2 \,, \tag{1.2.14}$$

where $\mathbb{E}[\,\cdot\,]$ denotes the expected value with respect to independent recordings and $|\hat{s}(k)|^2$ is the power spectrum of the ambient noise. Then using (1.1.1) we have

$$\mathbb{E}\left[\hat{p}(\mathbf{x_A}, k)\hat{p}^*(\mathbf{x_B}, k)\right] \propto |\hat{s}(k)|^2\hat{G}_{\text{hom}}(\mathbf{x_A}, \mathbf{x_B}, k) \,. \tag{1.2.15}$$

**Remark 1.2.3.** The assumption of non-correlated noise sources (1.2.14) is widely used in theoretical and practical studies of wavefield interferometry. Equation (1.2.15) acknowledges implicitly that the amplitude is not expected to be accurately retrieved, and this in fact seems to be accepted across the discipline (Wapenaar and Fokkema, 2006; Halliday and Curtis, 2009; Kimman and Trampert, 2010; Wapenaar et al., 2010b). However, by that

[3] Or equivalently, cross-correlating very long recordings, assuming ergodicity which seems a reasonable assumption in practice.

same assumption the inter-receiver phases retrieved from ambient noise are assumed to be accurate. We address this assumption and its consequences in Chapter 4.

In the following section, we briefly summarise the Green's functions used throughout this work.

### 1.2.6 Green's functions of the Helmholtz equation

In this Section, we briefly introduce the free-space Green's functions of the Helmholtz equation in one, two, and three dimensions, for reference throughout this thesis. Detailed derivations of these Green's functions in an applied context may be found for example in Snieder and Van Wijk (2015). In what follows, we assume $k = \omega/c$ is a wavenumber for the angular frequency $\omega$ and a medium where waves propagate at a constant speed $c$. Recall that the Helmholtz operator is the frequency-domain equivalent of the wave equation, so that all these Green's functions describe in fact wavefield dynamics.

The one dimensional Helmholtz operator with a point source forcing is given by

$$\left(\frac{d^2}{dx^2} + k^2\right) \hat{G}(x, y, k) = -\delta(x - y)\,, \tag{1.2.16}$$

with corresponding Green's function given by

$$\hat{G}(x, y, k) = -\frac{i}{2k} e^{-ik\,|x-y|}\,. \tag{1.2.17}$$

In two and three dimensions the Helmholtz operator with a point source located at $\mathbf{y}$ is given by

$$\left(\nabla^2_{\mathbf{x}} + k^2\right) \hat{G}(\mathbf{x}, \mathbf{y}, k) = -\delta(\mathbf{x} - \mathbf{y})\,. \tag{1.2.18}$$

The corresponding Green's function in two dimensions is

$$\hat{G}(\mathbf{x}, \mathbf{y}, k) = -\frac{i}{4} H_0^{(2)}(k|\mathbf{x} - \mathbf{y}|)\,, \tag{1.2.19}$$

where $H_0^{(2)}(\cdot)$ denotes the Hankel function of the second kind and order zero, or the far-field Green's function

$$\hat{G}(\mathbf{x}, \mathbf{y}, k) = -\frac{i}{4} e^{-i\left(k|\mathbf{x}-\mathbf{y}| - \frac{\pi}{4}\right)} \sqrt{\frac{2}{\pi k|\mathbf{x} - \mathbf{y}|}}\,, \tag{1.2.20}$$

which is arrived at by considering the asymptotic behaviour of the Hankel function in (1.2.19) for large argument $k|\mathbf{x} - \mathbf{y}| \gg 1$ (see e.g., Goldstein and Thaler (1958), or Section 8.25 of Gradshteyn and Ryzhik (2014)). The far-field Green's function (1.2.20) is indeed appro-

priate in the regime where $k|\mathbf{x}-\mathbf{y}| \gg 1$ (see e.g., Appendix A of Galetti et al. (2013)). Finally the Green's function in three dimensions is given by

$$\hat{G}(\mathbf{x},\mathbf{y},k) = \frac{1}{4\pi|\mathbf{x}-\mathbf{y}|}e^{-ik|\mathbf{x}-\mathbf{y}|}\,. \tag{1.2.21}$$

**Remark 1.2.4.** Note that the phase of these Green's functions generally involve a term of the form

$$k|\mathbf{x}-\mathbf{y}| = \omega\frac{|\mathbf{x}-\mathbf{y}|}{c}\,,$$

so that these phases carry information of the travel time of a wave generated from a source located at $\mathbf{y}$ and recorded at $\mathbf{x}$. These travel times in turn can provide insight on a medium's structure (for example, in imaging applications). On the other hand, the amplitude behaviour differs meaningfully across different dimensions, exhibiting varying kinds of dependence on the wavenumber (and hence, the frequency), and the distance between the source and the receiver $|\mathbf{x}-\mathbf{y}|$. These contrasting behaviours are discussed in general throughout this work.

## 1.3 Geophysical applications and limitations of current approaches

Wavefield interferometry is applied across a wide span of disciplines, including seismology (Draganov et al., 2006; Curtis et al., 2006, 2009), industrial exploration (Bakulin et al., 2007; Halliday and Curtis, 2010) and volcano monitoring (Brenguier et al., 2008; Wapenaar et al., 2010a). These applications exploit the fact that wavefield interferometry transforms real receivers into virtual sources, as described in the preceding sections, increasing in effect the number of available energy sources for subsequent use in imaging, tomography, and other applications. However, the first empirical demonstration of wavefield interferometry was not in geophysics but in a laboratory setting in 2001 by Weaver and Lobkis (2001), using ultrasonic noise. The first application of wavefield interferometry in a geophysical context was that of Campillo and Paul (2003), who used recordings of coda waves[4] at pairs of seismological stations in Mexico tens of kilometres apart to reconstruct the inter-station Green's functions. In 2005, an important regional application of cross-correlational inter-receiver interferometry was performed by Shapiro et al. (2005), who used cross-correlations of recordings in a receiver array in California to successfully image the known local geology.

[4] A seismic coda is the part of the seismic signal after the main earthquake arrival. They result from multiple scattering of the waves in the Earth's subsurface.

Since then, cross-correlational interferometry has been widely applied to recorded wavefields assumed be diffuse, as in Campillo and Paul (2003), or to arise from isotropic uncorrelated noise fields (Curtis et al., 2006; Wapenaar et al., 2011; Nicolson et al., 2012) that form a complete boundary of sources. Some real-world examples of sources that generate noise fields include natural phenomena such as maritime storms, ocean waves or wind (Gerstoft et al., 2006; Ardhuin et al., 2011, 2019), and man-made activities such as shipping (Sabra et al., 2005a) or even noise from road traffic (Halliday et al., 2008a; Nakata et al., 2011; Behm and Snieder, 2013) and trains (Quiros et al., 2016; Zhang et al., 2019; Brenguier et al., 2019; Dales et al., 2020).

While seismic interferometry is an exciting and rapidly developing field, there are still a number of limitations on its applications. As discussed in Section 1.2.3, an exact application requires that the medium be free from attenuation. Furthermore, the mathematical application of the divergence theorem, which requires a closed surface, translates into the practical requirement that when ambient noise is used (e.g. background noise in the Earth), the sources, must be homogeneously distributed around the receiver pair. However, many real sources of noise like the ones discussed above do no satisfy this requirement, and it is common to find situations such as the one illustrated in Figure 1.3, where a non-homogenous source distribution is depicted. Another requirement is that random sources be statistically

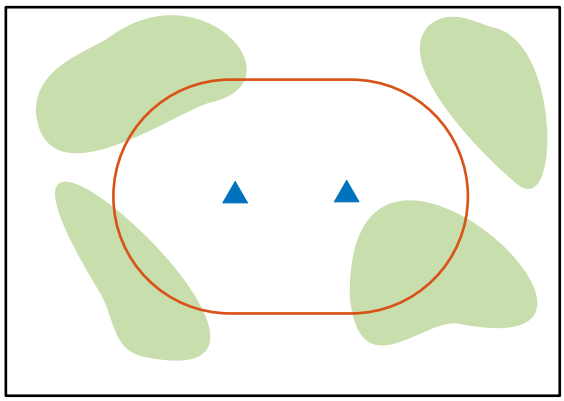

**Figure 1.3:** Inhomogeneously illuminated medium. Receivers are depicted as triangles and an ideal source boundary is portrayed in orange. Regions of increased source energy are depicted in green. These may be due to inhomogeneities in the medium, or in the source distribution.

uncorrelated, which is often not the case in practice (Curtis et al., 2006). Another complication is that the mathematical formulation of wavefield interferometry introduces the inherent assumption that the sources are ideal point sources that have been directly recorded at the receivers. When this is not the case, results in the introduction of spurious multiples,[5] which

[5]Multiples in seismic data refer to events that have undergone several reflections in the medium. They

can be mitigated only partially by filtering the data (Schuster et al., 2004; Snieder et al., 2006).

Many of these limitations arise as a consequence of the implicit assumptions imposed by the mathematical formulation of wavefield interferometry, and the fact that realistic sources of noise often do not satisfy them. In the following section, these assumptions and their impact on the interferometric estimate are discussed systematically.

## 1.4 Assumptions and approximations in wavefield interferometry

As discussed in Section 1.2, there is a hierarchy of assumptions and approximations necessary first, for the full interferometric representation (1.2.12) to be exact, and second, for the validity of the interferometric approximation (1.1.1) that arises from the full representation. The main assumptions and approximations have been pointed out throughout the previous sections. Here we condense and discuss them, explaining how they relate to the present work and to each other. Where approximations are involved, the implicit assumption is that the approximation in question is sufficiently good for practical applications.

**Assumption I: Sources are impulsive.**

The assumption that the recorded wavefields are impulsive point sources is implicit in the use of Green's functions and inherent to wavefield interferometry theory, as illustrated in Section 1.2. Noise sources in practice are not necessarily impulsive and this fact is acknowledged in literature. For example, the effect of transient sources[6] can be addressed with appropriately designed shaping filters, and cross-correlational interferometry can still be used effectively (Wapenaar and Fokkema, 2006). More generally, when sources are smeared in space or time, approaches involving de-blending and the point-spread-function, which quantifies the source blurring and can be empirically estimated, are effective in mitigating spurious effects of violating the impulsive-source assumption (Wapenaar et al., 2011, 2012; Zheng et al., 2011). While it is generally accepted that the amplitude may be unreliable, the phase is often assumed to be correct (Wapenaar and Fokkema, 2006).

occur when the signal does not take a direct path from the source to the receiver. They are spurious in the sense that they cause arrivals in the estimated signal that do not correspond to the inter-receiver travel time.

[6] A transient source is characterised by a wavelet which, while short-lived, is not an idealised delta pulse.

**Assumption II: The medium is lossless.**

As remarked in Section 1.2.3, equation (1.2.12) is exact in a lossless medium. In the presence of attenuation, interferometry by deconvolution (Wapenaar et al., 2008) or a propagator matrix approach (Mehta et al., 2007a) provide alternatives. Wapenaar et al. (2011) have shown that these deconvolution approaches compensate for attenuation in the medium.

**Assumption IIIa: The receivers are isotropically illuminated.**

The use of the divergence theorem in the derivation of the cross-correlation representation (1.2.12) implicitly imposes the condition that the receivers be surrounded by a closed boundary of sources. In practice this translates to the requirement that energy arrives at the receiver pair roughly equally from all azimuthal directions, and this is indeed a widely made assumption in theoretical derivations of seismic interferometry (see, e.g., Wapenaar and Fokkema (2006); Schuster (2009)). However, in many realistic applications the sources do not satisfy these conditions, and it has been shown that the azimuthal distribution of source variations is critical for successful interferometric retrieval (Fan and Snieder, 2009). Finally, spurious cross-terms are commonly assumed to integrate incoherently (Halliday and Curtis, 2008b), which relates to the assumption that sources are statistically uncorrelated (Assumption V).

**Assumption IIIb: If the medium is not isotropically illuminated, the variations are slowly varying.**

Some approaches have been developed to address non-ideal source distributions (Curtis and Halliday, 2010b; van Dalen et al., 2015; Fichtner et al., 2016), and it has been shown for example that cross-correlational interferometry is applicable in some regimes where the illumination is one-sided (Thorbecke and Wapenaar, 2008; Wapenaar et al., 2011; Brenguier et al., 2019) or more generally when sources can be found in the stationary phase zone of the receiver pair (see Assumption VI). However, it has also been shown that these azimuthal variations in source distribution are required to be smooth (Snieder et al., 2006; Fan and Snieder, 2009; Harmon et al., 2010) to mitigate spurious effects arising from the inhomogeneous intensity along the source boundary.

**Assumption IV: The far-field approximation.**

The far-field approximation is essential in reducing the full representation theorem (1.2.12), which requires that both dipole and monopole data be available for each source location,

to the more applicable interferometric approximation (1.1.1) involving only monopole data. In practical terms, the far-field approximation requires that the sources be far from the receivers, but this requirement is made with respect to the wavelength, so that at sufficiently high frequency regimes, cross-correlational interferometry continues to produce robust results in a wide array of applications. Wapenaar and Fokkema (2006) show that the far-field approximation is valid when arrivals are propagating in the same direction, but that in the presence of arrivals in multiple directions, "ghost" noise arises which is assumed to vanish in when the sources are random (Wapenaar and Fokkema, 2006). The latter assertion is connected to Assumption V below. On the other hand, the violation of the far-field approximation has been studied for example by Zheng et al. (2011), who propose a method to mitigate the resulting spurious arrivals using a cross-correlation kernel approach. Kimman and Trampert (2010) show that a thick boundary of sources surrounding the receivers may also be used to overcome spurious effects arising from the violation of the far-field assumption.

**Assumption V: The noise sources are statistically uncorrelated.**

The assumption that noise sources are statistically uncorrelated is widely found in literature (see, e.g., Lobkis and Weaver (2001); Wapenaar (2004); Snieder et al. (2009); Wapenaar et al. (2010a); Sabra (2010); Nakata et al. (2011); Wapenaar et al. (2011)). It is commonly stated in the form (1.2.15), or sometimes not explicitly acknowledged. Kimman and Trampert (2010) consider for example the connection between simultaneously acting sources and a slow rate of convergence to the inter-receiver Green's function estimate (a law of large numbers statement), and van Dalen et al. (2014) recognises that realistic sources present statistical correlations, proposing a deblending approach for the case of simultaneously acting sources. However, models introduced in these works and others (Weaver and Lobkis, 2005; Sabra, 2010; Lavoué et al., 2020) continue to implicitly assume that sources are statistically uncorrelated, even if acting simultaneously, and the effect of short and long-range statistical correlations in the sources remains unaccounted for, both theoretically and in practice.

**Assumption VI: The stationary phase approximation.**

While the stationary phase principle has been a long-standing classical technique of asymptotic analysis (Bleistein and Handelsman, 1986), it was first formally introduced to wavefield interferometry by Snieder (2004), who invoked this principle to approximate a triple integral with a single contour integration. The stationary phase principle is closely related to the physical interpretation of Fresnel zones (van Kampen, 1958), which are simply regions of constructive interference determined by the geometry of the receiver array. Since the

work of Snieder (2004), the stationary phase approximation has been commonly applied in wavefield interferometry, both in theoretical studies (Halliday and Curtis, 2008b; Snieder et al., 2009) and practical applications (e.g. Pinzon-Rincon et al. (2021)). While there have been some empirical explorations of the uncertainty associated with this approximation (see, e.g., Kimman and Trampert (2010)), the errors associated with the stationary phase method have not been formally addressed, and the effects of roughness and statistical source correlations have not been considered.

In this thesis we study the effects of anisotropic illumination (Assumption IIIa), noise roughness (Assumption IIIb), statistically correlated sources (Assumption V) and the stationary phase approximation (Assumption VI) on the inter-receiver interferometric estimate, both in active and passive source scenarios. We consider the interplay between the effects of violating these assumptions. Finally, note that the diffusivity assumption initially highlighted by Campillo and Paul (2003) has been shown not to be required (Wapenaar and Fokkema, 2006), and therefore that assumption is not part of this study. Moreover, we remark that the amplitude of the inter-receiver Green's function estimate is generally acknowledged to be unreliable (Wapenaar and Fokkema, 2006; Wapenaar et al., 2011), so that while amplitude effects are considered throughout, we pay particular attention to the phase of the interferometric estimate, which is fundamental for most applications.

## 1.5 Outline of the thesis

This work is organised as follows. Chapter 2 describes the general framework to quantify the errors introduced by anisotropic source variations as well as statistical correlations in the source. This framework is derived from first principles and encompasses both active source and passive noise interferometry. The source inhomogeneities along the contour and their local scale and long-range correlations are modelled using an appropriate covariance model, and the effects on the interferometric estimate are analised and numerically explored. A randomised multi-contour approach is proposed to mitigate these effects, and tested on synthetic data. Chapter 3 studies the widely used stationary phase approximation in wavefield interferometry using the framework derived in Chapter 2. The estimate is derived from first principles and the effects of source correlations and inhomogeneity are studied analytically and numerically, using a concentration inequality approach. The work of Olver (1974) is extended and applied to the case of ideal isotropic uncorrelated sources. Chapter 4 investigates the relationship between active source interferometry (as in (1.1.1)) and ambient noise interferometry (1.2.15), as well as the effects of violating the uncorrelatedness assumption (1.2.14). In that Chapter, we further study the effect of statistically correlated

sources on the inter-receiver Green's function estimated from ambient noise, and propose a method that significantly mitigates these effects and improves the phase retrieval. Chapter 5 concludes by summarising the results presented in this thesis, discussing the advantages and limitations of the proposed approaches as well as potential future work directions. Finally, Appendix A details how the framework developed in Chapter 2 can be extended to source-receiver interferometry, which would be required to apply the proposed multi-contour approach to real data, but is also a powerful and interesting form of interferometry in its own right. Appendix B contains technical details of the stationary phase derivations that were for brevity omitted from Chapter 3, in particular an analogous derivation for a line boundary that relates the stationary phase approximation to the method proposed in Chapter 4, as well as further numerical tests and considerations.

Chapter 2

# General framework for error quantification in Green's function interferometry

In this Chapter, we develop a general framework for error quantification framework in wavefield interferometry. This framework is derived from first principles and then incorporated into the interferometric representation theorems.

## 2.1 Introduction

Wavefield interferometry relies on the empirical acquisition of Green's functions of the Helmholtz equation, which is the frequency domain counterpart of the wave equation. In this thesis, we consider specific kinds of solutions to the inhomogeneous Helmholtz equation (namely, its fundamental solutions). Therefore, we consider wave dynamics governed by the linear wave equation

$$\partial_t^2 u(\mathbf{x},t) + c^2 \nabla_{\mathbf{x}}^2 u(\mathbf{x},t) = -f(\mathbf{x},\mathbf{x}',t)\,, \tag{2.1.1}$$

where $\mathbf{x}$ is a spatial variable in a medium of constant speed $c$ (in one, two or three dimensions) and $t$ stands for time. The spatial variable $\mathbf{x}'$ is a parameter of the forcing $f$, and in the present context it will often denote the location of a point source.

When wavefield recordings are acquired and used for interferometry, the following scenarios may be considered.

1. When the recorded waveform is the response of the medium to an instantaneous delta pulse emitted at a location $\mathbf{x}'$ and time $t = 0$. Then the forcing is given by

$$f(\mathbf{x},\mathbf{x}',t) = \delta(\mathbf{x}-\mathbf{x}')\delta(t)\,,$$

and in this case the solution $u(\mathbf{x}, t)$ to the wave equation (2.1.1) can be represented by the so-called free-space Green's function of the wave operator (i.e. the D'Alembert operator), denoted as

$$u(\mathbf{x}, t) = G(\mathbf{x}, \mathbf{x}', t)\,, \tag{2.1.2}$$

where the particular form of $G(\mathbf{x}, \mathbf{x}', t)$ is left unspecified in order to retain the generality of the subsequent derivations. The Green's function defined in (2.1.2) differs from those defined in Chapter 1 by a (constant) factor of $1/c^2$, which is henceforth omitted for simplicity. In this setup, conditions are ideal for the validity of the representation theorems presented in Section 1.2.

2. When the recorded waveform is the response of the medium to a pulse emitted at a location $\mathbf{x}'$ and time $t = 0$, scaled by an unknown random amplitude factor $\alpha(\mathbf{x}')$ that depends on the location of the pulse source $\mathbf{x}'$. In this scenario we set the forcing as

$$f(\mathbf{x}, \mathbf{x}', t) = \alpha(\mathbf{x}')\delta(\mathbf{x} - \mathbf{x}')\delta(t)\,,$$

The solution $u(\mathbf{x}, t)$ can be derived in a standard way by convolving the Green's function $G(\mathbf{x}, \mathbf{x}', t)$ of the linear wave operator with the forcing $f$. Using the sifting property of the delta distribution this results in a solution of the form

$$u(\mathbf{x}, t) = \alpha(\mathbf{x}')G(\mathbf{x}, \mathbf{x}', t)\,. \tag{2.1.3}$$

This type of solution no longer assumes that the medium is illuminated isotropically, i.e. that all source locations $\mathbf{x}'$ contribute an equal amount of energy to the interferometric estimate. Variations may be introduced for each source location by the random amplitude factor $\alpha(\mathbf{x}')$, and regions without sources can be accounted for by values of $\alpha$ close to zero. Therefore, incorporating these solutions in the standard retrieval formulas (for example (1.2.12) or (1.2.13)) allows us to account for the uncertainty introduced when the assumption of isotropic illumination is not satisfied. These derivations are presented later on in Section 2.2, as well as statistical study in Section 2.4 of the effect that the random amplitude $\alpha$ has on the retrieval when its values are determined by realisations of a correlated random field with varying degrees of smoothness. The situation where energy originates predominantly from the stationary phase regions (either by opportune noise distributions or deliberate signal processing measures) as well as the effects of noise correlation and smoothness are considered in Chapter 3.

3. When the recorded waveform is the response of the medium to an ambient noise source

where individual sources cannot necessarily be identified, due for example to simultaneously acting sources, sources in motion or sources generally smeared in time and space. This may be represented for example as a sequence of $n$ delta pulses centred at locations $\mathbf{x}_j$ for $j \in \{1, \ldots, n\}$ and firing at corresponding times $t_j$, and with associated amplitudes given by some function $A(\mathbf{x}_j)$, so that the forcing has the form

$$f(\mathbf{x}, \mathbf{x}'_1, \ldots, \mathbf{x}'_n, t) = \sum_{j=1}^{n} A(\mathbf{x}'_j)\delta(\mathbf{x} - \mathbf{x}'_j)\delta(t - t_j)\,,$$

or for sources spread over a continuous boundary $S$,

$$f(\mathbf{x}, S, t) = \int_S A(\mathbf{x}'(t'))\delta(\mathbf{x} - \mathbf{x}'(t'))\delta(t - t')\,dt'\,,$$

where the source boundary $S$ is parametrised by the time $t'$, since the exact locations of the sources are not usually known in this situation, and all one has access to is the recording of the sources acting over time. By the superposition principle, valid for linear systems, the medium response can be characterised by the sum of the Green's functions

$$u(\mathbf{x}, t) = \sum_{j=1}^{n} A(\mathbf{x}'_j)G(\mathbf{x}, \mathbf{x}'_j, t - t_j)\,. \tag{2.1.4}$$

or the convolution

$$u(\mathbf{x}, t) = \int_S \int_{-\infty}^{\infty} A(\mathbf{x}'(t'))\delta(\mathbf{x} - \mathbf{x}'(t'))G(\mathbf{x}, \mathbf{x}', t - t')dt'\,. \tag{2.1.5}$$

In this work, solutions of this form are denoted as

$$\beta(\mathbf{x}, t) := u(\mathbf{x}, t)\,, \tag{2.1.6}$$

That is, $\beta(\mathbf{x}, t)$ denotes an ambient noise recording at a receiver location $\mathbf{x}$ and time $t$, and the explicit source location and signature are not known. One may consider scenarios where the ambient noise source is spread over a continuous and explicit source boundary $S$, as in ambient noise generated for example by trains on railroads or traffic on highways, (see Brenguier et al. (2019) or Pinzon-Rincon et al. (2021) for two examples of this increasingly common scenario) or an implicit boundary, as in microseismic energy generated by storms and zones of constructive interference in the ocean, which is a well-known source of ambient noise (Ardhuin et al., 2011,

2019). The interferometric Green's function estimation from the former kinds of sources is considered in Chapter 4. We discuss common assumptions and the impact that violating them has on the interferometric estimate; as well as mitigation strategies to improve the phase estimate.

4. When the forcing is a combination of the latter two types, that is, identifiable point sources (with a random amplitude perturbation $\alpha$ that depends on the source location) as well as ambient noise where individual point sources of energy cannot always be identified. In this case the forcing may take the form

$$f(\mathbf{x},\mathbf{x}',\mathbf{x}'_1,\dots,\mathbf{x}'_n,t)=\alpha(\mathbf{x}')\delta(\mathbf{x}-\mathbf{x}')\delta(t)+\sum_{j=1}^{n}A(\mathbf{x}'_j)\delta(\mathbf{x}-\mathbf{x}'_j)\delta(t-t_j)\,,$$

or

$$f(\mathbf{x},\mathbf{x}',S',t)=\alpha(\mathbf{x}')\delta(\mathbf{x}-\mathbf{x}')\delta(t)+\oint_{S'}A(\mathbf{x}'(t'))\delta(\mathbf{x}-\mathbf{x}'(t'))\delta(t-t')\,dt'\,,$$

for a continuous boundary of sources $S$. The medium response in this case is denoted as

$$u(\mathbf{x},t)=\alpha(\mathbf{x}')G(\mathbf{x},\mathbf{x}',t)+\beta(\mathbf{x},t)\,, \tag{2.1.7}$$

where the principle of superposition has again been invoked and definition (2.1.6) has been used.

The first scenario is consistent with the formulation of the representation theorem of the correlation type (1.2.12) We note that active or controlled source interferometry corresponds to the second scenario, and ambient noise interferometry corresponds to the third scenario. While in practical settings signal processing procedures may be introduced to filter ambient noise out of active source acquisition, so that the quantities $\alpha$ and $\beta$ may not normally interact, we will develop our framework in the more general fourth scenario, which encompasses the first three, thus integrating both active source and ambient noise interferometry into a single formulation. Particular cases of the general framework may then be considered depending on the scenario under consideration.

Therefore, we approach quantification of uncertainty in wavefield interferometry by assuming that the empirical data is generally of the form (2.1.7) above, rather than the ideal response to a point source as given in (2.1.2) as required by interferometric theory. We incorporate this assumption into the representation theorem of the correlation type (1.2.12) and perform a procedure analogous to the derivation of the interferometric approximation (1.2.13) from (1.2.12), so that the resulting empirical interferometric estimate integrates the propagation of the amplitude inhomogeneity $\alpha$ and the ambient noise $\beta$ through the interferometric

machinery, and the approximations and assumptions discussed in Section 1.2. The resulting empirical estimate as well as the associated errors are presented below.

Taking the Fourier transform of the wave equation (2.1.1) yields the Helmholtz equation

$$\left(\nabla_{\mathbf{x}}^2 + k^2\right) \hat{u}(\mathbf{x}, k) = -\hat{f}(\mathbf{x}, \mathbf{x}', k)/c^2 \,, \tag{2.1.8}$$

where $\hat{\cdot}$ denotes data in the frequency domain, and the frequency dependency is expressed implicitly in terms of the wavenumber $k = \omega/c$. In the case when the forcing $\hat{f}(\mathbf{x}, \mathbf{x}', k)$ is a delta forcing, the solution of (2.1.8) is a Green's function of the Helmholtz equation. Consider instead the scenario where the forcing is of the form (2.1.7). Taking the Fourier transform of this time domain forcing yields

$$\hat{f}(\mathbf{x}, \mathbf{x}', S', k) = \alpha(\mathbf{x}')\delta(\mathbf{x} - \mathbf{x}') + \oint_S{}' \hat{A}(\mathbf{x}'', k)\delta(\mathbf{x} - \mathbf{x}'')d\mathbf{x}'' \,.$$

Invoking the principle of superposition we state that the solution to (2.1.8) with forcing $\hat{f}(\mathbf{x}, \mathbf{x}', S', k)$ is

$$\hat{u}(\mathbf{x}, k) = \hat{u}_1(\mathbf{x}, k) + \hat{u}_2(\mathbf{x}, k) \,,$$

where $\hat{u}_1(\mathbf{x}, k)$ is the solution of the Helmholtz equation, i.e.

$$\left(\nabla_{\mathbf{x}}^2 + k^2\right) \hat{u}_1(\mathbf{x}, k) = -\alpha(\mathbf{x}')\delta(\mathbf{x} - \mathbf{x}') \,, \tag{2.1.9}$$

and $\hat{u}_2(\mathbf{x}, k)$ satisfies the Helmholtz equation

$$\left(\nabla_{\mathbf{x}}^2 + k^2\right) \hat{u}_2(\mathbf{x}, k) = -\oint_S \hat{A}(\mathbf{x}'', k)\delta(\mathbf{x} - \mathbf{x}'')d\mathbf{x}'' \,. \tag{2.1.10}$$

Rearranging equation (2.1.9) below we have

$$(\nabla_{\mathbf{x}}^2 + k^2) \left( \frac{\hat{u}_1(\mathbf{x}, k)}{\alpha(\mathbf{x}')} \right) = -\delta(\mathbf{x} - \mathbf{x}') \,, \qquad \alpha(\mathbf{x}') > 0 \,,$$

where it is apparent that $\hat{u}_1(\mathbf{x}, k)/\alpha(\mathbf{x}')$ is the medium's response to a point source at $\mathbf{x}'$. Therefore, $\hat{u}_1(\mathbf{x}, k)$ is the Green's function $\hat{G}(\mathbf{x}, \mathbf{x}', k)$ of this Helmholtz equation, that is

$$\frac{\hat{u}_1(\mathbf{x}, k)}{\alpha(\mathbf{x}')} = \hat{G}(\mathbf{x}, \mathbf{x}', k) \,,$$

or equivalently

$$\hat{u_1}(\mathbf{x}, k) = \alpha(\mathbf{x}')\hat{G}(\mathbf{x}, \mathbf{x}', k)\,.$$

In other words, $\hat{u_1}(\mathbf{x}, k)$ is simply the Green's function of the Helmholtz operator rescaled by the factor $\alpha(\mathbf{x}')$. On the other hand, we define the solution $\hat{\beta}(\mathbf{x}, k)$ as above (see equation (2.1.6))

$$\hat{\beta}(\mathbf{x}, k) \coloneqq \hat{u}_2(\mathbf{x}, k)\,,$$

where $\hat{u}_2(\mathbf{x}, k)$ satisfies equation (2.1.10). That is, $\hat{\beta}(\mathbf{x}, k)$ is the medium's response to ambient or background noise measured at $\mathbf{x}$ for the wavenumber $k$. Hence, we define the *empirical Green's function* as the solution $\hat{u}(\mathbf{x}, k) = \hat{u}_1(\mathbf{x}, k) + \hat{u}_2(\mathbf{x}, k)$ to equation (2.1.8) and we denote it by

$$\hat{g}_{\alpha\beta}(\mathbf{x}, \mathbf{x}', k) = \alpha(\mathbf{x}')\hat{G}(\mathbf{x}, \mathbf{x}', k) + \hat{\beta}(\mathbf{x}, k)\,, \tag{2.1.11}$$

where the circumflex symbol $\hat{}$ denotes data in the frequency domain, a lowercase $\hat{g}$ is used to denote the empirical data, and an uppercase $\hat{G}$ denotes the true Green's functions. The subscripts $\alpha$ and $\beta$ are used to emphasise the dependence of the recorded data on these quantities. Note that (2.1.11) can also be derived directly by taking the Fourier transform of (2.1.7).

Henceforth, the unknown quantity $\alpha(\mathbf{x}')$ is interpreted as a random field over $\mathbb{R}^2$ or $\mathbb{R}^3$. For simplicity, the dependence on an event in the probability space is left implicit. Random fields are well-suited to model uncertainty in a geostatistical context (see e.g. Chiles and Delfiner (2009); Christakos (2012); Lantuéjoul (2013); Song and Jordan (2017)). Incorporating random fields into the framework has the further advantage of allowing for covariance structures that quantify spatial correlations in the sources. An appropriate choice of a geostatistical covariance model that accounts for long range correlations as well as smoothness is introduced in Section 2.4.2. The random field $\alpha$ may be real-valued, and hence only affect the amplitude of the signal, or it may be allowed take complex values in which case it may have an effect on the empirical phase as well as the amplitude. The construction (2.1.11) of an empirical Green's function captures the effect of uncertainty in the amplitude and phase of measured signals, and in the sections that follow will help quantify the deviation of interferometric estimates from the ideal Green's function. Note that when $\alpha \equiv 1$ and $\beta \equiv 0$, the empirical Green's function reduces to the actual Green's function, i.e.

$$\hat{g}_{10}(\mathbf{x}, \mathbf{x}', k) = \hat{G}(\mathbf{x}, \mathbf{x}', k)\,. \tag{2.1.12}$$

## 2.2 Interferometric retrieval of the empirical Green's function

### 2.2.1 Empirical representation theorem of the correlation type

Motivated by the representation theorem of the cross-correlation type, we define the *full empirical inter-receiver interferometric estimate* for a receiver pair $\mathbf{x_A}$, $\mathbf{x_B}$ as

$$\begin{aligned}\hat{\mathcal{G}}_{\text{int}}(\mathbf{x_A},\mathbf{x_B},k;\,\alpha,\beta) \coloneqq \oint_S \hat{g}_{\alpha\beta}(\mathbf{x_A},\mathbf{x},k)\,\partial\mathbf{n}_{\mathbf{x}}\hat{g}^*_{\alpha\beta}(\mathbf{x_B},\mathbf{x},k) \\ - \hat{g}^*_{\alpha\beta}(\mathbf{x_B},\mathbf{x},k)\,\partial\mathbf{n}_{\mathbf{x}}\hat{g}_{\alpha\beta}(\mathbf{x_A},\mathbf{x},k)\,d\mathbf{x}\,.\end{aligned} \tag{2.2.1}$$

where $S$ is a contour of sources and $\partial\mathbf{n}_{\mathbf{x}}g_{\alpha\beta}(\mathbf{x_R},\mathbf{x},k)$ denotes the directional derivative of $\hat{g}_{\alpha\beta}(\mathbf{x_R},\mathbf{x},k)$ with respect to the outward pointing normal to $S$ at $\mathbf{x}$. Substituting the definition for $g_{\alpha\beta}(\mathbf{x_R},\mathbf{x},k)$ given in (2.1.11) for each receiver yields

$$\begin{aligned}\hat{\mathcal{G}}_{\text{int}}(\mathbf{x_A},\mathbf{x_B},k;\,\alpha,\beta) = \oint_S |\alpha(\mathbf{x})|^2 \left(\hat{G}(\mathbf{x_A},\mathbf{x},k)\partial\mathbf{n}_{\mathbf{x}}\hat{G}^*(\mathbf{x_B},\mathbf{x},k) - \hat{G}^*(\mathbf{x_B},\mathbf{x},k)\partial\mathbf{n}_{\mathbf{x}}\hat{G}(\mathbf{x_A},\mathbf{x},k)\right) d\mathbf{x} \\ + \oint_S \left\{\,\alpha(\mathbf{x})\partial\mathbf{n}_{\mathbf{x}}\alpha^*(\mathbf{x}) - \alpha^*(\mathbf{x})\partial\mathbf{n}_{\mathbf{x}}\alpha(\mathbf{x})\,\right\} G(\mathbf{x_A},\mathbf{x},k)\hat{G}^*(\mathbf{x_B},\mathbf{x},k)\,d\mathbf{x} \\ + \hat{\beta}(\mathbf{x_A},k)\oint_S \partial\mathbf{n}_{\mathbf{x}}\left\{\alpha^*(\mathbf{x})\hat{G}^*(\mathbf{x_B},\mathbf{x})\right\} d\mathbf{x} \\ + \hat{\beta}^*(\mathbf{x_B},k)\oint_S \partial\mathbf{n}_{\mathbf{x}}\left\{\alpha(\mathbf{x})\hat{G}(\mathbf{x_A},\mathbf{x})\right\}\,d\mathbf{x} \\ +\beta(\mathbf{x_A},k)\beta^*(\mathbf{x_B},k)\ell(S)\,,\end{aligned} \tag{2.2.2}$$

where we have applied the product rule

$$\partial\mathbf{n}_{\mathbf{x}}\left\{\alpha(\mathbf{x})\hat{G}(\mathbf{x_R},\mathbf{x})\right\} = \alpha(\mathbf{x})\partial\mathbf{n}_{\mathbf{x}}\hat{G}(\mathbf{x_R},\mathbf{x}) + \hat{G}(\mathbf{x_R},\mathbf{x})\partial\mathbf{n}_{\mathbf{x}}\alpha(\mathbf{x})\,, \tag{2.2.3}$$

and $\ell(S)$ is a scaling factor depending on the length of the boundary $S$. Hence, we have assumed in (2.2.2) that the gradient of the random field $\alpha$ exists and is well defined. We make this assumption to gain further insight into (2.2.1). Note that in the ideal scenario where $\alpha \equiv 1$ and $\beta \equiv 0$, equation (2.2.2) reduces to the representation theorem of the correlation

type (1.2.12), so that

$$\hat{\mathcal{G}}_{\text{int}}(\mathbf{x_A}, \mathbf{x_B}, k;\, 1, 0) = \hat{G}_{\text{hom}}(\mathbf{x_A}, \mathbf{x_B}, k)\,. \tag{2.2.4}$$

Therefore, as a measure of error in the empirical retrieval (2.2.2), consider the difference

$$\begin{aligned}
\hat{\mathcal{G}}_{\text{int}}(\mathbf{x_A}, \mathbf{x_B}, k; \alpha, \beta) - \hat{\mathcal{G}}_{\text{int}}(\mathbf{x_A}, \mathbf{x_B}, k;\, 1, 0) = \\
&\oint_S \left\{|\alpha(\mathbf{x})|^2 - 1\right\} \left(\hat{G}(\mathbf{x_A}, \mathbf{x}, k)\partial_{\mathbf{n_x}}\hat{G}^*(\mathbf{x_B}, \mathbf{x}, k) - \hat{G}^*(\mathbf{x_B}, \mathbf{x}, k)\partial_{\mathbf{n_x}}\hat{G}(\mathbf{x_A}, \mathbf{x}, k)\right) d\mathbf{x} \\
&+ \oint_S \left\{\, \alpha(\mathbf{x})\partial_{\mathbf{n_x}}\alpha^*(\mathbf{x}) - \alpha^*(\mathbf{x})\partial_{\mathbf{n_x}}\alpha(\mathbf{x}) \,\right\} G(\mathbf{x_A}, \mathbf{x}, k)\hat{G}^*(\mathbf{x_B}, \mathbf{x}, k)\, d\mathbf{x} \\
&\quad + \hat{\beta}(\mathbf{x_A}, k) \oint_S \partial_{\mathbf{n_x}} \left\{\alpha^*(\mathbf{x})\hat{G}^*(\mathbf{x_B}, \mathbf{x})\right\} d\mathbf{x} \\
&\quad\quad + \hat{\beta}^*(\mathbf{x_B}, k) \oint_S \partial_{\mathbf{n_x}} \left\{\alpha(\mathbf{x})\hat{G}(\mathbf{x_A}, \mathbf{x})\right\}\, d\mathbf{x} \\
&\quad\quad\quad + \beta(\mathbf{x_A}, k)\beta^*(\mathbf{x_B}, k)\ell(S)\,,
\end{aligned} \tag{2.2.5}$$

where it becomes apparent that only the first and second terms in (2.2.2) make accurate contributions to the inter-receiver phase, if not the amplitude, and that the rest of the terms are spurious contributions.[1] Note that while the first term corresponds to the exact interferometric representation involving monopoles and dipoles, the second term corresponds to the simplified interferometric estimate discussed in Section 1.2.4. Next, note that the last two terms in (2.2.2) quantify the interference caused by ambient noise arriving at each of the receivers as active sources are recorded. These terms are comprised by the cross-correlation of ambient noise arriving at one receiver, with the aggregated dipole response recorded at the other receiver over the active source boundary $S$. However, filtering out ambient noise is a standard pre-processing procedure in an active source experiment. Therefore we assume the ambient noise is negligible ($\beta \equiv 0$) in the context of active source interferometry.

**Remark 2.2.1.** This is a sensible assumption given that the range and quality of the frequency spectrum of controlled (active) noise sources differs significantly from that of background noise, so that standard pre-processing techniques can separate them well enough for interferometric applications (see Bensen et al. (2007)). For example, an active source such as a truck-mounted seismic vibrator has a reasonably customisable frequency range,

[1] That is, contributions in the integral towards events other than the inter-receiver arrival, since the goal of inter-receiver interferometry is to estimate the travel time between the receivers.

capable of operating in a typical mid-band frequency of 10 to 30 Hz, or a higher band of 50 to 150 Hz depending on the target and application (Chapman et al., 1981). This differs significantly from the much lower frequency content of the Earth's background noise, referred to a microseismic noise. The main frequency band of microseisms ranges from 0.05 Hz to 0.4 Hz, typically peaking around 0.07 Hz and 0.14 Hz, corresponding to the primary and secondary microseisms, respectively (Gerstoft et al., 2006; Ardhuin et al., 2011). Hence, while the derivations in this section are performed in the simultaneous presence of the terms $\alpha$ and $\beta$ in order to derive a general, unified framework, the subsequent sections and chapters consider the active source case where $\beta \equiv 0$ (for example, Section 2.4 and Chapter 3) and the ambient noise case where $\alpha \equiv 0$ (4) separately, in line with interferometric applications.

Finally the second term is modulated by the factor

$$\alpha(\mathbf{x})\partial\mathbf{n}_{\mathbf{x}}\alpha^*(\mathbf{x}) - \alpha^*(\mathbf{x})\partial\mathbf{n}_{\mathbf{x}}\alpha(\mathbf{x})\,,$$

which vanishes when $\alpha$ is real-valued. This is a reasonable assumption for our purpose of quantifying the effect of azimuthal variations in amplitude, and henceforth we assume $\alpha$ is a real-valued random field. Under these assumptions, the error (2.2.5) reduces to

$$\hat{\mathcal{G}}_{\text{int}}(\mathbf{x_A},\mathbf{x_B},k;\alpha,0) - \hat{\mathcal{G}}_{\text{int}}(\mathbf{x_A},\mathbf{x_B},k;\,1,0) = \oint_S \left\{\alpha^2(\mathbf{x}) - 1\right\}\left(\hat{G}(\mathbf{x_A},\mathbf{x},k)\partial\mathbf{n}_{\mathbf{x}}\hat{G}^*(\mathbf{x_B},\mathbf{x},k) - \hat{G}^*(\mathbf{x_B},\mathbf{x},k)\partial\mathbf{n}_{\mathbf{x}}\hat{G}(\mathbf{x_A},\mathbf{x},k)\right)d\mathbf{x}\,. \tag{2.2.6}$$

The error expression (2.2.6) illustrates that the error in the full empirical retrieval (2.2.1) hinges on the behaviour of the statistical of the random field $\alpha$, specifically its second moment. This second order dependence is apparent when considering (2.2.1) under the assumptions of a real-valued $\alpha$ and $\beta \equiv 0$, since then the retrieval differs from the representation theorem (1.2.12) only in the term $\alpha^2(\mathbf{x})$.

**Remark 2.2.2.** It is immediate that if the second moment of the random field $\alpha$ is constant along the boundary $S$, i.e. $\mathbb{E}\left[\,\alpha^2(\mathbf{x})\,\right] = \mathbb{E}\left[\,\alpha_S^2\,\right]\ \forall\,\mathbf{x}\in S$ for some constant $\mathbb{E}\left[\,\alpha_S^2\,\right] > 0$, then

$$\mathbb{E}\left[\,\hat{\mathcal{G}}_{\text{int}}(\mathbf{x_A},\mathbf{x_B},k;\,\alpha,0)\,\right] \propto \hat{G}_{\text{hom}}(\mathbf{x_A},\mathbf{x_B},k)\,.$$

where the proportionality factor is $\mathbb{E}\left[\,\alpha_S^2\,\right] > 0$. Therefore, the full empirical estimate estimates the phase correctly on average (i.e. it is an unbiased phase estimator), but the amplitude is in general incorrect and the amplitude bias is quantified by the second moment of the random perturbations of recorded amplitude along the source boundary. Moreover,

since $\alpha \equiv 1$ corresponds to ideal data acquisition (i.e., the data recorded are true Green's functions), it is intuitive to allow $\alpha$ to oscillate around this ideal value (i.e. model $\alpha$ as a random field of mean one). It is interesting to note that due to the structure of the interferometric operation, $\alpha$ always enters the integrand squared, and there is no guarantee that the squared random field $\alpha^2$ is of mean one, even if $\alpha$ is. In fact, the only way in which $\mathbb{E}[\,\alpha^2\,] = 1$ can be guaranteed when $\mathbb{E}[\,\alpha\,] = 1$ is if the random field $\alpha$ is of variance zero (this follows directly from the definition of variance), i.e. the ideal case of a degenerate random field $\alpha \equiv 1$. On the other hand, if we allow for amplitude perturbations oscillating around an arbitrary non-negative value, i.e. $\mathbb{E}[\,\alpha\,] = \mu_\alpha > 0$, there are circumstances when $\mathbb{E}[\,\alpha^2\,] = 1$. This suggests that the interferometric retrieval is generally biased in the statistical sense except in either the most stringent ideal conditions, or in the presence of random perturbations that vary in a way that compensates implicitly for this bias (random amplitude perturbations with second moment equal to one). This behaviour is explored in the following sections as well as in Chapter 3.

### 2.2.2 Empirical interferometric approximation

While considering the behaviour of the cross-correlation representation theorem when applied to empirical data of the form (2.1.11), this formulation does not provide further insight without making more assumptions about the differentiability of the random field $\alpha$. Furthermore, it does not provide an integrated framework for active and passive noise interferometry. We are interested instead in the behaviour of the interferometric approximation (1.2.13), which is more representative of practical applications of wavefield interferometry. Therefore, motivated by equation (1.2.13), we define the *monopole empirical interferometric estimate as*

$$\hat{g}_{\text{int}}(\mathbf{x_A}, \mathbf{x_B}, k;\, \alpha, \beta) \coloneqq -2ik \oint_S \hat{g}_{\alpha\beta}(\mathbf{x_A}, \mathbf{x}, k)\hat{g}^*_{\alpha\beta}(\mathbf{x_B}, \mathbf{x}, k)\, d\mathbf{x}\,. \tag{2.2.7}$$

Substituting the definition for $g_{\alpha\beta}(\mathbf{x_R}, \mathbf{x}, k)$ given in (2.1.11) for each receiver yields

$$\begin{aligned}\hat{g}_{\text{int}}(\mathbf{x_A}, \mathbf{x_B}, k;\, \alpha, \beta) = &-2ik \oint_S \alpha^2(\mathbf{x})\hat{G}(\mathbf{x_A}, \mathbf{x}, k)\hat{G}^*(\mathbf{x_B}, \mathbf{x}, k)d\mathbf{x} \\ &-2ik\, \hat{\beta}(\mathbf{x_A}, k) \oint_S \alpha(\mathbf{x})\hat{G}^*(\mathbf{x_B}, \mathbf{x})d\mathbf{x} \\ &-2ik\, \hat{\beta}^*(\mathbf{x_B}, k) \oint_S \alpha(\mathbf{x})\hat{G}(\mathbf{x_A}, \mathbf{x})\, d\mathbf{x} \\ &-2ik\, \hat{\beta}(\mathbf{x_A}, k)\hat{\beta}^*(\mathbf{x_B}, k)\ell(S)\,,\end{aligned} \tag{2.2.8}$$

where $\ell(S)$ is the length of the contour $S$ and noting that real-valued $\alpha$ has been already assumed. Equation (2.2.8) provides an integrated framework for uncertainty in wavefield interferometry. When $\alpha \equiv 1$ and $\beta \equiv 0$, one recovers the interferometric approximation (1.2.13), i.e.

$$\hat{g}_{\text{int}}(\mathbf{x_A}, \mathbf{x_B}, k;\, 1, 0) \approx \hat{G}_{\text{hom}}(\mathbf{x_A}, \mathbf{x_B}, k)\,. \tag{2.2.9}$$

**Remark 2.2.3.** Contrast (2.2.9) above, which is an approximation, with the corresponding expression (2.2.4) for the full interferometric empirical estimate, which is exact. We consider the connection between the two empirical retrievals below.

For an active source scenario one considers negligible ambient noise, so that $\beta \equiv 0$, yielding

$$\hat{g}_{\text{int}}(\mathbf{x_A}, \mathbf{x_B}, k;\, \alpha, 0) = \oint_S \alpha^2(\mathbf{x}) \hat{G}(\mathbf{x_A}, \mathbf{x}, k) \hat{G}^*(\mathbf{x_B}, \mathbf{x}, k) d\mathbf{x}\,, \tag{2.2.10}$$

and conversely, when there are no active sources (i.e. $\alpha \equiv 0$) one recovers the ambient noise interferometry formulation laid out in (1.2.5)

$$\hat{g}_{\text{int}}(\mathbf{x_A}, \mathbf{x_B}, k;\, 0, \beta) \propto \hat{\beta}(\mathbf{x_A}, k) \hat{\beta}^*(\mathbf{x_B}, k)\,. \tag{2.2.11}$$

Therefore, equation (2.2.7) comprises a unified framework for uncertainty quantification in wavefield interferometry,and this work is dedicated to studying various deterministic and statistical aspects of this equation. In the following section, we use the ideal retrieval(2.2.4) as a benchmark to derive a general error expression.

**Remark 2.2.4.** For convenience and in line with the use of interferometry in practical settings, we chose to define the empirical interferometric estimate (2.2.7) directly. However, it is worth considering how it may be derived from the full empirical estimate (2.2.1), particularly in an active source scenario, as this highlights implicit assumptions on the behaviour of the random field $\alpha$. Consider the full empirical retrieval in an active source scenario that is, expression (2.2.1) with $\beta \equiv 0$,

$$\begin{aligned}\hat{\mathcal{G}}_{\text{int}}(\mathbf{x_A}, \mathbf{x_B}, k;\, \alpha, \beta) = \oint_S \alpha(\mathbf{x}) G(\mathbf{x_A}, \mathbf{x}, k) \partial \mathbf{n_x} \left\{ \alpha(\mathbf{x}) \hat{G}^*(\mathbf{x_B}, \mathbf{x}, k) \right\} \\ - \alpha(\mathbf{x}) \hat{G}^*(\mathbf{x_B}, \mathbf{x}, k) \partial \mathbf{n_x} \left\{ \alpha(\mathbf{x}) \hat{G}(\mathbf{x_A}, \mathbf{x}, k) \right\} d\mathbf{x}\,.\end{aligned}$$

In order to derive an expression akin to (2.2.10) one needs to enforce a Sommerfeld radiation condition and a far-field assumption (see Section 1.2.2) to the products $\alpha(\mathbf{x})\hat{G}(\mathbf{x_R}, \mathbf{x}, k)$, so that

$$\partial \mathbf{n_x} \left\{ \alpha(\mathbf{x}) \hat{G}(\mathbf{x_R}, \mathbf{x}, k) \right\} \approx ik\alpha(\mathbf{x}) \hat{G}(\mathbf{x_R}, \mathbf{x}, k)\,. \tag{2.2.12}$$

Using the product rule (2.2.3) illustrates that for (2.2.12) to be valid, we require

$$\partial \mathbf{n}_{\mathbf{x}} \{\alpha(\mathbf{x})\} \approx 0\,,$$

that is, that the amplitudes inhomogeneities along the source boundary vary slowly. This is in line with the numerical findings of e.g. Kimman and Trampert (2010), and imposes theoretical limitations on the roughness of the random field for accurate retrieval. We also point out that in this work the random field model is purely spatial, and does not depend on the frequency $k$. If $\alpha$ were frequency-dependent, it would be necessary to assume the Sommerfeld radiation condition and the validity of the far-field approximation for $\alpha$.

In the section below, we present an example of the active source interferometric retrieval (2.2.10) in the presence of a random field $\alpha$, to illustrate the effects of amplitude randomness on the retrieval and their physical intuition.

### Illustrative example of active source interferometry with inhomogeneous source amplitudes

Figure 2.1 illustrates a canonical source-receiver array, overlaid over an illustrative random field $\alpha$. The receivers are depicted as white triangles and the source boundary is to scale, with an inter-receiver distance of 100 m and a source boundary radius of 2.5 km.

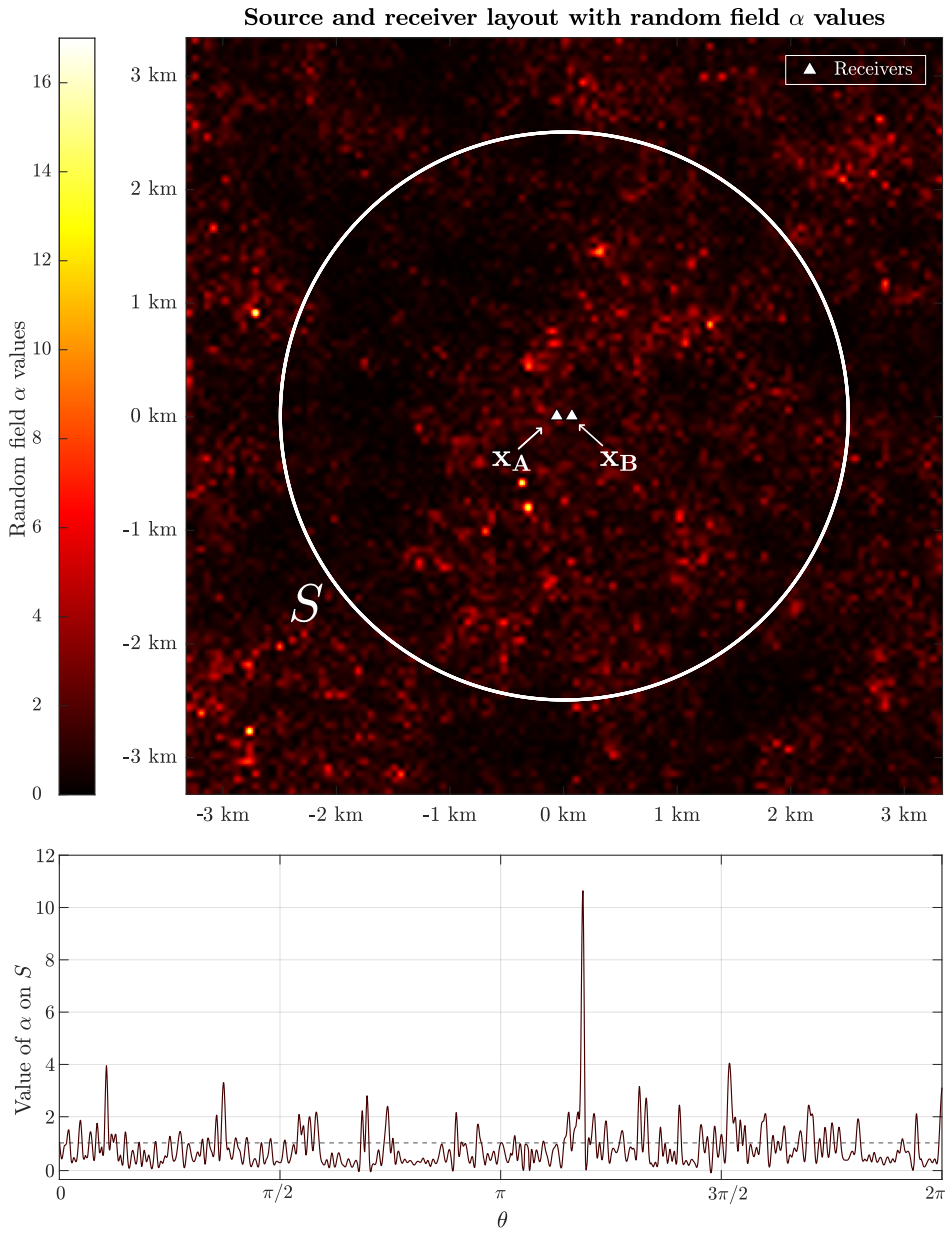


**Figure 2.1:** Illustration of the source boundary $S$ and a receiver pair $\mathbf{x_A}$,$\mathbf{x_B}$ laid over a random field $\alpha$ (**top**), along with the values of $\alpha$ over $S$ (**bottom**).

While this illustrative random field is of mean one, corresponding to ideal acquisition on average, it was allowed to take on large values to illustrate the spurious effects of amplitude inhomogeneities. The bottom panel of the same figure shows the values of the random field $\alpha$ along the contour $S$. Note a spike in energy at the azimuthal $\theta \approx 7\pi/6$. Consider also the axis determined by the receiver pair, which corresponds to the azimuthal directions $\theta = 0$ and $\theta = \pi$. Energy is relatively muted in the neighbourhood of $\theta = \pi$, and there is a peak of energy at $\theta = 0$ (equivalently $\theta = 2\pi$). Next, Figure 2.2 compares the interferometric

estimate (2.2.10) when $\alpha$ is the random field from Figure 2.1 in the time domain. The empirical waveform is shown in orange, and the waveform corresponding to an ideal empirical retrieval (i.e. $\alpha \equiv 1$) is included in grey for comparison. Moreover, the waveform of the corresponding homogeneous Green's function is shown in black dashes for reference, though it is indistinguishable from the empirical retrieval when $\alpha \equiv 1$. The medium speed was set at $c = 1000$ m/s, with an inter-receiver distance of 100 m and a spectrum varying between 0.1 Hz and 75 Hz. It is immediately apparent that the empirical retrieval overestimates the amplitude, consistent with the values of $\alpha$ shown in the bottom panel of Figure 2.1, which, while on average one, often exceed this mean. While the waveforms exhibit both the causal and acausal inter-receiver travel time at $t = 0.1$ s, the empirical waveform exhibits a large spurious arrival at around 0.05 s that obscures all other arrivals, as well as higher frequency artefacts between the acausal and causal inter-receiver arrivals. This large spurious arrival corresponds to the peak in energy at the azimuthal direction $\theta \approx 7\pi/6$ illustrated in the bottom panel of Figure 2.1, and the arrival time corresponds simply to the travel-time difference of a wave originating on $S$ at that azimuthal direction and arriving at each of the receivers. Finally, the amplitude at the causal inter-receiver arrival is consistent with the peak of energy at the azimuthal direction $\theta = 0$, which in line with the receivers. The underestimated amplitude at the acausal inter-receiver arrival $t = -0.1$ s is in turn consistent with the muted energy at the azimuthal direction $\theta = \pi$.

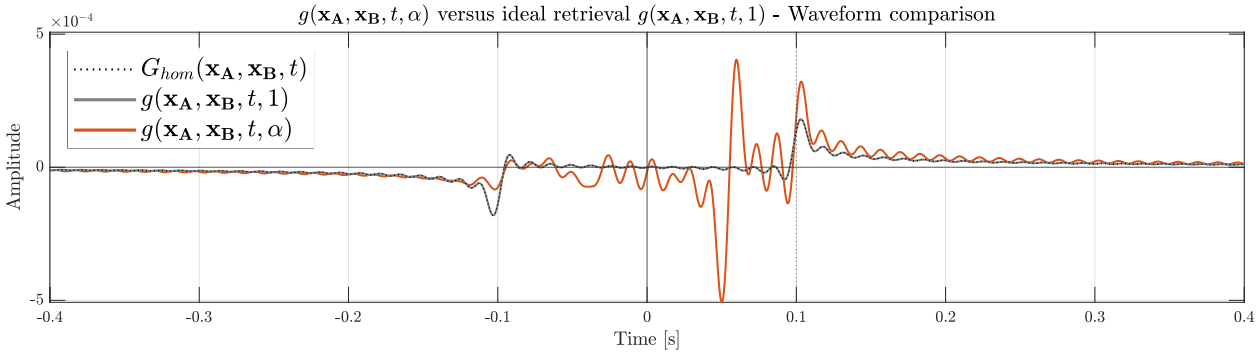


**Figure 2.2:** Comparison of the time-domain counterparts of the empirical interferometric estimate, i.e. $g_{\text{int}}(\mathbf{x_A}, \mathbf{x_B}, t;\, \alpha, 0)$ (orange) and the ideal retrieval $g_{\text{int}}(\mathbf{x_A}, \mathbf{x_B}, t;\, 1, 0)$ (grey), as well as the homogeneous inter-receiver Green's function $G_{\text{hom}}(\mathbf{x_A}, \mathbf{x_B}, t)$ (black dashes). The medium speed was $c = 1000$ m/s and the inter-receiver distance was $|\mathbf{x_A} - \mathbf{x_B}| = 100$ m.

**Remark 2.2.5.** Note that the spurious arrivals in the waveform $g(\mathbf{x_A}, \mathbf{x_B}, t : \alpha)$ are confined to the inter-receiver arrival time $t = 0.1$ s and its acausal counterpart $t = -0.1$ s. The phase differences in the correlation integrand are in fact bounded by the inter-receiver arrival as a direct consequence of the stationary phase approximation and its connection to wavefield interferometry, which is explored in detail in Chapter 3.

The spectra corresponding to these waveforms is shown in Figure 2.3, where again the spectrum of the ideal retrieval for $\alpha \equiv 1$ (grey) is virtually indistinguishable from the spectrum of the homogeneous inter-receiver Green's function (black dashes). The top panel of the figure shows respectively the modulus and the phase of the spectra. The bottom panels show the real and imaginary parts. Recall by definition (1.1.2) that the homogenous Green's function is a purely imaginary quantity, which is reflected in this figure and induces a discontinuous phase as the phase of the homogeneous Green's function oscillates between $-\pi/2$ and $\pi/2$. This discontinuous behaviour is reproduced by the ideal retrieval in grey, whose real part is negligible. However, the empirical retrieval (orange) has a non-trivial real part and it is apparent that the amplitude is overestimated across the frequency band. The empirical phase presents strong spurious effects, consistent with the waveforms shown in Figure 2.2.

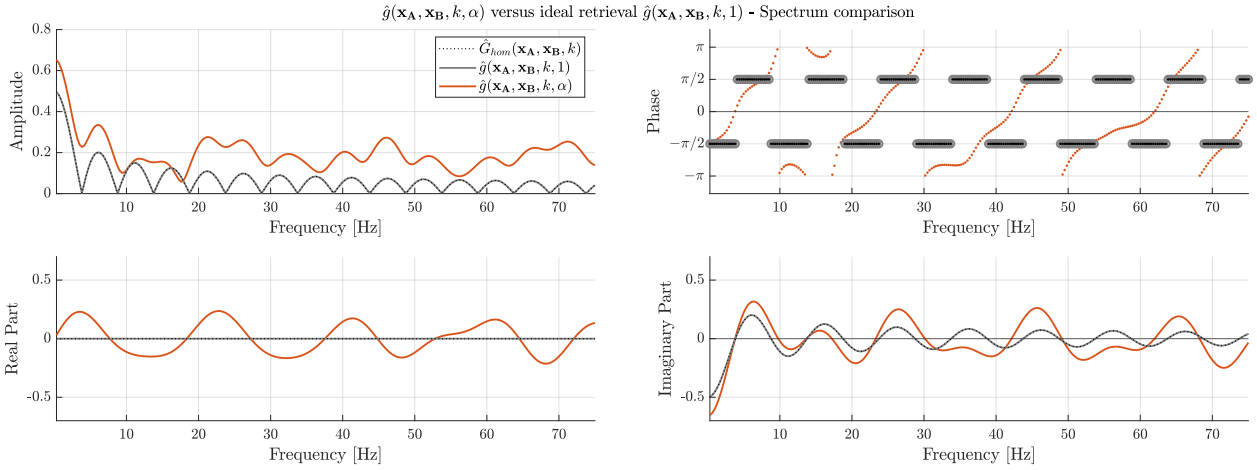


**Figure 2.3:** Comparison of the spectra of the empirical interferometric estimate $\hat{g}_{\text{int}}(\mathbf{x_A}, \mathbf{x_B}, k;\, \alpha, 0)$ (orange) and the ideal retrieval $\hat{g}_{\text{int}}(\mathbf{x_A}, \mathbf{x_B}, t;\, k, 0)$ (grey), as well as the homogeneous inter-receiver Green's function $G_{\text{hom}}(\mathbf{x_A}, \mathbf{x_B}, k)$ (black dashes). The medium speed was $c = 1000$ m/s and the inter-receiver distance was $|\mathbf{x_A} - \mathbf{x_B}| = 100$ m. The frequency band was 0.1 Hz to 75 Hz. The top panels show, respectively, the amplitude and phase of the spectra, while the bottom panels show the real and imaginary parts.

Finally, the empirical phase illustrated in the top right panel of Figure 2.3 exhibits jump discontinuities along the ordinate values $\pm\pi$, consistent with the range of the principal branch of the argument function. For illustration purposes, the phases are shown unwrapped for comparison in Figure 2.4. Note that in this particular example, the estimated retrieval does include a correct causal arrival at the inter-receiver travel time (see waveforms in Figure 2.2 and accompanying comments) so that the error appears smaller than expected at the lower end of the frequency spectrum. This behaviour may be due to the interaction of the waves with the random medium, and is explored and discussed further in Section 2.4.

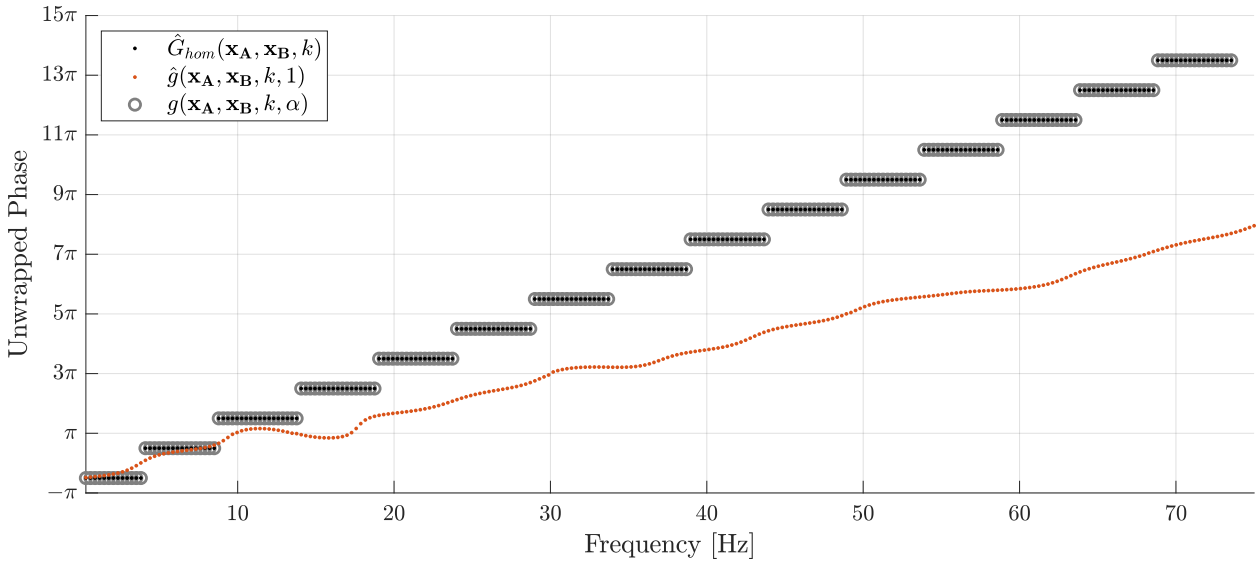


**Figure 2.4:** Unwrapped phases from the top right panel of Figure 2.3.

As this numerical example illustrates, azimuthal variations in the source amplitude can introduce significant errors to the interferometric retrieval. We aim to quantify the properties of the phase and amplitude errors illustrated in this section. To this end, we define general error expressions in what follows.

## 2.3 General error expression in wavefield interferometry

The uncertainty introduced by $\alpha$ and $\beta$ to the interferometric estimate can be quantified by defining the error

$$E(\mathbf{x_A}, \mathbf{x_B}, k;\, \alpha, \beta) = \hat{g}_{\text{int}}(\mathbf{x_A}, \mathbf{x_B}, k;\, \alpha, \beta) - \hat{g}_{\text{int}}(\mathbf{x_A}, \mathbf{x_B}, k;\, 1, 0)\,, \tag{2.3.1}$$

noting that by (2.2.9)

$$E(\mathbf{x_A}, \mathbf{x_B}, k;\, \alpha, \beta) \approx \hat{g}_{\text{int}}(\mathbf{x_A}, \mathbf{x_B}, k;\, \alpha, \beta) - \hat{G}_{\text{hom}}(\mathbf{x_A}, \mathbf{x_B}, k)\,, \tag{2.3.2}$$

Then, using equation (2.2.8), we have that

$$\begin{aligned} E(\mathbf{x_A}, \mathbf{x_B}, k;\, \alpha, \beta) = & -2ik \oint_S \left\{\alpha^2(\mathbf{x}) - 1\right\} \hat{G}(\mathbf{x_A}, \mathbf{x}, k)\hat{G}^*(\mathbf{x_B}, \mathbf{x}, k)d\mathbf{x} \\ & -2ik\, \hat{\beta}(\mathbf{x_A}, k) \oint_S \alpha(\mathbf{x})\hat{G}^*(\mathbf{x_B}, \mathbf{x})d\mathbf{x} \\ & -2ik\, \hat{\beta}^*(\mathbf{x_B}, k) \oint_S \alpha(\mathbf{x})\hat{G}(\mathbf{x_A}, \mathbf{x})\, d\mathbf{x} \\ & -2ik\, \hat{\beta}(\mathbf{x_A}, k)\hat{\beta}^*(\mathbf{x_B}, k)\ell(S)\,, \end{aligned} \tag{2.3.3}$$

In the next section we consider bounds for the error $E(\mathbf{x_A}, \mathbf{x_B}, k;\, \alpha, \beta)$ independently for active source and passive noise interferometry.

### 2.3.1 Expected error in the retrieved Green's function

We first consider an active source experiment, so that $\beta \equiv 0$. Error quantification in passive noise interferometry is considered in Chapter 4. Henceforth we assume $\alpha$ is a realisation of a real-valued random field, so that $|\alpha(\mathbf{x}')|^2 = \alpha^2(\mathbf{x}')$, and that the far-field approximation and the Sommerfeld radiation condition are satisfied whenever necessary. These assumptions are encapsulated in (2.2.9), so that approximation is invoked whenever necessary. Finally, we assume that Fubini's theorem is satisfied with respect to the contour integration over $S$ and the mean operator $\mathbb{E}\,[\,\cdot\,]$, which is also an integral operator. Consider the error expression (2.3.1) under the assumptions above

$$E(\mathbf{x_A}, \mathbf{x_B}, k;\, \alpha, 0) = -2ik \oint_S \left\{\alpha^2(\mathbf{x}') - 1\right\} \hat{G}(\mathbf{x_A}, \mathbf{x}', k)\hat{G}^*(\mathbf{x}', \mathbf{x_B}, k)\, d\mathbf{x}'\,. \tag{2.3.4}$$

In what follows, we give the expected value of $E(\mathbf{x_A}, \mathbf{x_B}, k;\, \alpha, 0)$ under the assumption that the first and second moments of $\alpha$ are constant along the boundary $S$. These values are then used to state probability bounds on the error in the sequel.

#### Expected value of the empirical error in active source interferometry

Taking the expected value of (2.3.4) yields

$$\mathbb{E}\,[\,E(\mathbf{x_A}, \mathbf{x_B}, k;\, \alpha, 0)\,] = -2ik \oint_S \left\{\mathbb{E}\left[\,\alpha^2(\mathbf{x}') - 1\,\right]\right\} \hat{G}(\mathbf{x_A}, \mathbf{x}', k)\hat{G}^*(\mathbf{x}', \mathbf{x_B}, k)\, d\mathbf{x}'\,.$$

If the random field $\alpha$ is further assumed of be of constant mean and variance, that is

$$\mathbb{E}\left[\,\alpha(\mathbf{x}')\,\right] = \mu_\alpha \qquad \text{for all } \mathbf{x}' \in S\,,$$

for some constant $\mu_\alpha \in \mathbb{R}$, and

$$\mathrm{Var}\left[\,\alpha(\mathbf{x}')\,\right] = \sigma_\alpha^2 < \infty \qquad \text{for all } \mathbf{x}' \in S\,,$$

for some positive constant $\sigma_\alpha^2 \in \mathbb{R}$, then

$$\mathbb{E}\left[\,\alpha^2(\mathbf{x}')\,\right] = \mu_\alpha^2 + \sigma_\alpha^2\,,$$

and hence

$$\mathbb{E}\left[\,E(\mathbf{x_A},\mathbf{x_B},k;\,\alpha,0)\,\right] = -2ik\left\{\mu_\alpha^2+\sigma_\alpha^2-1\right\}\oint_S \hat{G}(\mathbf{x_A},\mathbf{x}',k)G^*(\mathbf{x}',\mathbf{x_B},k)\,d\mathbf{x}'\,.$$

Applying assumption (2.2.9) we can conclude that

$$\mathbb{E}\left[\,E(\mathbf{x_A},\mathbf{x_B},k;\,\alpha,0)\,\right] \approx \left\{\mu_\alpha^2+\sigma_\alpha^2-1\right\}\hat{G}_{\mathrm{hom}}(\mathbf{x_A},\mathbf{x_B},k)\,.$$

Hence, the empirical interferometric estimate $\hat{g}_{\mathrm{int}}(\mathbf{x_A},\mathbf{x_B},k;\,\alpha,0)$ in active source interferometry is an unbiased phase estimator of the inter-receiver inhomogeneous Green's function, provided the second moment of $\alpha$ is finite and constant along the source boundary $S$. The relative amplitude bias is quantified by the second moment of the random amplitude variations, i.e.

$$\mathbb{E}\left[\frac{|E(\mathbf{x_A},\mathbf{x_B},k;\,\alpha,0)|}{|\hat{G}_{\mathrm{hom}}(\mathbf{x_A},\mathbf{x_B},k)|}\right] \approx \left\{\mu_\alpha^2+\sigma_\alpha^2-1\right\}\,.$$

## 2.4 Numerical study and results

In this Section, a numerical exploration of the errors in phase and amplitude incurred by the interferometric estimate is presented. First, fundamental results in probability bounds are briefly reviewed. Next, a specific distribution and correlation structure for the random field $\alpha$ are chosen, for practical purposes. The choice is distribution and correlation is justified and their relevance in applications is established. In particular, the correlation structure is chosen in order to allow for parameters that control the correlation at local and global scales independently from each other, as evaluating the performance of the interferometric estimate with respect to these noise characteristics is one of the goals of the present work. Finally,

the phase and amplitude errors are explored and their probability distribution functions are estimated in representative correlation regimes at different scales. Interesting behaviours are observed across this results, in particular a reduced error at lower frequency regimes due to the interaction of the wavelengths with the scale of the noise inhomogeneities.

### 2.4.1 Concentration inequalities and some auxiliary probabilistic results

Concentration inequalities are classic probability results that provide bounds on how much a random variable deviates from some specific value, usually its mean. As this thesis is concerned with studying and quantifying certain errors incurred in wavefield interferometry, concentration inequalities can be used to quantify the probability that these errors become large. In this Section, the classic probability results applied throughout this work are briefly introduced. For brevity, these results are presented without proof and references to standard literature are provided instead.

**Lemma 2.4.1** (Chebyshev's inequality)**.** *Let $X$ be a random variable with finite first and second moments, then for any real number $\xi > 0$*

$$\mathbb{P}\left(|X - \mathbb{E}\left[X\right]| > \xi\right) \leq \frac{1}{\xi^2} \operatorname{Var}\left[X\right] . \tag{2.4.1}$$

*Proof.* See for example Section 3.1 of Athreya and Lahiri (2006). □

In this work, Chebyshev's inequality is applied to complex-valued random variables that quantify different errors in wavefield interferometry. Hence, we point out that for a complex-valued random variable $Z$ the variance is defined in the usual way as

$$\operatorname{Var}\left[Z\right] = \mathbb{E}\left[\,|Z - \mathbb{E}\left[Z\right]|^2\,\right] .$$

where $\mathbb{E}\left[Z\right] = \mathbb{E}\left[\operatorname{Re}\{Z\}\right] + i\,\mathbb{E}\left[\operatorname{Im}\{Z\}\right]$ and $|\cdot|$ is the modulus function. Direct calculation shows that this definition of the variance is equivalent to

$$\operatorname{Var}\left[Z\right] = \operatorname{Var}\left[\operatorname{Re}\{Z\}\right] + \operatorname{Var}\left[\operatorname{Im}\{Z\}\right] . \tag{2.4.2}$$

Therefore, while the expected value of a complex-valued random variable is generally complex, its variance is always a non-negative real number.

Chebyshev's inequality states that no more than $1/\xi^2$ of a probability distribution's values can be $\xi$ or more standard deviations from the mean, for a wide class of probability

distributions, namely probability distributions with finite first and second moments, so that the mean variance exist. This makes Chebyshev's inequality quite useful in its generality, with the drawback that it generally does not produce tight bounds. In this work, Chebyshev's inequality has the further advantage of explicitly introducing the variance of the random variable into the bound, as this will allow us later on to derive error bounds in terms of certain physically interpretable parameters of interest.

Finally, we state the following auxiliary Lemma, which will be used later on.

**Lemma 2.4.2** (Law of total expectation for a finite partition)**.** *Let* $(\Omega, \mathcal{F}, \mathbb{P})$ *be a probability space with sample space* $\Omega$*, set of events* $\mathcal{F}$ *(where an event is a set of outcomes in* $\Omega$*) and probability function* $\mathbb{P}$*. Then, for a random variable* $X$ *defined on* $(\Omega, \mathcal{F}, \mathbb{P})$ *such that* $\mathbb{E}[X] < \infty$ *and a finite partition* $\{A_j\}_{j=1}^n$ *of* $\Omega$ *we have*

$$\mathbb{E}[X] = \sum_{j=1}^{n} \mathbb{E}[X \mid A_j]\, \mathbb{P}(A_j)\,, \tag{2.4.3}$$

*where* $\mathbb{E}[X \mid A_j]$ *is the conditional expectation of* $X$ *given* $A_j$ *.*

*Proof.* This statement is a particular case of the law of total expectation, which is a standard result in probability theory (see e.g., Grimmett and Welsh (2014)). □

### 2.4.2 The Matérn covariance function

In many modern applications of geostatistics, including remote sensing and wavefield interferometry, empirical data may be available with wide spatial coverage. Random fields are suitable for modelling such spatial data (Chiles and Delfiner, 2009; Lantuéjoul, 2013), and it is important to take into account the spatial correlation in the data for correct statistical analysis (Hoeting et al., 2006; Genton and Kleiber, 2015). As previously discussed the assumption that noise sources are uncorrelated is widely found in wavefield interferometry literature, both in theory and practical applications. While this assumption is mainly made in an ambient noise interferometry context, introducing a spatial covariance framework will allow us to consider the role of this assumption in active-source interferometry.

In particular, the Matérn family of positive definite functions is a common model for simulating spatial correlation and heterogeneity in geostatistics (Minasny and McBratney, 2007; Guttorp and Gneiting, 2006; Song and Jordan, 2017), and can be found in widely varying applications, such as soil science (Minasny and McBratney, 2007), hydrology (Mejía and Rodríguez-Iturbe, 1974), meteorology (Handcock and Wallis, 1994) and topography (Handcock and Stein, 1993). This rich family of covariance functions is based on the work of Matérn

(1960), and was initially popularised for geostatistical applications by Handcock and Stein (1993) and further by Stein (1999), who showed that the behaviour of this covariance function is well suited for predicting uncertainty due to its behaviour near the origin. Because it depends only on the distance $d$ between the spatial locations, it is a stationary covariance function, in the sense of translation invariance. Furthermore, it is isotropic in the average. The Matérn function includes a local smoothness parameter that controls the correlation at a local scale, as well as a large scale correlation parameter. These features make the Matérn family well suited for the application at hand, i.e. modelling spatial variation in the source intensity, quantifying the uncertainty introduced by these variations, and assessing the effect that sources correlation and smoothness has on the interferometric estimation of inter-receiver Green's functions.

The Matérn correlation function is given by

$$M(d;\, \rho_\alpha, \nu_\alpha) = \frac{2^{1-\nu_\alpha}}{\Gamma(\nu_\alpha)} \sqrt{2\nu_\alpha}\frac{d}{\rho_\alpha}\; K_{\nu_\alpha}\left(\sqrt{2\nu_\alpha}\frac{d}{\rho_\alpha}\right) , \tag{2.4.4}$$

for a distance $d$, where $\nu_\alpha > 0$ is a local smoothness parameter, in the sense that a realisation of a Matérn-correlated random field $\alpha$ is $\lceil \nu_\alpha \rceil - 1$ times differentiable in the mean square sense (Stein, 1999), $\rho_\alpha > 0$ is referred in this work as the correlation length and controls the large scale correlations, and $K_{\nu_\alpha}$ is the modified Bessel function of order $\nu_\alpha$ (Abramowitz et al., 1988). While other formulations of the Matérn function may be found in literature, here we use (2.4.4) as proposed by Handcock and Wallis (1994) which allows the parameters $\nu_\alpha$ and $\rho_\alpha$ to act more independently from each other (Stein, 1999). In this work, the subscript $\alpha$ in the Matérn parameters is used for clarity, to distinguish these parameters as related to the random field $\alpha$ in later sections.

When the smoothness parameter $\nu_\alpha$ is of the form $n + \frac{1}{2}$ for $n \in \mathbb{N}$, the Matérn function (2.4.4) decomposes into a product of a polynomial of degree $n$ and an exponential function (Guttorp and Gneiting, 2006). A notable special case is that of $\nu_\alpha = \frac{1}{2}$, resulting in the (scaled) exponential correlation function

$$M\big(d;\, \rho_\alpha, \tfrac{1}{2}\big) \propto e^{-\sqrt{2}d/\rho_\alpha} ,$$

which has been widely used in wave-scattering studies (e.g., Sato et al. (2012); Shapiro et al. (1996)). A further important case is found taking the limit as $\nu_\alpha \to \infty$, in which case a Gaussian correlation form is recovered,

$$\lim_{\nu_\alpha \to \infty} M(d;\, \rho_\alpha, \nu_\alpha) \propto \exp^{-(d/\rho_\alpha)^2} .$$

### 2.4.3 The log-normal distribution

Since the random field $\alpha$ is used to model amplitude variations in source intensity, we require a non-negative distribution. Furthermore, we wish to allow for the possibility that these variations are large. Motivated by these requirements, we model $\alpha$ as a log-normally distributed random field, a distribution with wide applications in Earth sciences (see for example Sarma (2010) and a wide variety of geophysical applications in Section 14 of Crow and Shimizu (2017)). We briefly summarise the main properties of this distribution. The defining characteristic of a log-normal random variable $X$ of mean $\mu_X$ and variance $\sigma_X$ is that

$$X = e^{m+sZ} \tag{2.4.5}$$

for a standard normal random variable $Z$, and $m_X$ and $s_X > 0$ real numbers defined as

$$m_X = \log\left(\frac{\mu_X^2}{\sqrt{\mu_X^2 + \sigma_X^2}}\right), \tag{2.4.6}$$

and

$$s_X^2 = \log\left(1 + \frac{\sigma_X^2}{\mu_X^2}\right). \tag{2.4.7}$$

The log-normal density function is given by

$$f_X = \frac{1}{x s_X \sqrt{2\pi}} e^{-\log(x-m_X)^2/2s_X^2}. \tag{2.4.8}$$

**Remark 2.4.1** (Moments of a log-normal random variable)**.** All the moments of the log-normal distribution exist and are given by

$$\mathbb{E}[X^n] = e^{nm+n^2s^2/2}, \tag{2.4.9}$$

where $m$ and $s^2$ are given by (2.4.6) and (2.4.7). This fact can be readily seen by taking the $n^{\text{th}}$ power of (2.4.5) and noting that $mn + snZ$ is a normal random variable with mean $mn$ and variance $s^2n^2$.

**Remark 2.4.2** (Product of log-normal variables)**.** By the additive property of logarithms, and the fact that the sum of normal distributions is again normally distributed, we note that the product of two lognormal distributions is again lognormal. To be precise, if $X \sim logN(\mu_X, \sigma_X^2)$ and $Y \sim logN(\mu_X, \sigma_Y^2)$, not necessarily independent, then by definition (2.4.5),

$$\log(X) \sim N(m_X, s_X^2) \qquad \text{and} \qquad \log(Y) \sim N(m_Y, s_Y^2),$$

where $m_X$, $s_X^2$, $m_Y$ and $s_Y^2$ are defined in (2.4.6) and (2.4.7). Hence

$$\log(XY) = \log(X) + \log(Y) \sim N(m_X + m_Y, s_X^2 + s_Y^2 + 2\,\mathrm{Cov}\,[\,X,\,Y\,])\,.$$

Applying definition (2.4.5) we have that $XY$ is again log-normally distributed, with mean $m_X + m_Y$ and variance $s_X^2 + s_Y^2 + 2\,\mathrm{Cov}\,[\,X,\,Y\,]$.

On the other hand, not much can be said in general about linear combinations of two correlated log-normally distributed random variables (Di Renzo et al., 2009; Lo, 2012). The linear combination may in fact not even be positive, so that definition (2.4.5) is not satisfied. Some approximations are available for particular cases of their sum (see, e.g., Mehta et al. (2006); Lo (2013)).

Figure 2.5 shows realisations of Matérn-correlated log-normally random fields $\alpha$ of mean $\mu_\alpha = 1$ and variance $\sigma_\alpha = 0.5$, for varying values of the parameters $\nu_\alpha$ and $\rho_\alpha$. The local and large-scale effects of the latter two parameters can be appreciated. The simulations were generated in MATLAB, generating multivariate normal random variables on a grid using definition (2.4.5) along with the parameter relationships (2.4.6) and (2.4.7) to ensure the resulting field has mean and variance $\mu_\alpha$ and $\sigma_\alpha$. On the other hand, the transformation approach proposed by Papalexiou (2018) was used to calculate a parent covariance function for the random variable $Z$ in (2.4.5), in terms of (2.4.4), so that the resulting random field $\alpha(\mathbf{x})$ exhibited the desired correlation (2.4.4) after the exponential transformation (2.4.5).

To validate these simulations, the numerical correlation of the simulated random fields $\alpha$ was calculated and compared directly to (2.4.4) for the parameters $\rho_\alpha$ and $\nu_\alpha$ in the simulated ranges. The probability density function of the values of the simulated random field at fixed locations $\mathbf{x}$ were numerically estimated and compared to (2.4.8) for the simulated range parameter $\sigma_\alpha$ and $\mu_\alpha$. The simulated random fields $\alpha$ exhibited the required correlation structure and probability distribution.

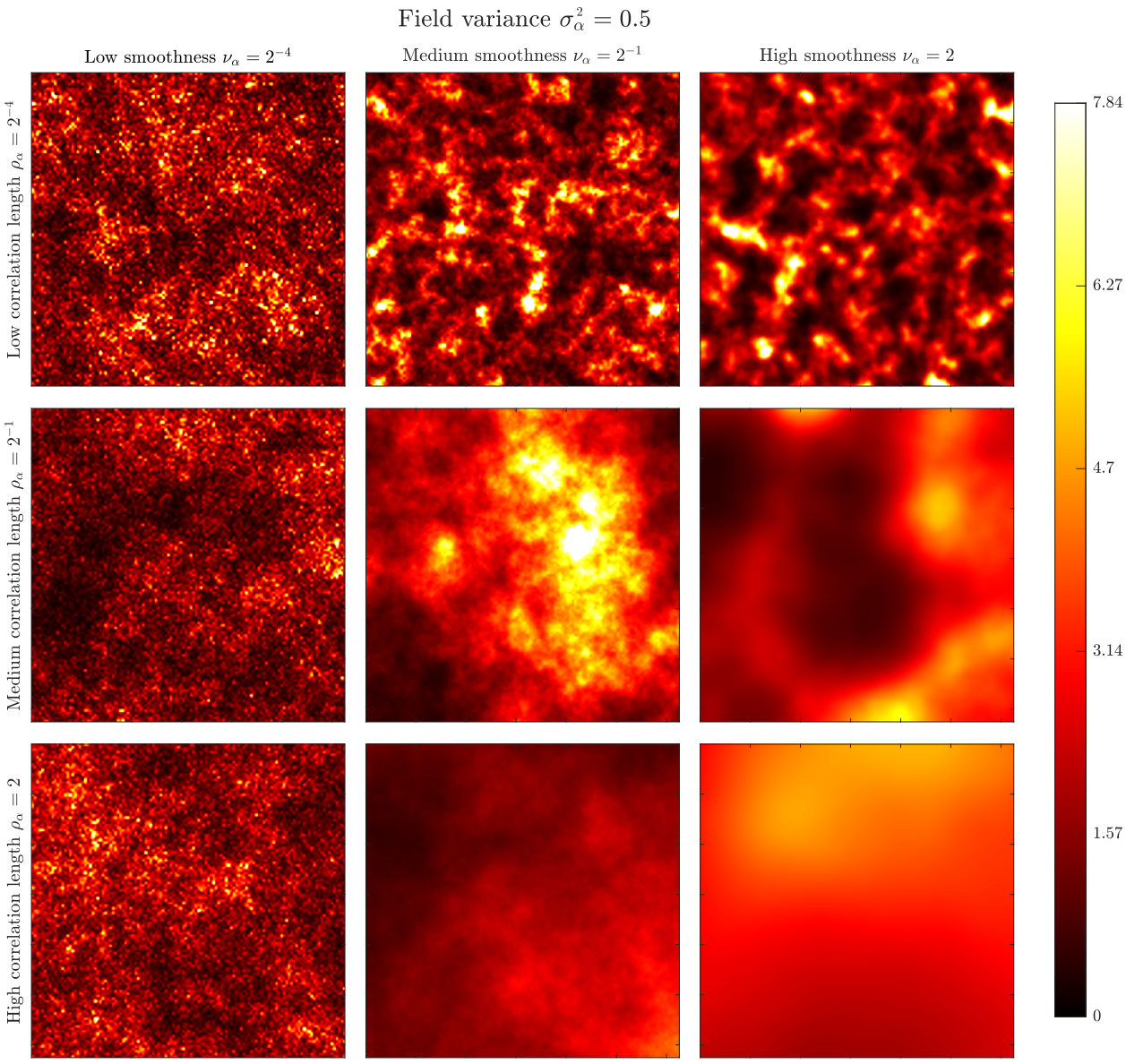


**Figure 2.5:** Nine realisations of a Matérn-correlated, log-normal random fields $\alpha$ with mean $\mu_\alpha = 1$, and variance $\sigma_\alpha^2 = 0.5$. The top, middle and bottom rows correspond to low ($2^{-4}$), medium ($2^{-1}$) and high (2) correlation lengths $\rho_\alpha$, respectively. The left, middle and right columns correspond to low ($2^{-4}$), medium ($2^{-1}$) and high (2) values of the smoothness parameter $\nu_\alpha$, respectively.

In the following Sections, we consider the error in the stationary phase approximation for the case where the random field $\alpha$ is Matérn-correlated and log-normally distributed. The suitability of this choice of covariance function and probability distribution for geostatistical applications has been established in Section 2.4.2. In what follows, $2.5 \times 10^4$ realisations of random fields $\alpha$ were simulated with the parameters detailed in the table below.

| Parameter | Range |
|---|---|
| Mean of log-normal distribution | $\mu_\alpha = 1$ |
| Variance of log-normal distribution | $0.05 \leq \sigma_\alpha^2 \leq 1$ |
| Matérn correlation length | $2^{-4} \leq \rho_\alpha \leq 2$ |
| Matérn smoothness | $2^{-4} \leq \nu_\alpha \leq 2$ |

The correlation length $\rho_\alpha$ is scaled with respect to the source-receiver array, so that a correlation length of e.g. $\rho_\alpha = 0.1$ should be interpreted as a correlation length of roughly a tenth of the scale of the source boundary $S$.

### 2.4.4 Phase error in the interferometric estimate

In this Section, we present numerical results for the estimated probability distribution function (p.d.f.) for the phase error incurred by the interferometric approximate $\hat{g}_{\text{int}}(\mathbf{x_A}, \mathbf{x_B}, k;\, \alpha, \beta)$, in a regime of a highly smooth random field $\alpha$ (Figure 2.6) and a very rough random field $\alpha$ (Figure 2.7).

The scenario where the noise variations are highly smooth illustrated in Figure 2.6 is desirable, since the resulting probability distributions of the error are highly concentrated around zero across the $kr$ regime observed. On the other hand, Figure 2.7 shows the effect that roughness in the noise field has on the phase estimate, with significantly more spread out probability distributions, pointing to a higher uncertainty and an increased likelihood of a large phase error. Interestingly, while in the previous figure the behaviour is relatively homogeneous across values of $kr$, in the rough noise case the probability distribution is mostly highly concentrated at low values of $kr$, and the undesirable spreading effect increases with $kr$. This is a counter-intuitive result, as we expect the phase estimate to be better as $kr$ increases. A plausible explanation for this behaviour is that the main contributions to the interferometric integral arise from the stationary phase regions of the source boundary. This regions become larger as the wavenumber $k$ decreases, and hence finer-scale variations of the source amplitude have an opportunity to average out over a longer portion of the boundary, resulting in a error reduction for lower values of $k$. As $k$ increases, the opposite is true. The regions that provide the main contributions to the interferometric estimate become narrower, and hence the fine-scale perturbations of the rough random field have a larger impact on the estimate, producing a larger phase error.

In both regimes the p.d.f. presents transitions between unimodal and bimodal regimes, corresponding to the discontinuity points of the phase of the inter-receiver homogeneous Green's function. The counter-intuitive behaviour of the p.d.f.s in the presence of rougher fields, spread out for larger $kr$ but concentrated at lower frequencies is studied in more detail

in Chapter 3, which is dedicated to the stationary phase approximation.

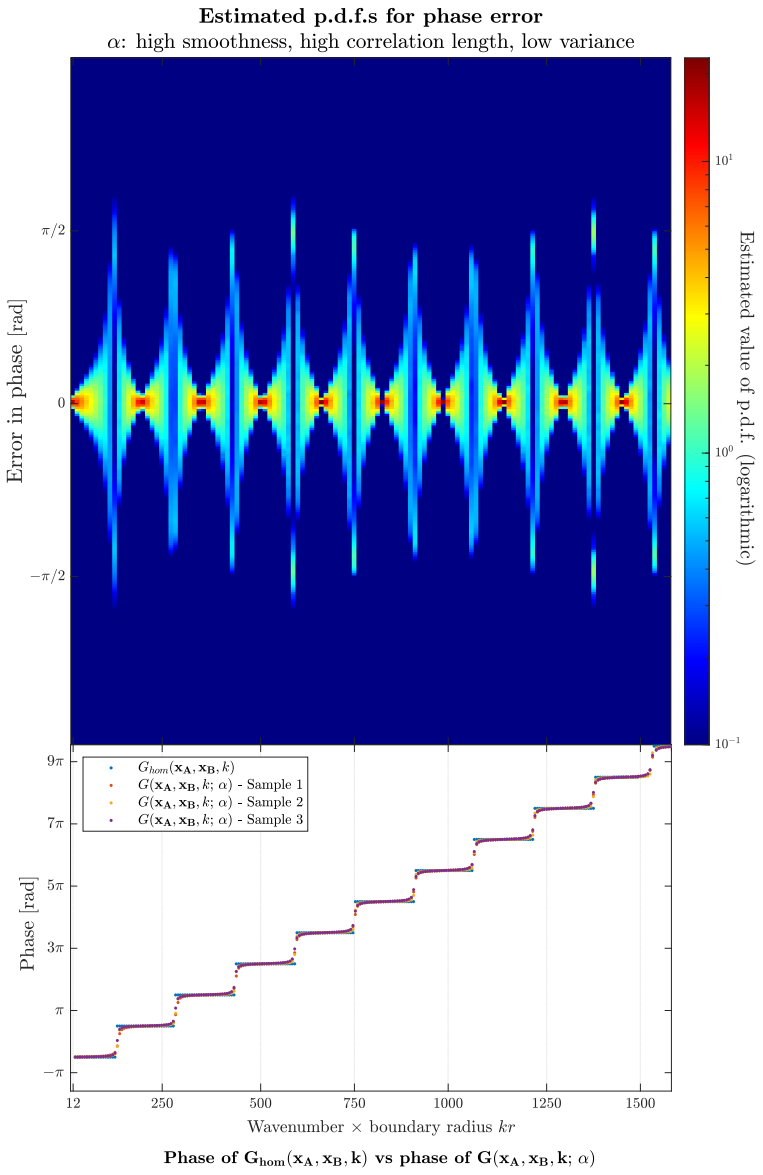


**Figure 2.6:** Estimation of the p.d.f. of the phase error in the empirical interferometric estimate. The top panel shows along the y-axis the value of the error, and the wavenumber along the x-axis. The colour value in the figure corresponds to the value of the error p.d.f. for a given wavenumber $k$. The bottom panel shows the phase of three realisations of the empirical Green's function, along with the homogeneous Green's function for reference.

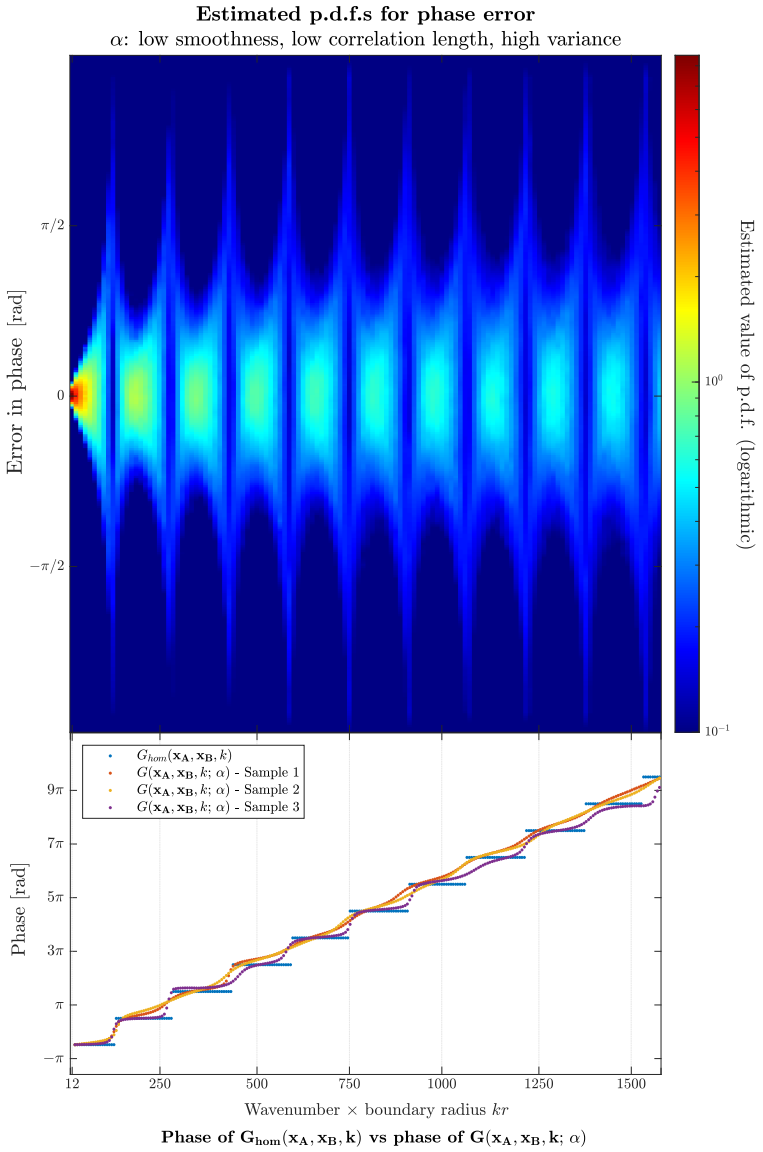


**Figure 2.7:** Estimation of the p.d.f. of the phase error in the empirical interferometric estimate. The top panel shows along the y-axis the value of the error, and the wavenumber along the x-axis. The colour value in the figure corresponds to the value of the error p.d.f. for a given wavenumber $k$. The bottom panel shows the phase of three realisations of the empirical Green's function, along with the homogeneous Green's function for reference.

### 2.4.5 Amplitude error in the interferometric estimate

In this Section, we present numerical results for the estimated probability distribution function (p.d.f.) for the amplitude error incurred by the interferometric approximate $\hat{g}_{\text{int}}(\mathbf{x_A}, \mathbf{x_B}, k; \alpha, \beta)$, in a regime of a highly smooth random field $\alpha$ (Figure 2.8) and a very rough random field $\alpha$ (Figure 2.9). Several conclusions become apparent upon examination of these figures. First, there is a clear bias in the amplitude and it generally tends to be overestimated. The

magnitude of the relative error worsens for rough random fields. On the other hand, the probability distributions are more concentrated for a smooth field, as they were in the case of the phase. As expected, there is a higher uncertainty when the variance of the noise field is high.

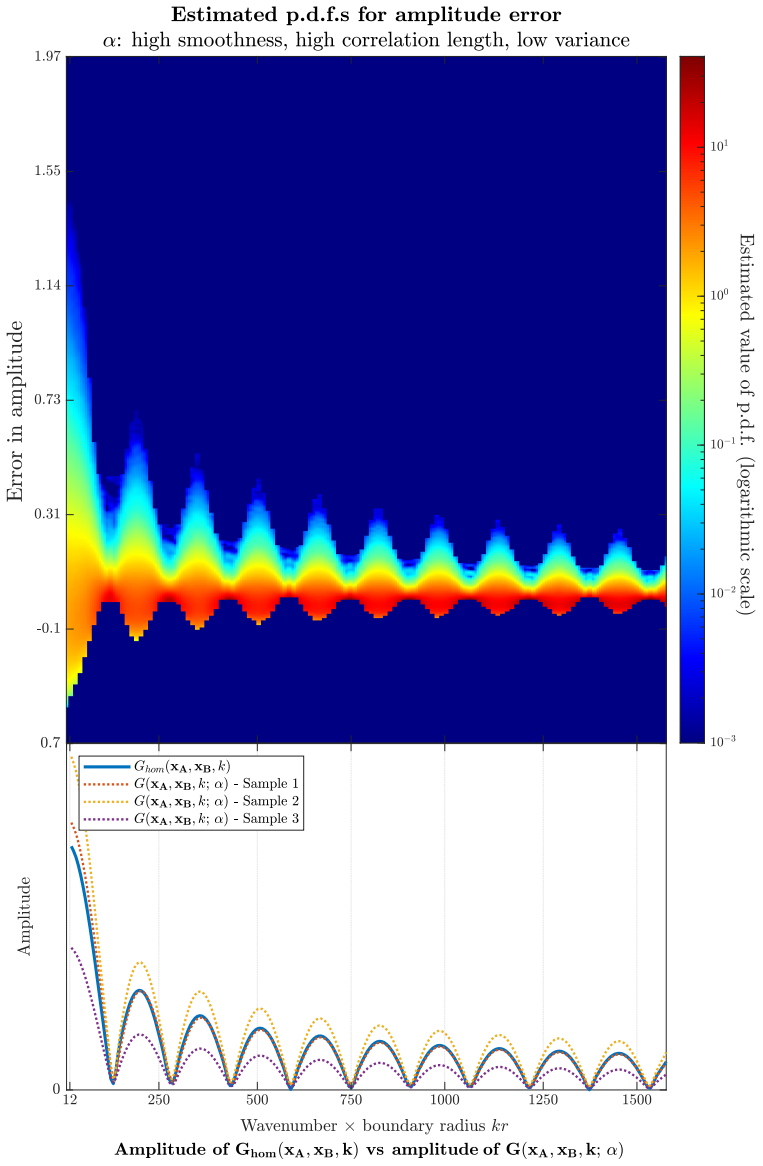


**Figure 2.8:** Estimation of the p.d.f. of the amplitude error in the empirical interferometric estimate. The top panel shows along the y-axis the value of the error, and the wavenumber along the x-axis. The colour value in the figure corresponds to the value of the error p.d.f. for a given value of $kr$. The colour code is in a logarithmic scale. The bottom panel shows the amplitude of three realisations of the empirical Green's function for illustration, along with the homogeneous Green's function for reference.

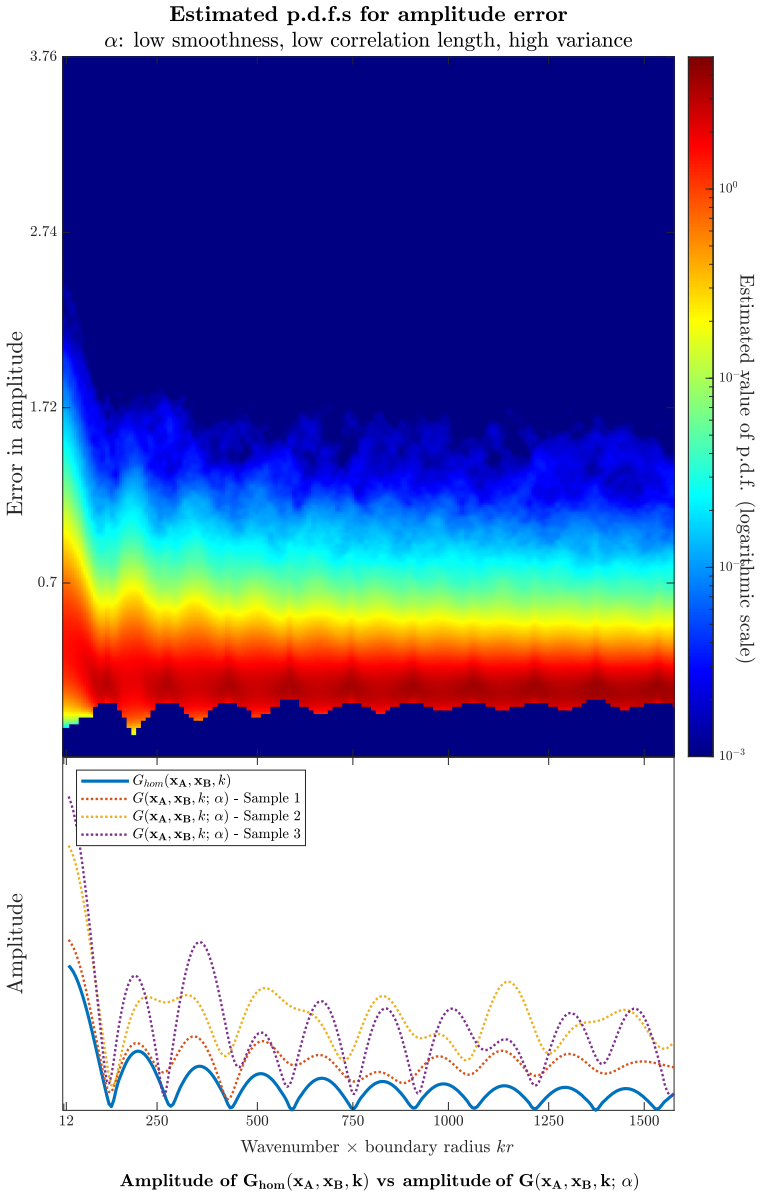


**Figure 2.9:** Estimation of the p.d.f. of the amplitude error in the empirical interferometric estimate. The top panel shows along the y-axis the value of the error, and the wavenumber along the x-axis. The colour value in the figure corresponds to the value of the error p.d.f. for a given wavenumber $k$. The bottom panel shows the amplitude of three realisations of the empirical Green's function, along with the homogeneous Green's function for reference.

In both figures the distribution becomes more concentrated for higher values of $kr$. This is due however to the natural amplitude decay of the Green's function itself. To eliminate this obscuring effect, the probability distribution function of the relative error were numerically estimated, and they are shown in Figure 2.10. In the panels of this figure, the correlation length and smoothness of the random field were systematically increased from left to right, so that the leftmost panel corresponds to the roughest field explored and the rightmost panel

corresponds to the smoothest field explored. An interesting effect can be appreciated, where the error is more concentrated around zero for rougher fields (see leftmost panel), and this effect gradually dissipates as the field becomes smoother, so that in the final panel to the right the behaviour of the error probability distribution is essentially periodic across the range of $kr$. This unexpected behaviour is consistent with our observations for the phase, and it can be physically explained as in Section 2.4.4, when one considers the interactions between the wavelength, the radius of the region around the stationary points that make up the main contributions to the interferometric integral and the scale of the inhomogeneities of the random amplitude perturbations in relation to the two previous quantities.

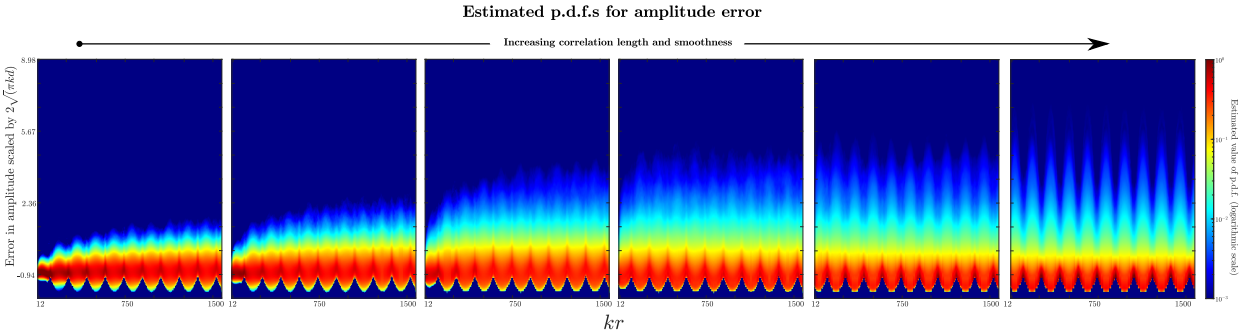


**Figure 2.10:** Estimated p.d.f.s of the amplitude error as the smoothness and correlation length of the field increase from left to right. The value of the p.d.f is colour coded in a logarithmic scale and the vertical axes correspond to the error values. The horizontal axis corresponds to $kr$

In the next section, we explore a boundary randomisation approach to mitigate the errors explored above, particularly where the phase is concerned.

## 2.5 The multi-contour technique

We now consider the scenario where we do not expect samples of different realisations of the random field $\alpha$ to be available. This could be the case, for example, when perturbations in amplitude change over a timescale much larger than the experiment allows. In this scenario one would have only a single realization of the random field $\alpha$, and would not be able to rely on averaging over time to induce incoherency in the spurious parts of the estimate (i.e. contributions to the integral that do not correspond to the inter-receiver arrival time, introducing erroneous events to the estimate). Hence, we propose instead randomising the contour of sources $S$ over a fixed realisation of the random field $\alpha$, defining the averaged

retrieval

$$\overline{\hat{g}}(\mathbf{x_A}, \mathbf{x_B};\, k, \alpha, 0, N) = -2ik\frac{1}{N}\sum_{j=1}^{N}\oint_{S_j} \alpha^2(\mathbf{x}')\hat{G}(\mathbf{x_A}, \mathbf{x}', k)\hat{G}^*(\mathbf{x}', \mathbf{x_B}, k)\, d\mathbf{x}'\,. \tag{2.5.1}$$

That is, the particular realisation of the random field $\alpha$ remains fixed, but the boundary $S$ is randomised in space to introduce incoherence to the spurious arrivals in the retrieved trace. Figure 2.12 illustrates conceptually the randomisation of contours, where the receiver pair is denotes as blue rectangles, and three different source contours are shown on yellow, purple and orange.

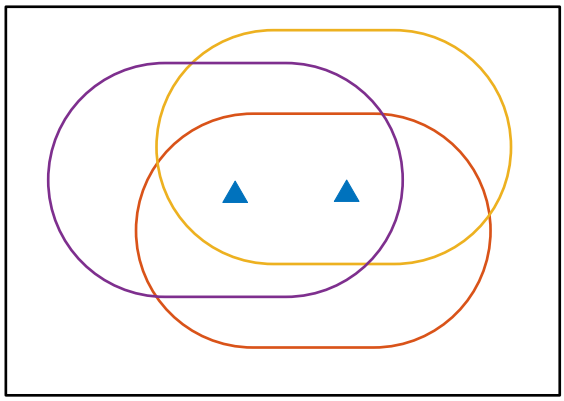

**Figure 2.11:** Unknown inhomogeneous medium with two receivers depicted as small triangles and three source contours in different colours.

In this Section, we present a proof-of-concept demonstration to illustrate how randomising the source contour in space can help mitigate the error in phase introduced by amplitude inhomogeneities along the source boundary. A brief numerical exploration of the effect of the phase is presented for both a low and a high frequency regime in Figures 2.14 and 2.13. A result is also presented for the amplitude in Figure 2.15.

To implement the average (2.5.1), a single realisation of a random field $\alpha$ is taken. This field is, as in previous sections, log-normally distributed and Matérn correlated. The receiver pair location is fixed. Circular source boundaries of fixed radius $r$ were chosen for simplicity. To generate these randomised contours, $N$ random uniform locations were simulated in a neighbourhood of the midpoint between the receivers, corresponding to the centres of $N$ random circular boundaries. The radius of the neighbourhood around the receivers was adjusted to ensure a distance of at least $0.8r$ was maintained between each source boundary and each of the receivers, in order to avoid introducing artefacts due to the violation of the far-field approximation. Recall that a far-field regime is required a simplified monopole form of interferometry, as in equation (2.5.1) (see Sections 1.2.2 and 1.2.4).

Figure 2.12 illustrates the results of implementing this randomisation. For this simulation, the inter-receiver distance was set at 100 m and horizontally oriented, with a medium speed of $c = 1000$ m/s. Note that this yields an inter-receiver travel time of $t = 0.1$ s. A frequency range from 0.15 Hz to 40 Hz was allowed, and circular source boundaries of fixes radius of $r = 5000$ m were used to implement the multicontour interferometric estimate (2.5.1). A single realisation of a random field was taken. The random field was log-normally distributed with mean $\mu_\alpha = 1$ and a medium variance of $\sigma_\alpha^2 = 0.5$. It was Matérn correlated with a medium correlation length of $\rho_alpha = 0.5$ and a smoothness parameter of $\nu_\alpha = 2$. The medium-range parameters were chosen with the purpose of constructing this illustrative example, and the parameter space is explored more thoroughly in the subsequent figures.

The bottom panel of this Figure shows the values of the particular realisation of the random field $\alpha$ along a single source boundary, centred at the midpoint between the receivers. Given the geometry of the source receiver array, the main contributions to the interferometric integral in ideal circumstances (that is, $\alpha \equiv 1$) would arise from the neighbourhoods of the sources located at 0 and $\pi$ radians on the circular boundary, that is, directly on the line that passes through both receivers. This is explored and explained in detail in Chapter 3. For now, note that the source energy at these locations is relatively suppressed, especially around the 0 radians location. On the other hand, there is a large peak of energy around the $3\pi/4$ radians location. The waveform that results from retrieving the inter-receiver interferometric estimate from this source boundary is depicted in the top panel, with an orange dotted line, where the ideal retrieval with $\alpha \equiv 1$ is shown in solid grey for reference. The effects of the source amplitude inhomogeneities can be plainly appreciated. The grey reference waveform shows the expected causal and acausal arrivals at $t = 0.1$ s and $t = -0.1$ s, respectively. However, the orange waveform exhibits no significant arrival at the acausal time $t = -0.1$ s, consistent with the muted sources around the 0 radians location. While there is a distinguishable arrival at the correct time $t = 0.1$ s, this is significantly obscured by the large spurious arrival close to $t = 0$. In fact, without the reference waveform, one would not be able to tell which event in the orange waveform corresponds to the inter-receiver arrival.

It is worth discussing this spurious arrival further, as it provides insight into the effects of non-homogeneous medium illumination and the inner workings of the interferometric estimate. This erroneous arrival corresponds to the large energy peak that the $\alpha$ random field exhibits just after the $3\pi/4$ radians location (see bottom panel of the same Figure). This energy peak is located right above and almost symmetrical with respect to the receiver pair. Hence, the travel times from sources in this region to the horizontally-oriented receiver pair is very similar for each receiver, and hence the travel time difference detected by the

cross-correlation is very close to zero.

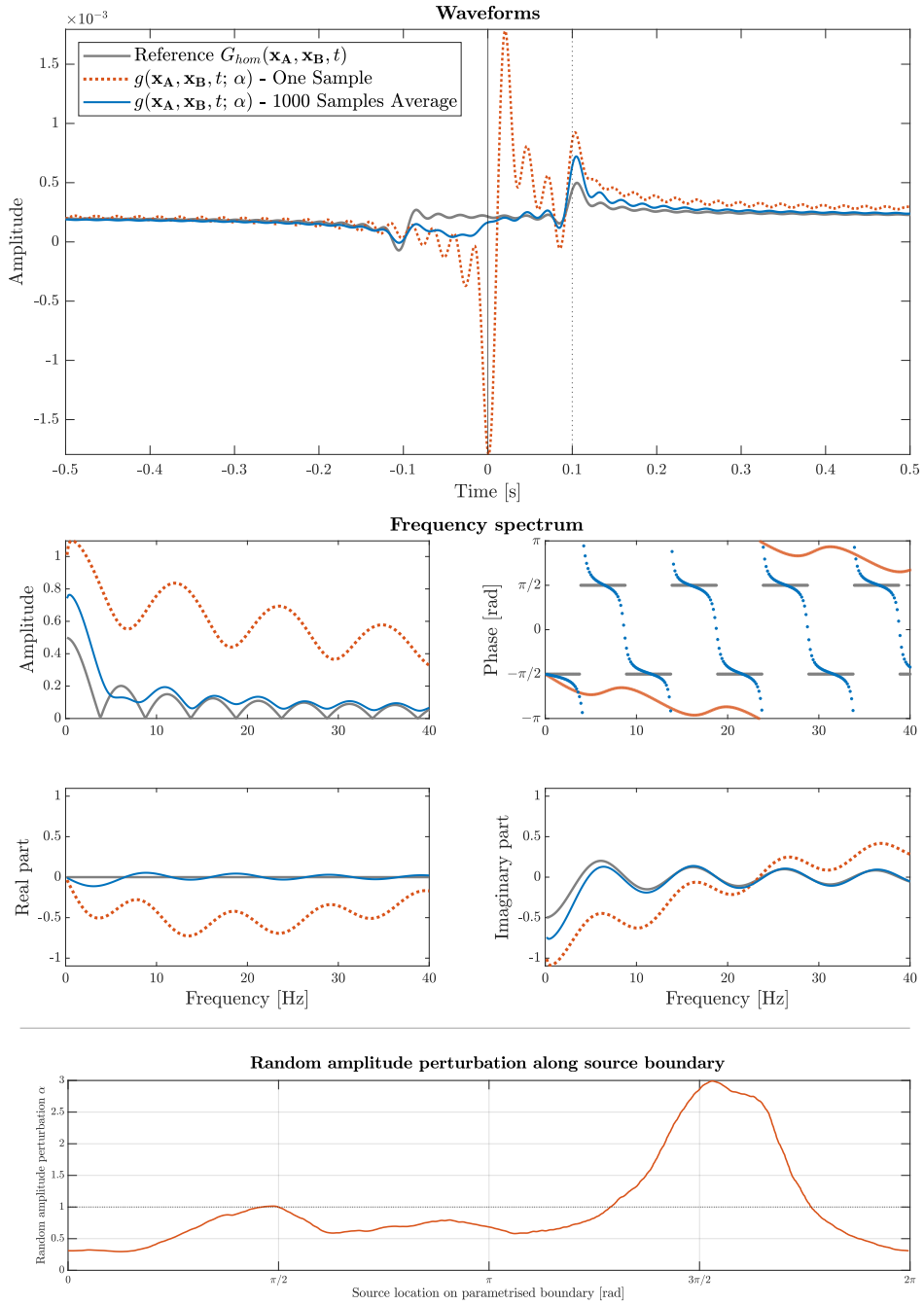


**Figure 2.12:** Example of the improved empirical retrieval resulting from randomising the spatial location of the boundary $S$. The orange retrieval results from using a single random boundary $S$. The blue retrieval results from randomising the location of $S$ around the receivers, taking care to remain in the farfield. The homogeneous Green's function is shown in grey as reference.

Figures 2.13 and 2.14 show the phase error as a function of the number of contours,

for low and high frequency regimes. The gain in randomising the contour depends on the smoothness and correlation regime of the noise, and the higher frequency regime is more sensitive to small-scale inhomogeneities in the field. Figure 2.13 shows the amplitude error in a high frequency regime. Since the interferometric estimate is biased in amplitude, averaging over more contours will not necessarily improve the estimate as the amplitude of the estimate converges to an incorrect value.

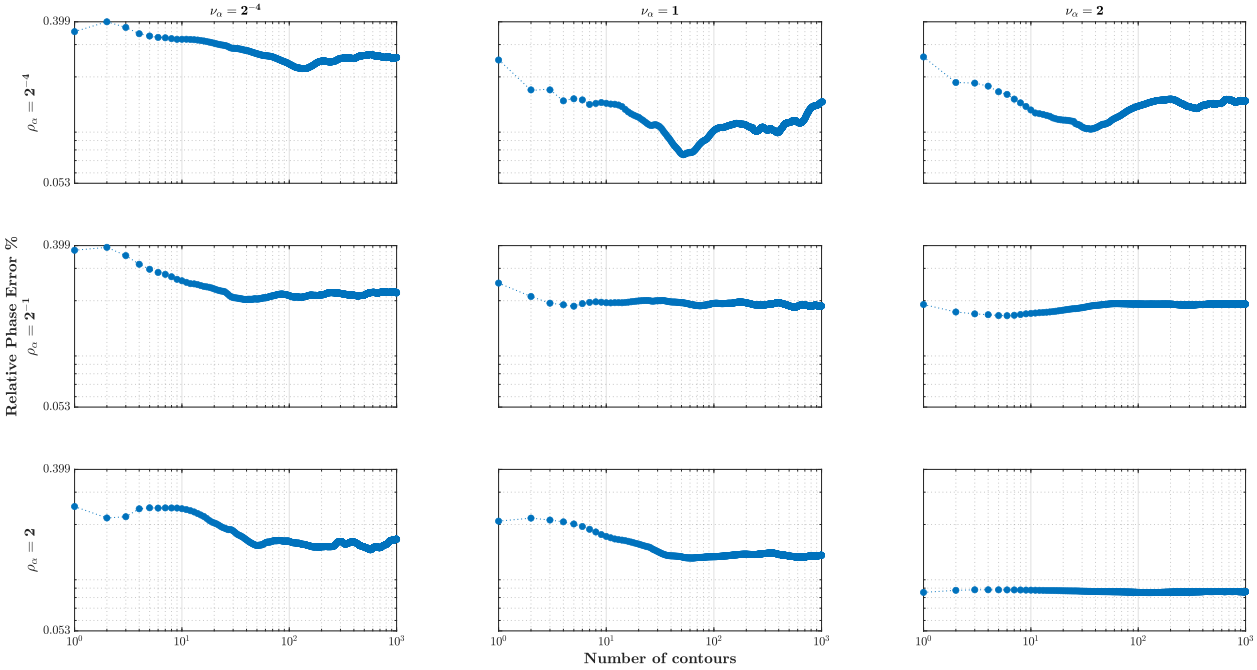


**Figure 2.13:** Expected phase error as a function of number of random contours used for a range of smoothness and correlation values, for a frequency value of 25 Hz.

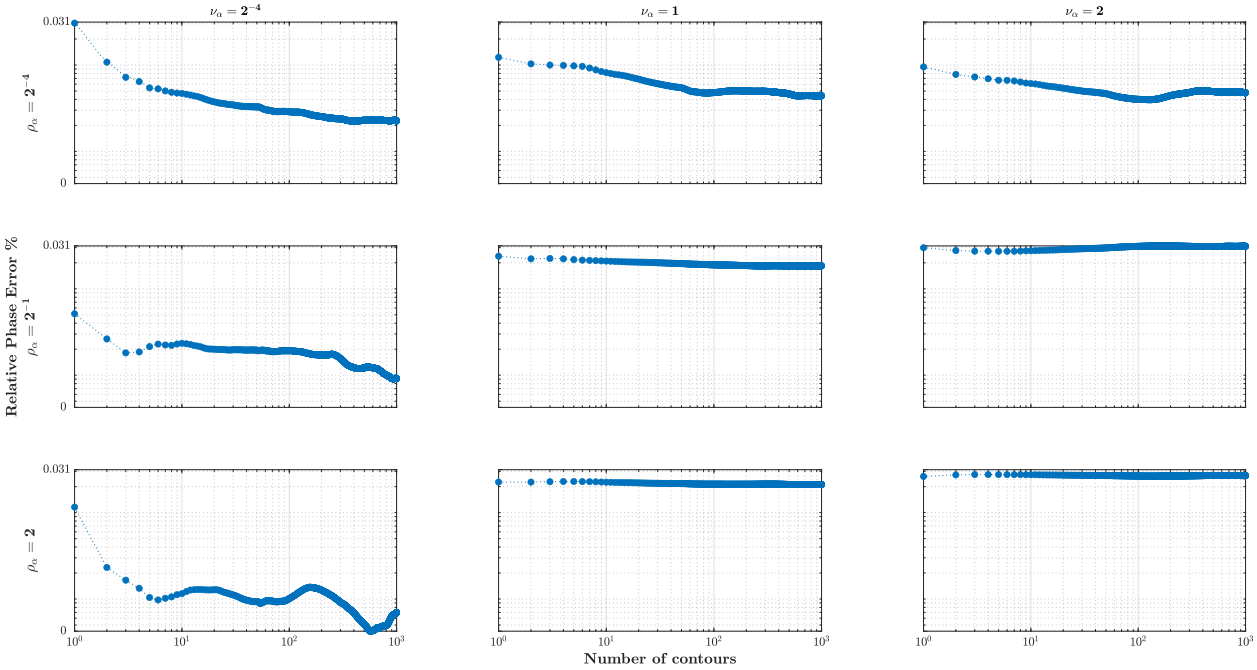


**Figure 2.14:** Expected phase error as a function of number of random contours used for a range of smoothness and correlation values, for a frequency value of 0.01 Hz.

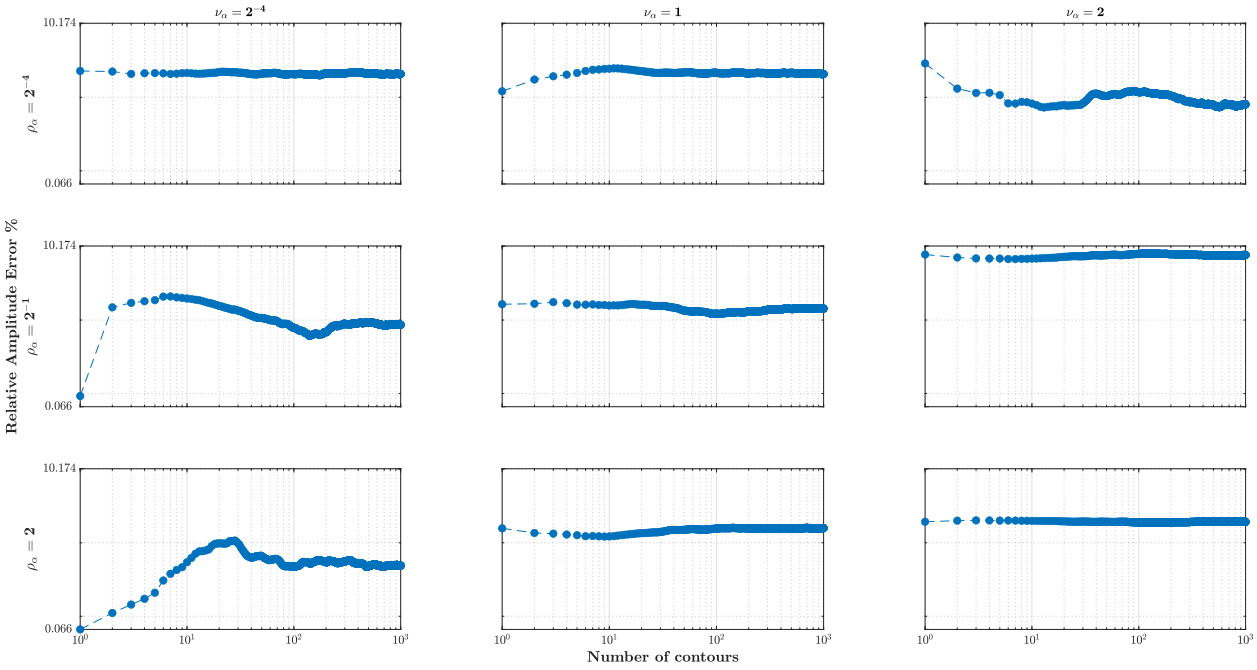


**Figure 2.15:** Expected amplitude error as a function of number of random contours used for a range of smoothness and correlation values, for a frequency value of 25 Hz.

## 2.6 Discussion

In this Chapter we derived a general framework for error quantification in wavefield interferometry and performed an initial numerical exploration of the errors induced in an active source scenario. Error quantification and mitigation in the ambient noise case is presented in Chapter 4. Broadly speaking, we generally found that lower values of the spectrum are less sensitive to small scale inhomogeneities of the noise. This is physically consistent in the sense that longer wavelengths may not interact with small scale randomness in the medium (see. e.g. Shapiro et al. (1996) for a discussion of the effects of random medium inhomogeneities on waves travelling through them). Our random field model is spatially dependent and the potential interactions with the frequency are encoded in the smoothness parameter. A possible extension could be incorporating a frequency dependence into the model. Moreover, should one wish to consider non stationary random fields (i.e. loss of translation invariance) an approach such as the one proposed by Paciorek and Schervish (2006) may be used to extend the Matérn covariance model. We found an apparent unimodal-bimodal behaviour in the probability distribution of the phase error. This behaviour is studied in more detail in Chapter 3.

The random noise was modelled using a random field approach and the error was shown to depend on the moments of this random amplitude perturbation, as well as its smoothness and its long range correlations. In a dynamic noise field that changes at a time scale significantly shorter than the data acquisition window one can take advantage of empirical knowledge of the statistical characteristics of the noise field. However, for the case where the amplitude perturbation can be considered relatively fixed, we briefly presented a randomisation of the source contour as an approach to reduce acausal energy in the retrieval. Because the interferometric approximate is generally biased in amplitude, there is a limited benefit in increasing the number of boundaries and depending on the characteristics of the particular random field, the amplitude error may be compounded rather than mitigated. On the other hand, the phase estimate does benefit from this approach because under certain assumptions on the moments of the random field $\alpha$, the interferometrix approximate is an unbiased phase estimator. The phase improvement would improvement will be limited by the particular characteristics of the individual realisation of the random field, though in any case spurious arrivals are mitigated. This approach is consistent with the band-of-sources argument presented in Kimman and Trampert (2010), as the randomised boundaries would form a thick ring around the receiver pair, a key difference being that statistical correlations are considered in the present work. The error estimates using the multi-contour approach in a lower frequency regime are consistent with the 1% figure proposed by Kimman and

Trampert (2010). We find a larger error percentage in a higher frequency regime, due to the interactions between shorter wavelengths and local roughness of the random field, which are not detected at lower frequencies.

To apply such a scheme in practice, one could consider the source-receiver approach proposed by Curtis and Halliday (2010a), where virtual source boundaries can be constructed on dense receiver arrays. An error quantification approach in this scenario is sketched in Appendix A.

Chapter 3

# Estimation of error due to the stationary phase approximation in wavefield interferometry

In this Chapter we quantify the error introduced through the stationary phase approximation in the context of wavefield interferometry. In Section 3.1 the stationary phase method is briefly summarised and placed in the context of wavefield interferometry. The work of Olver (1974, 1970) on asymptotic expansions of Fourier integrals and error bounds in the stationary phase approximation is revisited, extended, and applied to wavefield interferometry in two dimensions, using the uncertainty framework developed in Chapter 2 to account for the effect of non-ideal source distributions on this widely used approximation. Olver's work is extended by deriving an explicit formulation for the coefficients of the asymptotic expansion that is required for a rigorous approximation to the Fourier integral by the stationary phase method, allowing for a random amplitude function. This formulation as well as the stationary phase method are implemented and subsequently numerically validated. In Section 3.5 the stationary phase method is applied to the wavefield interferometric, and error expressions are derived, in particular for the error in phase and the error in amplitude of the estimated Green's function due to the stationary phase approximation. These errors are considered in the presence of perturbations to the source amplitude, modelled as a random field. Bounds for these errors are given in terms of the inter-receiver distance, the wavenumber and the characteristics of the random field. Sufficient conditions are given for the stationary phase approximation to be an unbiased estimator of the inter-receiver Green's function, in terms of the moments of the random amplitude perturbation of the sources. Section 3.6 presents numerical results for the phase and amplitude errors analysed in the preceding sections for a specific distribution and covariance function of the random field $\alpha$. Section 3.7 deals with error quantification of the stationary phase approximation under the ideal conditions where

the intensity of the sources along the boundary does not vary. Error bounds are given in terms of the inter-receiver distance and the wavenumber.

## 3.1 Introduction

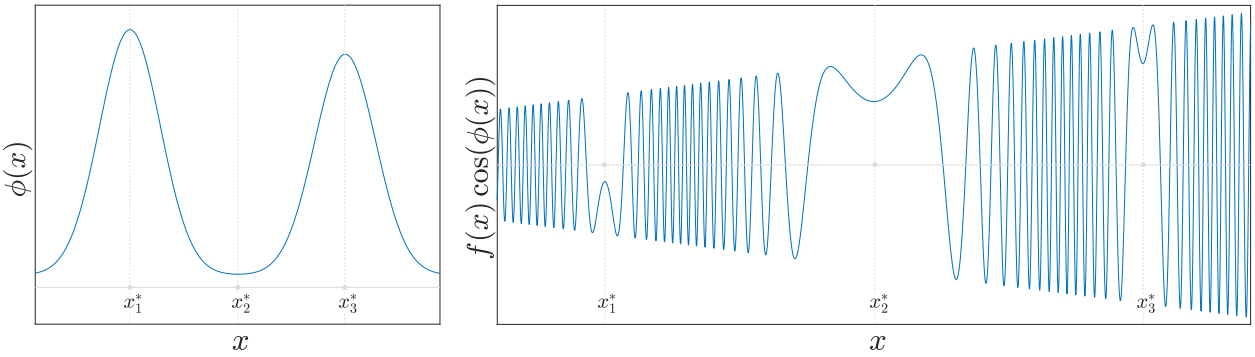


**Figure 3.1:** Illustration of the stationary phase principle. The left panel shows a phase function $\phi$ with three stationary points at $x_1^*, x_2^*, x_3^*$. The right panel shows the corresponding real component of the complex exponential with phase $\phi$ (with amplitude $f$ taken as the identity, i.e. $f(x) = x$). The main contributions to an integral of the form $\int f(x)exp\{\phi(x)\}dx$ will arise from neighbourhoods around the stationary points of $\phi$.

The principle of stationary phase is a standard tool of asymptotic analysis (Erdélyi, 1955; Jones, 1966; Bleistein and Handelsman, 1986; Bleistein, 2012; Bender and Orszag, 2013) that provides approximations to oscillatory integrals in high-frequency regimes. Broadly speaking, this classical method relies on the fact that the integral of a highly oscillatory function vanishes (the Riemann-Lebesgue lemma), and any non-trivial contributions to the integral arise from the regions around stationary points of the integrand's phase (see Figure 3.1).

This principle underpins the physical interpretation of interferometric equations, such as (1.2.12) or (1.2.13). It is widely invoked in wavefield interferometry to derive and simplify interferometric formulas (Schuster and Rickett, 2000; Aki and Richards, 2002; Schuster et al., 2004; Snieder, 2004; Schuster, 2009; Wapenaar et al., 2010a), and closely related to the Fresnel zones (Southwell, 1981; van Kampen, 1958) The stationary phase approximation is also used to address the effects of anisotropy and insufficient source coverage on the retrieved inter-receiver Green's functions in practical applications (Snieder et al., 2006, 2008; Halliday and Curtis, 2008b, 2009; Yao and Van Der Hilst, 2009; Kimman and Trampert, 2010; Snieder and Sens-Schönfelder, 2015).

In applications of wavefield interferometry, the stationary phase method is used an ad-hoc fashion, and in the absence of explicit expressions for the errors introduced through this approximation. In this Chapter, we aim to analyse the impact that introducing this

approximation has on the interferometric estimation of the inter-receiver Green's, particularly where its phase is concerned. Moreover, when the stationary phase principle is applied to heterogeneous media, the variations in the medium are assumed to be smooth (Snieder et al., 2006). To address the effect of smoothness (or lack thereof) on the stationary phase estimate, we perform a numerical study using particular choice of correlation function that allows us to link the behaviour of the error in the stationary phase estimate to the local smoothness and the long-range correlations of the random field that models variations in source intensity.

In this Chapter, the principle of stationary phase is briefly introduced, followed by a summary of the error analysis developed in Olver (1974). Then we present a derivation of the stationary phase approximation to the interferometric retrieval equation of the form (1.2.13) using an asymptotic expansion of the integral about the stationary points of the phase of the cross-correlation integrand. In particular, a general and explicit formula for the coefficients in asymptotic expansions of Fourier integrals is derived and numerically validated, expanding on the work of Olver (1974) by extending the framework to integrands with random amplitudes. This formula facilitates the exact numerical implementation of the stationary phase method to whatever order is desired, without requiring the use of series inversion techniques. Next, we address the effect that variations of source intensity have on the stationary phase approximation, and on the resulting phase and amplitude estimates. This is achieved by making use of the framework developed in Chapter 2 (see, e.g., (2.1.3) or (2.2.10)). We model the variations in source intensity as a correlated random field. Explicit expressions are derived for the stationary phase approximation in wavefield interferometry, as well as the general error in the resulting spectra, the error in phase and the error in amplitude. Sufficient conditions are given for the stationary phase approximate to be an unbiased estimator of the phase of the inter-receiver Green's function in terms of statistical properties of the random field governing the variations in source intensity. On the other hand, the stationary phase approximation is shown to be a biased estimator of the inter-receiver Green's function amplitude. The probability density function of the phase error is evaluated numerically for a specific random field distribution, and shown to be unimodal or bimodal depending on the parameters that control the random field (correlation length, smoothness and variance). The variance of the phase error is evaluated numerically and linked to the mode behaviour of the probability density function.

Finally, deterministic derivations, as well as relevant bounds are given for the ideal scenario where the source intensity is constant along the source boundary. Error terms are linked to end-point effects in the interferometric retrieval and error bounds are given in terms of the wave number and the inter-receiver distance.

The main results presented in this Chapter are as follows:

1. The stationary phase approximation to the interferometric estimate of the inter-receiver Green's function on a two-dimensional circular boundary is given by

$$\hat{g}_{\mathrm{sp}}(\mathbf{x_A}, \mathbf{x_B}, k\,;\,\alpha) = \alpha^2(\mathbf{x}_0)\hat{G}(\mathbf{x_A}, \mathbf{x_B}, k) - \alpha^2(\mathbf{x}_\pi)\hat{G}^*(\mathbf{x_A}, \mathbf{x_B}, k)\,, \tag{3.1.1}$$

where $\alpha(\mathbf{x})$ is a realisation of a random field at $\mathbf{x}$ that models variations in the source intensity, $\hat{G}(\mathbf{x_A}, \mathbf{x_B}, k)$ denotes the inter-receiver Green's function for the receiver pair $\mathbf{x_A}$ and $\mathbf{x_B}$ at the wavenumber $k$, and $\mathbf{x}_0$ and $\mathbf{x}_\pi$ denote the location of stationary phase contributions, which are shown to be the two points where the line that passes through the receiver pair intersects the source boundary (see Figure 3.5). Note that for a degenerate random field $\alpha(\mathbf{x}) \equiv 1$ the stationary phase estimate (3.1.1) reduces to the homogeneous Green's function defined in (1.1.2), i.e.

$$\hat{g}_{\mathrm{sp}}(\mathbf{x_A}, \mathbf{x_B}, k\,;\,1) = \hat{G}(\mathbf{x_A}, \mathbf{x_B}, k) - \hat{G}^*(\mathbf{x_A}, \mathbf{x_B}, k) = \hat{G}_{\mathrm{hom}}(\mathbf{x_A}, \mathbf{x_B}, k)\,. \tag{3.1.2}$$

2. The expected value of the error incurred through the stationary phase approximation is given by

$$\begin{aligned}\mathbb{E}\left[\,E_{\mathrm{sp}}(\mathbf{x_A}, \mathbf{x_B}, k\,;\,\alpha)\,\right] = &\left(\mathbb{E}\left[\,\alpha^2(\mathbf{x}_0)\,\right] - 1\right)\hat{G}(\mathbf{x_A}, \mathbf{x_B}, k) \\ &- \left(\mathbb{E}\left[\,\alpha^2(\mathbf{x}_\pi)\,\right] - 1\right)\hat{G}^*(\mathbf{x_A}, \mathbf{x_B}, k)\,,\end{aligned}$$

and its variance is given by

$$\begin{aligned}\mathrm{Var}\left[\,E_{\mathrm{sp}}(\mathbf{x_A}, \mathbf{x_B}, k\,;\,\alpha)\,\right] = &\left|\hat{G}(\mathbf{x_A}, \mathbf{x_B}, k)\right|^2\left\{\mathrm{Var}\left[\,\alpha^2(\mathbf{x}_0)\,\right] + \mathrm{Var}\left[\,\alpha^2(\mathbf{x}_\pi)\,\right]\right\} \\ &+ 2\left(\mathrm{Im}\left\{\hat{G}(\mathbf{x_A}, \mathbf{x_B}, k)\right\}^2 - \mathrm{Re}\left\{\hat{G}(\mathbf{x_A}, \mathbf{x_B}, k)\right\}^2\right)\mathrm{Cov}\left[\,\alpha^2(\mathbf{x}_0), \alpha^2(\mathbf{x}_\pi)\,\right]\end{aligned} \tag{3.1.3}$$

where $E_{\mathrm{sp}}(\mathbf{x_A}, \mathbf{x_B}, k\,;\,\alpha)$ denotes the error at the wavenumber $k$, defined as

$$E_{\mathrm{sp}}(\mathbf{x_A}, \mathbf{x_B}, k\,;\,\alpha) = \hat{g}_{\mathrm{sp}}(\mathbf{x_A}, \mathbf{x_B}, k\,;\,\alpha) - \hat{G}_{\mathrm{hom}}(\mathbf{x_A}, \mathbf{x_B}, k)\,.$$

3. Moreover, if the first and second moments if the random field $\alpha$ have the same value at the stationary phase locations $\mathbf{x}_0$ and $\mathbf{x}_\pi$, i.e.

$$\begin{aligned}\mathbb{E}\left[\,\alpha(\mathbf{x}_0)\,\right] &= \mathbb{E}\left[\,\alpha(\mathbf{x}_\pi)\,\right] = \mu_\alpha\,, \\ \mathrm{Var}\left[\,\alpha(\mathbf{x}_0)\,\right] &= \mathrm{Var}\left[\,\alpha(\mathbf{x}_\pi)\,\right] = \sigma_\alpha^2\,,\end{aligned} \tag{3.1.4}$$

for some $\mu_\alpha$, $\sigma_\alpha^2 \in \mathbb{R}$, then

$$\mathbb{E}\,[\,E_{\rm sp}(\mathbf{x_A},\mathbf{x_B},k\,;\,\alpha)\,] = (\,\mu_\alpha^2+\sigma_\alpha^2-1\,)\,\hat{G}_{\rm hom}(\mathbf{x_A},\mathbf{x_B},k)\,.$$

If, in addition, the fourth moment of the random field $\alpha$ has the same value at the locations $\mathbf{x}_0$ and $\mathbf{x}_\pi$, that is

$$\mathbb{E}\left[\,\alpha^4(\mathbf{x}_0)\,\right] = \mathbb{E}\left[\,\alpha^4(\mathbf{x}_\pi)\,\right] = \kappa_\alpha\,, \tag{3.1.5}$$

for some constant $\kappa_\alpha \in \mathbb{R}$, then

$$\begin{aligned}\mathrm{Var}\,[\,E_{\rm sp}(\mathbf{x_A},\mathbf{x_B},k\,;\,\alpha)\,] =& 2\,|\hat{G}(\mathbf{x_A},\mathbf{x_B},k)|^2(\kappa_\alpha-(\mu_\alpha^2+\sigma_\alpha^2)^2)\\ &+2\,\Lambda(\mathbf{x_A},\mathbf{x_B},k)\big\{\,\mathrm{Var}\,[\,\alpha(\mathbf{x}_0)\alpha(\mathbf{x}_\pi)\,]-(\mu_\alpha^2+\sigma_\alpha^2)^2\\ &+\big(\mathrm{Cov}\,[\,\alpha(\mathbf{x}_0),\alpha(\mathbf{x}_\pi)\,]+\mu_\alpha^2\big)^2\,\big\}\,,\end{aligned} \tag{3.1.6}$$

where $\Lambda(\mathbf{x_A},\mathbf{x_B},k)$ is defined as

$$\Lambda(\mathbf{x_A},\mathbf{x_B},k) = \mathrm{Im}\left\{\hat{G}(\mathbf{x_A},\mathbf{x_B},k)\right\}^2 - \mathrm{Re}\left\{\hat{G}(\mathbf{x_A},\mathbf{x_B},k)\right\}^2.$$

Note that assumptions (3.1.4) and (3.1.5) are satisfied in the more general case that the first, second and fourth moment of $\alpha$ are not spatially dependent. Further, (3.1.4) and (3.1.5) implicitly assume that these moments of $\alpha$ are finite. Furthermore, when the random field $\alpha$ is Matérn correlated and log-normally distributed, the variance of the error is given explicitly by

$$\begin{aligned}\mathrm{Var}\,[\,E_{\rm sp}(\mathbf{x_A},\mathbf{x_B},k\,;\,\alpha)\,] =& 2|\hat{G}(\mathbf{x_A},\mathbf{x_B},k)|^2\left\{\frac{(\mu_\alpha^2+\sigma_\alpha^2)^6}{\mu_\alpha^8}-(\mu_\alpha^2+\sigma_\alpha^2)^2\right\}\\ &+2\Lambda(\mathbf{x_A},\mathbf{x_B},k)\left\{\frac{(\mu_\alpha^2+\sigma_\alpha^2)^2}{\mu_\alpha^8}\left(\,M(2r;\,\rho_\alpha,\nu_\alpha)+\mu_\alpha^2\right)^4\right.\\ &\left.-(\mu_\alpha^2+\sigma_\alpha^2)^2\right\},\end{aligned}$$

4. The following bound is derived for any constant $\xi > 0$, for the probability of incurring a large error in the stationary phase approximation.

$$\mathbb{P}\,[\,|\mathrm{E}_{\rm sp}(\mathbf{x_A},\mathbf{x_B},\mathrm{k}\,;\,\alpha)\text{-}\,\mathbb{E}\,[\,\mathrm{E}_{\rm sp}(\mathbf{x_A},\mathbf{x_B},\mathrm{k}\,;\,\alpha)\,]\,|\geq\xi\,] \leq \frac{1}{\xi^2}\,\mathrm{Var}\,[\,E_{\rm sp}(\mathbf{x_A},\mathbf{x_B},k\,;\,\alpha)\,]\,,$$

5. The stationary phase estimate is an unbiased estimator of the phase of the homogeneous

inter-receiver Green's function, provided conditions (3.1.4) and (3.1.5) are satisfied. That is

$$\mathbb{E}\left[\, e_{\mathrm{ph}}(\mathbf{x_A}, \mathbf{x_B}, k;\, \alpha)\,\right] = 0\,,$$

where $e_{\mathrm{ph}}(\mathbf{x_A}, \mathbf{x_B}, k;\, \alpha)$ is the error in the estimated phase due to the stationary phase approximation, defined as

$$e_{\mathrm{ph}}(\mathbf{x_A}, \mathbf{x_B}, k;\, \alpha) = \arg\left(\hat{g}_{\mathrm{sp}}(\mathbf{x_A}, \mathbf{x_B}, k\,;\, \alpha)\right) - \arg\left(\hat{G}_{\mathrm{hom}}(\mathbf{x_A}, \mathbf{x_B}, k)\right)\,.$$

and $\arg(\cdot)$ is the argument function. That is, the stationary phase approximation is an unbiased estimator of the phase of the interferometric inter-receiver Green's function.

6. In an ideal retrieval scenario, i.e. $\alpha \equiv 1$, the error incurred through the stationary phase approximation in wavefield interferometry to the inter-receiver homogeneous Green's function in two dimensions is bounded above by

$$|\hat{g}_{\mathrm{sp}}(\mathbf{x_A}, \mathbf{x_B}, k; 1, 0) - \hat{G}_{\mathrm{hom}}(\mathbf{x_A}, \mathbf{x_B}, k)| \leq 2\sqrt{2}\left(\frac{\sqrt{2}-1}{k\,|\mathbf{x_A}-\mathbf{x_B}|} + \frac{1}{k^2\,|\,\mathbf{x_A}-\mathbf{x_B}|^2}\right)\,, \tag{3.1.7}$$

where $|\,\mathbf{x_A}-\mathbf{x_B}|$ is the inter-receiver distance and $k$ is a fixed wavenumber.

7. Let $\hat{g}_{\mathrm{sp}}(\mathbf{x_A}, \mathbf{x_B}, k)$ denote the stationary phase approximate to the monopole interferometric retrieval. In this Chapter I show the following

$$\oint_S \hat{G}(\mathbf{x_A}, \mathbf{x}, k)\hat{G}^*(\mathbf{x_B}, \mathbf{x}, k)\, d\mathbf{x} = \hat{g}_{\mathrm{sp}}(\mathbf{x_A}, \mathbf{x_B}, k) + E(\mathbf{x_A}, \mathbf{x_B}, k)\,, \qquad k \gg 1\,,$$

where

$$\hat{g}_{\mathrm{sp}}(\mathbf{x_A}, \mathbf{x_B}, k) = \hat{G}(\mathbf{x_A}, \mathbf{x_B}, k) - \hat{G}^*(\mathbf{x_A}, \mathbf{x_B}, k)$$

and

$$E(\mathbf{x_A}, \mathbf{x_B}, k) = \frac{4i}{k}\int_0^{\pi/2} p(t)e^{ik\phi(t)}\, dt \;-\; \frac{e^{i\left(\frac{\pi}{4}-2k|\mathbf{x_A}-\mathbf{x_B}|\right)}}{\sqrt{k|\mathbf{x_A}-\mathbf{x_B}|}}\,\Gamma\left(-\frac{1}{2},\, -2ki|\mathbf{x_A}-\mathbf{x_B}|\right)\,,$$

where $p(t)$ is a polynomial whose coefficients depend on the inter-receiver distance $|\mathbf{x_A}-\mathbf{x_B}|$ and the radius $r$ of the source boundary $S$, and the function $\phi(t)$ is the phase of the cross-correlation integrand $\hat{G}(\mathbf{x_A}, \mathbf{x}, k)\hat{G}^*(\mathbf{x_B}, \mathbf{x}, k)$ along the source boundary.

That is, an explicit error term $E(\mathbf{x_A}, \mathbf{x_B}, k)$ is derived for the difference between the exact cross correlational representation theorem (equivalent to the homogeneous inter-

receiver Green's funciton), and its monopole approximation.

## 3.2 The stationary phase approximation

The stationary phase method provides an asymptotic approximation of oscillatory integrals. Consider the Riemman integral

$$I(k) = \int_a^b f(t)e^{ik\phi(t)}\,dt\,, \qquad k \gg 1\,. \tag{3.2.1}$$

As illustrated in Figure 3.1, the phase of an exponential integrand is highly oscillatory except in the neighbourhoods of stationary points of the phase $\phi(t)$, so that destructive interference happens away from these distinguished points. Hence the value of the integral (3.2.1) can be estimated by considering only contributions around stationary points of the phase $\phi(t)$.

To derive this approximation, repeated integration by parts may be used to derive an asymptotic expansion of $I(k)$ as $k \to \infty$, assuming the phase and amplitude of the integrand are sufficiently differentiable. The most comprehensive justification for the stationary phase method is that of Erdélyi (1955, 1956) on asymptotic expansions of Fourier integrals. However, the approach employed by Erdelyi does not readily lend itself to the calculation of explicit error bounds (Olver, 1974; Cooke, 1978). Instead, Olver (1974) proposes an approach based on Hardy's theory of generalised integrals (Hardy, 1903, 1908), and gives explicit error expressions and bounds for the stationary phase approximation. We briefly summarise these results, followed by an extension that allows for an efficient numerical implementation of the stationary phase method, and proceed to apply this work to wavefield interferometry.

### 3.2.1 Main statement of the stationary phase approximation

In this Section, the main statements of the stationary phase method are stated. Their necessary assumptions summarised in Sections 3.2.2 and for brevity the proof is relegated to the Appendix B.1.

**Proposition 3.2.1** (Olver (1974))**.** *The stationary phase approximation to the integral* (3.2.1) *for* $k \gg 1$ *is given by*

$$\int_a^b f(t)e^{ik\phi(t)} \approx A_n(k) - B_m(k)\,, \tag{3.2.2}$$

*with*

$$A_n(k) = e^{ik\phi(a)} \sum_{j=0}^{n-\eta} e^{i\pi\frac{j+\lambda}{2\mu}} \Gamma\left(\tfrac{j+\lambda}{\mu}\right) \frac{a_j}{k^{\frac{j+\lambda}{\mu}}}\,, \tag{3.2.3}$$

$$B_m(k) = e^{ik\phi(b)} \sum_{j=0}^{m-1} P_j(b) \left(\tfrac{i}{k}\right)^{j+1}\,, \tag{3.2.4}$$

*where in* (3.2.3) *the coefficients* $a_j$ *and the parameters* $\mu$ *and* $\lambda$ *arise through certain asymptotic expansions that will be detailed below,* $n$ *is a non-negative integer such that*

$$m\mu - \lambda \leq n < (m+1)\mu - \lambda + 1\,, \tag{3.2.5}$$

*and*

$$\eta = \begin{cases} 0\,, & \text{if } n = m\mu - \lambda\,, \\ 1\,, & \text{otherwise ;} \end{cases} \tag{3.2.6}$$

*and in* (3.2.4) *the functions* $P_j(t)$ *are defined as*

$$P_j(t) = \left\{ \frac{1}{\phi'(t)} \frac{d}{dt} \right\}^j \frac{f(t)}{\phi'(t)}\,, \qquad j \in \{0, 1, \ldots, m\}\,, \tag{3.2.7}$$

*with* $P_0(t) = f(t)/\phi'(t)$*, and* $P_{-1}(t) = \int f(t)$ *is interpreted as the antiderivative of* $f(t)$*.*

*Furthermore, the error in the approximation* (3.2.2) *is given by*

$$E_{mn}(k) = \delta_{mn}(k) - \epsilon_{mn}(k)\,, \tag{3.2.8}$$

*where*

$$\delta_{mn}(k) = \left(\tfrac{i}{k}\right)^m \int_a^b e^{ik\phi(t)} Q'_{mn}(t)\, dt\,, \tag{3.2.9}$$

*and*

$$\epsilon_{mn}(k) = e^{ik\phi(a)} \sum_{j=0}^{n-1} e^{i\pi\frac{j+\lambda}{2\mu}} \frac{\Gamma\left(\frac{j+\lambda}{\mu}\right)}{\Gamma\left(\frac{j+\lambda}{\mu} - m\right)} \Gamma\left(\tfrac{j+\lambda}{\mu} - m,\, ik\{\phi(a) - \phi(b)\}\right) \frac{a_j}{k^{\frac{j+\lambda}{\mu}}}\,, \tag{3.2.10}$$

*where the functions* $Q_{mn}(t)$ *in* (3.2.9) *are defined as*

$$Q_{mn}(t) = P_{m-1}(t) - \sum_{j=0}^{n-1} \frac{\Gamma\left(\frac{j+\lambda}{\mu}\right)}{\Gamma\left(\frac{j+\lambda}{\mu} + 1 - m\right)} \frac{a_j}{(\,\phi(t) - \phi(a)\,)^{m-\frac{j+\lambda}{\mu}}}\,. \tag{3.2.11}$$

In (3.2.10), the upper incomplete gamma function $\Gamma(x, z)$ is used, i.e. the principal value of

$$\Gamma(x, z) = \int_z^\infty e^{-t} t^{x-1}\, dt\,.$$

This formulation of the stationary phase approximation was given by Olver (1974). We apply his framework to wavefield interferometry. A summary of the proof of Proposition 3.2.1 can be found in Section B.1 of Appendix B. However, the required assumptions for the validity of (3.2.2) and bounds for the errors (3.2.9) and (3.2.10) are detailed in Sections 3.2.2 and 3.2.3, due to their relevance the present work.

### 3.2.2 Assumptions

In Proposition 3.2.1, the following conditions are assumed to be satisfied:

(*i*) The limits of integration $a$ and $b$ do not depend on $k$, $a$ is finite with $a < b$, and $b$ may be finite or infinite.

(*ii*) The phase and amplitude functions $\phi(t)$ and $f(t)$ do not depend on the parameter $k$. In this work they are both assumed to be real.

(*iii*) On $(a, b)$, $f(t)$ and $\phi(t)$ are assumed to be $m$ and $m+1$ times continuously differentiable, respectively, for some positive integer $m$.

(*iv*) The phase function $\phi(t)$ is increasing on $(a, b)$, i.e. $\phi'(t) > 0$ for $t \in (a, b)$.

(*v*) The lower limit of integration $a$ is a local minimum of the phase $\phi(t)$, and it is in fact the only stationary point of the phase $\phi(t)$ on $(a, b)$. That is, for $t \in (a, b)$ we have $\phi'(t) = 0$ if and only if $t = a$. In particular, the upper limit $b$ is not a stationary point of $\phi(t)$.

(*vi*) As $t$ approaches $a$ from the right, $f(t)$ and $\phi(t)$ can be expanded as

$$f(t) \sim \sum_{j=0}^{\infty} f_j (t-a)^{j+\lambda-1}\,, \tag{3.2.12}$$

and

$$\phi(t) \sim \phi(a) + \sum_{j=0}^{\infty} \phi_j (t-a)^{j+\mu}, \tag{3.2.13}$$

respectively, where the coefficients $f_0$ and $\phi_0$ are not zero and $\mu$ and $\lambda$ are positive constants such that $\lambda < (m+1)\mu + 1$. These expansions are also assumed to be $m$ and $m+1$ times differentiable, respectively.

(*vii*) When $p(b) < \infty$, the functions $P_j(t)$ defined in (3.2.7) tend to a finite limit as $t \to b^-$ for every $j \in \{0, 1, \ldots, m\}$.

(*viii*) When $p(t) \to \infty$ as $t \to b^-$, $f(t)/\phi'(t) \to 0$, and the integrals

$$\int e^{ik\phi(t)} P_j(t) \phi'(t) dt$$

converge uniformly at $t = b$ for every $j \in \{0, 1, \ldots, m\}$ and $k$ sufficiently large.

Note that cases where condition (vi) is not satisfied, i.e. the phase is increasing rather than decreasing, it suffices to apply a complex conjugation before performing the approximation, and then apply a conjugation again to recover the original phase. The situation where assumption (v) is not satisfied, i.e. there is more than one stationary point in the interval of integration, can be readily addressed by subdividing the interval of integration appropriately. For example, one could take subintervals starting at each stationary point and finishing at each midpoint between consecutive stationary points. If the stationary point is a maximum, the results can be readily adapted by conjugating the integrand. On the other hand, condition *(vii)* is satisfied when $\phi^{(m+1)}(t)$ and $f^{(m)}(t)$ are continuous at $b$, in combination with assumption *(v)*, which establishes $\phi'(b) \neq 0$. Note that the smoothness requirement *(ii)* for the amplitude $f(t)$ is relevant for the application of the stationary phase approximation in practical settings, as it imposes the assumption that random variations in the amplitude of the integrand (and therefore the noise field) be smoothly varying. As will be seen in the subsequent derivations, a higher order approximation (which can be interpreted as a larger neighbourhood round the stationary location) requires the amplitude $f(t)$ to have a higher order of differentiability.

**Remark 3.2.1.** In the stationary phase approximation (3.2.2) the term $A_n(k)$ corresponds to a main contribution from the stationary point $a$, and the term $B_m(k)$ corresponds to an endpoint contribution from the upper limit of integration $b$. This interpretation becomes relevant in Section 3.5, where the stationary phase approximation is applied to wavefield interferometry and these terms are given a physical interpretation.

**Remark 3.2.2.** While the error term $\delta_{mn}(k)$ in (3.2.9) is well-defined owing to assumptions *(i)-(vii)*, it may not always be possible to find a closed form of the definite integral. On the other hand, its numerical integration can be challenging owing to the presence of the functions $Q_{mn}(t)$ and $P_{m-1}(t)$. These functions include high order inverse powers of either $\phi(t)'$ or the difference $\phi(t) - \phi(a)$, so that numerical cancellation and significant loss of accuracy may occur as $t \to a^+$ (see (3.2.11) and (3.2.7)). This issue is addressed in Section 3.4.

### 3.2.3 Bounds for the error in the stationary phase approximation

In this Section, the error bounds derived in Olver (1974) for the stationary phase approximation are briefly presented.

**Proposition 3.2.2** (Olver (1974))**.** *The total error* (3.2.8) *is bounded above by*

$$|E_{mn}(k)| \leq \frac{1}{k^m} \int_a^b |Q'_{mn}(t)|\, dt + \frac{2}{k^{m+1}} \sum_{j=0}^{n-1} \frac{\Gamma\left(\frac{j+\lambda}{\mu}\right)}{\left|\Gamma\left(\frac{j+\lambda}{\mu} - m\right)\right|} \frac{|a_j|}{(\,\phi(b) - \phi(a)\,)^{m+1-\frac{j+\lambda}{\mu}}}\,. \quad (3.2.14)$$

The bound (3.2.14) is derived here by taking the bounds given by Olver (1974) for each of the error terms (3.2.9) and (3.2.10). The former is derived directly from the definition of $\delta_{mn}(k)$, taking the modulus of the integral. The latter is established by invoking a particular bound for incomplete gamma functions. Details are relegated to Appendix B.1.

Throughout the application of the stationary phase method, it becomes indispensable to know the values of the asymptotic coefficients $\{a_j\}_{j=0}^{\infty}$. The first two coefficients are given in Olver (1974) and sometimes the third may be found across literature. However, these coefficients are not given in general due to the cumbersome nature of the series inversion procedures necessary to derive them, and because authors are often only interested in lower order approximations. However, in the application of the stationary phase approximation to wavefield interferometry, the order of the approximation can be interpreted as a parameter that controls the radius of the neighbourhood surrounding the stationary point, in line with practical applications and the physical interpretation of the Fresnel zone, so that higher order terms are of interest. Furthermore, in the numerical implementation of the stationary phase method, certain terms are liable to catastrophic cancellation due to specific limiting behaviours near the stationary point (see Remark 3.2.2). These numerical issues can be addressed by deriving high order approximations of the problematic terms, which are well-suited for direct implementation and help circumvent numerical instability. The high order is required to maintain accuracy in their numerical estimation. In the following section, we derive a general and exact closed formula for the coefficients $\{a_j\}_{j=0}^{\infty}$, expanding on the work

of Olver (1974).

## 3.3 Derivation of an explicit formula for the asymptotic coefficients in the stationary phase approximation

In this Section, an explicit formula for the asymptotic coefficients $\{a_j\}_{j=0}^{\infty}$ in the stationary phase approximation is derived constructively. This formula is given in terms of the coefficients $\{f_j\}_{j=0}^{\infty}$ and $\{\phi_j\}_{j=0}^{\infty}$ of the asymptotic expansions of $f(t)$ and $\phi(t)$ about $t = a$, as given in (3.2.12) and (3.2.13), respectively. These coefficients are assumed to be known to the desired order of the stationary phase approximation of the integral (3.2.1).

In order to state the main result, we establish some preliminary notation. In what follows, $\mathcal{P}(m)$ denotes the collection of unique integer partitions of a non-negative integer $m$, i.e. a collection of positive integers $\{p_i\}_{i=1}^{M}$ with $M \leq m$ such that $\sum_{i=1}^{M} p_i = m$, while $\tilde{\mathcal{P}}(m)$ denotes the ordered integer partitions of $m$. For an integer partition $\mathbf{p} \in \mathcal{P}(m)$ or $\mathbf{p} \in \tilde{\mathcal{P}}(m)$, multi-index notation is used as described below:

1. $\boldsymbol{p} = (p_1, \ldots, p_{\ell(\mathbf{p})})$, with $p_i \in \mathbb{N}$ and $\ell(\mathbf{p})$ referred to as the length of the partition.
2. $|\boldsymbol{p}| = \sum_{i=1}^{\ell(\mathbf{p})} p_i$. If $\mathbf{p} \in \mathcal{P}(m)$ or $\mathbf{p} \in \tilde{\mathcal{P}}(m)$, then $|\boldsymbol{p}| = m$.
3. $\phi_{\boldsymbol{p}} = \prod_{i=1}^{\ell(\mathbf{p})} \phi_{p_i}$, where $\phi_{p_i}$ is the coefficient in the expansion (3.2.13) with index $p_i$.
4. $\boldsymbol{q} = (q_1, \ldots, q_m)$, where $q_i$ is the exponent of $\phi_i$ in the product $\phi_{\boldsymbol{p}}$.
5. $\boldsymbol{q}! = \prod_{i=1}^{m} q_i!$
6. $m_{|\mathbf{q}|} = m(m-1)\cdots(m-|\boldsymbol{q}|+1)$, i.e. a falling factorial of length $|\boldsymbol{q}|$ for a non-negative integer $m$.

Throughout this Section, the convention is taken that the set of integer partitions of zero is empty, that empty sums are zero and empty products are one. Finally, define the auxiliary function

$$\Phi^{\lambda\mu}(m, j) = \sum_{\boldsymbol{p}\in\mathcal{P}(m)} \frac{1}{\boldsymbol{q}!} \left(\tfrac{j+\lambda}{\mu} - 1\right)_{|\boldsymbol{q}|} \phi_0^{s_{\lambda\mu}-|\boldsymbol{q}|} \phi_{\boldsymbol{p}}\,, \tag{3.3.1}$$

using the multi-index notation described above and where $s_{\lambda\mu} = (s+\lambda)/\mu - 1$. Having established the necessary preliminaries, we state the main result of this section

**Proposition 3.3.1.** *The asymptotic coefficients* $\{a_j\}_{j=0}^{\infty}$ *in Proposition 3.2.1 are given explicitly by*

$$a_j = \sum_{i=0}^{j-1} C^{\lambda\mu}(j,i) D^{\lambda\mu}(i) + D^{\lambda\mu}(j)\,, \tag{3.3.2}$$

*where*

$$C^{\lambda\mu}(j,i) = \sum_{\mathbf{p}\in\widetilde{\mathcal{P}}(j-i)} \prod_{r=1}^{\ell(\mathbf{p})} \left\{ -\frac{\Phi^{\lambda\mu}(j-|\mathbf{p}|_{r-1}, j-|\mathbf{p}|_r)}{\Phi^{\lambda\mu}(0,j)} \right\}\,, \tag{3.3.3}$$

*and*

$$D^{\lambda\mu}(j) = \frac{d_j}{\Phi^{\lambda\mu}(0,j)}\,, \tag{3.3.4}$$

*where* $d_j$ *is the* $j^{th}$ *coefficient in the series expansion of the function* $h(t) = f(t)/\phi'(t)$ *about the stationary point of* $\phi(t)$, $t = a$.

The coefficients $d_j$ in Proposition 3.3.1 are given explicitly in terms of the known coefficients of $f(t)$ and $\phi(t)$ in (3.3.7), and the functions $\Phi^{\lambda\mu}(m,j)$ have been defined in (3.3.1). Finally, we recall that the parameters $\lambda$ and $\mu$ are the those given in (3.2.12) and (3.2.13) for the asymptotic expansions of $f(t)$ and $\phi(t)$ about $t = a$, respectively.

*Proof.* This Proposition is now proven constructively. Define

$$h(t) = \frac{f(t)}{\phi'(t)}\,.$$

The series expansion for $\phi'$ can be obtained by taking the derivative of (3.2.13), yielding

$$\phi'(t) = \sum_{s=0}^{\infty} \phi_s (s+\mu)(t-a)^{s+\mu-1}\,. \tag{3.3.5}$$

Then the quotient of series (3.2.12) and (3.3.5) is given by

$$h(t) = (t-a)^{\lambda-\mu} \sum_{s=0}^{\infty} d_s (t-a)^s\,, \tag{3.3.6}$$

where

$$d_s = \frac{(-1)^s}{(\mu\phi_0)^{s+1}} \det\left(M_s^{f\phi}\right)\,, \tag{3.3.7}$$

and $M_s^{f\,\phi}$ is the matrix given by

$$M_s^{f\phi} = \begin{pmatrix} f_0 & \phi'_0 & 0 & 0 & \dots & 0 \\ f_1 & \phi'_1 & \phi'_0 & 0 & \dots & 0 \\ f_2 & \phi'_2 & \phi'_1 & \phi'_0 & \dots & 0 \\ \vdots & \vdots & \vdots & \vdots & \ddots & \vdots \\ f_{s-1} & \phi'_{s-1} & \phi'_{s-2} & \phi'_{s-3} & \cdots & \phi'_0 \\ f_s & \phi'_s & \phi'_{s-1} & \phi'_{s-2} & \cdots & \phi'_1 \end{pmatrix}_{(s+1)\times(s+1)} \tag{3.3.8}$$

where $\phi'_j$ are the coefficients in the series expansion (3.2.13) of $\phi'(t)$, that is $\phi'_j = (j+\mu)\phi_j$. Note that matrix (3.3.8) is upper Hessenberg, so the calculation of its determinant can be simplified using a recursive formula, a useful fact when considering the numerical implementation of the stationary phase approximation. Consider first the case where $\mu = 1$. Under this assumption (3.3.5) becomes

$$\phi(t) = \phi(a) + \sum_{s=0}^{\infty} \phi_s (t-a)^{s+1}\,. \tag{3.3.9}$$

Hence, taking $\mu = 1$ and $v = \phi(t) - \phi(a)$, and using expression (B.1.2) the following alternative expression for $h(t)$ around $a$ is found

$$h(t) = \sum_{s=0}^{\infty} a_s (\phi(t) - \phi(a))^{s+\lambda-1}\,. \tag{3.3.10}$$

To derive an expansion in powers of $(t-a)$, use (3.3.9) to write

$$\phi(t) - \phi(a) = \sum_{s=0}^{\infty} \phi_s (t-a)^{s+1}\,, \tag{3.3.11}$$

and substitute this expression into (3.3.10), yielding

$$\begin{aligned} h(t) &= \sum_{s=0}^{\infty} a_s \left( \sum_{m=0}^{\infty} \phi_m (t-a)^{m+1} \right)^{s+\lambda-1} \\ &= (t-a)^{\lambda-1} \sum_{s=0}^{\infty} a_s (t-a)^s \left( \sum_{m=0}^{\infty} \phi_m (t-a)^m \right)^{s_\lambda}\,, \end{aligned} \tag{3.3.12}$$

where for brevity we have defined $s_\lambda = s + \lambda - 1$. Next, note that for a fixed positive integer

$s_\lambda$ we have

$$\left(\sum_{m=0}^{\infty}\phi_m(t-a)^m\right)^{s_\lambda}=\sum_{m=0}^{\infty}\left(\sum_{\boldsymbol{p}\in\mathcal{P}(m)}\frac{(s_\lambda)_{|\boldsymbol{q}|}}{\boldsymbol{q}!}\phi_0^{s_\lambda-|\boldsymbol{q}|}\phi_{\boldsymbol{p}}\right)(t-a)^m\,, \tag{3.3.13}$$

where multi-index notation is used as described at the beginning of this Section. Substituting (3.3.13) into (3.3.12) yields

$$h(t)=(t-a)^{\lambda-1}\sum_{s=0}^{\infty}\sum_{m=0}^{\infty}a_s\Phi_{ms}^{\lambda 1}(t-a)^{m+s}\,, \tag{3.3.14}$$

where

$$\Phi_{ms}^{\lambda 1}=\sum_{\boldsymbol{p}\in\mathcal{P}(m)}\frac{(s_\lambda)_{|\boldsymbol{q}|}}{\boldsymbol{q}!}\phi_0^{s_\lambda-|\boldsymbol{q}|}\phi_{\boldsymbol{p}}\,, \tag{3.3.15}$$

and the superscripts stand for $\lambda$ and $\mu=1$, respectively. For the case $m=0$ the convention is taken that there is no integer partition of zero. Further, we use the conventions that an empty sum is zero and an empty product is one, respectively. Hence $\Phi_{0s}^{\lambda\mu}=\phi_0^{s_\lambda}$. When $\mu=1$, (3.3.6) becomes

$$h(t)=(t-a)^{\lambda-1}\sum_{s=0}^{\infty}d_s(t-a)^s\,. \tag{3.3.16}$$

Next we note that since both (3.3.16) and (3.3.14) are expansions of $h(t)$ in powers of $t-a$, their coefficients must be the same. They can be directly compared to determine the coefficients $a_s$. This procedure yields

$$d_s=\sum_{i=0}^{s}a_i\Phi_{s-i\,i}^{\lambda 1}\,.$$

The latter expression can be rearranged to yield a recurrence relation for the coefficients $a_s$, namely

$$a_s=\frac{1}{\Phi_{0s}^{\lambda 1}}\left(d_s-\sum_{i=0}^{s-1}a_i\Phi_{s-i\,i}^{\lambda 1}\right)\,,\qquad a_0=\frac{d_0}{\Phi_{00}^{\lambda 1}}\,. \tag{3.3.17}$$

Expression (3.3.17) provides a recursive formula to calculate the coefficients $a_s$ for the case $\mu=1$. The term $d_s$ is determined by equation (3.3.7) in terms of coefficients in the expansions of $f(t)$ and $\phi(t)$, which are assumed to be known to the required order. The terms $\Phi_{r-i\,i}^{\lambda 1}$ are determined using (3.3.15), taking the specified combinations of the coefficients of $\phi$. The next step is to consider the more general case of $\mu\geq 1$. An explicit formula is derived for this general case. We proceed similarly, noting that from (3.2.13) and the fact that

$v = \phi(t) - \phi(a)$, we have

$$v = \sum_{m=0}^{\infty} \phi_m (t-a)^{m+\mu} \,. \tag{3.3.18}$$

We can now substitute (3.3.18) in (3.3.10) to obtain

$$h(t) = (t-a)^{\lambda-\mu} \sum_{s=0}^{\infty} a_s (t-a)^s \left( \sum_{m=0}^{\infty} \phi_m (t-a)^m \right)^{s_{\lambda\mu}} , \tag{3.3.19}$$

where

$$s_{\lambda\mu} = \frac{s+\lambda}{\mu} - 1 \,.$$

Next we expand the fractional exponent $s_{\lambda\mu}$ and collect powers of $(t-a)$ in order to compare the coefficients with those of (3.3.6) and obtain a recurrence relation for $a_s$, valid for any real values of $\lambda$ and $\mu$. Using multi-index notation we have by the multinomial theorem that

$$\left( \sum_{m=0}^{\infty} \phi_m (t-a)^m \right)^{s_{\lambda\mu}} = \sum_{m=0}^{\infty} \left( \sum_{\boldsymbol{p} \in \mathcal{P}(m)} \frac{(s_{\lambda\mu})_{|\boldsymbol{q}|}}{\boldsymbol{q}!} \, \phi_0^{s_{\lambda\mu}-|\boldsymbol{q}|} \phi_{\boldsymbol{p}} \right) (t-a)^m \,, \tag{3.3.20}$$

where multi-index notation is used as defined at the beginning of this Section, and we further define

$$\Phi_{ms}^{\lambda\mu} = \sum_{\boldsymbol{p} \in \mathcal{P}(m)} \frac{(s_{\lambda\mu})_{|\boldsymbol{q}|}}{\boldsymbol{q}!} \, \phi_0^{s_{\lambda\mu}-|\boldsymbol{q}|} \phi_{\boldsymbol{p}} \,.$$

As before, for the case $m = 0$ the convention is taken that there is no integer partition of zero, and that empty sums and products are zero and one, respectively. Hence $\Phi_{0s}^{\lambda\mu} = \phi_0^{s_{\lambda\mu}}$. This notation allows us to rewrite (3.3.20) in a more tractable way as

$$\left( \sum_{m=0}^{\infty} \phi_m (t-a)^m \right)^{s_{\lambda\mu}} = \sum_{m=0}^{\infty} \Phi_{ms}^{\lambda\mu} (t-a)^m \,.$$

If we now turn our attention back to (3.3.19), we have that

$$h(t) = (t-a)^{\lambda-\mu} \sum_{s=0}^{\infty} \sum_{m=0}^{\infty} a_s \Phi_{ms}^{\lambda\mu} (t-a)^{m+s} \,, \tag{3.3.21}$$

and by the same argument used for the case $\mu = 1$ we can equate the series for $h(t)$ given in (3.3.16) to the series (3.3.21), leading to

$$\sum_{s=0}^{\infty} d_s (t-a)^s = \sum_{r=0}^{\infty} \sum_{m=0}^{\infty} a_r \Phi_{mr}^{\lambda\mu} (t-a)^{m+r} \,, \tag{3.3.22}$$

where the index in the right hand side has been changed from $s$ to $r$, for clarity. Equating coefficients in (3.3.22) results in

$$d_s = \sum_{i=0}^{s} a_i \Phi^{\lambda\mu}_{s-i\,i}\,.$$

Finally, rearranging the terms in this expression yields as before a recurrence relation for the coefficients $a_s$. Namely

$$a_s = \frac{1}{\Phi^{\lambda\mu}_{0s}}\left(d_s - \sum_{i=0}^{s-1} a_i \Phi^{\lambda\mu}_{s-i\,i}\right), \qquad a_0 = \frac{d_0}{\Phi^{\lambda\mu}_{00}}\,. \tag{3.3.23}$$

This result for the general case $\mu \geq 1$ agrees with (3.3.17), since $s_{\lambda 1} = s_\lambda$. In order to prevent numerical instabilities in the forthcoming implementations, we derive an explicit solution to the recurrence relation (3.3.23) as follows. Rearranging equation (3.3.23) we have

$$a_s = \frac{d_s}{\Phi^{\lambda\mu}_{0\,s}} + \sum_{i=0}^{s-1}\left(-\frac{\Phi^{\lambda\mu}_{s-i\,i}}{\Phi^{\lambda\mu}_{0\,s}}\right) a_i\,. \tag{3.3.24}$$

Let

$$B^{\lambda\mu}_{si} = -\frac{\Phi^{\lambda\mu}_{s-i\,i}}{\Phi^{\lambda\mu}_{0\,s}}\,,$$

and

$$D^{\lambda\mu}(s) = \frac{d_s}{\Phi^{\lambda\mu}_{0\,s}}\,.$$

Then equation (3.3.24) may be recast as

$$a_s = \sum_{i=0}^{s-1} B^{\lambda\mu}_{si} a_i + D^{\lambda\mu}(s)\,,$$

and it becomes apparent this is a non-homogeneous linear recurrence with variable coefficients $B^{\lambda\mu}_{si}$ and forcing function $D^{\lambda\mu}(s)$. Hence a solution can be directly given in the fashion of e.g. Mallik (1998) as

$$a_s = \sum_{i=0}^{s-1} C^{\lambda\mu}_{si} D^{\lambda\mu}(i) + D^{\lambda\mu}(s)\,, \tag{3.3.25}$$

where the coefficients $C^{\lambda\mu}_{si}$ are given by

$$C^{\lambda\mu}_{si} = \sum_{\mathbf{p}\in\widetilde{\mathcal{P}}(s-i)} \prod_{j=1}^{\ell(\mathbf{p})} B^{\lambda\mu}_{s-|\mathbf{p}|_{j-1}\,s-|\mathbf{p}|_j}\,, \tag{3.3.26}$$

where $\widetilde{\mathcal{P}}(s-i)$ again denotes integer partitions, but in this case their permutations are counted separately, [1] $\mathbf{p}$ is one of such partitions, $\ell(\mathbf{p})$ denotes the length of $\mathbf{p}$ and

$$|\mathbf{p}|_j = \sum_{k=1}^{j} p_k \,,$$

so that $|\mathbf{p}|_{\ell(\mathbf{p})} = |\mathbf{p}| = s-i$, and $|\mathbf{p}|_0 = 0$ (see remarks after equation (3.3.13)). For the case $s=0$, we note that $a_0 = D^{\lambda\mu}(0)$, which is in agreement with the known analytical value of $a_0$ (see (3.3.27) below). The coefficients defined in (3.3.26) yield expression (3.3.3), and together with equation (3.3.25) establish the result set out in Proposition 3.3.1. □

In the next Section, result (3.3.2) is numerically validated.

### Validation of the coefficient formula

The coefficients calculated using the explicit formula (3.3.2) are in full agreement with the analytical expressions for $a_0$, $a_1$ and $a_2$ given in Olver (1970) and Olver (1974), as well as the particular cases presented in Cooke (1978). These coefficients are restated below for reference.

$$a_0 = \frac{f_0}{\mu \phi_0^{\frac{\lambda}{\mu}}} \,, \tag{3.3.27}$$

$$a_1 = \frac{1}{\phi_0^{\frac{\lambda+1}{\mu}}} \left( \frac{f_1}{\mu} - \frac{(\lambda+1)\phi_1 f_0}{\mu^2 \phi_0} \right) \,, \tag{3.3.28}$$

$$a_2 = \frac{1}{\phi_0^{\frac{\lambda+2}{\mu}}} \left( \frac{f_2}{\mu} - \frac{(\lambda+2)\phi_1 f_1}{\mu^2 \phi_0} + \left\{ (\lambda+\mu+2)\phi_1^2 - 2\mu\phi_0\phi_2 \right\} \frac{(\lambda+2) f_0}{2\mu^3 \phi_0^2} \right) \,. \tag{3.3.29}$$

[1] For example, $(2,1)$ and $(1,2)$ count as different partitions of 3 in equation (3.3.26). The behaviour of the sub-indices in this case is not commutative, as opposed to equation (3.3.15) for example, where only sums and products of coefficients were involved. Hence the notation $\widetilde{\mathcal{P}}$ is introduced.

For illustration purposes, formula (3.3.2) is used to calculate the value for the next asymptotic coefficient, yielding

$$a_3 = \frac{1}{\phi_0^{\frac{\lambda+3}{\mu}}}\left(\frac{f_3}{\mu} - \frac{(\lambda+3)f_2\phi_1}{\mu^2\phi_0} + \frac{(\lambda+3)f_1}{2\mu^3\phi_0^2}\left(2\mu\phi_0\phi_2 - (\lambda+\mu+3)\phi_1^2\right) + \right.$$
$$\left. + \frac{f_0(\lambda+3)}{6\mu^4\phi_0^3}\left\{\phi_1(\lambda+\mu+3)(\phi_1^2(\lambda+2\mu+3) - 6\mu\phi_0\phi_2) + 6\mu^2\phi_o^2\phi_3\right\}\right). \tag{3.3.30}$$

The coefficients (3.3.27) - (3.3.30) further agree with the sample case presented in Sections 5 and 6 of Cooke (1978).

Formula (3.3.2) was numerically validated in MATLAB. One example is presented below for illustrations purposes. For this example, the phase and amplitude functions for an integral of the form (3.2.1) are

$$\phi(t) = \cos(t)\,, \qquad \text{and} \qquad f(t) = \sin^2(t)\,.$$

These choices result in the function $h(v)$ (see remarks above equation (B.1.2)) given by

$$\tilde{h}(v) = \sqrt{-v^2 + 2v}\,. \tag{3.3.31}$$

The phase function $\phi(t)$ given above has a minimum at $a = \pi$. Expanding the phase and amplitude functions about $a = \pi$ in the manner of (3.2.13) and (3.2.12) respectively, yields the parameters $\mu = 2$, and $\lambda = 3$. Figure 3.2 shows the first fifty exact asymptotic coefficients calculated from the Puiseux series expansion of $\tilde{h}(v)$ in blue circles, and the coefficients calculated using equation (3.3.2) as orange crosses, exhibiting good agreement. Further test cases may be found in Appendix B, as well as a summary of the numerical challenges encountered in this implementation and how they were addressed, pertaining in particular ratios of gamma functions.

Having established these results, we proceed to implement the stationary phase method in MATLAB, testing the implementation using the example given in Section 7 of Olver (1974), where exact expressions are readily available for comparison and validation.

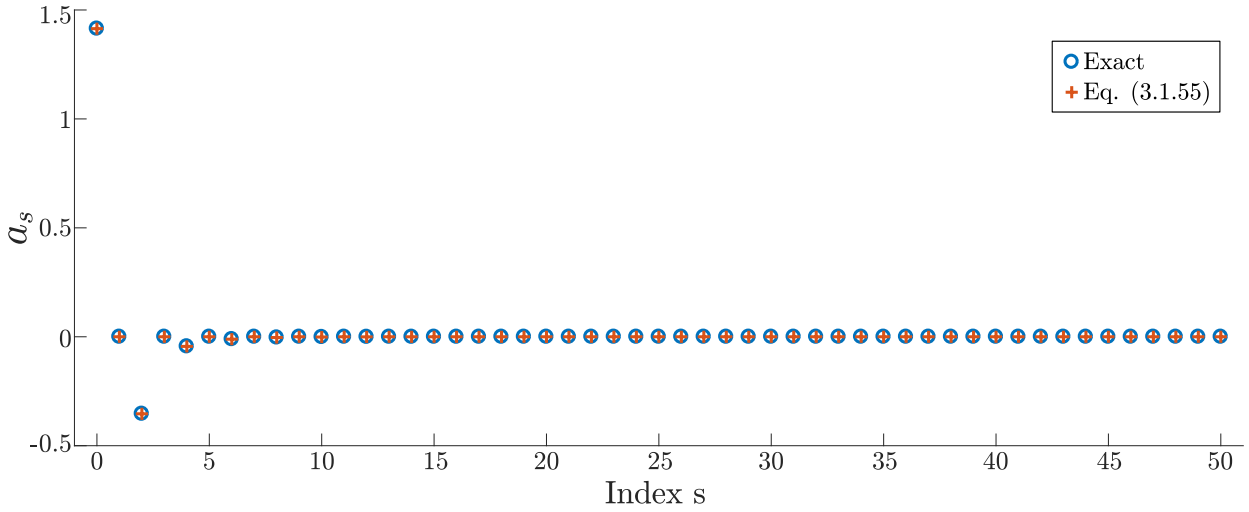


**Figure 3.2:** Comparison of the first fifty coefficients $\{a_s\}_{s=1}^{50}$ calculated from (3.3.25) (blue circles) and those extracted directly from the Puiseaux series expansion of $\tilde{h}$ in (3.3.31) about $a = \pi$ (orange crosses).

## 3.4 Numerical implementation of the stationary phase method

While literature covering the subject commonly evaluates the first few terms of the stationary phase asymptotic expansion, details of higher order terms are not generally given (Cooke, 1978) owing to the generality of Erdelyi's derivations (Erdélyi, 1955, 1956) and the cumbersome series inversion techniques involved. The first and second term are stated in Olver (1974), and the third term is further included in Olver (1970). Cooke (1978) gives the first three terms for a simplified case. However, a general formula for the coefficients has not yet been given. In this Section, an explicit general formula for the asymptotic coefficients $a_j$ is derived (see equation (B.1.2) and accompanying remarks). These coefficients are indispensable to calculate the terms in the stationary phase approximation, as well as the associated error bounds. With this formula, we are able to systematically implement the stationary phase method in MATLAB. This implementation is tested using as a reference the example provided in Section 7 of Olver (1974), so that explicit expressions are readily available to verify the correctness of the implementation and illustrate the approximation as well as the bounds, on the error incurred. The bounds on these errors are illustrated and the numerical challenges encountered are highlighted, as well as the strategy employed to address them.

The formula (3.3.2) derived in the preceding Section comprises an extension of the work in Olver (1970) and Olver (1974), as it explicitly produces the asymptotic coefficients indispensable a general and accurate numerical implementation of the stationary phase method,

as well as the evaluation of the error incurred. In this Section, the MATLAB implementation of the stationary phase approximation is presented and validated. In order to test this implementation, we apply it to an example presented in Section 7 of Olver (1974), where explicit expressions are readily available for comparison and validation. Consider the integral

$$I(k) = \int_0^\pi e^{ik(t-\sin(t))}\, dt\,. \tag{3.4.1}$$

In accordance with expression (3.2.1) we have the limits of integration $a = 0$ and $b = \pi$, the phase function $\phi(t) = t - \sin(t)$, which has a minimum at the lower limit of integration $a = 0$, and amplitude function $f(t) = 1$. These functions are infinitely differentiable, so that the expansions (3.2.12) and (3.2.13) are in fact their Taylor series about $a = 0$. Taking these series expansions readily shows that $\mu = 3$ and $\lambda = 1$. Next, definition (3.2.7) yields

$$P_j(t) = \frac{1}{2^{j+1}} \left\{ \frac{1}{\sin^2\left(\frac{t}{2}\right)} \frac{d}{dt} \right\}^j \frac{1}{\sin^2\left(\frac{t}{2}\right)}\,.$$

It is straightforward to verify that

$$P_0(t) = \frac{1}{2\sin^2\left(\frac{t}{2}\right)}\,, \quad P_1(t) = -\frac{\cos\left(\frac{t}{2}\right)}{4\sin^5\left(\frac{t}{2}\right)}\,, \quad P_2(t) = \frac{5 - 4\sin^2\left(\frac{t}{2}\right)}{16\sin^8\left(\frac{t}{2}\right)}\,. \tag{3.4.2}$$

On the other hand, direct use of equation (3.3.25) shows that the asymptotic coefficients of odd index vanish, which yields the following values for the even indexed coefficients,

$$a_0 = \tfrac{1}{3}\sqrt[3]{6}\,, \quad a_2 = \tfrac{1}{10}\,, \quad a_4 = \tfrac{324}{35}\sqrt[3]{6}\,, \quad a_6 = \tfrac{648}{25}\sqrt[3]{6}\,, \quad a_8 = \tfrac{3483}{2156000}\,, \ldots \tag{3.4.3}$$

and so on, which are in agreement with those derived in Olver (1974). Then, using (3.2.3) and (3.2.4) together with (3.2.2) we have that the stationary phase approximation to (3.4.1) is

$$\int_0^\pi e^{ik(\,t-\sin(t)\,)} \sim \sum_{j=0}^{n-1} e^{(j+1)i\frac{\pi}{6}} \Gamma\left(\tfrac{j+1}{3}\right) \frac{a_j}{k^{\frac{j+1}{3}}} - e^{\pi i k} \sum_{j=0}^{m-1} P_j(\pi) \left(\tfrac{i}{k}\right)^{j+1}\,, \quad k \gg 1\,, \tag{3.4.4}$$

where $m$ is an arbitrary non-negative integer, owing to the fact that both $\phi(t)$ and $f(t)$ are infinitely differentiable, $n$ is a non-negative integer such that $3m - 1 \leq n < 3m + 3$, in accordance to (3.2.5). The error in this approximation is given using (3.2.8) together

with (3.2.9) and (3.2.10), yielding

$$E_{mn}(k) = \left(\tfrac{i}{k}\right)^m \int_0^\pi e^{ik(\,t-\sin(t)\,)} Q'_{mn}(t)\,dt - \sum_{j=0}^{n-1} e^{i\pi\frac{j+1}{6}} \frac{\Gamma\left(\frac{j+1}{3}\right)}{\Gamma\left(\frac{j+1}{3}-m\right)} \Gamma\left(\tfrac{j+1}{3}-m,\,-ik\pi\right) \frac{a_j}{k^{\frac{j+1}{3}}}\,,$$

where the functions $Q_{mn}(t)$ are

$$Q_{mn}(t) = P_{m-1}(t) - \sum_{j=0}^{n-1} \frac{\Gamma\left(\frac{j+1}{3}\right)}{\Gamma\left(\frac{j+1}{3}+1-m\right)} \frac{a_j}{(\,t-\sin(t)\,)^{m-\frac{j+1}{3}}}\,. \tag{3.4.5}$$

To show a concrete example, take $m = 0$ and $n = 1$. For this choice of $m$ and $n$, approximation (3.4.4) yields

$$\int_0^\pi e^{ik(t-\sin(t))} \sim \frac{1}{3} e^{i\frac{\pi}{6}} \Gamma\left(\tfrac{1}{3}\right) \left(\tfrac{6}{x}\right)^{\frac{1}{3}}\,, \quad k \gg 1\,. \tag{3.4.6}$$

Figure 3.3 shows the resulting phase and amplitude estimated using approximation (3.4.6), as a function of $k$. As expected, there is a noticeable error for low values of $k$ and the approximation improves as $k$ grows larger.

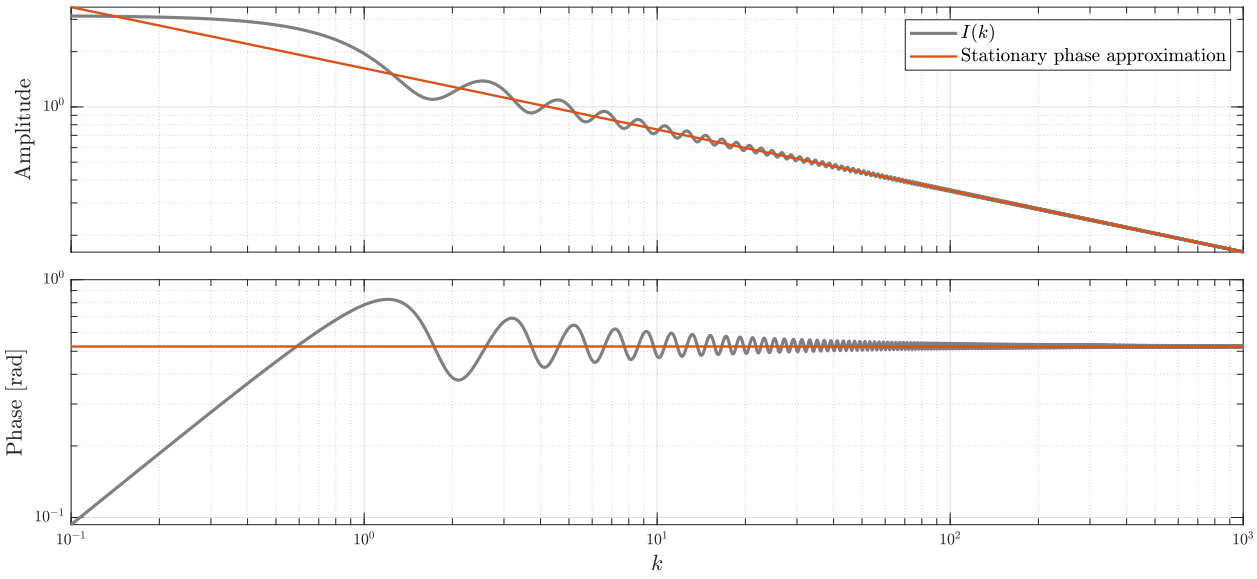


**Figure 3.3:** Comparison of the value of the integral $I(k)$ given in (3.4.1) in grey, and its stationary phase approximation (3.4.6) as a function of $k$. The amplitude (**top**) and phase (**bottom**) are compared. Logarithmic scale is used in both axes.

The error in the approximation (3.4.6) is given by

$$E_{01}(k) = \int_0^{\pi} e^{ik(\,t-\sin(t)\,)} Q'_{01}(t)dt - e^{i\frac{\pi}{6}} \left(\tfrac{2}{9k}\right)^{\frac{1}{3}} \Gamma\left(\tfrac{1}{3}, -ik\pi\right) . \tag{3.4.7}$$

where (3.4.5) has been used to calculate

$$Q'_{01}(t) = 1 - \frac{2-2\cos(t)}{\{\,6t-6\sin(t)\,\}^{\frac{2}{3}}} . \tag{3.4.8}$$

To derive a bound for (3.4.7) the bound for the term $\delta_{01}(k)$ is evaluated first using (B.1.13). Equation (3.2.11) is used again to obtain

$$Q_{11}(t) = \frac{1}{2\sin^2\left(\frac{t}{2}\right)} - \frac{2}{\{6(t-\sin(t))\}^{\frac{2}{3}}} , \tag{3.4.9}$$

and after simplification the right hand side of (B.1.13), yields the following

$$|\delta_{01}(k)| \leq \left( \frac{3}{5} - \frac{2}{(6\pi)^{\frac{2}{3}}} + \int_0^{\pi} |Q'_{11}(t)|dt \right) \frac{1}{k} . \tag{3.4.10}$$

On the other hand, the bound (B.1.14) for $\epsilon$ is given by

$$|\epsilon_{01}(k)| \leq \frac{4}{(6\pi)^{\frac{2}{3}}} \frac{1}{k} . \tag{3.4.11}$$

Therefore, a bound for the error (3.4.7) can be given combining (3.4.10) and (3.4.11) with the triangle inequality, yielding

$$|E_{01}(k)| \leq \left( \frac{3}{5} + \frac{2}{(6\pi)^{\frac{2}{3}}} + \int_0^{\pi} |Q'_{11}(t)|dt \right) \frac{1}{k} . \tag{3.4.12}$$

The top panel of Figure 3.4 shows the error (3.4.7) as well as the bound (3.4.12). For illustration purposes, that same figure shows the terms $\delta_{01}(k)$ and $\epsilon_{01}(k)$ and their corresponding bounds (3.4.10) and (3.4.11), respectively. For illustration, some examples of the numerical value of the error $|E_{01}(k)|$ and the bound (3.4.12) shown in the top panel of Figure 3.4 are given below across different scales of the wavenumber $k$.

| $k$ | $\lvert E_{01}(k)\rvert$ | $\lvert\delta_{01}(k) - \epsilon_{01}(k)\rvert$ |
|---|---|---|
| 0.1 | 1.4591 | 10.0475 |
| 1 | 0.5657 | 1.0048 |
| 10 | 0.0397 | 0.1005 |
| 100 | 0.0040 | 0.0100 |

As visible in the Figure, the bound overestimates the error for small values of $k$, and becomes tighter as $k$ increases. This is likely due to the relatively rough upper bound taken for $\delta_{mn}(k)$ in (B.1.12), and the roughness of this bound for low $k$ values can be appreciated in the middle panel of Figure 3.4, whereas the bound for the $\epsilon_{mn}$ is relatively tighter. In the subsequent sections, the integral $\delta_{mn}(k)$ is addressed analytically in order to circumvent this issue. Note that Olver (1974) does give a further bound that is one order higher, with the caveat that convergence of the relevant integrals can no longer be guaranteed.

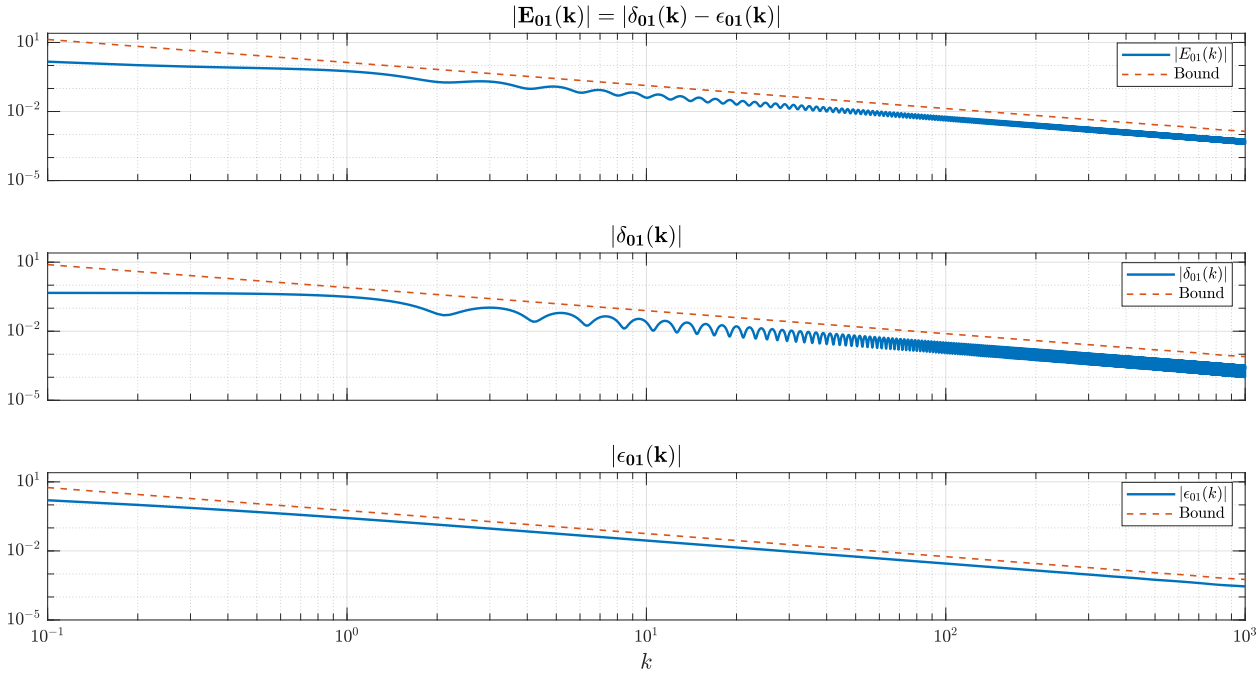


**Figure 3.4:** Error $E_{01}(k)$ in the stationary phase approximation (3.4.4) as given by equation (3.4.7) in blue, and the corresponding bound (3.4.12) in orange dashes (**top**). For illustration purposes, the error term $\delta_{01}(k)$ calculated directly from (3.2.9) and its bound (3.4.10) are included (**middle**), as well as the error term $\epsilon_{01}(k)$ and its bound (3.4.11) (**bottom**).

## 3.5 Stationary phase approximation in wavefield interferometry

In this Section, we apply the stationary phase approximation to wavefield interferometry in two dimensions, using the framework developed in Chapter 2 for error quantification. In this context, we consider an active-source scenario, so that recordings are available for each location $\mathbf{x}$ on a source boundary $S$, and ambient noise is assumed to not have significantly interfered with these active-source recordings. Accordingly we set the term $\beta$ to zero in the empirical interferometric equation (1.1.2), which results in the representation

$$\hat{g}_{\text{int}}(\mathbf{x_A}, \mathbf{x_B}, k\,;\,\alpha, 0) = -2ik \oint_S |\alpha(\mathbf{x})|^2\, \hat{G}(\mathbf{x_A}, \mathbf{x}, k)\hat{G}^*(\mathbf{x_B}, \mathbf{x}, k)d\mathbf{x}\,, \tag{3.5.1}$$

where $\alpha(\mathbf{x})$ denotes a realisation of a random field at $\mathbf{x}$ and $S$ is a source boundary that encloses the receiver pair $\mathbf{x_A}$, $\mathbf{x_B}$. Moreover, in this Chapter we assume for simplicity that the random field $\alpha(\mathbf{x})$ is real-valued, so that $|\alpha(\mathbf{x})|^2 = \alpha^2(\mathbf{x})$. For simplicity, the term $\beta \equiv 0$ is left implicit throughout.

**Proposition 3.5.1** (Stationary phase approximation to the interferometric estimate)**.** *The stationary phase approximation to* (3.5.1) *is given by*

$$\hat{g}_{int}(\mathbf{x_A}, \mathbf{x_B}, k\,;\,\alpha, 0) \approx \alpha_S^2(0)\hat{G}(\mathbf{x_A}, \mathbf{x_B}, k) - \alpha_S^2(\pi)\hat{G}^*(\mathbf{x_A}, \mathbf{x_B}, k)\,.$$

*where $\alpha_S^2(0)$ and $\alpha_S^2(\pi)$ are the squared values of the random field $\alpha$ at the points where the line through the receiver pair intersects the source boundary $S$. When the $\hat{G}(\mathbf{x}, \mathbf{y}, k)$ is the far-field Green's function of the Helmholtz equation in two dimensions, defined in* (1.2.20) *and reproduced below for reference*

$$\hat{G}(\mathbf{x}, \mathbf{x}', k) = -\frac{i}{4} e^{-i\left(k|\mathbf{x}-\mathbf{x}'|-\frac{\pi}{4}\right)} \sqrt{\frac{2}{\pi k|\mathbf{x}-\mathbf{x}'|}}\,,$$

*the stationary phase approximation is given by*

$$\hat{g}_{int}(\mathbf{x_A}, \mathbf{x_B}, k\,;\,\alpha, 0) \approx -\frac{i}{4}\left(e^{-i\left(2kd-\frac{\pi}{4}\right)}\alpha_S^2(0)\sqrt{\frac{\pi}{kd}} + e^{i\left(2kd-\frac{\pi}{4}\right)}\alpha_S^2(\pi)\sqrt{\frac{\pi}{kd}}\right)\,.$$

*where $2d = |\mathbf{x_A} - \mathbf{x_B}|$ is the inter-receiver distance.*

The validity of this proposition is derived in this Section. As a starting point the stationary phase approximation to equation (3.5.1) is considered, and highlighting the fact that

the presence of the random field $\alpha(\mathbf{x})$ does not affect the phase of the integrand in (3.5.1) as it enters the integral with a modulus square. We wish to write equation (3.5.1) in the form given by (3.2.1) in such a way that the phase and amplitude functions are analytically tractable, with the goal of applying the analytical results from Sections 3.2 and 3.3, and derive explicit expressions for the error incurred in taking a stationary phase approximation, as well as bounds for these errors. We begin by recalling that the stationary phase approximation is valid in a high frequency regime, i.e. $k \gg 1$, therefore the asymptotic (far-field) form of the Green's function of the Helmholtz equation in two dimensions (1.2.20) will be use, i.e.

$$\hat{G}(\mathbf{x}, \mathbf{x}', k) = -\frac{i}{4} e^{-i\left(k|\mathbf{x}-\mathbf{x}'|-\frac{\pi}{4}\right)} \sqrt{\frac{2}{\pi k|\mathbf{x}-\mathbf{x}'|}}\,,$$

for a receiver location $\mathbf{x}$, a source location $\mathbf{x}'$ and a wavenumber $k = \omega/c$ where $c$ denotes the speed in a homogeneous medium, assumed in this work to be constant. As previously discussed, in the context of wavefield interferometry, equation (1.2.20) is interpreted as the far-field of the wavefield (see for example Appendix A in Galetti et al. (2013)). This corresponds in the current context to the regime where $kr \gg 1$ where $r$ is the source-receiver distance and $k$ is a wavenumber. As discussed in Section 1.2.2, the monopole approximation (1.2.13) to the full interferometric retrieval given by equation (1.2.12) is valid in this regime. Substituting equation (1.2.20) into the monopole retrieval equation (3.5.1) for each receiver and simplifying yields

$$\hat{g}_{\text{int}}(\mathbf{x_A}, \mathbf{x_B}, k;\, \alpha, 0) = -\frac{i}{4\pi} \oint_S \frac{\alpha^2(\mathbf{x})}{\sqrt{|\mathbf{x_A}-\mathbf{x}||\mathbf{x_B}-\mathbf{x}|}} e^{ik(\,|\mathbf{x_B}-\mathbf{x}|-|\mathbf{x_A}-\mathbf{x}|\,)} d\mathbf{x}\,. \tag{3.5.2}$$

Assume that $S$ is a circular boundary of radius $r$ as depicted in Figure 3.5 and that the reference axes have been placed at the centre of $S$. Moreover, assume that the receivers $\mathbf{x_A}$ and $\mathbf{x_B}$ are placed symmetrically with respect to the origin and along the $x$-axis, with an inter-receiver distance given by

$$|\mathbf{x_A}-\mathbf{x_B}| = 2d \qquad \text{for} \qquad d > 0\,,$$

as depicted in Figure 3.5, so that the coordinates of the receivers are given by

$$\mathbf{x_A} = [\,-d,\, 0\,]\,, \qquad \text{and} \qquad \mathbf{x_B} = [\,d,\, 0\,]\,. \tag{3.5.3}$$

Having set the geometry of the problem, consider the following parametrisation of the

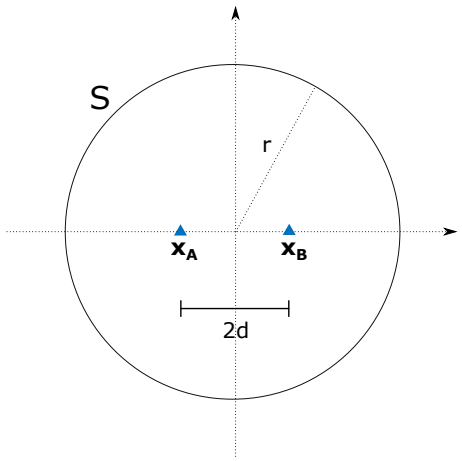


**Figure 3.5:** Sketch of source boundary and receiver layout used for wavefield interferometry in this Chapter. The radius $r \gg d$ of the boundary $S$ is not to scale for illustration purposes.

boundary $\mathbf{x}(t) \in S$,

$$\mathbf{x}(t) = [\, r\cos(t),\, r\sin(t)\,] \quad \text{for} \quad t \in \left[-\tfrac{\pi}{2},\, \tfrac{3\pi}{2}\right) , \tag{3.5.4}$$

where the range of the parametrisation has been chosen for convenience without loss of generality. Note that over the range defined in (3.5.4), the integrand phase $\phi(t)$ is not monotonous. However, this issue is easily circumvented by subdividing the interval of integration appropriately as will be shown below. Using this parametrisation the integral in the right hand side of equation (3.5.2) can be written as

$$\hat{g}_{\text{int}}(\mathbf{x_A}, \mathbf{x_B}, k;\, \alpha, 0) = -\frac{i}{4\pi} I^{\alpha}(\mathbf{x_A}, \mathbf{x_B}, k)\,, \tag{3.5.5}$$

where $I^{\alpha}(\mathbf{x_A}, \mathbf{x_B}, k)$ is given as

$$I^{\alpha}(\mathbf{x_A}, \mathbf{x_B}, k) = \int_{-\pi/2}^{3\pi/2} f^{\alpha}(t)\, e^{ik\phi(t)}\, dt\,, \tag{3.5.6}$$

$\phi(t)$ is the deterministic phase function

$$\phi(t) = \sqrt{r^2 - 2\,rd\cos(t) + d^2} - \sqrt{r^2 + 2\,rd\cos(t) + d^2}\,, \tag{3.5.7}$$

and $f^{\alpha}(t)$ is the random amplitude function

$$f^{\alpha}(t) = \frac{r\,\alpha^2(t)}{\{\,(r^2+d^2)^2 - 4r^2d^2\cos^2(t)\,\}^{\frac{1}{4}}}\,, \tag{3.5.8}$$

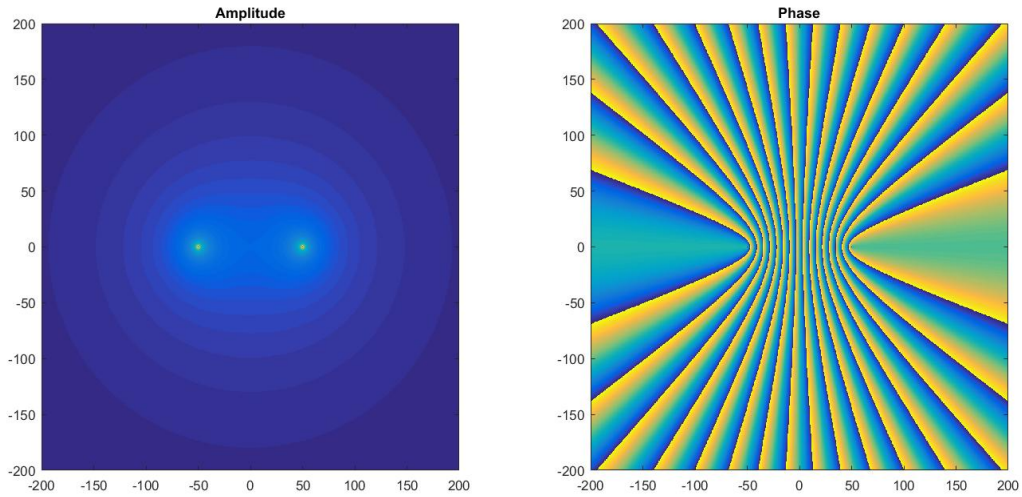


**Figure 3.6:** Amplitude (**left**) and phase (**right**) of the two-dimensional correlation integrand in (3.5.2), showing the symmetry with respect to the axis defined by the receiver locations.

where the notation $\alpha(t)$ is used to denote the restriction of the spatial random field $\alpha(\mathbf{x}')$ to the parametrised boundary $\mathbf{x}(t) \in S$, defined as

$$\alpha_S(t) \coloneqq \alpha(\mathbf{x}(t)) \qquad \text{for } t \in \left[-\tfrac{\pi}{2}, \tfrac{3\pi}{2}\right) ,$$

noting that a fixed value of the parameter $t$ corresponds to a fixed location $\mathbf{x}(t)$ and hence $\alpha_S(t)$ is a random field continuous in $t$, since it is a restriction the spatially continuous random field $\alpha$ to the source boundary $S$. Moreover, define for convenience the deterministic amplitude function

$$f(t) = \frac{r}{\{\,(r^2+d^2)^2 - 4r^2d^2\cos^2(t)\,\}^{\frac{1}{4}}} , \tag{3.5.9}$$

then the random amplitude function $f^\alpha(t)$ can be expressed in terms of $f(t)$ and the random field $\alpha_S(t)$ as

$$f^\alpha(t) = \alpha_S^2(t) f(t) . \tag{3.5.10}$$

We now consider the stationary phase approximation to the random integral $I^\alpha(\mathbf{x_A}, \mathbf{x_B}, k)$. The first task is to find the stationary points of the phase function (3.5.7), which are given by the zeros of the first derivative

$$\phi'(t) = \frac{dr\sin(t)}{\sqrt{r^2 - 2\,rd\cos(t) + d^2}} + \frac{dr\sin(t)}{\sqrt{r^2 + 2\,rd\cos(t) + d^2}} . \tag{3.5.11}$$

where $(\cdot)'$ denotes a differentiation with respect to $t$. It is immediate that $t = 0$ and $t = \pi$

are roots of equation (3.5.11), since the factor $\sin(t)$ is zero for these two values of $t$. On the other hand, it is straightforward to show that $\phi'(t)$ is zero if and only if

$$\sqrt{r^2 - 2\,rd\cos(t) + d^2} + \sqrt{r^2 + 2\,rd\cos(t) + d^2} = 0\,, \tag{3.5.12}$$

where we that the condition $r > d > 0$ imposed by the geometry of the problem implies the only roots of (3.5.12) (and hence $\phi'(t)$) are $t = 0$ and $t = \pi$. Therefore, these are the only stationary points of the phase $\phi(t)$. Direct evaluation of $\phi''(t)$ at these points readily shows that $\phi''(0) > 0$ and $\phi''(\pi) < 0$, A similar analysis shows that $t = 0$ and $t = \pi$ are maxima of the amplitude $f$, though this has no bearing on the principle of stationary phase approximation. Figure 3.7 shows the plots of the phase and amplitude functions (3.5.7) and (3.7.6), where the phase $\phi(t)$ exhibits a minimum at $t = 0$ and a maximum at $t = \pi$.

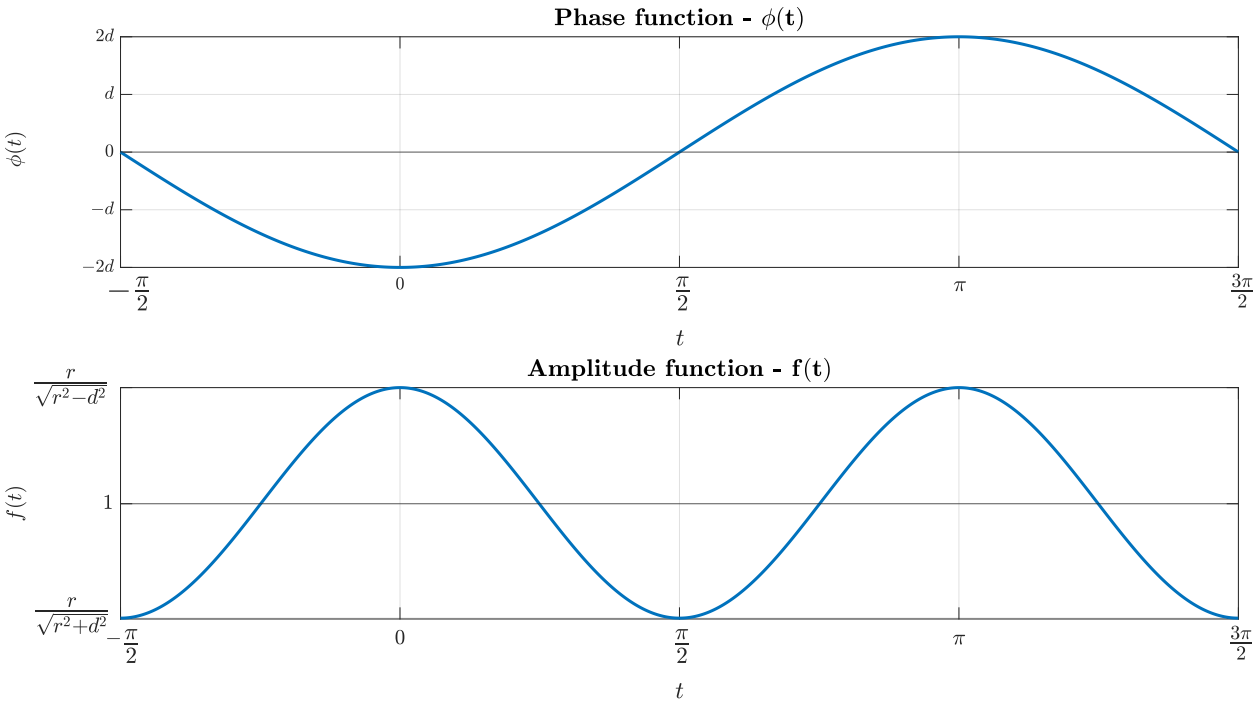


**Figure 3.7:** Plot of the phase function (3.5.7) (**top**) and amplitude function (3.7.6) (**bottom**) in terms of the parameter $t$. The values $r = 1000$ m and $d = 100$ m were used to generate these plots.

Note that $\phi(t)$ is $2\pi$-periodic and $f(t)$ is $\pi$-periodic, so that for any $t$

$$\phi(t + 2n\pi) = \phi(t) \qquad \text{and} \qquad f(t + n\pi) = f(t) \qquad \text{for } n \in \mathbb{Z}\,, \tag{3.5.13}$$

Moreover, direct evaluation shows that both $\phi(t)$ and $f(t)$ are even functions, so that for any $t$

$$\phi(-t) = \phi(t) \qquad \text{and} \qquad f(-t) = f(t)\,. \tag{3.5.14}$$

Both their periodicity and their symmetry around $t = 0$ can be plainly appreciated in Figure 3.7. Finally, the following property will be useful

$$\begin{aligned}\phi(t \pm \pi) &= \sqrt{r^2 - 2\,rd\cos(t \pm \pi) + d^2} - \sqrt{r^2 + 2\,rd\cos(t \pm \pi) + d^2} \\ &= \sqrt{r^2 + 2\,rd\cos(t) + d^2} - \sqrt{r^2 - 2\,rd\cos(t) + d^2} \\ &= -\phi(t)\,.\end{aligned} \tag{3.5.15}$$

Note that while these properties cannot immediately be extended to $f^\alpha(t)$, the properties presented below may nevertheless be derived by combining (3.5.10) with (3.5.14) and (3.5.13), respectively,

$$f^\alpha(-t) = \alpha_S^2(-t) f(t)\,, \tag{3.5.16}$$

and

$$f^\alpha(t + n\pi) = \alpha_S^2(t + n\pi) f(t) \qquad \text{for } n \in \mathbb{Z}\,, \tag{3.5.17}$$

The locations on the boundary corresponding to the stationary points of the phase are, according to the parametrisation given in (3.5.4),

$$\mathbf{x}_0 = \mathbf{x}(0) = [\,r,\,0\,]\,, \tag{3.5.18}$$

and

$$\mathbf{x}_\pi = \mathbf{x}(\pi) = [\,-r,\,0\,]\,. \tag{3.5.19}$$

Hence the stationary phase approximation is taken around the antipodal points on the boundary $S$ that result from the intersection of the boundary and the axis on which the receiver pair lies. Moreover, this analysis agrees with the well-known geometry of the Fresnel zones for a pair of receivers enclosed by a boundary, which are found in neighbourhoods of the intersection of the axis determined by the receiver pair with the enclosing source boundary (see for example van Kampen (1958); Curtis and Halliday (2010a)).

Since the interval $t \in [\frac{\pi}{2}, \frac{3\pi}{2})$ contains two stationary points, we split the interval of integration into the four quadrants

$$\begin{aligned}I^\alpha(\mathbf{x_A}, \mathbf{x_B}, k) = I^{\alpha,\,0^-}(\mathbf{x_A}, \mathbf{x_B}, k) + I^{\alpha,\,0^+}(\mathbf{x_A}, \mathbf{x_B}, k) + \\ + I^{\alpha,\,\pi^-}(\mathbf{x_A}, \mathbf{x_B}, k) + I^{\alpha,\,\pi^+}(\mathbf{x_A}, \mathbf{x_B}, k)\,,\end{aligned} \tag{3.5.20}$$

where we define

$$I^{\alpha,\,0^-}(\mathbf{x_A},\mathbf{x_B},k) = \int_{-\pi/2}^{0} f^\alpha(t)e^{ik\phi(t)}\,dt\,, \tag{3.5.21}$$

$$I^{\alpha,\,0^+}(\mathbf{x_A},\mathbf{x_B},k) = \int_{0}^{\pi/2} f^\alpha(t)e^{ik\phi(t)}\,dt\,, \tag{3.5.22}$$

$$I^{\alpha,\,\pi^-}(\mathbf{x_A},\mathbf{x_B},k) = \int_{\pi/2}^{\pi} f^\alpha(t)e^{ik\phi(t)}\,dt\,, \tag{3.5.23}$$

and

$$I^{\alpha,\,\pi^+}(\mathbf{x_A},\mathbf{x_B},k) = \int_{\pi}^{3\pi/2} f^\alpha(t)e^{ik\phi(t)}\,dt\,. \tag{3.5.24}$$

The stationary phase approximation to $I^\alpha(\mathbf{x_A},\mathbf{x_B},k)$ will be implemented by applying the results from Sections 3.2 and 3.3 separately to each of the four integrals (3.5.21) to (3.5.24). By decomposing the original interval of integration in this manner, we are closer to satisfying conditions 3.2.2, as none of the four intervals of integrations contains any interior stationary points, so that we can ensure that the phase $\phi(t)$ is monotonic. Furthermore, the stationary points $t \in \{0,\pi\}$ appear only at one of the limits of integration in each of these four integrals. It is apparent however that only $I^{\alpha,\,0^+}(\mathbf{x_A},\mathbf{x_B},k)$, satisfies conditions 3.2.2 since $t=0$ is a minimum of the the phase $\phi(t)$, this phase is strictly increasing on the interval $t \in (0,\frac{\pi}{2})$, and the upper limit of this integral, $t=\frac{\pi}{2}$, is not a stationary point of $\phi(t)$. The other three integrals require similar manipulations before they meet all conditions and the stationary phase approximation can be applied. The stationary phase approximation to $I^{\alpha,\,0^+}(\mathbf{x_A},\mathbf{x_B},k)$ is considered first. Each of the other three integrals will be considered later on a case-by-case basis, though the procedure is analogous so that the calculations for the latter three are relegated to the Appendix B.

First, consider the stationary phase approximation to the integral $I^{\alpha,\,0^+}$ at $t=0$

$$I^{\alpha,\,0^+}(\mathbf{x_A},\mathbf{x_B},k) = \int_{0}^{\pi/2} f^\alpha(t)e^{ik\phi(t)}\,dt\,,$$

An expansion of the form (3.2.13) is now derived for the phase of the integrand. The phase

function $\phi(t)$ is analytic and can therefore be expanded about $t = 0$ in a Taylor series. Moreover, the previous analysis of the stationary points and the first and second derivatives of $\phi(t)$ shows that the first non-trivial power of $t$ to appear in the series about $t = 0$ is $t^2$ (since $\phi'(0) = 0$ but $\phi''(0) \neq 0$), and hence using equation (3.2.13) we have $\mu = 2$. Therefore $\phi(t)$ can be expressed as

$$\phi(t) = \phi(0) + \phi_0 t^2 + \phi_1 t^3 + \dots$$

where

$$\phi_j = \phi^{(j+2)}(t)\Big|_{t=0} .$$

Calculating these coefficients yields

$$\phi(t) \approx -2d + \frac{r^2 d}{r^2 - d^2}\, t^2 + O(t^4)\,, \tag{3.5.25}$$

which is of the form (3.2.13), noting that $\phi(a) = \phi(0) = -2d$ and $\mu = 2$. Moreover, all coefficients corresponding to odd powers of $t$ are found to be zero (consistent with the fact that $\phi(t)$ is an even function). The first few non-trivial coefficients in the series expansion of $\phi(t)$ are given explicitly as

$$\phi_0 = \frac{r^2 d}{r^2 - d^2}\,, \tag{3.5.26}$$

$$\phi_2 = -r^2 d\, \frac{r^4 + 7\, r^2 d^2 + 4\, d^2}{12\, (r^2 - d^2)^3}\,,$$

$$\phi_4 = r^2 d\, \frac{r^8 + 86\, r^6 d^2 + 381\, r^4 d^4 + 236\, r^2 d^6 + 16\, d^8}{360\, (r^2 - d^2)^5}\,,$$

$$\begin{aligned}\phi_6 = -r^2 d\, \frac{r^{12} + 813\, r^{10} d^2 + 15387\, r^8 d^4 + 47167\, r^6 d^6}{128\, (r^2 - d^2)^7} - \\ - r^2 d\, \frac{32712\, r^4 d^8 + 4656\, r^2 d^{10} + 64\, d^{12}}{128\, (r^2 - d^2)^7}\end{aligned} \tag{3.5.27}$$

with $\phi_j = 0$ for odd values of the index $j$. These higher order coefficients are given here explicitly due to their utility in deriving accurate approximations of the error terms, for their subsequent numerical implementation.

In order to derive a local expansion of the form (3.2.12) for the random amplitude $f^\alpha(t)$ around $t = 0$, the first the deterministic part of $f(t)$ defined in (3.5.9) is analysed first. This

function is analytic and therefore can be expressed as the series

$$f(t) = f_0 + f_1 t + f_2 t^2 + \dots$$

where the coefficients $f_j$ are given as

$$f_j = f^{(j)}(t)\Big|_{t=0}, \tag{3.5.28}$$

so that

$$f(t) \approx \frac{r}{\sqrt{r^2 - d^2}} - \frac{r^3 d^2}{\sqrt{(r^2 - d^2)^5}}\, t^2 + O(t^4)\,, \tag{3.5.29}$$

noting that (3.5.28) yields $f_j = 0$ for odd indices $j$, consistent with the fact that $f(t)$ is an even function. Comparing this expansion to the expansion for $f(t)$ in (3.2.12), we note that $\lambda = 1$. The first few coefficients of this expansion of $f(t)$ are given by

$$f_0 = \frac{r}{\sqrt{r^2 - d^2}}\,, \tag{3.5.30}$$

$$f_2 = -\frac{r^3 d^2}{\sqrt{(r^2 - d^2)^5}}\,,$$

$$f_4 = \frac{r^3 d^2 (2\, r^4 + 11\, r^2 d^2 + 2\, d^4)}{6\sqrt{(r^2 - d^2)^9}}\,,$$

$$f_6 = -\frac{r^3 d^2 (4\, r^8 + 134\, r^6 d^2 + 399\, r^4 d^4 + 134\, r^2 d^6 + 4\, d^8)}{90\sqrt{(r^2 - d^2)^{13}}}\,,$$

with $f_j = 0$ for odd indices $j$. Figure 3.8 shows an example of the phase $\phi(t)$ and the homogeneous amplitude $f(t)$ (in grey) and their corresponding approximations (3.5.25) and (3.5.29) over the current interval of integration $(0, \frac{\pi}{2})$, showing the series (3.5.25) and (3.5.29) truncated up to one (yellow), two (green) and three (orange) non-trivial terms, using the coefficients (3.5.26) and (3.5.30), respectively.

The expansion of the random amplitude $f^\alpha(t) = \alpha_S(t)^2 f(t)$ is now derived. Note that, $\alpha_S(t)$ may be interpreted as a real-valued smooth function of $t$. Hence, using the Leibniz formula we have

$$\left\{\, \alpha_S(t)^2 f(t) \,\right\}^{(j)} = \sum_{\ell=1}^{j} \binom{j}{\ell} \left\{\alpha_S^2(t)\right\}^{(j-\ell)} f^{(\ell)}(t)\,, \tag{3.5.31}$$

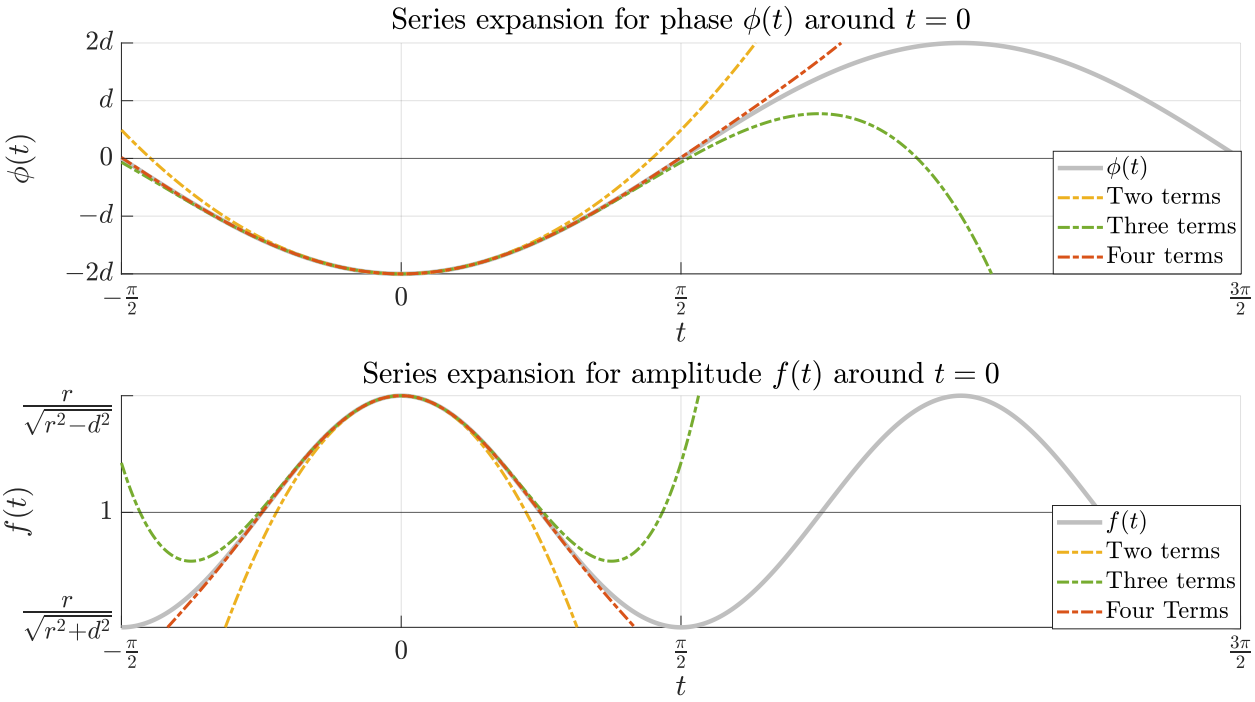


**Figure 3.8:** Plot of the phase function (3.5.7) (**top**) and amplitude function (3.7.6) (**bottom**) in terms of the parameter $t$ over the interval $(-\frac{\pi}{2}, \frac{3\pi}{2})$ in grey, and their approximations including terms up to second order (yellow), fourth order (green) and sixth order (orange) in dots and dashes. The values $r = 1000$ m and $d = 100$ m were used to generate these plots.

where $(\cdot)^{(j)}$ denotes the $j^{\text{th}}$ derivative with respect to $t$ and the superindex is omitted if $j = 0$. The Leibniz formula may be used again to find the derivatives of $\alpha_S^2(t)$ as

$$\left\{\alpha_S^2(t)\right\}^{(j)} = \sum_{\ell=1}^{j} \binom{j}{\ell} \left\{\alpha_S(t)\right\}^{(j-\ell)} \left\{\alpha_S(t)\right\}^{(\ell)} . \tag{3.5.32}$$

Then $f^\alpha(t)$ can be expanded around $t = 0$ as

$$f^\alpha(t) \approx f_0^{\alpha,0} + f_1^{\alpha,0} t + f_2^{\alpha,0} t^2 + \dots$$

where the coefficients $f_j^{\alpha,0}$ are defined as

$$f_j^{\alpha,0} = \left\{ \alpha_S(t)^2 f(t) \right\}^{(j)} \Big|_{t=0} .$$

Moreover, for simplicity let $\alpha_j^0$ denote the $j^{\text{th}}$ derivative of $\alpha_S(t)$ at $t = 0$, i.e.

$$\alpha_j^0 = \left\{\alpha_S(t)\right\}^{(j)} \Big|_{t=0} ,$$

where the superindex $(\cdot)^0$ has been used to highlight the fact that these coefficients correspond to the values of $\alpha_S(t)$ and its derivatives at the stationary point $t = 0$ (that corresponds to location $\mathbf{x}_0$ on $S$), and distinguish them from the coefficients resulting from the corresponding expansion around the other stationary point, namely $t = \pi$, that will be taken later on. Then using (3.5.31) and the coefficients $f_j$ given for the homogeneous amplitude function $f(t)$ in (3.5.30), the first few coefficients $f_j^{\alpha,\,0^+}$ are given explicitly by

$$\begin{aligned}
f_0^{\alpha,\,0^+} &= \left(\alpha_0^0\right)^2 \frac{r}{\sqrt{r^2-d^2}}\,, \\
f_1^{\alpha,\,0^+} &= \alpha_0^0\alpha_1^0 \frac{2\,r}{\sqrt{r^2-d^2}}\,, \\
f_2^{\alpha,\,0^+} &= \left(\,\alpha_0^0\alpha_2^0 + \left(\alpha_1^0\right)^2\,\right) \frac{2\,r}{\sqrt{r^2-d^2}} - \left(\alpha_0^0\right)^2 \frac{r^3 d^2}{\sqrt{(r^2-d^2)^5}}\,, \\
f_3^{\alpha,\,0^+} &= \left(\,\alpha_0^0\alpha_3^0 + 3\,\alpha_1^0\alpha_2^0\,\right) \frac{2\,r}{\sqrt{r^2-d^2}} - \alpha_0^0\alpha_1^0 \frac{6\,r^3 d^2}{\sqrt{(r^2-d^2)^5}}
\end{aligned} \tag{3.5.33}$$

and so on, noting that the fact that $f_j = 0$ for odd values of $j$ simplifies the calculation of these coefficients somewhat. Figure 3.9 shows an example of one realisation of the random amplitude $f^\alpha(t)$ and its series approximation about $t = 0$ using the random coefficients calculated in (3.5.33). Compare this random amplitude with the homogeneous amplitude shown in the bottom panel of Figure 3.8. An important distinction between the homogeneous amplitude $f(t)$ and the random amplitude $f^\alpha(t)$ is that in general $f^\alpha(t)$ is not symmetric about $t = 0$, and correspondingly the coefficients $f_j^{\alpha,\,0^+}$ are no longer zero for odd values of the index $j$.

**Remark 3.5.1.** Moreover, note that the allowable order of this approximation depends on the order of differentiability of the random amplitude $f^\alpha(t)$ of the cross-correlation integrand, which is in turn linked to the smoothness of the random field $\alpha$.

Having determined the coefficients (3.5.26) and (3.5.33) for the phase $\phi(t)$ and the random amplitude $f^\alpha(t)$, respectively, the coefficients $a_j^{\alpha,\,0^+}$ can now be calculated directly using the formula (3.3.25) derived in Section 3.3. The first few coefficients are given explicitly below, as they can be used directly to implement higher-order stationary phase approximations,

$$a_0^{\alpha,\,0^+} = \frac{\left(\alpha_0^0\right)^2}{2\sqrt{d}}\,,$$

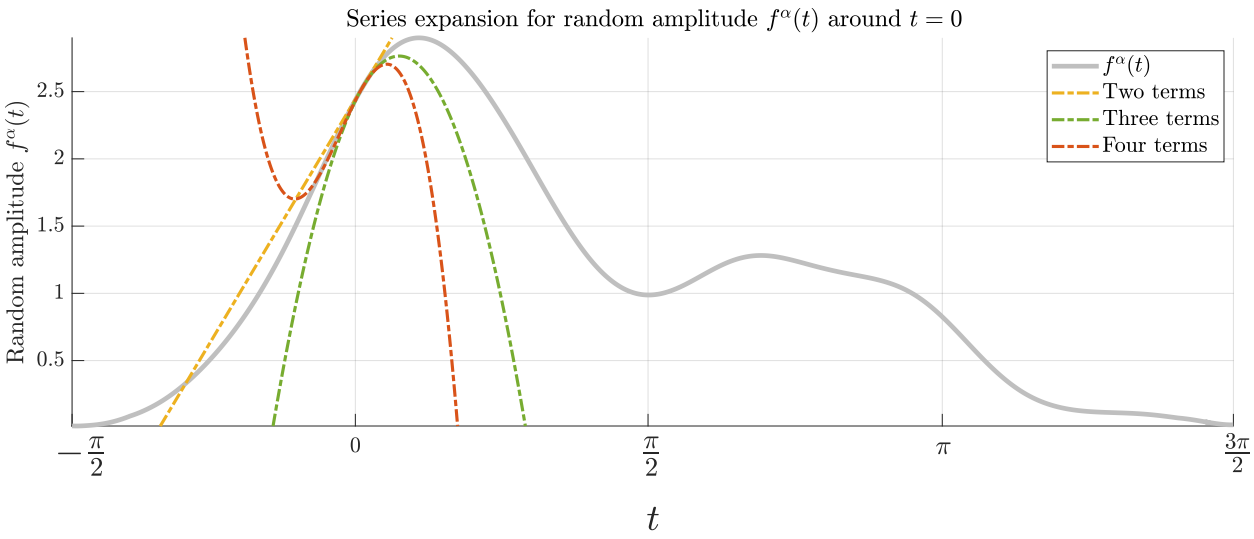


**Figure 3.9:** Example of a realisation of the random amplitude $f^\alpha(t)$ (in grey) and its series approximation about $t = 0$ using the random coefficients calculated in (3.5.33), using two (yellow), three (green) and four terms (orange). Note the loss of symmetry as well as the increased radius of convergence as the order of approximation is increased.

$$
\begin{aligned}
a_1^{\alpha,\,0^+} &= \alpha_0^0 \alpha_1^0 \frac{\sqrt{r^2 - d^2}}{rd}\,, \\
a_2^{\alpha,\,0^+} &= \left( \left(\alpha_1^0\right)^2 + \alpha_0^0 \alpha_2^0 \right) \frac{r^2 - d^2}{2\, r^2 \sqrt{d^3}} + \left(\alpha_0^0\right)^2 \frac{r^4 - r^2 d^2 + 4d^4}{16\, r^2 \left(r^2 - d^2\right) \sqrt{d^3}}\,, \\
a_3^{\alpha,\,0^+} &= \left(\alpha_0^0 \alpha_3^0 + 3\, \alpha_1^0 \alpha_2^0\right) \frac{\sqrt{(r^2 - d^2)^3}}{6\, r^3 d^2} + \alpha_0^0 \alpha_1^0 \frac{r^4 + r^2 d^2 + 4d^4}{6\, r^3 d^2 \sqrt{r^2 - d^2}}\,,
\end{aligned}
\tag{3.5.34}
$$

and so on.

Having successfully derived the coefficients (3.5.34), we can proceed to write the stationary phase approximation to the integral $I^{\alpha,\,0^+}(\mathbf{x_A}, \mathbf{x_B}, k)$. First we use equations (3.2.11) and (3.2.7) to define the auxiliary functions $Q_{mn}^{\alpha,\,0^+}(t)$ and $P_m^{\alpha,\,0^+}(t)$ as

$$
Q_{mn}^{\alpha,\,0^+}(t) = P_{m-1}^{\alpha,\,0^+}(t) - \sum_{j=0}^{n-1} \frac{\Gamma\left(\frac{j+1}{2}\right)}{\Gamma\left(\frac{j+1}{2} + 1 - m\right)} \frac{a_j^{\alpha,\,0^+}}{\left(\,\phi(t) + 2d\,\right)^{m - \frac{j+1}{2}}}\,, \tag{3.5.35}
$$

for $t \in \left(0, \frac{\pi}{2}\right)$, where

$$
P_m^{\alpha,\,0^+}(t) = \left\{ \frac{1}{\phi'(t)} \frac{d}{dt} \right\}^m \frac{f^\alpha(t)}{\phi'(t)} \qquad \text{for } t \in \left(0, \tfrac{\pi}{2}\right)\,. \tag{3.5.36}
$$

Therefore, using equation (B.1.1) and definitions (3.2.3) to (3.2.10), as well as the formula for the gamma function with positive half-integer argument (see for example Section 8.339 in Gradshteyn and Ryzhik (2014))

$$\Gamma\left(\tfrac{n}{2}\right) = \frac{\sqrt{\pi}}{2^{\frac{n-1}{2}}}(n-2)!!\,,$$

where $(\cdot)!!$ denotes the double factorial, the $n^{\text{th}}$ order stationary phase approximation of $I^{\alpha,0^+}(\mathbf{x_A},\mathbf{x_B},k)$ defined in (3.5.22) is given by

$$I^{\alpha,0^+}(\mathbf{x_A},\mathbf{x_B},k) \approx A_n^{\alpha,0^+}(k) - B_m^{\alpha,0^+}(k) \tag{3.5.37}$$

where

$$A_n^{\alpha,0^+}(k) = e^{-2d\,ik}\sqrt{\pi}\sum_{j=0}^{n-\eta} e^{(j+1)\frac{\pi}{4}i}\,\frac{(j-1)!!}{\sqrt{2^j k^{j+1}}}\,a_j^{\alpha,0^+}\,, \tag{3.5.38}$$

and

$$B_m^{\alpha,0^+}(k) = \sum_{j=0}^{m-1} P_j^{\alpha,0^+}\left(\tfrac{\pi}{2}\right)\left(\frac{i}{k}\right)^{j+1}\,, \tag{3.5.39}$$

where $\phi\left(\frac{\pi}{2}\right) = 0$ has been used in (3.5.39), noting that the term $A_n^{\alpha,0^+}(k)$ comprehends the main contribution to the approximation, and $B_m^{\alpha,0^+}(k)$ can be interpreted as an endpoint effect at the upper limit of integration $t = \frac{\pi}{2}$. That this interpretation is appropriate for the application in mind will become apparent when inspecting the waveforms associated with these terms later on. Furthermore,

$$2m-1 \leq n < 2m+2 \tag{3.5.40}$$

according to (3.2.5), and $\eta = 1$ unless $n = 2m-1$, in which case $\eta = 0$ as specified by (3.2.6). The error incurred in the approximation (3.5.37) is given by

$$E_{mn}^{\alpha,0^+}(k) = \delta_{mn}^{\alpha,0^+}(k) - \epsilon_{mn}^{\alpha,0^+}(k),\,, \tag{3.5.41}$$

where

$$\delta_{mn}^{\alpha,0^+}(k) = \left(\frac{i}{k}\right)^m \int_0^{\pi/2} e^{ik\phi(t)} Q_{mn}^{\alpha,0^+\,\prime}(t)\,dt \tag{3.5.42}$$

and

$$\epsilon_{mn}^{\alpha,0^+}(k) = e^{-2dik}\sum_{j=0}^{n-1} e^{(j+1)\frac{\pi}{4}i}\frac{\Gamma\left(\frac{j+1}{2}\right)}{\Gamma\left(\frac{j+1}{2}-m\right)}\Gamma\left(\tfrac{j+1}{2}-m,\,-2d\,ik\right)\frac{a_j^{\alpha,0^+}}{k^{\frac{j+1}{2}}}\,, \tag{3.5.43}$$

and bounds for each of these error terms are determined using (B.1.12) and (B.1.14), yielding

$$|\delta_{mn}^{\alpha,0^+}(k)| \leq \left(\frac{1}{k}\right)^m \int_0^{\pi/2} |Q_{mn}^{\alpha\,0^+\,\prime}(t)|\,dt \tag{3.5.44}$$

and

$$|\epsilon_{mn}^{\alpha,0^+}(k)| \leq \frac{2}{k^{m+1}}\sum_{j=0}^{n-1}\frac{\Gamma\left(\frac{j+1}{2}\right)}{\left|\Gamma\left(\frac{j+1}{2}-m\right)\right|}\frac{\left|a_j^{\alpha,0^+}\right|}{(\,2d\,)^{m+1-\frac{j+1}{2}}}\,, \tag{3.5.45}$$

noting that $\phi(\frac{\pi}{2}) = 0$ and $\phi(0) = -2d$ has been used in the right-hand side of (3.5.45), so that using the triangle inequality the bound for the total error $E_{mn}^{\alpha,0^+}(k)$ defined in (3.5.41) is given by

$$|E_{mn}^{\alpha,0^+}(k)| \leq \left(\frac{1}{k}\right)^m \int_0^{\pi/2} |Q_{mn}^{\alpha,0^+\,\prime}(t)|\,dt + \frac{2}{k^{m+1}}\sum_{j=0}^{n-1}\frac{\Gamma\left(\frac{j+1}{2}\right)}{\left|\Gamma\left(\frac{j+1}{2}-m\right)\right|}\frac{\left|a_j^{\alpha,0^+}\right|}{(\,2d\,)^{m+1-\frac{j+1}{2}}}\,. \tag{3.5.46}$$

equation (3.5.37) provides a general expression for the stationary phase contribution from the stationary point at $\mathbf{x}_0$ to the empirical interferometric retrieval of the Green's function in a two-dimensional homogeneous medium, where variations in the energy arriving to the receiver pair from different directions is accounted for by the random field $\alpha$. Moreover, expression (3.5.41) quantifies the error incurred in this approximation and inequality (3.5.46) provides a bound for this error. Note further that due to the presence of the random field $\alpha$, all these quantities are themselves random.

The procedure outlined above is applied similarly to the integrals (3.5.21), (3.5.23) and (3.5.24). The details of these calculations can be found in Appendix B and through the rest of this section, expressions from this Appendix are referenced directly without further proof.

The main contribution from the stationary point at $t = \pi$ is given by the stationary phase approximation to the integral $I^\alpha(\mathbf{x_A}, \mathbf{x_B}, k)$ restricted to the interval $t \in \left(\frac{\pi}{2}, \frac{3\pi}{2}\right)$, which can

be stated combining equations (B.3.41) and (B.3.26), resulting in the exact equation

$$\begin{aligned}\int_{\pi/2}^{3\pi/2} f^{\alpha}(t)e^{ik\phi(t)}\,dt &= \left(I^{\alpha,\pi^-}(\mathbf{x_A},\mathbf{x_B},k)\right)^* + \left(I^{\alpha,\pi^+}(\mathbf{x_A},\mathbf{x_B},k)\right)^* \\ &= \left(A_n^{\alpha,\pi^-}(k)+A_n^{\alpha,\pi^+}(k)\right)^* - \left(B_m^{\alpha,\pi^-}(k)+B_m^{\alpha,\pi^+}(k)\right)^* \\ &\quad + \left(\delta_{mn}^{\alpha,\pi^-}(k)+\delta_{mn}^{\alpha,\pi^+}(k)\right)^* - \left(\epsilon_{mn}^{\alpha,\pi^-}(k)+\epsilon_{mn}^{\alpha,\pi^+}(k)\right)^*\end{aligned} \tag{3.5.47}$$

Hence, the stationary phase approximation corresponding to the stationary point at $t=\pi$ is given by

$$\int_{\pi/2}^{3\pi/2} f^{\alpha}(t)e^{ik\phi(t)}\,dt \approx \left(A_n^{\alpha,\pi^-}(k)+A_n^{\alpha,\pi^+}(k)\right)^* - \left(B_m^{\alpha,\pi^-}(k)+B_m^{\alpha,\pi^+}(k)\right)^*, \tag{3.5.48}$$

with the associated error given by

$$E_{mn}^{\alpha,\pi}(k) = \left(\delta_{mn}^{\alpha,\pi^-}(k)+\delta_{mn}^{\alpha,\pi^+}(k)\right)^* - \left(\epsilon_{mn}^{\alpha,\pi^-}(k)+\epsilon_{mn}^{\alpha,\pi^+}(k)\right)^* \tag{3.5.49}$$

equation (3.5.47) added together with (B.3.18) provide the general expression of the stationary phase approximation to the integral $I^{\alpha}(\mathbf{x_A},\mathbf{x_B},k)$, as well as the associated error terms, with a general bound given by the sum of the bounds (3.5.46), (B.3.17),(B.3.35) and (B.3.49).

In order to derive concrete expressions for the stationary phase approximation and its associated error bounds, we consider[2] the case $n=m=1$, noting that this choice satisfies the restriction (3.5.40), and that according to the remark made under that equation, $\eta=0$ in this case. We begin by evaluating the auxiliary functions (3.5.36), (B.3.4), (B.3.24) and (B.3.39) at $\frac{\pi}{2}$, for the order $m-1=0$

$$P_0^{\alpha,0^+}\left(\tfrac{\pi}{2}\right) = \left.\frac{f^{\alpha}(t)}{\phi'(t)}\right|_{t=\frac{\pi}{2}} = |\alpha\left(\tfrac{\pi}{2}\right)|^2\frac{1}{2d}, \tag{3.5.50}$$

$$P_0^{\alpha,0^-}\left(\tfrac{\pi}{2}\right) = \left.\frac{f^{\alpha}(-t)}{\phi'(t)}\right|_{t=\frac{\pi}{2}} = |\alpha\left(-\tfrac{\pi}{2}\right)|^2\frac{1}{2d}, \tag{3.5.51}$$

[2]Further note that this choice of the approximation order is consistent with the random field framework applied earlier, where the possibility of non-smooth random amplitude $f^{\alpha}(t)$ is allowed. When the differentiability of the source amplitude variations can be guaranteed, the expressions presented so far can be readily used to derive higher order approximations.

$$P_0^{\alpha,\pi^+}\left(\tfrac{\pi}{2}\right) = \left.\frac{f^\alpha(\pi+t)}{\phi'(t)}\right|_{t=\frac{\pi}{2}} = |\alpha\left(-\tfrac{\pi}{2}\right)|^2\frac{1}{2d}\,, \tag{3.5.52}$$

$$P^{\alpha,\pi^-}\left(\tfrac{\pi}{2}\right) = \left.\frac{f^\alpha(\pi-t)}{\phi'(t)}\right|_{t=\frac{\pi}{2}} = |\alpha\left(\tfrac{\pi}{2}\right)|^2\frac{1}{2d}\,, \tag{3.5.53}$$

where the properties of the random amplitude function $f^\alpha$ derived in (3.5.16) and (3.5.17) have been used in these evaluations. The identity $\alpha\left(\frac{3\pi}{2}\right) = \alpha\left(-\frac{\pi}{2}\right)$ has been used in (3.5.52), noting that owing to the $2\pi$-periodicity of the parametrisation (3.5.4), the location on the boundary corresponding to the direction $t = \frac{3\pi}{2}$ is the same as for $t = -\frac{\pi}{2}$. Next the auxiliary functions (3.5.35) (B.3.6) (B.3.25) (B.3.40) are examined for $m = n = 1$, resulting in

$$Q_{11}^{\alpha,0^+}(t) = P_0^{\alpha,0^+}(t) - \frac{a_0^{\alpha,0^+}}{\sqrt{\phi(t)+2d}} = \alpha_S^2(t)\frac{f(t)}{\phi'(t)} - \frac{\alpha_S^2(0)}{2\sqrt{d(\phi(t)+2d)}}\,, \tag{3.5.54}$$

$$Q_{11}^{\alpha,0^-}(t) = P_0^{\alpha,0^-}(t) - \frac{a_0^{\alpha,0^-}}{\sqrt{\phi(t)+2d}} = \alpha_S^2(-t)\frac{f(t)}{\phi'(t)} - \frac{\alpha_S^2(0)}{2\sqrt{d(\phi(t)+2d)}}\,, \tag{3.5.55}$$

$$Q_{11}^{\alpha,\pi^+}(t) = P_0^{\alpha,\pi^+}(t) - \frac{a_0^{\alpha,\pi^+}}{\sqrt{\phi(t)+2d}} = \alpha_S^2(\pi+t)\frac{f(t)}{\phi'(t)} - \frac{\alpha_S^2(\pi)}{2\sqrt{d(\phi(t)+2d)}}\,, \tag{3.5.56}$$

$$Q_{11}^{\alpha,\pi^-}(t) = P_0^{\alpha,\pi^-}(t) - \frac{a_0^{\alpha,\pi^-}}{\sqrt{\phi(t)+2d}} = \alpha_S^2(\pi-t)\frac{f(t)}{\phi'(t)} - \frac{\alpha_S^2(\pi)}{2\sqrt{d(\phi(t)+2d)}}\,, \tag{3.5.57}$$

$$\begin{aligned} B_1^{\alpha,0^+}(k) &= \alpha^2\left(\tfrac{\pi}{2}\right)\frac{i}{2kd} & B_1^{\alpha,0^-}(k) &= \alpha^2\left(-\tfrac{\pi}{2}\right)\frac{i}{2kd} \\ B_1^{\alpha,\pi^+}(k) &= \alpha^2\left(-\tfrac{\pi}{2}\right)\frac{i}{2kd} & B_1^{\alpha,\pi^-}(k) &= \alpha^2\left(\tfrac{\pi}{2}\right)\frac{i}{2kd} \end{aligned} \tag{3.5.58}$$

$$A_1^{\alpha,0^+}(k) = e^{-i\left(2kd-\frac{\pi}{4}\right)}\alpha_S^2(0)\sqrt{\frac{\pi}{4\,kd}} + e^{-i\left(2kd-\frac{\pi}{2}\right)}\alpha_S(0)\alpha_S'(0)\frac{\sqrt{\frac{\pi}{2}(r^2-d^2)}}{rkd} \tag{3.5.59}$$

$$A_1^{\alpha,0^-}(k) = e^{-i\left(2kd-\frac{\pi}{4}\right)}\alpha_S^2(0)\sqrt{\frac{\pi}{4\,kd}} - e^{-i\left(2kd-\frac{\pi}{2}\right)}\alpha_S(0)\alpha_S'(0)\frac{\sqrt{\frac{\pi}{2}(r^2-d^2)}}{rkd} \tag{3.5.60}$$

$$A_1^{\alpha,\pi^+}(k) = e^{-i\left(2kd-\frac{\pi}{4}\right)}\alpha_S^2(\pi)\sqrt{\frac{\pi}{4\,kd}} + e^{-i\left(2kd-\frac{\pi}{2}\right)}\alpha_S(\pi)\alpha_S'(\pi)\frac{\sqrt{\frac{\pi}{2}(r^2-d^2)}}{rkd} \tag{3.5.61}$$

$$A_1^{\alpha,\pi^-}(k) = e^{-i\left(2kd-\frac{\pi}{4}\right)}\alpha_S^2(\pi)\sqrt{\frac{\pi}{4\,kd}} - e^{-i\left(2kd-\frac{\pi}{2}\right)}\alpha_S(\pi)\alpha_S'(\pi)\frac{\sqrt{\frac{\pi}{2}(r^2-d^2)}}{rkd}\,, \tag{3.5.62}$$

where the first two asymptotic coefficients (3.5.34), (B.3.3), (B.3.23) and (B.3.38) have been used. Using (3.5.43) and (B.3.32) we note that

$$\epsilon_{11}^{\alpha,0^+}(k) = \epsilon_{11}^{\alpha,0^-}(k) \qquad \text{and} \qquad \epsilon_{11}^{\alpha,\pi^+}(k) = \epsilon_{11}^{\alpha,\pi^-}(k)\,.$$

Hence we define

$$\epsilon_{11}^{\alpha,0}(k) := \epsilon_{11}^{\alpha,0^-}(k) = \epsilon_{11}^{\alpha,0^+}(k)\,,$$

and

$$\epsilon_{11}^{\alpha,\pi}(k) := \epsilon_{11}^{\alpha,\pi^-}(k) = \epsilon_{11}^{\alpha,\pi^+}(k)\,,$$

where

$$\begin{aligned}\epsilon_{11}^{\alpha,0}(k) &= -\Gamma\left(-\tfrac{1}{2},\,-2d\,ik\right)\frac{a_0^{\alpha,0}}{2\sqrt{k}}e^{-i\left(2kd-\frac{\pi}{4}\right)} \\ &= -\alpha_S^2(0)\Gamma\left(-\tfrac{1}{2},\,-2d\,ik\right)\frac{1}{4\sqrt{kd}}e^{-i\left(2kd-\frac{\pi}{4}\right)}\end{aligned} \tag{3.5.63}$$

$$\begin{aligned}\epsilon_{11}^{\alpha,\pi}(k) &= -\Gamma\left(-\tfrac{1}{2},\,-2d\,ik\right)\frac{a_0^{\alpha,\pi}}{2\sqrt{k}}e^{-i\left(2kd-\frac{\pi}{4}\right)} \\ &= -\alpha_S^2(\pi)\Gamma\left(-\tfrac{1}{2},\,-2d\,ik\right)\frac{1}{4\sqrt{kd}}e^{-i\left(2kd-\frac{\pi}{4}\right)}\end{aligned} \tag{3.5.64}$$

The delta terms are defined for $\ell \in \{0^+, 0^-, \pi^+, \pi^-\}$ as

$$\delta_{11}^{\alpha,\ell}(k) = \frac{i}{k}\int_0^{\frac{\pi}{2}} e^{ik\phi(t)}Q_{11}^{\alpha,\ell\,\prime}(t)dt\,,$$

where each of the functions $Q_{11}^{\alpha,\ell}(t)$ are defined in equations (3.5.54) to (3.5.57).

Hence, using equation (B.3.19) for the contribution from the stationary point at $t = 0$, together with equation (3.5.48) for the contribution from the stationary point at $t = \pi$, the stationary phase approximation to the integral $I^\alpha(\mathbf{x_A}, \mathbf{x_B}, k)$ is given by

$$I^\alpha(\mathbf{x_A}, \mathbf{x_B}, k) = \int_{-\frac{\pi}{2}}^{\frac{3\pi}{2}} f^\alpha(t) e^{ik\phi(t)} dt = \int_{-\frac{\pi}{2}}^{\frac{\pi}{2}} f^\alpha(t) e^{ik\phi(t)} dt + \int_{\frac{\pi}{2}}^{\frac{3\pi}{2}} f^\alpha(t) e^{ik\phi(t)} dt$$

$$\approx A_1^{\alpha,0^+}(k) + A_1^{\alpha,0^-}(k) + \left(A_1^{\alpha,\pi^+}(k) + A_1^{\alpha,\pi^-}(k)\right)^* - \\ - \left(B_1^{\alpha,0^-}(k) + B_1^{\alpha,0^+}(k) + \left(B_1^{\alpha,\pi^-}(k) + B_1^{\alpha,\pi^-}(k)\right)^*\right)$$

Using equations (3.5.58) for the endpoint terms corresponding to $t = \frac{\pi}{2}$.

$$B_1^{\alpha,0^+}(k) + \left(B_1^{\alpha,\pi^-}(k)\right)^* = \alpha^2\left(\tfrac{\pi}{2}\right)\frac{i}{2kd} - \alpha^2\left(\tfrac{\pi}{2}\right)\frac{i}{2kd} = 0\,, \tag{3.5.65}$$

and similarly for the endpoint terms corresponding to $t = -\frac{\pi}{2}$.

$$B_1^{\alpha,0^-}(k) + \left(B_1^{\alpha,\pi^+}(k)\right)^* = \alpha^2\left(-\tfrac{\pi}{2}\right)\frac{i}{2kd} - \alpha^2\left(-\tfrac{\pi}{2}\right)\frac{i}{2kd} = 0\,. \tag{3.5.66}$$

equations (3.5.65) and (3.5.66) behave as expected, as integrating over the whole contour implies there must be no contributions from endpoints, and so it is natural that these terms cancel out. However, note the important physical implication to wavefield interferometry, that is that by incorporating the contributions from both stationary points, each of which lies on either side of the receiver pair, endpoint effects are mitigated even in the presence of the random field $\alpha$. On the other hand, using equations (3.5.59) and (3.5.60) we have

$$A_1^{\alpha,0^+}(k) + A_1^{\alpha,0^-}(k) = e^{-i\left(2kd-\frac{\pi}{4}\right)}\alpha_S^2(0)\sqrt{\frac{\pi}{kd}}\,,$$

$$A_1^{\alpha,\pi^+}(k) + A_1^{\alpha,\pi^-}(k) = e^{-i\left(2kd-\frac{\pi}{4}\right)}\alpha_S^2(\pi)\sqrt{\frac{\pi}{kd}}\,.$$

Therefore, the stationary phase approximation to $I^\alpha(\mathbf{x_A}, \mathbf{x_B}, k)$ is given by

$$I^\alpha(\mathbf{x_A}, \mathbf{x_B}, k) \approx e^{-i\left(2kd-\frac{\pi}{4}\right)}\alpha_S^2(0)\sqrt{\frac{\pi}{kd}} + e^{i\left(2kd-\frac{\pi}{4}\right)}\alpha_S^2(\pi)\sqrt{\frac{\pi}{kd}}\,,$$

Finally, using $2d = |\mathbf{x_A} - \mathbf{x_B}|$, the stationary phase approximation to the empirical retrieval

given in equation (3.5.5) is given by

$$\hat{g}(\mathbf{x_A}, \mathbf{x_B}, k\,;\, \alpha, 0) = -\frac{i}{4\pi} I^{\alpha}(\mathbf{x_A}, \mathbf{x_B}, k)$$

$$\approx -\frac{i}{4}\sqrt{\frac{2}{\pi k|\mathbf{x_A}-\mathbf{x_B}|}}\left\{\alpha_S^2(0)e^{-i\left(k|\mathbf{x_A}-\mathbf{x_B}|-\frac{\pi}{4}\right)} + \alpha_S^2(\pi)e^{i\left(k|\mathbf{x_A}-\mathbf{x_B}|-\frac{\pi}{4}\right)}\right\}$$

and using the Green's function defined in (1.2.20) we conclude

$$\hat{g}(\mathbf{x_A}, \mathbf{x_B}, k\,;\, \alpha, 0) \approx \alpha_S^2(0)\hat{G}(\mathbf{x_A}, \mathbf{x_B}, k) - \alpha_S^2(\pi)\hat{G}^*(\mathbf{x_A}, \mathbf{x_B}, k)\,.$$

Let $\hat{g}_{\text{sp}}(\mathbf{x_A}, \mathbf{x_B}, k\,;\, \alpha)$ denote the stationary phase approximation to $\hat{g}(\mathbf{x_A}, \mathbf{x_B}, k\,;\, \alpha, 0)$. Then motivated by the result derived above we define this approximation as

$$\hat{g}_{\text{sp}}(\mathbf{x_A}, \mathbf{x_B}, k\,;\, \alpha) \coloneqq \alpha_S^2(0)\hat{G}(\mathbf{x_A}, \mathbf{x_B}, k) - \alpha_S^2(\pi)\hat{G}^*(\mathbf{x_A}, \mathbf{x_B}, k)\,.$$

In the subsequent sections, we return to the notation (3.5.18) and (3.5.19) for the stationary phase locations $\alpha_S^2(0)$ and $\alpha_S^2(\pi)$, so that the stationary phase estimate above can be equivalently written as

$$\hat{g}_{\text{sp}}(\mathbf{x_A}, \mathbf{x_B}, k\,;\, \alpha) = \alpha^2(\mathbf{x}_0)\hat{G}(\mathbf{x_A}, \mathbf{x_B}, k) - \alpha^2(\mathbf{x}_\pi)\hat{G}^*(\mathbf{x_A}, \mathbf{x_B}, k)\,. \tag{3.5.67}$$

**Remark 3.5.2.** While the present derivation for (3.5.67) has been performed in two dimensions, this expression can nevertheless be interpreted for inter-receiver Green's functions in one, two or three dimensions. In the following Section, the behaviour of the error is analised in this light whenever possible.

### 3.5.1 Error in the stationary phase approximation $\hat{g}_{\text{sp}}(\mathbf{x_A}, \mathbf{x_B}, k\,;\, \alpha)$

While it is possible to quantify the error incurred in approximating $\hat{g}_{\text{int}}(\mathbf{x_A}, \mathbf{x_B}, k\,;\, \alpha, 0)$ through the stationary method using the framework developed in Section 3.2, we remark that the quantity we wish to approximate is in fact $\hat{g}_{\text{int}}(\mathbf{x_A}, \mathbf{x_B}, k\,;\, 1, 0)$, i.e. the interferometric estimate in the ideal case when the source intensity is equal along the whole boundary $S$ (i.e. $\alpha \equiv 1$). The case where the stationary phase approximation is applied in the ideal scenario of sources of equal intensity is considered separately in Section 3.7 of this Chapter, where the results from Section 3.2 are applied.

Hence, rather than examining the quantity $\hat{g}_{\text{sp}}(\mathbf{x_A}, \mathbf{x_B}, k\,;\,\alpha) - \hat{g}_{\text{int}}(\mathbf{x_A}, \mathbf{x_B}, k\,;\,\alpha)$, we wish to consider

$$\hat{g}_{\text{sp}}(\mathbf{x_A}, \mathbf{x_B}, k\,;\,\alpha) - \hat{g}_{\text{int}}(\mathbf{x_A}, \mathbf{x_B}, k\,;\,1)\,.$$

Accordingly, we define the error in the stationary phase approximation as

$$E_{\text{sp}}(\mathbf{x_A}, \mathbf{x_B}, k\,;\,\alpha) \coloneqq \hat{g}_{\text{sp}}(\mathbf{x_A}, \mathbf{x_B}, k) - \hat{g}_{\text{int}}(\mathbf{x_A}, \mathbf{x_B}, k\,;\,1)\,. \tag{3.5.68}$$

To investigate the quantity above, note that in this Chapter the far-field conditions are assumed to be satisfied ($kr \gg 1$),[3] as this is the appropriate regime for the application of the stationary phase method. Therefore we assume

$$\hat{g}_{\text{int}}(\mathbf{x_A}, \mathbf{x_B}, k\,;\,1) = \hat{G}_{\text{hom}}(\mathbf{x_A}, \mathbf{x_B}, k)\,, \qquad k \gg 1\,,$$

where for clarity we recall the definition (1.1.2) of the homogeneous Green's function,

$$\hat{G}_{\text{hom}}(\mathbf{x_A}, \mathbf{x_B}, k) \coloneqq \hat{G}(\mathbf{x_A}, \mathbf{x_B}, k) - \hat{G}^*_{\text{hom}}(\mathbf{x_A}, \mathbf{x_B}, k)\,.$$

Hence, (3.5.68) may we written as

$$\begin{aligned} E_{\text{sp}}(\mathbf{x_A}, \mathbf{x_B}, k\,;\,\alpha) &= \hat{g}_{\text{sp}}(\mathbf{x_A}, \mathbf{x_B}, k) - \hat{G}_{\text{hom}}(\mathbf{x_A}, \mathbf{x_B}, k\,;\,\alpha) \\ &= \left(\alpha^2(\mathbf{x}_0) - 1\right) \hat{G}(\mathbf{x_A}, \mathbf{x_B}, k) - \left(\alpha^2(\mathbf{x}_\pi) - 1\right) \hat{G}^*(\mathbf{x_A}, \mathbf{x_B}, k)\,. \end{aligned} \tag{3.5.69}$$

where (3.5.67) has been used. Note that in the ideal scenario where the source traces are acquired perfectly (i.e. $\alpha$ is a degenerate random field such that $\alpha \equiv 1$, so that $\mu_\alpha = 1$ and $\sigma^2_\alpha = 0$) the error $E_{\text{sp}}(\mathbf{x_A}, \mathbf{x_B}, k\,;\,\alpha)$ is immediately zero.

A bound for this error can be given directly as

$$\left|E_{\text{sp}}(\mathbf{x_A}, \mathbf{x_B}, k\,;\,\alpha)\right| \leq \left\{|\alpha^2(\mathbf{x}_0) - 1| + |\alpha^2(\mathbf{x}_\pi) - 1|\right\} |\hat{G}(\mathbf{x_A}, \mathbf{x_B}, k)|\,.$$

**Remark 3.5.3.** While we have assumed a two-dimensional medium, the error in the stationary phase approximation (3.5.69) can be interpreted more generally in one, two or three dimensions. The behaviour of its amplitude with respect to the wavenumber $k$ and the inter-receiver distance $|\mathbf{x_A} - \mathbf{x_B}|$ can be contrasted using the Green's functions in Section 1.2.6. In one dimension, $|E_{\text{sp}}(\mathbf{x_A}, \mathbf{x_B}, k\,;\,\alpha)|$ decays linearly with $k$, while the inter-receiver distance has no bearing on the error behaviour (see (1.2.17)). In two dimensions, the error exhibits an inverse-square law with the frequency and the inter-receiver distance, decaying

[3] Essentially $kr \gg 1$. See Section 1.2, equation (1.2.13), and accompanying arguments.

with $\sqrt{k|\mathbf{x_A}-\mathbf{x_B}|}$ (see (1.2.20)). Finally, in three dimensions, the error decays linearly with the inter-receiver distance $|\mathbf{x_A}-\mathbf{x_B}|$, but there is no decay with the wavenumber $k$. A stationary phase regime is assumed throughout (i.e. $kr \gg 1$ for the wavenumber $k$ and the source boundary radius $r$).

We now turn our attention back to the two-dimensional case. Using definition (3.5.2) we can immediately give the bound.

$$\left|E_{\mathrm{sp}}(\mathbf{x_A},\mathbf{x_B},k\,;\,\alpha)\right| \leq \left(|\alpha^2(\mathbf{x}_0)-1|+|\alpha^2(\mathbf{x}_\pi)-1|\right)\sqrt{\frac{1}{8\pi k|\mathbf{x_A}-\mathbf{x_B}|}}\,,$$

where we note that the error in the stationary phase approximation in two dimensions decays with the wavenumber $k$ and the inter-receiver distance $|\mathbf{x_A}-\mathbf{x_B}|$.

### 3.5.2 Mean and variance of $E_{\mathrm{sp}}(\mathbf{x_A},\mathbf{x_B},k,\alpha)$

The expected value of the error $E_{\mathrm{sp}}(\mathbf{x_A},\mathbf{x_B},k,\alpha)$ can be calculated directly from (3.5.69), yielding

$$\begin{aligned}\mathbb{E}\left[\,E_{\mathrm{sp}}(\mathbf{x_A},\mathbf{x_B},k\,;\,\alpha)\,\right] = &\left(\mathbb{E}\left[\,\alpha^2(\mathbf{x}_0)\,\right]-1\right)\hat{G}(\mathbf{x_A},\mathbf{x_B},k)\\ &-\left(\mathbb{E}\left[\,\alpha^2(\mathbf{x}_\pi)\,\right]-1\right)\hat{G}^*(\mathbf{x_A},\mathbf{x_B},k)\,.\end{aligned} \tag{3.5.70}$$

Using expression (3.5.70), we can readily establish conditions for the stationary phase approximate to be an unbiased estimator of the inter-receiver homogeneous Green's function. These conditions are established in the following

**Proposition 3.5.2.** *The stationary phase estimate $\hat{g}_{\mathrm{sp}}(\mathbf{x_A},\mathbf{x_B},k)$ is an unbiased estimator of the homogeneous inter-receiver Green's function $\hat{G}_{\mathrm{hom}}(\mathbf{x_A},\mathbf{x_B},k)$ (i.e. $\mathbb{E}\left[\,E_{\mathrm{sp}}(\mathbf{x_A},\mathbf{x_B},k\,;\,\alpha)\,\right]=0$) if and only if one or more of the following conditions are satisfied:*

*(i)* $\mathbb{E}\left[\,\alpha^2(\mathbf{x}_0)\,\right]=\mathbb{E}\left[\,\alpha^2(\mathbf{x}_\pi)\,\right]=1.$

*(ii)* $\mathbb{E}\left[\,\alpha^2(\mathbf{x}_0)\,\right]+\mathbb{E}\left[\,\alpha^2(\mathbf{x}_\pi)\,\right]=2$ *and* $\mathrm{Re}\left\{\hat{G}(\mathbf{x_A},\mathbf{x_B},k)\right\}$ *vanishes at* $k$

*(iii)* $\hat{G}(\mathbf{x_A},\mathbf{x_B},k)$ *vanishes at* $k$.

*Proof.* It is immediate that any of conditions (i)-(iii) are sufficient for the right hand side of (3.5.70) to vanish. To establish the necessity of these conditions, assume that

$$\mathbb{E}\left[\,E_{\mathrm{sp}}(\mathbf{x_A},\mathbf{x_B},k\,;\,\alpha)\,\right]=0\,.$$

Then the real and imaginary parts of the right hand side of (3.5.70) must be zero, i.e.

$$\mathrm{Re}\left\{\hat{G}(\mathbf{x_A},\mathbf{x_B},k)\right\}\left(\mathbb{E}\left[\,\alpha^2(\mathbf{x}_0)\,\right]-\mathbb{E}\left[\,\alpha^2(\mathbf{x}_0)\,\right]\right)=0\,,$$

and

$$\mathrm{Im}\left\{\hat{G}(\mathbf{x_A},\mathbf{x_B},k)\right\}\left(\mathbb{E}\left[\,\alpha^2(\mathbf{x}_0)\,\right]+\mathbb{E}\left[\,\alpha^2(\mathbf{x}_0)\,\right]-2\right)=0\,.$$

It readily follows that one of conditions (i)-(iii) must be true for the equations above to be satisfied simultaneously. □

Next, the expected value of the error $\mathbb{E}\left[\,E_{\mathrm{sp}}(\mathbf{x_A},\mathbf{x_B},k\,;\,\alpha)\,\right]$ is considered under condition (3.1.4) established at the beginning of this Chapter.

**Proposition 3.5.3.** *If the first and second moment of the random variables $\alpha(\mathbf{x}_0)$ and $\alpha(\mathbf{x}_\pi)$ coincide, i.e.*

$$\mathbb{E}\left[\,\alpha(\mathbf{x}_0)\,\right]=\mathbb{E}\left[\,\alpha(\mathbf{x}_\pi)\,\right]=\mu_\alpha\,,$$

*and*

$$\mathrm{Var}\left[\,\alpha(\mathbf{x}_0)\,\right]=\mathrm{Var}\left[\,\alpha(\mathbf{x}_\pi)\,\right]=\sigma_\alpha^2\,,$$

*then*

$$\mathbb{E}\left[\,E_{\mathrm{sp}}(\mathbf{x_A},\mathbf{x_B},k\,;\,\alpha)\,\right]=\left(\,\mu_\alpha^2+\sigma_\alpha^2-1\,\right)\left(\hat{G}(\mathbf{x_A},\mathbf{x_B},k)-\hat{G}^*(\mathbf{x_A},\mathbf{x_B},k)\right)$$

$$=\left(\,\mu_\alpha^2+\sigma_\alpha^2-1\,\right)\hat{G}_{hom}(\mathbf{x_A},\mathbf{x_B},k)\,.$$

*Proof.* Under the assumptions imposed on the first and second moments of $\alpha$ at $\mathbf{x}_0$ and $\mathbf{x}_\pi$, we have that $\mathbb{E}\left[\,\alpha^2(\mathbf{x}_0)\,\right]=\mathbb{E}\left[\,\alpha^2(\mathbf{x}_\pi)\,\right]=\mu_\alpha+\sigma_\alpha^2$. The result follows directly from (3.5.70). □

**Remark 3.5.4.** Note that under the assumptions (3.1.4), $\hat{g}_{\mathrm{sp}}(\mathbf{x_A},\mathbf{x_B},k)$ is an unbiased estimator of the homogeneous inter-receiver phase even though the amplitude is in general biased. In practice, these assumptions translate to the condition that the statistics of the noise at the stationary phase source locations be sufficiently similar. This is a reasonable assumption in an active source experiment, where one has control over the time and location that the sources fire, and where presumably the same mechanism is used to generate the source signals (e.g. dynamite explosions down a well or a seismic vibrator). On the other hand, while ambient noise is often assumed to be essentially isotropic (Pilz and Parolai, 2014), facilitating conditions (3.1.4), this cannot always be expected in practical applications. For example, a survey performed near the coast or a highway would have a strong directional bias in the source strength, and conditions (3.1.4) would likely be invalid in such circumstances.

Nevertheless, even in those situations the directional bias of the energy can be quantified (e.g. using beamforming techniques (Löer et al., 2018)) and the more general expressions (3.1.1) to (3.1.3) applied to quantify the error introduced by the stationary phase approximation in such circumstances.

On the other hand, any random field satisfying

$$\mu_\alpha^2 + \sigma_\alpha^2 = 1 \tag{3.5.71}$$

would guarantee $\mathbb{E}\left[\, E_{\text{sp}}(\mathbf{x_A}, \mathbf{x_B}, k\,;\, \alpha)\,\right] = 0$. Hence, the condition $\alpha \equiv 1$ is not necessary for unbiased estimation of the inter-receiver Green's function. It suffices that

$$\mu_\alpha \in (0, 1)$$

and

$$\sigma_\alpha^2 = 1 - \mu_\alpha^2 \,.$$

The phase and amplitude error are discussed further in Sections 3.5.3 and 3.5.4, respectively.

We now move on to calculate the variance of $E_{\text{sp}}(\mathbf{x_A}, \mathbf{x_B}, k, \alpha)$. The variance of a complex-valued random variable $Z$ is defined as

$$\text{Var}\left[\, Z \,\right] = \mathbb{E}\left[\, |Z - \mathbb{E}\left[\, Z \,\right]|^2 \,\right] \,, \tag{3.5.72}$$

noting that the variance is always real and non-negative. Direct calculation shows that this definition is equivalent to the sum of the variances of the real and imaginary parts of $Z$, i.e.

$$\text{Var}\left[\, Z \,\right] = \text{Var}\left[\, \text{Re}\left\{Z\right\} \,\right] + \text{Var}\left[\, \text{Im}\left\{Z\right\} \,\right] \,.$$

Hence

$$\begin{aligned} \text{Var}\left[\, E_{\text{sp}}(\mathbf{x_A}, \mathbf{x_B}, k\,;\, \alpha)\,\right] = |\hat{G}(\mathbf{x_A}, \mathbf{x_B}, k)|^2 \left\{ \text{Var}\left[\, \alpha^2(\mathbf{x}_0) \,\right] + \text{Var}\left[\, \alpha^2(\mathbf{x}_\pi) \,\right] \right\} \\ + 2\Lambda(\mathbf{x_A}, \mathbf{x_B}, k)\, \text{Cov}\left[\, \alpha^2(\mathbf{x}_0), \alpha^2(\mathbf{x}_\pi) \,\right] \,. \end{aligned} \tag{3.5.73}$$

where for convenience the quantity $\Lambda(\mathbf{x_A}, \mathbf{x_B}, k)$ is defined as

$$\Lambda(\mathbf{x_A}, \mathbf{x_B}, k) = \text{Im}\left\{\hat{G}(\mathbf{x_A}, \mathbf{x_B}, k)\right\}^2 - \text{Re}\left\{\hat{G}(\mathbf{x_A}, \mathbf{x_B}, k)\right\}^2 \,. \tag{3.5.74}$$

An alternative expression for the variance (3.5.73) can be written using the identity

$$\begin{aligned}\mathrm{Cov}\left[\,\alpha^2(\mathbf{x}_0),\alpha^2(\mathbf{x}_\pi)\,\right] = \mathrm{Var}\left[\,\alpha(\mathbf{x}_0)\alpha(\mathbf{x}_\pi)\,\right] - \mathbb{E}\left[\,\alpha^2(\mathbf{x}_0)\,\right]\mathbb{E}\left[\,\alpha^2(\mathbf{x}_\pi)\,\right] \\ + \left(\mathrm{Cov}\left[\,\alpha(\mathbf{x}_0),\alpha(\mathbf{x}_\pi)\,\right] + \mathbb{E}\left[\,\alpha(\mathbf{x}_0)\,\right]\mathbb{E}\left[\,\alpha(\mathbf{x}_\pi)\,\right]\right)^2 ,\end{aligned} \tag{3.5.75}$$

which yields

$$\begin{aligned}\mathrm{Var}\left[\,E_{\mathrm{sp}}(\mathbf{x_A},\mathbf{x_B},k\,;\,\alpha)\,\right] =& |\hat{G}(\mathbf{x_A},\mathbf{x_B},k)|^2\left\{\mathbb{E}\left[\,\alpha^4(\mathbf{x}_0)\,\right]) + \mathbb{E}\left[\,\alpha^4(\mathbf{x}_\pi)\,\right]\right. \\ &\left. - \mathbb{E}\left[\,\alpha^2(\mathbf{x}_0)\,\right]^2 - \mathbb{E}\left[\,\alpha^2(\mathbf{x}_\pi)\,\right]^2\right\} \\ &+ 2\Lambda(\mathbf{x_A},\mathbf{x_B},k)\Big\{\,\mathrm{Var}\left[\,\alpha(\mathbf{x}_0)\alpha(\mathbf{x}_\pi)\,\right] - \mathbb{E}\left[\,\alpha^2(\mathbf{x}_0)\,\right]\mathbb{E}\left[\,\alpha^2(\mathbf{x}_\pi)\,\right] \\ &+ \left(\mathrm{Cov}\left[\,\alpha(\mathbf{x}_0),\alpha(\mathbf{x}_\pi)\,\right] + \mathbb{E}\left[\,\alpha(\mathbf{x}_0)\,\right]\mathbb{E}\left[\,\alpha(\mathbf{x}_\pi)\,\right]\right)^2\Big\}\,.\end{aligned} \tag{3.5.76}$$

If conditions (3.1.4) and (3.1.5) are satisfied, i.e. the first, second and fourth moments of the random field $\alpha$ coincide at the stationary locations, expression (3.5.76) reduces to

$$\begin{aligned}\mathrm{Var}\left[\,E_{\mathrm{sp}}(\mathbf{x_A},\mathbf{x_B},k\,;\,\alpha)\,\right] =& 2\,|\hat{G}(\mathbf{x_A},\mathbf{x_B},k)|^2(\kappa_\alpha - (\mu_\alpha^2+\sigma_\alpha^2)^2) \\ &+ 2\,\Lambda(\mathbf{x_A},\mathbf{x_B},k)\Big\{\,\mathrm{Var}\left[\,\alpha(\mathbf{x}_0)\alpha(\mathbf{x}_\pi)\,\right] - (\mu_\alpha^2+\sigma_\alpha^2)^2 \\ &+ \left(\mathrm{Cov}\left[\,\alpha(\mathbf{x}_0),\alpha(\mathbf{x}_\pi)\,\right] + \mu_\alpha^2\right)^2\Big\}\,,\end{aligned} \tag{3.5.77}$$

where it becomes apparent that the variance of the error in the stationary phase approximation depends not only on the moments of the random field $\alpha$ at the stationary phase locations, but on the particular distribution of the product $\alpha(\mathbf{x}_0)\alpha(\mathbf{x}_\pi)$, specifically its variance, as well as a square dependence on the covariance of this pair of variables.

**Remark 3.5.5.** Recall that due to the presence of the second order terms $|\hat{G}(\mathbf{x_A},\mathbf{x_B},k)|^2$ and $\Lambda(\mathbf{x_A},\mathbf{x_B},k)$, the variance for the one dimensional case decays linearly with $k^2$ but not with the inter-receiver distance. The decay in two dimensions is proportional to $k|\mathbf{x_A}-\mathbf{x_B}|$, and in three dimensions the error decays linearly with the squared inter-receiver distance $|\mathbf{x_A}-\mathbf{x_B}|^2$ but not with the wavenumber $k$.

### 3.5.3 Expected error in phase

In this Section, we show that the phase of the stationary phase estimate $\hat{g}_{\mathrm{sp}}(\mathbf{x_A},\mathbf{x_B},k\,;\,\alpha)$ is an unbiased estimator of the phase of the homogeneous Green's function when conditions when the first, second and fourth moments of the random field $\alpha$ coincide at the stationary phase locations (i.e. conditions (3.1.4) and (3.1.5)).

Begin by defining the phase error in the stationary phase approximation as

$$e_{\mathrm{ph}}(\mathbf{x_A}, \mathbf{x_B}, k\,;\,\alpha)) = \arg \hat{g}_{\mathrm{sp}}(\mathbf{x_A}, \mathbf{x_B}, k\,;\,\alpha) - \arg \hat{G}_{\mathrm{hom}}(\mathbf{x_A}, \mathbf{x_B}, k). \tag{3.5.78}$$

where the function $\arg z$ is defined for $z \in \mathbb{C}$, $z = x + iy$, as

$$\arg z = \begin{cases} \operatorname{atan}\left(\frac{y}{x}\right) & \text{if } x > 0\,, \\ \operatorname{atan}\left(\frac{y}{x}\right) + \pi & \text{if } x < 0 \text{ and } y \geq 0\,, \\ \operatorname{atan}\left(\frac{y}{x}\right) - \pi & \text{if } x < 0 \text{ and } y < 0\,, \\ \frac{\pi}{2} & \text{if } x = 0 \text{ and } y > 0\,, \\ -\frac{\pi}{2} & \text{if } x = 0 \text{ and } y < 0\,, \\ \text{undefined} & \text{if } x = 0 \text{ and } y = 0\,. \end{cases} \tag{3.5.79}$$

Then we have the following

**Proposition 3.5.4.** *If the first and second moment of the random variables $\alpha(\mathbf{x}_0)$ and $\alpha(\mathbf{x}_\pi)$ coincide, i.e.*

$$\mathbb{E}\left[\,\alpha(\mathbf{x}_0)\,\right] = \mathbb{E}\left[\,\alpha(\mathbf{x}_\pi)\,\right] = \mu_\alpha\,,$$

$$\mathrm{Var}\left[\,\alpha(\mathbf{x}_0)\,\right] = \mathrm{Var}\left[\,\alpha(\mathbf{x}_\pi)\,\right] = \sigma_\alpha^2\,,$$

*and*

$$\mathbb{E}\left[\,\alpha^4(\mathbf{x}_0)\,\right] = \mathbb{E}\left[\,\alpha^4(\mathbf{x}_\pi)\,\right] = \kappa_\alpha\,,$$

*then*

$$\mathbb{E}\left[\,e_{\mathrm{ph}}(\mathbf{x_A}, \mathbf{x_B}, k\,;\,\alpha))\,\right] = 0\,,$$

*i.e.* $\arg \hat{g}_{\mathrm{sp}}(\mathbf{x_A}, \mathbf{x_B}, k\,;\,\alpha)$ *is an unbiased estimator of the phase of the homogeneous inter-receiver Green's function.*

*Proof.* We begin by evaluating the real and imaginary parts of the stationary phase estimate as well as the homogeneous Green's function, in order to apply definition (3.5.79) to calculate their phases. For the former, recall

$$\hat{g}_{\mathrm{sp}}(\mathbf{x_A}, \mathbf{x_B}, k\,;\,\alpha) = \alpha^2(\mathbf{x}_0)\,\hat{G}(\mathbf{x_A}, \mathbf{x_B}, k) \;- \alpha^2(\mathbf{x}_\pi)\,\hat{G}^*(\mathbf{x_A}, \mathbf{x_B}, k)\,.$$

Then

$$\mathrm{Re}\left\{\hat{g}_{\mathrm{sp}}(\mathbf{x_A}, \mathbf{x_B}, k\,;\,\alpha)\right\} = \left(\alpha^2(\mathbf{x}_0) - \alpha^2(\mathbf{x}_\pi)\right) \mathrm{Re}\left\{\hat{G}(\mathbf{x_A}, \mathbf{x_B}, k)\right\} \tag{3.5.80}$$

$$\operatorname{Im}\{\hat{g}_{\mathrm{sp}}(\mathbf{x_A},\mathbf{x_B},k\,;\,\alpha)\} = \left(\alpha^2(\mathbf{x}_0)+\alpha^2(\mathbf{x}_\pi)\right)\operatorname{Im}\left\{\hat{G}(\mathbf{x_A},\mathbf{x_B},k)\right\}\,. \tag{3.5.81}$$

On the other hand, recall the definition of the homogeneous Green's function

$$\hat{G}_{\mathrm{hom}}(\mathbf{x_A},\mathbf{x_B},k) = \hat{G}(\mathbf{x_A},\mathbf{x_B},k)\; - \hat{G}^*(\mathbf{x_A},\mathbf{x_B},k)\,.$$

Then

$$\operatorname{Re}\left\{\hat{G}_{\mathrm{hom}}(\mathbf{x_A},\mathbf{x_B},k)\right\} = 0 \quad \text{and} \quad \operatorname{Im}\left\{\hat{G}_{\mathrm{hom}}(\mathbf{x_A},\mathbf{x_B},k)\right\} = 2\operatorname{Im}\left\{\hat{G}(\mathbf{x_A},\mathbf{x_B},k)\right\}\,, \tag{3.5.82}$$

so that

$$\arg G_{\mathrm{hom}}(\mathbf{x_A},\mathbf{x_B},k) = \operatorname{sgn}\operatorname{Im}\left\{\hat{G}(\mathbf{x_A},\mathbf{x_B},k)\right\}\frac{\pi}{2}\,, \tag{3.5.83}$$

where $\operatorname{sgn}(\cdot)$ stands for the sign function. Therefore, the error in phase incurred by the stationary phase approximation is

$$e_{\mathrm{ph}}(\mathbf{x_A},\mathbf{x_B},k\,;\,\alpha)) = \arg\hat{g}_{\mathrm{sp}}(\mathbf{x_A},\mathbf{x_B},k\,;\,\alpha) - \operatorname{sgn}\operatorname{Im}\left\{\hat{G}(\mathbf{x_A},\mathbf{x_B},k)\right\}\frac{\pi}{2}.$$

Note that if $\operatorname{Re}\{\hat{G}(\mathbf{x_A},\mathbf{x_B},k)\} = 0$, then by (3.5.80), (3.5.79) and (3.5.83) we have that $\arg\hat{g}_{\mathrm{sp}}(\mathbf{x_A},\mathbf{x_B},k\,;\,\alpha) = \arg(\hat{G}_{\mathrm{hom}}(\mathbf{x_A},\mathbf{x_B},k)$ and no phase error is incurred. Therefore, we consider the expected value of $e_{\mathrm{ph}}(\mathbf{x_A},\mathbf{x_B},k\,;\,\alpha))$ in the case when $\operatorname{Re}\{\hat{G}(\mathbf{x_A},\mathbf{x_B},k)\} \neq 0$. Under this assumption we have by (3.5.79) that $e_{\mathrm{ph}}(\mathbf{x_A},\mathbf{x_B},k\,;\,\alpha))$ depends on the random quantity

$$\operatorname{atan}\left(\frac{\left(\alpha^2(\mathbf{x}_0)+\alpha^2(\mathbf{x}_\pi)\right)\operatorname{Im}\left\{\hat{G}(\mathbf{x_A},\mathbf{x_B},k)\right\}}{\left(\alpha^2(\mathbf{x}_0)-\alpha^2(\mathbf{x}_\pi)\right)\operatorname{Re}\left\{\hat{G}(\mathbf{x_A},\mathbf{x_B},k)\right\}}\right)\,. \tag{3.5.84}$$

We will determine the expected value of (3.5.84) by estimating the expected value of the quantity inside the brackets, and then taking a Taylor approximation of the inverse tangent function. To this end, consider the auxiliary random variable

$$X_\epsilon = \frac{\left(\alpha^2(\mathbf{x}_0)+\alpha^2(\mathbf{x}_\pi)\right)\operatorname{Im}\left\{\hat{G}(\mathbf{x_A},\mathbf{x_B},k)\right\}}{\epsilon+\left(\alpha^2(\mathbf{x}_0)-\alpha^2(\mathbf{x}_\pi)\right)\operatorname{Re}\left\{\hat{G}(\mathbf{x_A},\mathbf{x_B},k)\right\}}\,, \qquad \text{for } \epsilon>0\,.$$

so that owing to the continuity of the inverse tangent function, we have

$$\lim_{\epsilon\to 0}\operatorname{atan} X_\epsilon = \operatorname{atan}\left(\frac{\left(\alpha^2(\mathbf{x}_0)+\alpha^2(\mathbf{x}_\pi)\right)\operatorname{Im}\left\{\hat{G}(\mathbf{x_A},\mathbf{x_B},k)\right\}}{\left(\alpha^2(\mathbf{x}_0)-\alpha^2(\mathbf{x}_\pi)\right)\operatorname{Re}\left\{\hat{G}(\mathbf{x_A},\mathbf{x_B},k)\right\}}\right)\,. \tag{3.5.85}$$

Further define

$$Y_+ = \big(\alpha^2(\mathbf{x}_0) + \alpha^2(\mathbf{x}_\pi)\big)\,\mathrm{Im}\left\{\hat{G}(\mathbf{x_A}, \mathbf{x_B}, k)\right\} \tag{3.5.86}$$

$$Y_- = \big(\epsilon + \alpha^2(\mathbf{x}_0) - \alpha^2(\mathbf{x}_\pi)\big)\,\mathrm{Re}\left\{\hat{G}(\mathbf{x_A}, \mathbf{x_B}, k)\right\}\,, \tag{3.5.87}$$

so that $X_\epsilon = Y_+/Y_-$. The first moments of $Y_+$ and $Y_-$ are given respectively by

$$\mathbb{E}\,[\,Y_+\,] = 2(\mu_\alpha^2 + \sigma_\alpha^2)\,\mathrm{Im}\left\{\hat{G}(\mathbf{x_A}, \mathbf{x_B}, k)\right\} \tag{3.5.88}$$

$$\mathbb{E}\,[\,Y_-\,] = \epsilon\,\mathrm{Re}\left\{\hat{G}(\mathbf{x_A}, \mathbf{x_B}, k)\right\}\,. \tag{3.5.89}$$

Direct calculation shows that the corresponding variances are given by

$$\mathrm{Var}\,[\,Y_+\,] = 2\,\mathrm{Im}\left\{\hat{G}(\mathbf{x_A}, \mathbf{x_B}, k)\right\}^2 \left(\,\kappa_\alpha - (\mu_\alpha^2 + \sigma_\alpha^2)^2 + \mathrm{Cov}\left[\,\alpha^2(\mathbf{x}_0), \alpha^2(\mathbf{x}_\pi)\,\right]\right)\,, \tag{3.5.90}$$

and

$$\mathrm{Var}\,[\,Y_-\,] = 2\,\mathrm{Im}\left\{\hat{G}(\mathbf{x_A}, \mathbf{x_B}, k)\right\}^2 \left(\,\kappa_\alpha - (\mu_\alpha^2 + \sigma_\alpha^2)^2 - \mathrm{Cov}\left[\,\alpha^2(\mathbf{x}_0), \alpha^2(\mathbf{x}_\pi)\,\right]\right)\,, \tag{3.5.91}$$

where (3.1.4) and (3.1.5) have been used to calculate

$$\mathrm{Var}\left[\,\alpha^2(\mathbf{x}_0)\,\right] = \mathrm{Var}\left[\,\alpha^2(\mathbf{x}_\pi)\,\right] = \kappa_\alpha - (\mu_\alpha^2 + \sigma_\alpha^2)^2\,. \tag{3.5.92}$$

Next, using the bilinearity and translation invariance of the covariance operator, we have that the covariance of $Y_+$ and $Y_-$ is given by

$$\begin{aligned}
\mathrm{Cov}\,[\,Y_+, Y_-\,] &= \mathrm{Im}\left\{\hat{G}(\mathbf{x_A}, \mathbf{x_B}, k)\right\} \cdot \mathrm{Re}\left\{\hat{G}(\mathbf{x_A}, \mathbf{x_B}, k)\right\} \times \\
&\qquad\qquad \mathrm{Cov}\left[\,\alpha^2(\mathbf{x}_0) + \alpha^2(\mathbf{x}_\pi),\, \alpha^2(\mathbf{x}_0) - \alpha^2(\mathbf{x}_\pi)\,\right] \\
&= \mathrm{Im}\left\{\hat{G}(\mathbf{x_A}, \mathbf{x_B}, k)\right\} \cdot \mathrm{Re}\left\{\hat{G}(\mathbf{x_A}, \mathbf{x_B}, k)\right\} \left(\mathrm{Var}\left[\,\alpha^2(\mathbf{x}_0)\,\right] - \mathrm{Var}\left[\,\alpha^2(\mathbf{x}_\pi)\,\right]\right)\,. \\
&= 0\,,
\end{aligned} \tag{3.5.93}$$

where (3.5.92) has been used in the last equality.

We have established the necessary elements to estimate the mean and variance of $X_\epsilon$. Consider the following multivariate Taylor approximations to the mean and variance of the

ratio $Y_+/Y_-$

$$\mathbb{E}\left[\frac{Y_+}{Y_-}\right] \approx \frac{\mathbb{E}[Y_+]}{\mathbb{E}[Y_-]} - \frac{1}{\mathbb{E}[Y_-]^2}\operatorname{Cov}[Y_+, Y_-] + \frac{\mathbb{E}[Y_+]}{\mathbb{E}[Y_-]^3}\operatorname{Var}[Y_-] ,$$

and

$$\operatorname{Var}\left[\frac{Y_+}{Y_-}\right] \approx \frac{\operatorname{Var}[Y_+]}{\mathbb{E}[Y_-]^2} - 2\frac{\mathbb{E}[Y_+]}{\mathbb{E}[Y_-]^3}\operatorname{Cov}[Y_+, Y_-] + \frac{\mathbb{E}[Y_+]^2}{\mathbb{E}[Y_-]^4}\operatorname{Var}[Y_-] .$$

Using (3.5.88), (3.5.90), (3.5.91) and (3.5.93) we have the approximations

$$\begin{aligned}\mathbb{E}[X_\epsilon] \approx \frac{\operatorname{Im}\{\hat{G}(\mathbf{x_A}, \mathbf{x_B}, k)\}}{\operatorname{Re}\{\hat{G}(\mathbf{x_A}, \mathbf{x_B}, k)\}} \Bigg( &\frac{2(\mu_\alpha^2 + \sigma_\alpha^2)}{\epsilon} \\ &+ \frac{4(\mu_\alpha^2 + \sigma_\alpha^2)}{\epsilon^3}\left(\kappa_\alpha - (\mu_\alpha^2 + \sigma_\alpha^2)^2 - \operatorname{Cov}\left[\alpha^2(\mathbf{x}_0), \alpha^2(\mathbf{x}_\pi)\right]\right)\Bigg) ,\end{aligned} \tag{3.5.94}$$

and

$$\begin{aligned}\operatorname{Var}[X_\epsilon] \approx &\frac{\operatorname{Im}\{\hat{G}(\mathbf{x_A}, \mathbf{x_B}, k)\}^2}{\operatorname{Re}\{\hat{G}(\mathbf{x_A}, \mathbf{x_B}, k)\}^2}\left(\frac{2}{\epsilon^2} + \frac{8(\mu_\alpha^2 + \sigma_\alpha^2)^2}{\epsilon^4}\right) \\ &\times \left(\kappa_\alpha - (\mu_\alpha^2 + \sigma_\alpha^2)^2 - \operatorname{Cov}\left[\alpha^2(\mathbf{x}_0), \alpha^2(\mathbf{x}_\pi)\right]\right) ,\end{aligned} \tag{3.5.95}$$

noting that for fixed $\epsilon > 0$ and $\operatorname{Re}\{\hat{G}(\mathbf{x_A}, \mathbf{x_B}, k)\} \neq 0$ as we have assumed, the first two moments of $X_\epsilon$ are finite. Next, we estimate the expected value of $\operatorname{atan}(X_\epsilon)$. To this end, consider the following Taylor approximations to the mean and variance of a smooth function $f$ of a random variable, for $f$ sufficiently differentiable and a random variable $X_\epsilon$ of finite moments.

$$\mathbb{E}[f(X_\epsilon)] \approx f(\mathbb{E}[X_\epsilon]) + \frac{1}{2}f''(\mathbb{E}[X_\epsilon])\operatorname{Var}[X_\epsilon] .$$

Taking $f(x) = \operatorname{atan}(x)$, we have

$$\mathbb{E}[\operatorname{atan}(X_\epsilon)] \approx \operatorname{atan}(\mathbb{E}[X_\epsilon]) - \frac{\mathbb{E}[X_\epsilon]\operatorname{Var}[X_\epsilon]}{(1 + \mathbb{E}[X_\epsilon]^2)^2} . \tag{3.5.96}$$

Invoking the continuity of the arctangent function (equation (3.5.85)), we have that

$$\mathbb{E}\left[\operatorname{atan}\left(\frac{\left(\alpha^2(\mathbf{x}_0) + \alpha^2(\mathbf{x}_\pi)\right)\operatorname{Im}\left\{\hat{G}(\mathbf{x_A}, \mathbf{x_B}, k)\right\}}{\left(\alpha^2(\mathbf{x}_0) - \alpha^2(\mathbf{x}_\pi)\right)\operatorname{Re}\left\{\hat{G}(\mathbf{x_A}, \mathbf{x_B}, k)\right\}}\right)\right] \approx \lim_{\epsilon\to 0}\operatorname{atan}(\mathbb{E}[X_\epsilon]) - \frac{\mathbb{E}[X_\epsilon]\operatorname{Var}[X_\epsilon]}{(1 + \mathbb{E}[X_\epsilon]^2)^2} .$$

We now determine the limit of the right hand side of equation (3.5.96) as $\epsilon \to 0$. Using

equations (3.5.94) and (3.5.95) we have that

$$\lim_{\epsilon\to 0} \frac{\mathbb{E}\left[\, X_\epsilon \,\right] \mathrm{Var}\left[\, X_\epsilon \,\right]}{(\, 1 + \mathbb{E}\left[\, X_\epsilon \,\right]^2 \,)^2} = 0\,,$$

and

$$\lim_{\epsilon\to 0} \mathrm{atan}(\mathbb{E}\left[\, X_\epsilon \,\right]) = \mathrm{sgn}\left(\frac{\mathrm{Im}\{\hat{G}(\mathbf{x_A}, \mathbf{x_B}, k)\}}{\mathrm{Re}\{\hat{G}(\mathbf{x_A}, \mathbf{x_B}, k)\}}\right) \frac{\pi}{2}\,.$$

Hence,

$$\lim_{\epsilon\to 0} \mathbb{E}\left[\, \mathrm{atan}\, X_\epsilon \,\right] = \mathrm{sgn}\left(\frac{\mathrm{Im}\{\hat{G}(\mathbf{x_A}, \mathbf{x_B}, k)\}}{\mathrm{Re}\{\hat{G}(\mathbf{x_A}, \mathbf{x_B}, k)\}}\right) \frac{\pi}{2}\,.$$

Combining this result with the application of Lemma 2.4.2 to definition (3.5.79) yields

$$\mathbb{E}\left[\, \arg \hat{g}_{\mathrm{sp}}(\mathbf{x_A}, \mathbf{x_B}, k;\, \alpha) \,\right] = \mathrm{sgn}\left(\mathrm{Im}\{\hat{G}(\mathbf{x_A}, \mathbf{x_B}, k)\}\right) \frac{\pi}{2} = \arg \hat{G}_{\mathrm{hom}}(\mathbf{x_A}, \mathbf{x_B}, k)$$

Therefore, we conclude that under assumptions (3.1.4) and (3.1.5),

$$\mathbb{E}\left[\, e_{\mathrm{ph}}(\mathbf{x_A}, \mathbf{x_B}, k;\, \alpha) \,\right] = 0\,,$$

i.e. the stationary phase estimate is an unbiased estimator of the phase of the inter-receiver Green's function. □

**Remark 3.5.6.** Allowing for the interpretation of (3.1.1) in one, two or three dimensions the result above is in general valid, as no specific form of the Green's function is assumed within the proof Proposition 3.5.4. Only conditions (3.1.4) and (3.1.5) on the moments of the random field $\alpha$ at the stationary locations are required for the unbiased estimation of the phase of the inter-receiver Green's function via the stationary phase approximation.

### 3.5.4 Expected error in amplitude

For convenience, we define the square amplitude error in the stationary phase approximation as

$$e^2_{\mathrm{amp}}(\mathbf{x_A}, \mathbf{x_B}, k;\, \alpha) = |\hat{g}_{\mathrm{sp}}(\mathbf{x_A}, \mathbf{x_B}, k;\, \alpha)|^2 - |\hat{G}_{\mathrm{hom}}(\mathbf{x_A}, \mathbf{x_B}, k)|^2\,,$$

where we note using the definition of the homogeneous Green's function, we have

$$|\hat{G}_{\mathrm{hom}}(\mathbf{x_A}, \mathbf{x_B}, k)|^2 = 4\,\mathrm{Im}\left\{\hat{G}(\mathbf{x_A}, \mathbf{x_B}, k)\right\}^2\,. \tag{3.5.97}$$

On the other hand, using (3.5.80) and (3.5.81) we have

$$\begin{aligned}|\hat{g}_{\text{sp}}(\mathbf{x_A}, \mathbf{x_B}, k;\, \alpha)|^2 = &|\hat{G}(\mathbf{x_A}, \mathbf{x_B}, k)|^2 \left(\alpha^4(\mathbf{x}_0) + \alpha^4(\mathbf{x}_\pi)\right) \\ &+ 2\,\Lambda(\mathbf{x_A}, \mathbf{x_B}, k) \left(\alpha^2(\mathbf{x}_0)\alpha^2(\mathbf{x}_\pi)\right) ,\end{aligned} \tag{3.5.98}$$

for the function $\Lambda(\mathbf{x_A}, \mathbf{x_B}, k)$ given in (3.5.74). Therefore

$$\begin{aligned}e^2_{\text{amp}}(\mathbf{x_A}, \mathbf{x_B}, k;\, \alpha) = &|\hat{G}(\mathbf{x_A}, \mathbf{x_B}, k)|^2 \left(\alpha^4(\mathbf{x}_0) + \alpha^4(\mathbf{x}_\pi)\right) \\ &+ 2\,\Lambda(\mathbf{x_A}, \mathbf{x_B}, k) \left(\alpha^2(\mathbf{x}_0)\alpha^2(\mathbf{x}_\pi)\right) \\ &- 4\,\text{Im}\left\{\hat{G}_(\mathbf{x_A}, \mathbf{x_B}, k)\right\}^2 .\end{aligned} \tag{3.5.99}$$

and its expected value is given directly by

$$\begin{aligned}\mathbb{E}\left[\, e^2_{\text{amp}}(\mathbf{x_A}, \mathbf{x_B}, k;\, \alpha)\,\right] = &|\hat{G}(\mathbf{x_A}, \mathbf{x_B}, k)|^2 \left(\mathbb{E}\left[\,\alpha^4(\mathbf{x}_0)\,\right] + \mathbb{E}\left[\,\alpha^4(\mathbf{x}_\pi)\,\right]\right) \\ &+ 2\,\Lambda(\mathbf{x_A}, \mathbf{x_B}, k)\, \mathbb{E}\left[\,\alpha^2(\mathbf{x}_0)\alpha^2(\mathbf{x}_\pi)\,\right] \\ &- 4\,\text{Im}\left\{\hat{G}_(\mathbf{x_A}, \mathbf{x_B}, k)\right\}^2 .\end{aligned} \tag{3.5.100}$$

Under assumptions (3.1.4) and (3.1.5), the expected value of the stationary phase approximation reduces to

$$\begin{aligned}\mathbb{E}\left[\, e^2_{\text{amp}}(\mathbf{x_A}, \mathbf{x_B}, k;\, \alpha)\,\right] = &2|\hat{G}(\mathbf{x_A}, \mathbf{x_B}, k)|^2\kappa_\alpha \\ &+ 2\,\Lambda(\mathbf{x_A}, \mathbf{x_B}, k) \left(\text{Var}\left[\,\alpha(\mathbf{x}_0)\alpha(\mathbf{x}_\pi)\,\right] - \left(\text{Cov}\left[\,\alpha(\mathbf{x}_0),\, \alpha(\mathbf{x}_\pi)\,\right] + \mu_\alpha^2\right)^2\right) \\ &- 4\,\text{Im}\left\{\hat{G}_(\mathbf{x_A}, \mathbf{x_B}, k)\right\}^2 .\end{aligned} \tag{3.5.101}$$

Consistent with the discussion of the general error $E_{\text{sp}}(\mathbf{x_A}, \mathbf{x_B}, k;\, \alpha)$ in Section 3.5.2, the error in amplitude depends on the first, second and fourth moments of the random variables $\alpha(\mathbf{x}_0)$ and $\alpha(\mathbf{x}_\pi)$, as well as the covariance of these random variables and the variance of their product. Importantly, even under these simplifying assumptions, the error $\mathbb{E}\left[\, e^2_{\text{amp}}(\mathbf{x_A}, \mathbf{x_B}, k;\, \alpha)\,\right]$ is in general not zero, and so the stationary phase estimate is always biased in amplitude.

Considering expressions (3.5.77) or (3.5.101), it becomes apparent that even under assumptions (3.1.4) and (3.1.5), further information regarding the distribution of the product $\alpha(\mathbf{x}_0)\alpha(\mathbf{x}_\pi)$ and the covariance of $\alpha(\mathbf{x}_0)$ and $\alpha(\mathbf{x}_\pi)$ is necessary to give bounds in probability for the error in the stationary phase approximation. To this end, we consider a particular choice of covariance structure and probability distribution of the random field $\alpha$ in the following section.

## 3.6 Numerical study and results

In order to be concrete, we consider the error in the stationary phase approximation for the case where the random field $\alpha$ is Matérn-correlated and log-normally distributed. The suitability of this choice of covariance function and probability distribution for geostatistical applications has been established in Section 2.4.2. In what follows, $2.5 \times 10^4$ realisations of random fields $\alpha$ were simulated with the parameters detailed in the table below.

| Parameter | Range | Number of samples (uniform) |
|---|---|---|
| Mean of log-normal distribution | $\mu_\alpha = 1$ | - |
| Variance of log-normal distribution | $0.05 \leq \sigma_\alpha^2 \leq 1$ | 20 |
| Matérn correlation length | $2^{-4} \leq \rho_\alpha \leq 2$ | 6 |
| Matérn smoothness | $2^{-4} \leq \nu_\alpha \leq 2$ | 11 |

We remark that the correlation length $\rho_\alpha$ is scaled with respect to the source-receiver array, so that a correlation length of e.g. $\rho_\alpha = 0.25$ should be interpreted as a correlation length of roughly a quarter of the scale of the source boundary $S$. Section 3.6.1 presents a numerical study of the phase error defined in Sections 3.5.3, exploring how this error and its empirical probability distribution relates to the long-range correlations of the random field $\alpha$, parametrised by $\rho_\alpha$, and the smoothness of $\alpha$ which is parametrised by $\nu_\alpha$, recalling that this parameter can also be interpreted as a measure of local correlations in the random field. Next, Section 3.6.2 presents a brief exploration of the amplitude errors defined in 3.5.4. Finally, Section 3.6.3 gives analytical bounds for the error in probability using the results derived in Section 3.5.2, in terms of the parameters that control the behaviour of the random field $\alpha$, as well as the wavenumber and the inter-receiver distance, and explores these bounds numerically.

### 3.6.1 Phase error in the stationary phase approximate

The phase error $e_{\text{ph}}(\mathbf{x_A}, \mathbf{x_B}, k; \alpha)$ defined in (3.5.78) was simulated with a Matérn-correlated random field $\alpha$, which was log-normally distributed with mean $\mu_\alpha = 1$. An appropriate far-field regime was ensured by fixing the value of the wavenumber at $k = 10\ \text{m}^{-1}$ with a boundary radius of $r = 5000$ m. The empirical probability density function (henceforth abbreviated as p.d.f.) of $e_{\text{ph}}(\mathbf{x_A}, \mathbf{x_B}, k; \alpha)$ was estimated from the simulated data, and a scaled Beta distribution was fitted to the empirical data. The Beta distribution is well-suited to this purpose for a number of reasons. First, it is compactly supported. Secondly, it can transition between unimodal and bimodal regimes, a behaviour that was observed in the empirical distributions.

Finally, it is a more general case of some inverse trigonometric distributions (such as the Arcsine distribution), and therefore compatible with the presence of the arctangent function in the definition of the phase error in the stationary phase approximation.

Figure 3.10 illustrates the convergence of the empirical p.d.f. of the phase error as the sample number increases, in blue, to the Beta fit in orange dashes. The bottom panels show the empirical p.d.f. for a very rough random field $\alpha$ (i.e. low correlation length $\rho_\alpha$ and low smoothness $\nu_\alpha$), while conversely the top panels show the corresponding p.d.f.s for a very smooth random field $\alpha$ (high correlation length $\rho_\alpha$ and high smoothness $\nu_\alpha$). The former case exhibits a bimodal behaviour, with a minimum at zero, whereas the latter case is unimodal with a maximum at zero. The distributions are symmetric.

**Remark 3.6.1.** The bimodal distribution in Figure 3.10 is striking. While the stationary phase estimate has been shown to be an unbiased estimator of the homogeneous inter-receiver phase, the bimodal distribution with a minimum at zero implies there are regimes of noise correlation and smoothness that make a small value of the error the *least* likely.

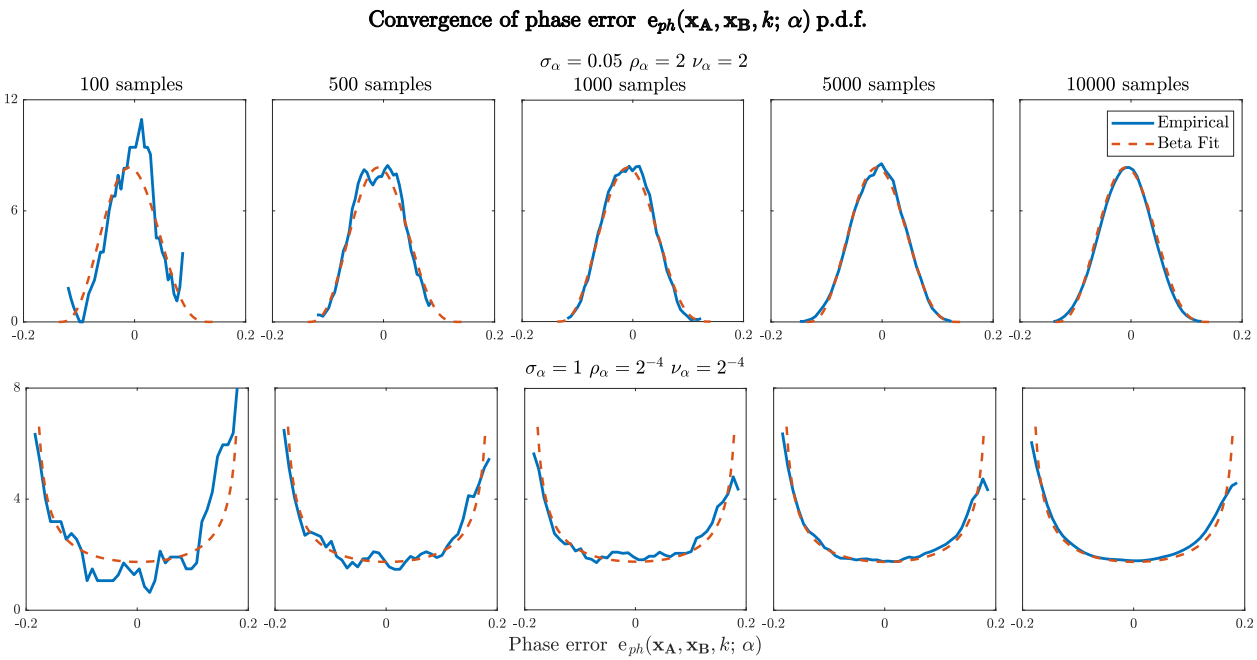


**Figure 3.10:** Illustration of the convergence of the empirically estimated probability density function of the phase error $E_{\text{ph}}(\mathbf{x_A}, \mathbf{x_B}, k; \alpha)$ (in blue) and the Beta-distributed fit (in orange dashes), for increasing number of samples from left to right. The random field parameters (correlation length, smoothness and variance) were chosen to produce the two behaviours of interest: unimodal (**top**) and bimodal (**bottom**). A value of $k = 10$ was used in these simulations.

Figure 3.11 shows the empirically estimated p.d.f.s of the phase error in blue, and the corresponding Beta fitted p.d.f.s in orange for a random field of high variance $\sigma_\alpha^2 = 1$ and for

a range of smoothness and correlation values $\nu_\alpha$ and $\rho_\alpha$. In this figure, all but the bottom right p.d.f.s are bimodal with a minimum at zero. The bottom left panel corresponds to a very smooth random field, with practically constant values with respect to the scale of the source-receiver geometry (see, e.g., the bottom right panel of Figure 2.5 for an illustration of this behaviour). Note that for this higher value of the variance, all the the error p.d.f.s are all bimodal, and this is only mitigated when the noise is very smooth a both local and long range scales. As previously discussed, as a consequence of the symmetric bimodal distribution, a small phase error is possible but unlikely. It is in fact the least likely outcome. On the other hand, once the random field smoothness at local and global scales is sufficiently high, the transition to a unimodal behaviour appears to be sharp. In the unimodal regime, small error values are the most likely.

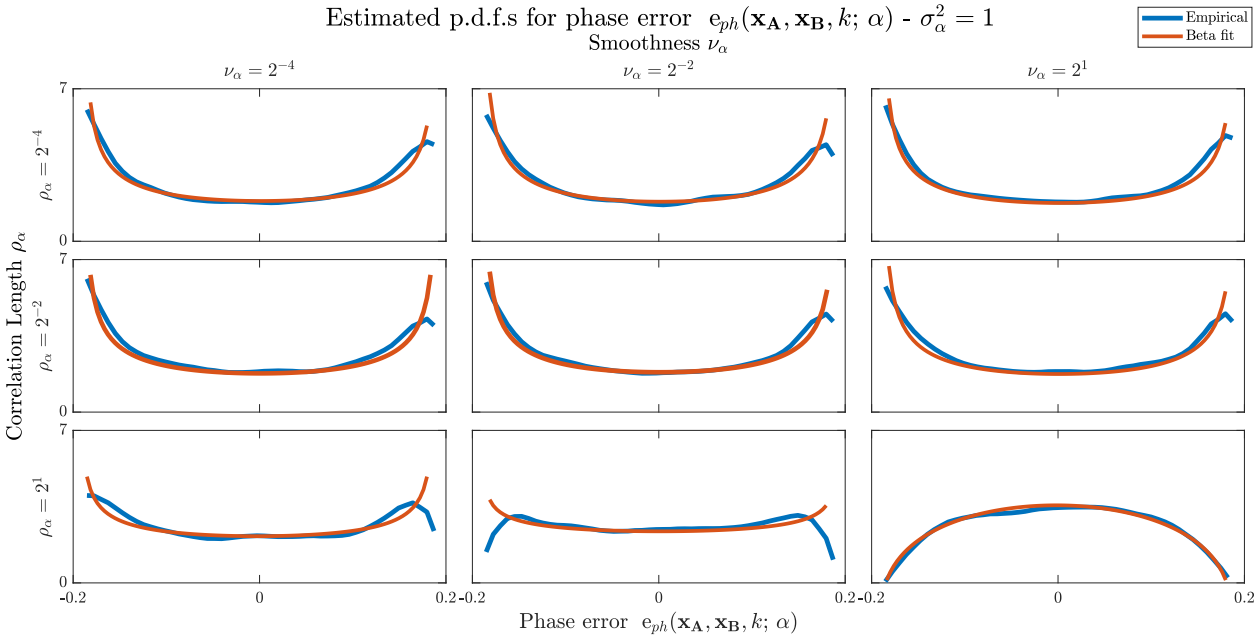


**Figure 3.11:** Examples of the empirically estimated probability density function of the phase error $e_{\text{ph}}(\mathbf{x_A}, \mathbf{x_B}, k; \alpha)$ (in blue) and the Beta-distributed fit (in orange), for a random field variance of $\sigma_\alpha^2 = 1$, and varying values of the correlation length $\rho_\alpha$ (along rows) and smoothness parameter $\nu_\alpha$ (along columns). A value of $k = 10$ was used in these simulations.

Figure 3.12 shows the empirically estimated p.d.f.s of the phase error in blue, and the corresponding Beta fitted p.d.f.s in orange for a random field of medium variance $\sigma_\alpha^2 = 0.5$ and for a range of smoothness and correlation values $\nu_\alpha$ and $\rho_\alpha$. The bimodality of the p.d.f.s is relatively mitigated in comparison to a higher variance of $\alpha$. Nevertheless, most of the distributions in this figure are almost completely flat, which corresponds to a uniform distribution. In terms of the error this is not favourable behaviour, as a low value error is as likely as any other. This error behaviour becomes mitigated as the smoothness and

correlation length of the random field increase, with the correlation length appearing to play a larger role in the transition to a more desirable unimodal behaviour.

**Remark 3.6.2.** While a reduced noise variance mitigates the bimodality of the phase error distribution, there remains a high degree of uncertainty as for rougher fields the p.d.f. is essentially uniform over its support, so that any error value is as likely as any other.

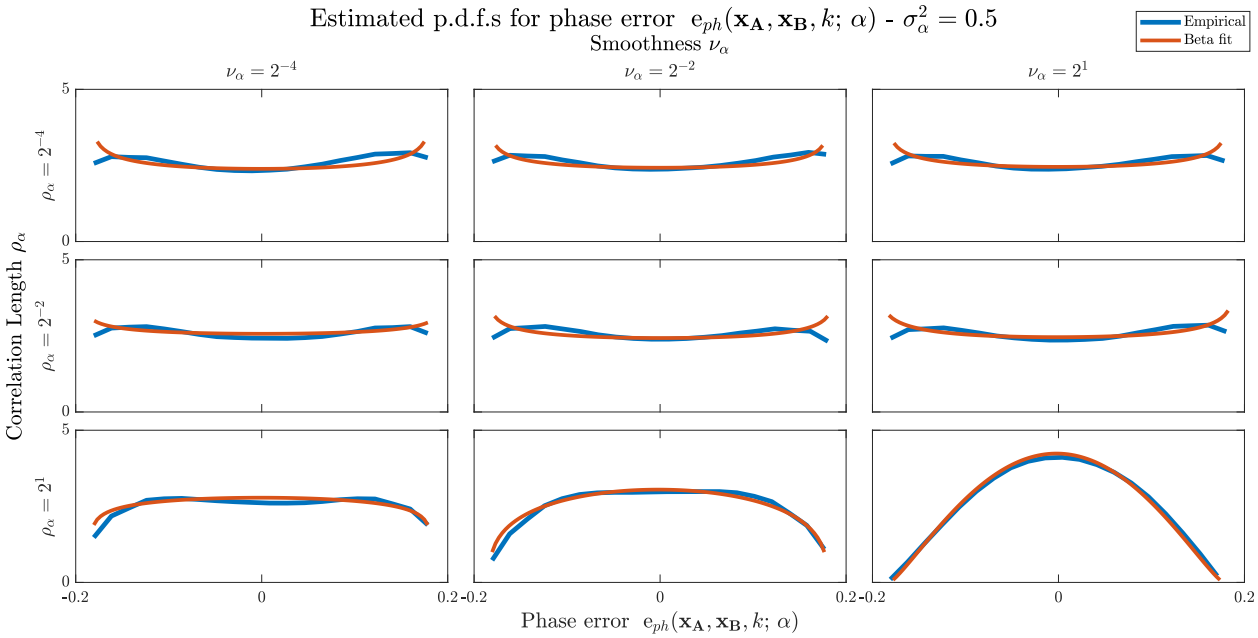


**Figure 3.12:** Examples of the empirically estimated probability density function of the phase error $e_{\text{ph}}(\mathbf{x_A}, \mathbf{x_B}, k; \alpha)$ (in blue) and the Beta-distributed fit (in orange), for a random field variance of $\sigma_\alpha^2 = 0.5$, and varying values of the correlation length $\rho_\alpha$ (along rows) and smoothness parameter $\nu_\alpha$ (along columns). A value of $k = 10$ was used in these simulations.

Figure 3.13 shows the empirically estimated p.d.f.s of the phase error in blue, and the corresponding Beta fitted p.d.f.s in orange for a random field of low variance $\sigma_\alpha^2 = 0.05$ and for a range of smoothness and correlation values $\nu_\alpha$ and $\rho_\alpha$. The probability distribution concentrates around the mean and all p.d.f.s are unimodal, but an very low variance had to be imposed in order to achieve this for rough random fields $\alpha$ (i.e. low $\rho_\alpha$, low $\nu_\alpha$).

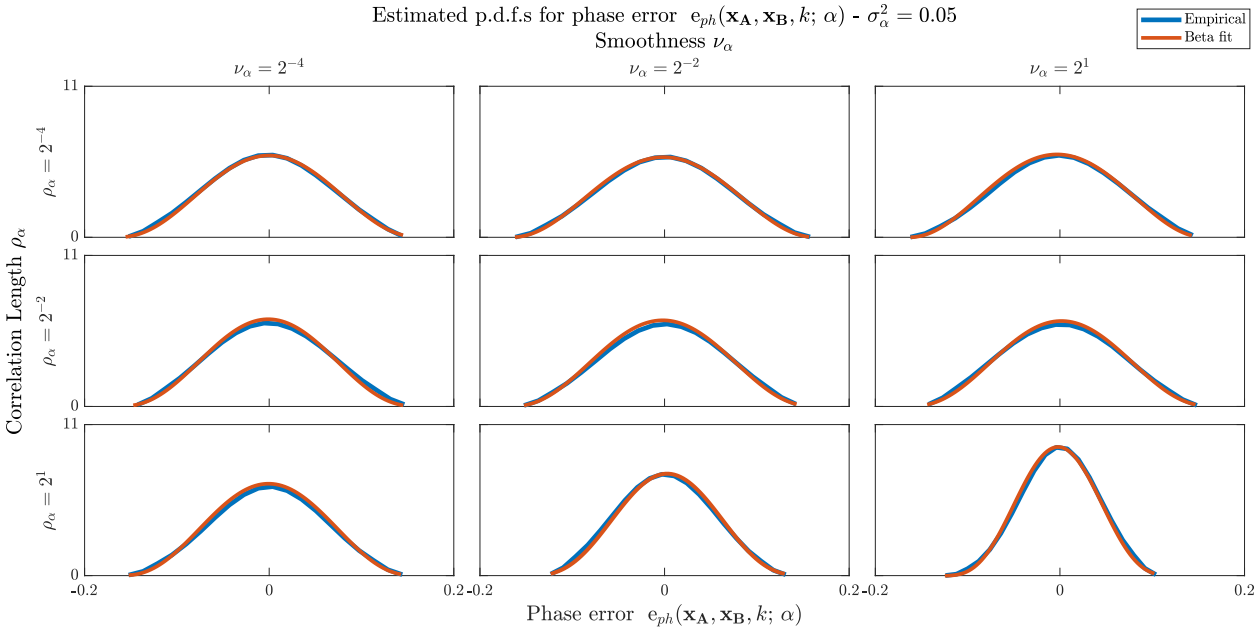


**Figure 3.13:** Examples of the empirically estimated probability density function of the phase error $e_{\text{ph}}(\mathbf{x_A}, \mathbf{x_B}, k; \alpha)$ (in blue) and the Beta-distributed fit (in orange), for a random field variance of $\sigma_\alpha^2 = 0.05$, and varying values of the correlation length $\rho_\alpha$ (along rows) and smoothness parameter $\nu_\alpha$ (along columns). A value of $k = 10$ was used.

The transitions between unimodal and bimodal behaviours are illustrated in Figure 3.14, in terms of the full range of parameters simulated. Each panel in the figure shows the modulus of the maximum likelihood value of the phase error $e_{\text{ph}}(\mathbf{x_A}, \mathbf{x_B}, k; \alpha)$, estimated numerically using the Beta p.d.f.s illustrated in Figures 3.11-3.13. Each panel corresponds to a different value of the correlation length $\rho_\alpha$. Within each panel, the y-axis corresponds to decreasing values of the variance $\sigma_\alpha^2$, and the x-axis corresponds to increasing values of the smoothness parameter $\nu_\alpha$. The blue regions correspond to a most likely value of zero for the error, whereas the yellow region corresponds to a non-zero value.

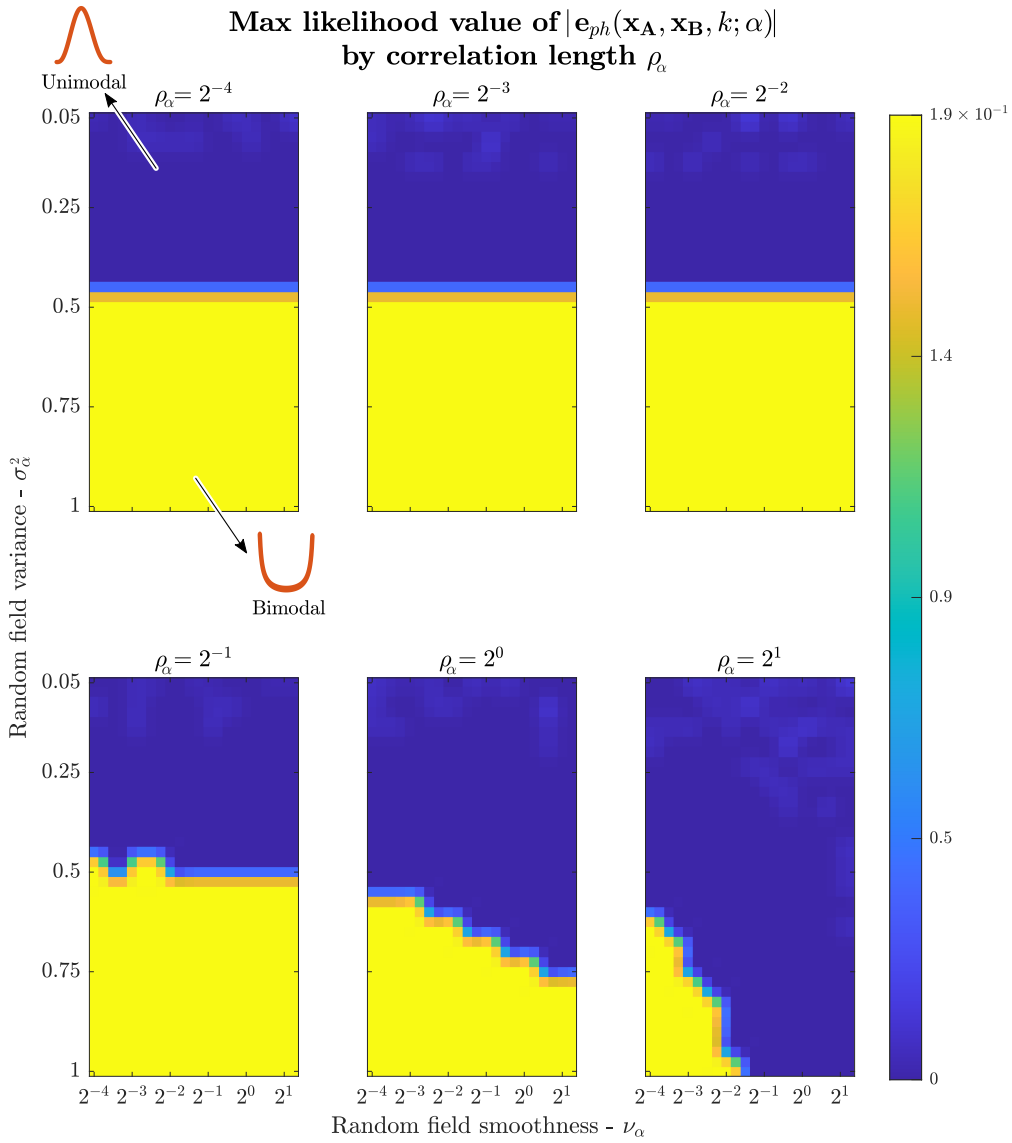


**Figure 3.14:** Numerical estimation of the maximum likelihood value of the absolute value of the phase error $|e_{\text{ph}}(\mathbf{x_A}, \mathbf{x_B}, k; \alpha)|$ for $k = 10$. Each insert corresponds to a different value of the correlation length $\rho_\alpha$ of the random field $\alpha$, ranging from $2^{-4}$ to 2, in proportion to the scale of the source boundary. The horizontal axis of each insert corresponds to the random field smoothness parameter $\nu_\alpha$, ranging from $2^{-4}$ to 2, while the vertical axis corresponds to the variance $\sigma_\alpha^2$ of the random field, ranging from 0.05 to 1.

Finally, Figure 3.15 shows the variance of $e_{\text{ph}}(\mathbf{x_A}, \mathbf{x_B}, k; \alpha)$ for each of the parameter ranges in Figure 3.14. Overlaid over each panel is the transition line separating unimodal and bimodal distributions extracted from Figure 3.15, in solid white, as well as the level curve of the variance at 0.012 for all the panels.

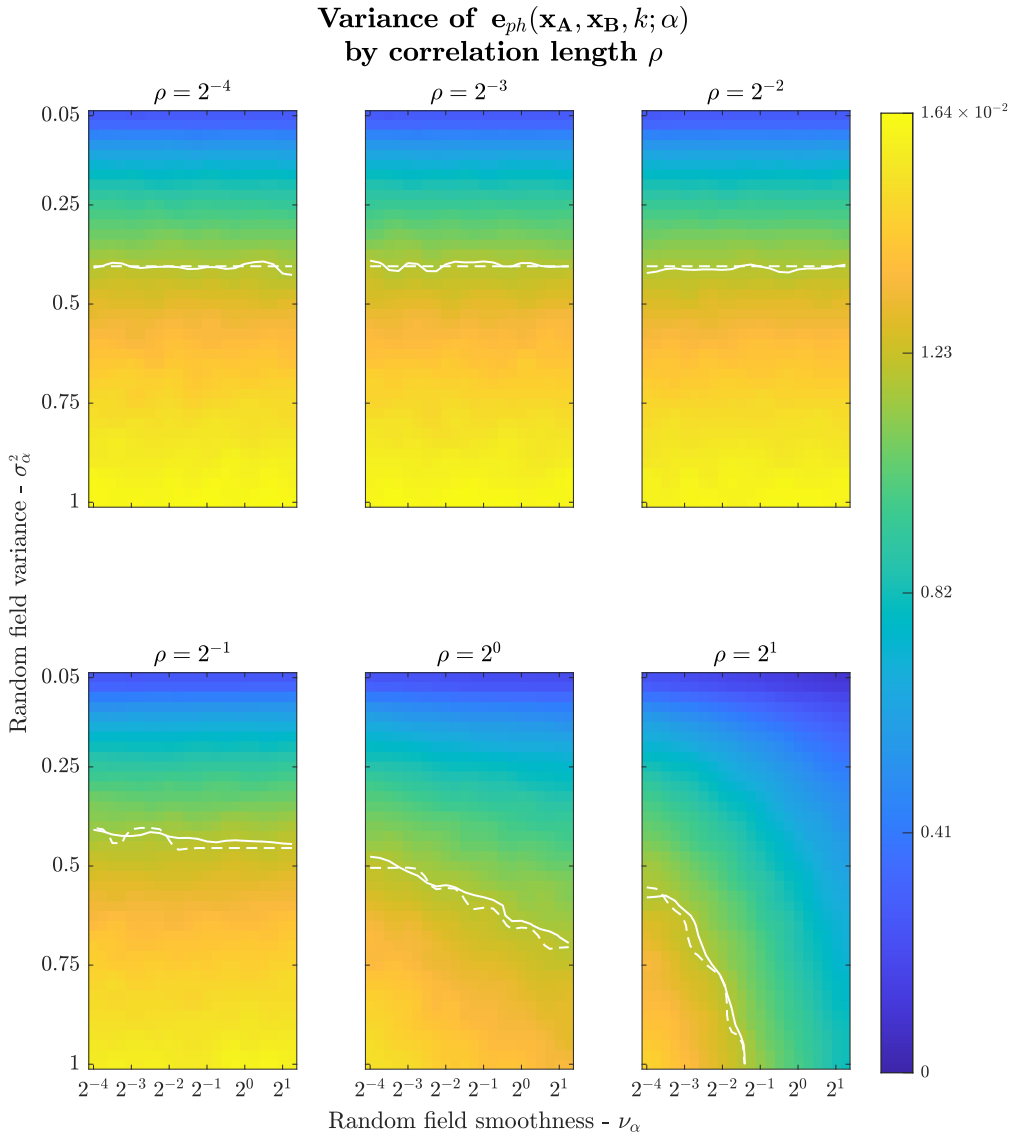


**Figure 3.15:** Numerical estimation of the variance of the phase error $E(\mathbf{x_A}, \mathbf{x_B}, k;\, \alpha)$ for $k = 10$. Each insert corresponds to a different value of the correlation length $\rho_\alpha$ of the random field $\alpha$, ranging from $2^{-4}$ to 2, in proportion to the scale of the source boundary. The horizontal axis of each insert corresponds to the random field smoothness parameter $\nu_\alpha$, ranging from $2^{-4}$ to 2, while the vertical axis corresponds to the variance $\sigma_\alpha^2$ of the random field, ranging from 0.05 to 1. The dashed solid line corresponds to the boundary between unimodal and bimodal p.d.f.'s extracted from the data shown in Figure 3.14, whereas the white solid line is the level curve for the variance value $\mathrm{Var}\,[\,E(\mathbf{x_A}, \mathbf{x_B}, k;\, \alpha)\,] = 0.012$.*

*Please note that this particular value of the variance is chosen with the sole purpose of illustrating the transition between unimodal and bimodal regimes of the error p.d.f., and is itself of no specific significance.

### 3.6.2 Amplitude error in the stationary phase approximate

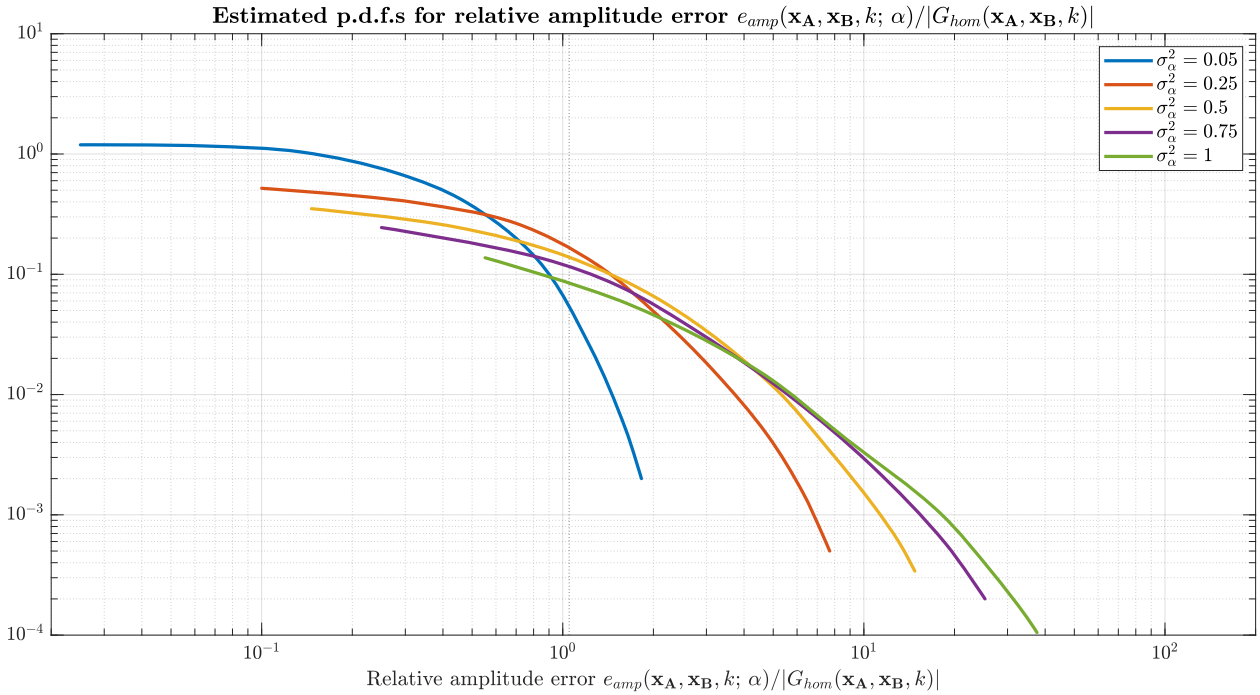


**Figure 3.16:** Representative examples of the numerically estimated probability density functions of the relative amplitude error $e_{\text{amp}}(\mathbf{x_A}, \mathbf{x_B}, k; \alpha)/|G_{\text{hom}}(\mathbf{x_A}, \mathbf{x_B}, k)|$ for $k = 10$. The correlation length is set to $\rho_\alpha = 2^{-2}$, and the smoothness parameter is $\nu_\alpha = 2^{-1}$. Each colour corresponds to a different value of the variance of the random field $\sigma_\alpha^2$, ranging from 0.05 to 1. The scale is logarithmic in both axes and a simple moving average smoothing has been applied.

In this Section, examples of the numerically estimated p.d.f. of the relative amplitude error defined in (3.5.4) are presented for a rough field, illustrating that the stationary phase approximate is a biased estimator of the amplitude of the homogeneous inter-receiver Green's function. Figure 3.16 shows numerically calculated examples of the p.d.f. of the relative amplitude error

$$\frac{e_{\text{amp}}(\mathbf{x_A}, \mathbf{x_B}, k; \alpha)}{|G_{\text{hom}}(\mathbf{x_A}, \mathbf{x_B}, k)|},$$

where

$$e_{\text{amp}}(\mathbf{x_A}, \mathbf{x_B}, k; \alpha) = \sqrt{|\hat{g}_{\text{sp}}(\mathbf{x_A}, \mathbf{x_B}, k; \alpha)|^2 - |\hat{G}_{\text{hom}}(\mathbf{x_A}, \mathbf{x_B}, k)|^2}\,.$$

The p.d.f.s were calculated for five values of $\sigma_\alpha^2$ ranging from 0.05 to 1, each illustrated with a different colour in the Figure. A logarithmic scale was used in both axes to better illustrate the behaviour of this error. As one would expect, the Figure illustrates how the likelihood of large errors increases as the variance of the source amplitudes $\sigma_\alpha^2$ increases. Interestingly, even when this variance is small (e.g. $\sigma_\alpha^2 = 0.05$, in blue) the amplitude is likely to be

underestimated. As the value of the variance increases, it becomes very likely that the amplitude if the inter-receiver Green's function will be overestimated. This is consistent with the previous discussions in Sections 3.5.4 and 3.5.2, where the analytical derivations of the error in amplitude make it apparent that the interferometric estimate of the inter-receiver Green's function is biased in all but the most favourable conditions for isotropic medium illumination.

While Figure 3.16 shows the behaviour of the relative amplitude error in terms of the variance of the random field $\alpha$ for a specific choice of the smoothness and correlation length parameters, $\nu_\alpha$ and $\rho_\alpha$, Figure 3.17 shows the mean of this relative amplitude error for a range of values of the random field parameters. The mean was chosen as an illustrative statistic to explore the bias in the amplitude estimation. This Figure shows six panels, each corresponding to a different correlation length, ranging from $\rho_\alpha = 2^{-4}$ to $\rho_\alpha = 2$. Within a single panel, the horizontal axes corresponds to the value of the smoothness parameter ranging from $\nu_\alpha = 2^{-4}$ to $\nu_\alpha = 2$, and the vertical axis corresponds to the variance of the random field $\sigma_\alpha^2$ decreasing from 1 to 0.05. The value of the error mean is colour coded, with blue corresponding to lower values and yellow corresponding to the largest values. It is notable that the expected relative error exhibits a strong dependence on the variance of the random field $\sigma_\alpha^2$. For the smallest variance value explored, the relative error is about 4%, while a variance of $\sigma_\alpha^2 = 5$ induces a bias of around 60% in the estimated amplitude. For the largest variance value explored, $\sigma_\alpha^2 = 1$, the expected amplitude bias increases to approximately 120%. On the other hand, there appear to be little qualitative or quantitative effects either in terms of the correlation length $\rho_\alpha$ or the smoothness $\nu_\alpha$ of the random field. Hence, the amplitude bias of the stationary phase approximate of the interferometric inter-receiver Green's function depends primarily on the variance of the source intensities along the boundary. This is consistent with the analytical expressions (3.5.100) and (3.5.101), where it is apparent that the moments of the random field $\alpha$ control to a large extent the behaviour of this error.

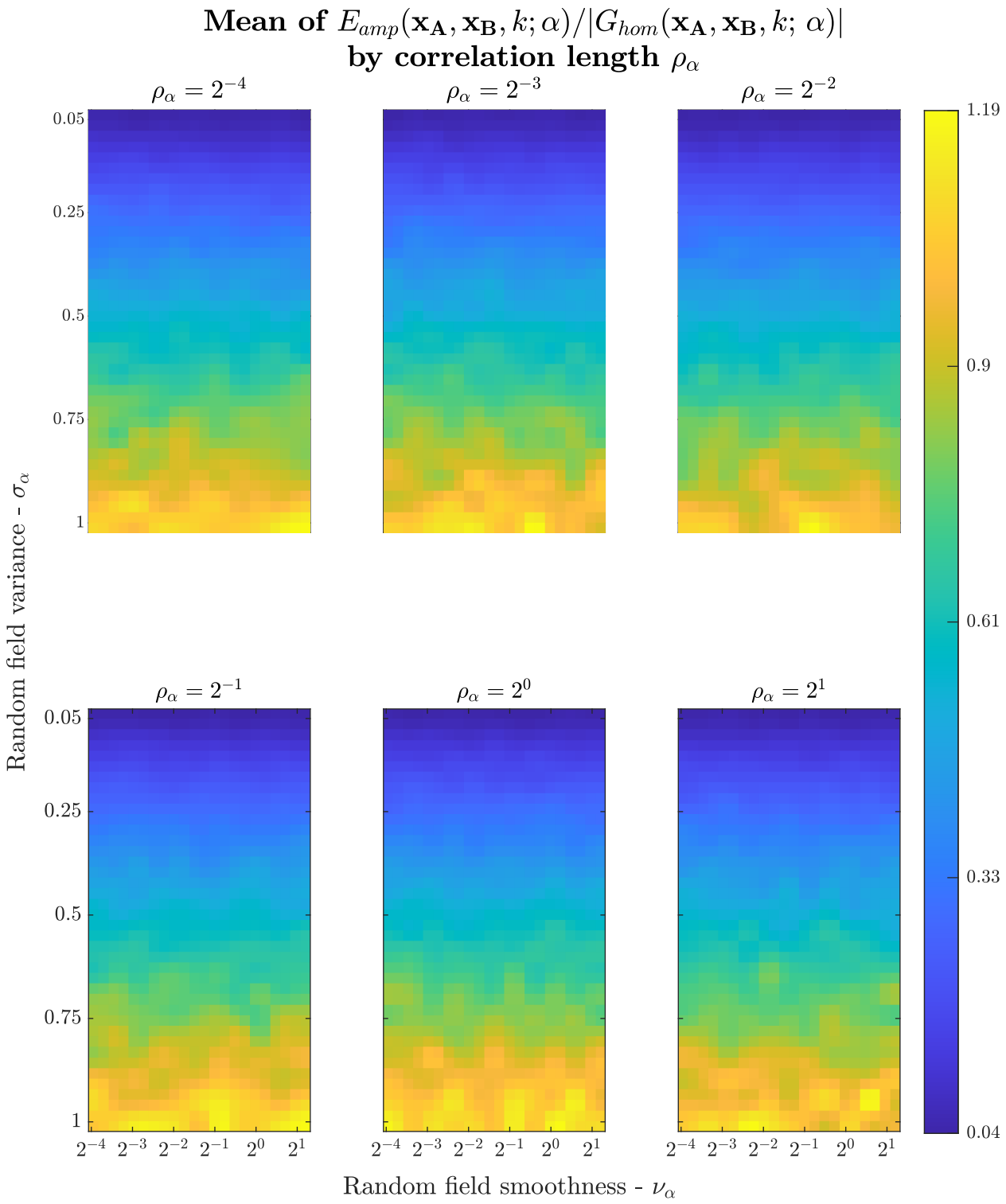


**Figure 3.17:** Numerical estimation of the mean of the relative amplitude error $E_{\text{amp}}(\mathbf{x_A}, \mathbf{x_B}, k;\ \alpha)/|G_{\text{hom}}(\mathbf{x_A}, \mathbf{x_B}, k)|$ for $k = 10$. Each insert corresponds to a different value of the correlation length $\rho_\alpha$ of the random field $\alpha$, ranging from $2^{-4}$ to 2, in proportion to the scale of the source boundary. The horizontal axis of each insert corresponds to the random field smoothness parameter $\nu_\alpha$, ranging from $2^{-4}$ to 2, while the vertical axis corresponds to the variance $\sigma_\alpha$ of the random field, ranging from 0.05 to 1.

### 3.6.3 Bounds in probability on the error in the stationary phase approximation

Consider now the complex-valued random variable $E_{\mathrm{sp}}(\mathbf{x_A}, \mathbf{x_B}, k\,;\,\alpha)$, which summarises the error in the stationary phase approximation. Lemma (2.4.1) will be used in this Section to give a bound for this error. In order to apply the Lemma, an explicit expressions for the mean and variance of $E_{\mathrm{sp}}(\mathbf{x_A}, \mathbf{x_B}, k\,;\,\alpha)$ are required. We derive these quantities under the log-normal and Matérn assumptions below.

Recall from Section 3.5.2 the expected value and variance of this error under assumption (3.1.4), reproduced below for reference.

$$\mathbb{E}\,[\,E_{\mathrm{sp}}(\mathbf{x_A}, \mathbf{x_B}, k\,;\,\alpha)\,] = (\,\mu_\alpha^2 + \sigma_\alpha^2 - 1\,)\,\hat{G}_{\mathrm{hom}}(\mathbf{x_A}, \mathbf{x_B}, k)\,.$$

and

$$\begin{aligned}\mathrm{Var}\,[\,E_{\mathrm{sp}}(\mathbf{x_A}, \mathbf{x_B}, k\,;\,\alpha)\,] =& |\hat{G}(\mathbf{x_A}, \mathbf{x_B}, k)|^2(\kappa_\alpha - 2(\mu_\alpha^2 + \sigma_\alpha^2)^2) \\ &+ 2\Lambda(\mathbf{x_A}, \mathbf{x_B}, k)\big\{\,\mathrm{Var}\,[\,\alpha(\mathbf{x}_0)\alpha(\mathbf{x}_\pi)\,] - (\mu_\alpha^2 + \sigma_\alpha^2)^2 \\ &+ \big(\mathrm{Cov}\,[\,\alpha(\mathbf{x}_0), \alpha(\mathbf{x}_\pi)\,] + \mu_\alpha^2\big)^2\,\big\}\,,\end{aligned}$$

While the assumption of a log-normal Matérn-correlated random field $\alpha$ has no further implications for the expected value of the error $E_{\mathrm{sp}}(\mathbf{x_A}, \mathbf{x_B}, k\,;\,\alpha)$, its variance can be further specified under these assumptions. First, consider the value of the fourth moment $\kappa_\alpha$. Note that for in the log-normal case, (3.1.5) follows from (3.1.4). Using formula (2.4.9) for the $4^{\mathrm{th}}$ moment of $\alpha(\mathbf{x}_0)$, along with (2.4.6) and (2.4.7), we have

$$\kappa_\alpha = \frac{(\mu_\alpha^2 + \sigma_\alpha^2)^6}{\mu_\alpha^8}\,. \tag{3.6.1}$$

Next, we calculate the term $\mathrm{Var}\,[\,\alpha(\mathbf{x}_0)\alpha(\mathbf{x}_\pi)\,]$ under the log-normal assumption. To this end, recall Remark 2.4.2 regarding the log-normality of the product of log-normally distributed random variables. We have that $\alpha(\mathbf{x}_0)\alpha(\mathbf{x}_\pi)$ is a log-normal random variable with variance

$$\begin{aligned}\mathrm{Var}\,[\,\alpha(\mathbf{x}_0)\alpha(\mathbf{x}_\pi)\,] = \big(\exp\big(2s^2 + 2\,\mathrm{Cov}\,[\,\log\alpha(\mathbf{x}_0), \log\alpha(\mathbf{x}_\pi)\,]\big) - 1\big) \times \\ \exp\big(4m + 2s^2 + 2\,\mathrm{Cov}\,[\,\log\alpha(\mathbf{x}_0),\, \log\alpha(\mathbf{x}_\pi)\,]\big)\,,\end{aligned} \tag{3.6.2}$$

where $m$ and $s^2$ can be given in terms of $\mu_\alpha$ and $\sigma_\alpha^2$ using (2.4.6) and (2.4.7). Next, note

that

$$\mathrm{Cov}\left[\log X,\, \log Y\right] = \log\left(1 + \frac{\mathrm{Cov}\left[X,\, Y\right]}{\mathbb{E}\left[X\right]\mathbb{E}\left[Y\right]}\right) . \tag{3.6.3}$$

The validity[4] of (3.6.3) can be established by direct calculation, invoking Remark (2.4.2) again along with equations (2.4.6) and (2.4.7). Combining (3.6.2) and (3.6.3) results in

$$\begin{aligned}\mathrm{Var}\left[\alpha(\mathbf{x}_0)\alpha(\mathbf{x}_\pi)\right] = \frac{(\mu_\alpha^2+\sigma_\alpha^2)^2}{\mu_\alpha^8}\Big(\mathrm{Cov}\left[\alpha(\mathbf{x}_0),\alpha(\mathbf{x}_\pi)\right] + \mu_\alpha^2\Big)^4 \\ - \Big(\mathrm{Cov}\left[\alpha(\mathbf{x}_0),\alpha(\mathbf{x}_\pi)\right] + \mu_\alpha^2\Big)^2\end{aligned} \tag{3.6.4}$$

Having fully specified $\mathrm{Var}\left[\alpha(\mathbf{x}_0)\alpha(\mathbf{x}_\pi)\right]$, we introduce the the Matérn correlation assumption, i.e.

$$\mathrm{Cov}\left[\alpha(\mathbf{x}),\alpha(\mathbf{x}')\right] = M(|\mathbf{x}-\mathbf{x}'|;\,\rho_\alpha,\nu_\alpha)\ , \tag{3.6.5}$$

where $M(|\mathbf{x}-\mathbf{x}'|;\,\rho_\alpha,\nu_\alpha)$ is defined in (2.4.4). Finally, substituting (3.6.1), (3.6.4) and (3.6.5) into (3.1.4) yields

$$\begin{aligned}\mathrm{Var}\left[E_{\mathrm{sp}}(\mathbf{x_A},\mathbf{x_B},k\,;\,\alpha)\right] =& 2|\hat{G}(\mathbf{x_A},\mathbf{x_B},k)|^2\left\{\frac{(\mu_\alpha^2+\sigma_\alpha^2)^6}{\mu_\alpha^8} - (\mu_\alpha^2+\sigma_\alpha^2)^2\right\} \\ &+ 2\Lambda(\mathbf{x_A},\mathbf{x_B},k)\Bigg\{\frac{(\mu_\alpha^2+\sigma_\alpha^2)^2}{\mu_\alpha^8}\left(M(2r;\,\rho_\alpha,\nu_\alpha)+\mu_\alpha^2\right)^4 \\ &- (\mu_\alpha^2+\sigma_\alpha^2)^2\Bigg\},\end{aligned} \tag{3.6.6}$$

where $2r = |\mathbf{x}_0 - \mathbf{x}_\pi|$ is the diameter of the source boundary $S$. This expression was validated by comparing it against the numerically calculated variance of the simulated error $E_{\mathrm{sp}}(\mathbf{x_A},\mathbf{x_B},k;\,\alpha)$ for a range of values of the field variance $\sigma_\alpha$, and the Matérn correlation parameters $\rho_\alpha$ and $\nu_\alpha$. Figure 3.18 shows an illustrative example of the validation for a particular set of parameters. The rate of decay with the wavenumber $k$ corresponds to the decay of the Green's function $\hat{G}(\mathbf{x_A},\mathbf{x_B},k)$ in two dimensions (1.2.20), which decays with $1/\sqrt{k|\mathbf{x_A}-\mathbf{x_B}|}$. This Green's function enters the variance (3.6.6) squared, so that the variance decays with $1/k|\mathbf{x_A}-\mathbf{x_B}|$ in two dimensions.

[4]Equation (3.6.3) is in general approximately true. This can be shown by taking the change of variables $X = e^U$ and $Y = e^V$, and a Taylor expansion of the exponential function to approximate the expectations. It is exact when $X$ and $Y$ are log-normally distributed.

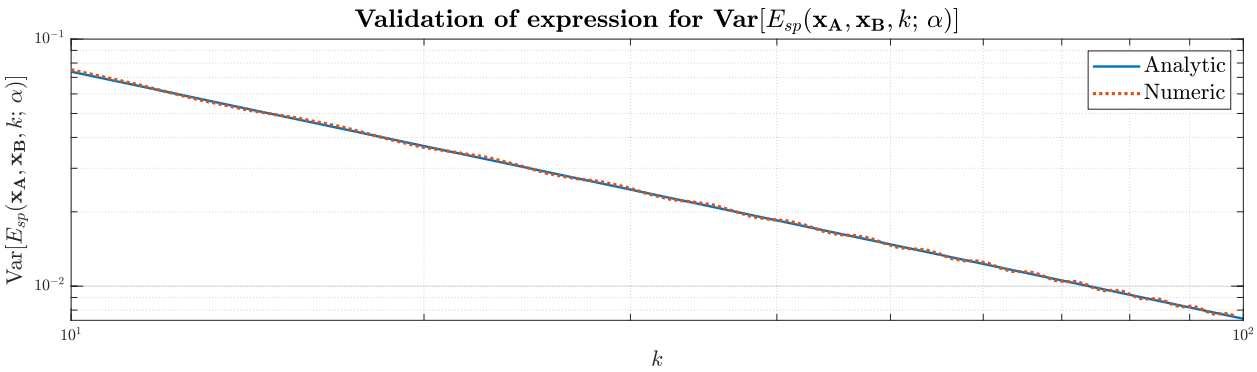


**Figure 3.18:** Example of the validation of equation (3.6.6) for the variance of $E_{\text{sp}}(\mathbf{x_A}, \mathbf{x_B}, k; \alpha)$, in terms of the wavenumber $k$. The error was simulated and its numerical variance (orange dashes) was compared to (3.6.6) (solid blue), exhibiting good agreement. In this figure, results are shown for a log-correlated random field $\alpha$ with mean $\mu_\alpha = 1$ and variance $\sigma_\alpha^2 = 0.5$, with Matérn correlation (2.4.4) parameters $\rho_\alpha = 0.25$ and $\nu_\alpha = 1$. The inter-receiver distance was $|\mathbf{x_A} - \mathbf{x_B}| = 100$ m and the radius of the source boundary $S$ was $r = 5000$ m. The wavenumber $k$ ranges from 10 to 100, and a logarithmic scale is used in both axes.

**Remark 3.6.3.** Due to the presence of the second-order terms in (3.6.6), the variance in the one dimensional case would decay with $k^2$ (see (1.2.17)), whereas in three dimensions the variance would decay with the square of the inter-receiver distance $|\mathbf{x_A} - \mathbf{x_B}|$ but not with $k$ (see (1.2.21)). The two-dimensional case is discussed above.

With an analytical expression for the variance in the case of log-normally distributed, Matérn-correlated random fields, a bound for the centred error can be give directly using Lemma 2.4.1.

**Proposition 3.6.1** (Chebyshev bound for the error in the stationary phase approximation)**.** *When $\alpha$ is a log-normally distributed random field with mean $\mu_\alpha$ and variance $\sigma_\alpha^2$, Matérn-correlated in space with correlation length $\rho_\alpha$ and smoothness $\nu_\alpha$, the probability that the centred error in the stationary phase approximation to the homogeneous inter-receiver Green's function $\hat{G}(\mathbf{x_A}, \mathbf{x_B}, k)$ exceeds any given real positive value $\xi$ is no larger than the function $B(\xi, \mathbf{x_A}, \mathbf{x_B}, k; \alpha)$, defined as*

$$\begin{aligned} B(\xi, \mathbf{x_A}, \mathbf{x_B}, k; \alpha) = \frac{2}{\xi^2}\Bigg( & |\hat{G}(\mathbf{x_A}, \mathbf{x_B}, k)|^2 \left\{ \frac{(\mu_\alpha^2 + \sigma_\alpha^2)^6}{\mu_\alpha^8} - (\mu_\alpha^2 + \sigma_\alpha^2)^2 \right\} \\ & + \Lambda(\mathbf{x_A}, \mathbf{x_B}, k) \left\{ \frac{(\mu_\alpha^2 + \sigma_\alpha^2)^2}{\mu_\alpha^8} \left( M(1; \rho_\alpha, \nu_\alpha) + \mu_\alpha^2 \right)^4 \right. \\ & \left. - (\mu_\alpha^2 + \sigma_\alpha^2)^2 \right\} \Bigg), \end{aligned} \tag{3.6.7}$$

*i.e.*

$$\mathbb{P}\left(|E_{\text{sp}}(\mathbf{x_A}, \mathbf{x_B}, k;\, \alpha) - \mathbb{E}\left[\, E_{\text{sp}}(\mathbf{x_A}, \mathbf{x_B}, k;\, \alpha)\,\right]| > \xi\right) \leq B(\xi, \mathbf{x_A}, \mathbf{x_B}, k;\, \alpha) \tag{3.6.8}$$

*Proof.* Combining equations (2.4.1) with (3.6.6) yields the bound. □

In definition (3.6.7), the correlation length $\rho_\alpha$ of the random field $\alpha$ has been normalised with respect to the diameter of the source boundary $S$, hence the Matérn correlation function is evaluated at $d = 1$ and $\rho_\alpha$ should be interpreted accordingly. Note that for the case where the random field $\alpha$ oscillates around the amplitude of the homogeneous inter-receiver $G_{\text{hom}}(\mathbf{x_A}, \mathbf{x_B}, k)$, i.e. $\mu_\alpha = 1$ and $\sigma_\alpha^2 = 1$, the bound above can be written as

$$\mathbb{P}\left(|E_{\text{sp}}(\mathbf{x_A}, \mathbf{x_B}, k;\, \alpha) - \sigma_\alpha^2 \hat{G}_{\text{hom}}(\mathbf{x_A}, \mathbf{x_B}, k)| > \xi\right) \leq B(\xi, \mathbf{x_A}, \mathbf{x_B}, k;\, \alpha)\,, \tag{3.6.9}$$

where

$$\begin{aligned} B(\xi, \mathbf{x_A}, \mathbf{x_B}, k;\, \alpha) = \frac{2}{\xi^2}\Bigg( & |\hat{G}(\mathbf{x_A}, \mathbf{x_B}, k)|^2 \left\{(1+\sigma_\alpha^2)^6 - (1+\sigma_\alpha^2)^2\right\} \\ & + \Lambda(\mathbf{x_A}, \mathbf{x_B}, k)\Bigg\{(1+\sigma_\alpha^2)^2\left(\, M(2r;\, \rho_\alpha, \nu_\alpha) + 1\right)^4 \\ & - (1+\sigma_\alpha^2)^2\Bigg\}\Bigg)\,. \end{aligned} \tag{3.6.10}$$

Figure 3.19 illustrates the Chevyshev bound (2.4.1) for a log-normally distributed, Matérn correlated random field $\alpha$ of mean $\mu_\alpha = 1$ and a range of values of the variance $\sigma_\alpha$. In this Figure, the correlation length of the random field $\rho_\alpha$ is scaled with respect to the diameter of the source boundary $S$. The Figure shows the probability of incurring a large error in the stationary phase approximation (left hand side of (3.6.8)), numerically estimated from $2.5 \times 10^4$ samples of the error $E_{\text{sp}}(\mathbf{x_A}, \mathbf{x_B}, k;\, \alpha)$ in solid blue, and the corresponding Chebyshev bound $B(\xi)$ in dashes.

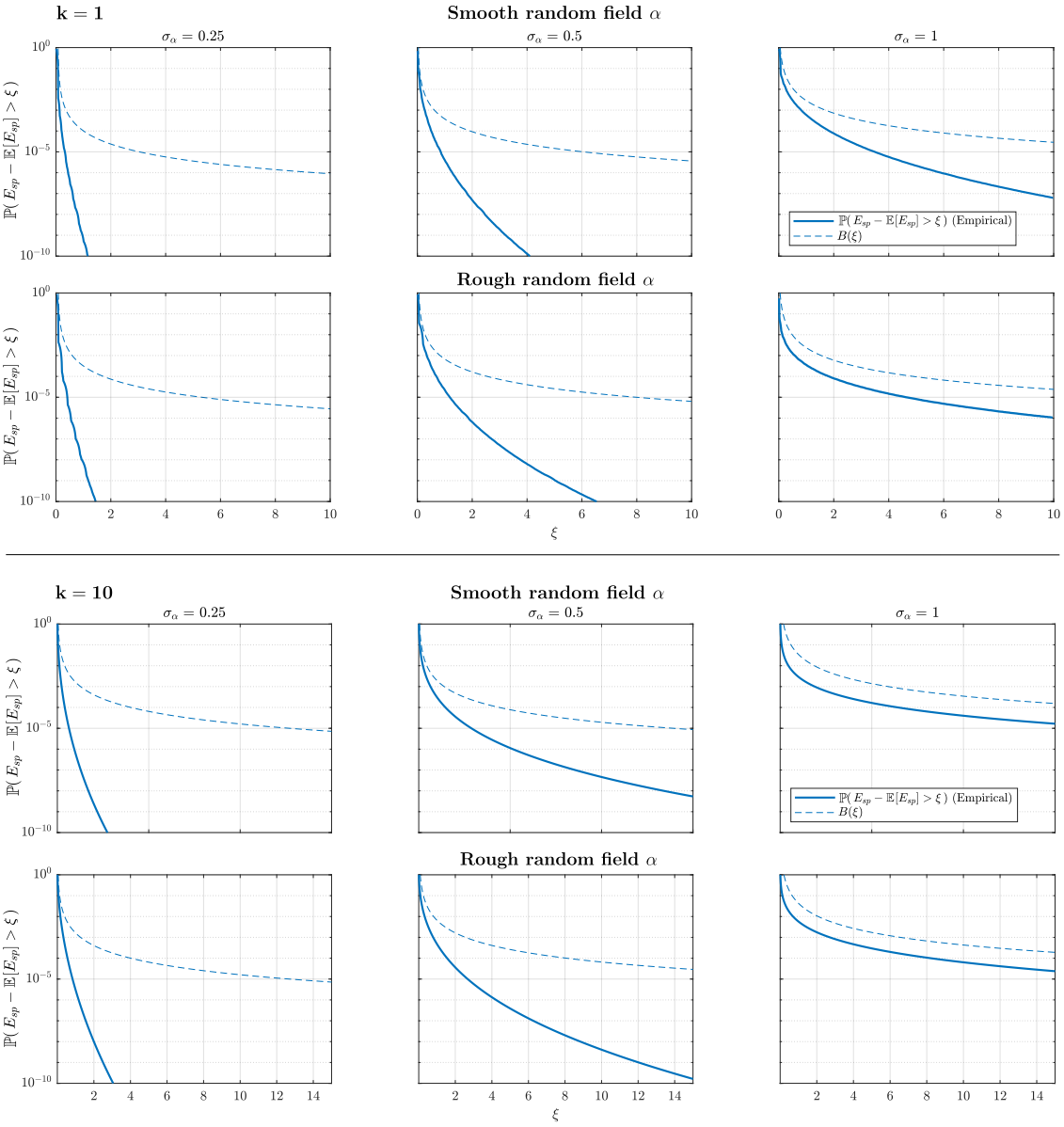


**Figure 3.19:** Comparison of the left (solid) and right hand side (dashes) of bound (3.6.8) for $k = 10$ (**top panel**) and $k = 1$ (**bottom panel**). In each panel bound is shown for highly smooth $\alpha$ ($\rho_\alpha = \nu_\alpha = 2$) (**top**), and very rough $\alpha$ ($\rho_\alpha = \nu_\alpha = 2^{-4}$) (**bottom**). Low (**left**), medium (**middle**) and high (**right**) values of the variance $\sigma_\alpha$ are shown. A logarithmic scale is used on the vertical axes. The inter-receiver distance is $|\mathbf{x_A} - \mathbf{x_B}| = 100$ m. The mean of the random field is $\mu_\alpha = 1$.

## 3.7 Error quantification when sources are of equal intensity

In this Section, we consider error quantification in the case where the source intensity is equal along the whole source boundary $S$. We assume the random field $\alpha$ to be identically 1. A bound for the error is given in terms of the wavenumber $k$ and the inter-receiver distance $|\mathbf{x_A} - \mathbf{x_B}|$. Namely, we prove the following

**Proposition 3.7.1.** *The error incurred through the stationary phase approximation in wavefield interferometry to the inter-receiver homogeneous Green's function in two dimensions is bounded above by*

$$|\hat{g}_{sp}(\mathbf{x_A}, \mathbf{x_B}, k; 1, 0) - \hat{G}_{hom}(\mathbf{x_A}, \mathbf{x_B}, k)| \leq 2\sqrt{2}\left(\frac{\sqrt{2}-1}{k\,|\mathbf{x_A} - \mathbf{x_B}|} + \frac{1}{k^2\,|\,\mathbf{x_A} - \mathbf{x_B}|^2}\right), \quad (3.7.1)$$

*where* $|\,\mathbf{x_A} - \mathbf{x_B}|$ *is the inter-receiver distance and* $k$ *is a fixed wavenumber.*

This result is established in the arguments presented below. As opposed to the preceding sections where a probabilistic approach is taken, the error bounds derived by Olver (1974), introduced in the Section 3.2.3 are used directly in this context.

Consider the interferometric equation (3.5.1) in the ideal case of $\alpha \equiv 1$ and $\beta \equiv 0$,

$$\hat{g}_{\text{int}}(\mathbf{x_A}, \mathbf{x_B}, k; 1, 0) = -2ik \oint_S \hat{G}(\mathbf{x_A}, \mathbf{x}, k)\hat{G}^*(\mathbf{x_B}, \mathbf{x}, k)d\mathbf{x}\,. \quad (3.7.2)$$

Then the integral in equation (3.5.2) can be parametrised as in (3.5.5), reproduced below for convenience

$$\hat{g}_{\text{int}}(\mathbf{x_A}, \mathbf{x_B}; 1, 0) = \frac{i}{4\pi}\int_{-\pi/2}^{3\pi/2} \frac{re^{ik(\,|\mathbf{x_A}-\mathbf{x}(t)| - |\mathbf{x_B}-\mathbf{x}(t)|\,)}}{\sqrt{|\mathbf{x_A} - \mathbf{x}(t)|\,|\mathbf{x_B} - \mathbf{x}(t)|}}\,dt\,,$$

where we note that the integral

$$I(\mathbf{x_A}, \mathbf{x_B}, k) = \int_{-\pi/2}^{3\pi/2} \frac{e^{ik(\,|\mathbf{x_B}-\mathbf{x}(t)| - |\mathbf{x_A}-\mathbf{x}(t)|\,)}}{\sqrt{|\mathbf{x_A} - \mathbf{x}(t)|\,|\mathbf{x_B} - \mathbf{x}(t)|}}\,dt \quad (3.7.3)$$

is of the form (3.2.1) with phase function

$$\phi(t) = |\mathbf{x_B} - \mathbf{x}(t)| \; - \; |\mathbf{x_A} - \mathbf{x}(t)| \quad (3.7.4)$$

and amplitude function

$$f(t) = \frac{r}{\sqrt{|\mathbf{x_A} - \mathbf{x}(t)|\,|\mathbf{x_B} - \mathbf{x}(t)|}}\,. \tag{3.7.5}$$

Consider the placement of a two dimensional coordinate system so that the origin is in the midpoint of the receiver pair and the receivers lie along the $x$-axis. Moreover, place the centre of the source boundary $S$ at the origin. Finally, denote the inter-receiver distance as $2d$. See Figure 3.5 for a sketch illustrating this layout (not to scale, as the radius $r$ is assumed to be very much larger than the inter-receiver distance $2d$) Hence, the coefficients of the expansion of $f^\alpha(t)$ about $t = 0$ are given by

$$f(t) = \frac{r}{(\,(r^2 + d^2)^2 - 4r^2d^2\cos^2(t)\,)^{\frac{1}{4}}}\,, \tag{3.7.6}$$

respectively.

with the amplitude function $f(t)$ given by equation (3.7.6) and the phase function $\phi(t)$ given by (3.5.7). Next, recall that the stationary phase approximation derived in Section 3.2 requires that stationary point corresponds to the lower limit of the integral, that this stationary point is a minimum and that the phase is increasing in the interval of integration. To bring the integrals in the right hand side of (3.5.6) to the required form, consider first the the change of variable $\eta = -t$ for the first integral,

$$\begin{aligned}\int_{-\pi/2}^{0} f(t)e^{ik\phi(t)}\,dt &= -\int_{\pi/2}^{0} f(-\eta)e^{ik\phi(-\eta)}d\eta \\ &= \int_{0}^{\pi/2} f(-\eta)e^{ik\phi(-\eta)}d\eta\,, \\ &= \int_{0}^{\pi/2} f(\eta)e^{ik\phi(\eta)}d\eta\,,\end{aligned}$$

where the even property given in (3.5.14) has been used. This change of variable ensures that the lower limit of the first integral is indeed a minimum ($t = 0$) and that the interval of integration $\left(0, \frac{\pi}{2}\right)$ is such that the phase is increasing, in agreement with conditions 3.2.2. Hence, if we define

$$I_0(\mathbf{x_A}, \mathbf{x_B}, k) = \int_{0}^{\pi/2} f(t)e^{ik\phi(t)}\,dt\,, \tag{3.7.7}$$

we have

$$\int_{-\pi/2}^{0} f(t)e^{ik\phi(t)}\,dt + \int_{0}^{\pi/2} f(t)e^{ik\phi(t)}\,dt = 2I_0(\mathbf{x_A}, \mathbf{x_B}, k)\,. \tag{3.7.8}$$

For the remaining two integrals, consider the change of variable $\eta = 2\pi - t$ in the third integral appearing on the right hand side of equation (3.7.7), so that

$$\begin{aligned}\int_{\pi/2}^{\pi} f(t)e^{ik\phi(t)}\,dt &= -\int_{3\pi/2}^{\pi} f(2\pi-\eta)e^{ik\phi(2\pi-\eta)}d\eta \\ &= \int_{\pi}^{3\pi/2} f(\eta)e^{ik\phi(\eta)}d\eta\,,\end{aligned}$$

where both the even property and the periodicity of $f(t)$ and $\phi(t)$ has been used (see equations (3.5.14) and (3.5.13). Therefore

$$\int_{\pi/2}^{\pi} f(t)e^{ik\phi(t)}\,dt + \int_{\pi}^{3\pi/2} f(t)e^{ik\phi(t)}\,dt = 2\int_{\pi}^{3\pi/2} f(t)e^{ik\phi(t)}\,dt\,. \tag{3.7.9}$$

The integral in the right hand side of equation (3.7.9) satisfies the requirement that the lower limit be a stationary point. However, this integral is not yet suitable for the application of the stationary phase approximation as described in Section 3.2, as the stationary point corresponding to $t = \pi$ is a maximum rather than a minimum, and the phase $\phi(t)$ is not increasing in the range of integration $(\pi, 3\pi/2)$. This can be remedied however by defining

$$I_\pi(\mathbf{x_A}, \mathbf{x_B}, k) = \int_{\pi}^{3\pi/2} f(t)e^{ik\phi^-(t)}\,dt\,, \tag{3.7.10}$$

where $\phi^-(t) = -\phi(t)$, so that $t = \pi$ is a minimum of $\phi^-(t)$, and this phase function is decreasing in the interval of integration. Hence, the integral $I_\pi(\mathbf{x_A}, \mathbf{x_B}, k)$ is in a suitable

form for the application of the stationary phase approximation, and moreover

$$\begin{aligned}\int_{\pi}^{3\pi/2} f(t)e^{ik\phi(t)}\,dt &= \left(\int_{\pi}^{3\pi/2} f(t)e^{-ik\phi(t)}\,dt\right)^{*} \\ &= \left(\int_{\pi}^{3\pi/2} f(t)e^{ik\phi^{-}(t)}\,dt\right)^{*} \\ &= I_{\pi}^{*}(\mathbf{x_A},\mathbf{x_B},k)\,,\end{aligned}$$

where $(\cdot)^*$ denotes complex conjugation, so that the sign of the phase is recovered. In consequence, the original integral can be expressed as

$$I(\mathbf{x_A},\mathbf{x_B},k) = 2\,I_0(\mathbf{x_A},\mathbf{x_B},k) + 2\,I_{\pi}^{*}(\mathbf{x_A},\mathbf{x_B},k)\,, \tag{3.7.11}$$

where each of the integrals $I_0(\mathbf{x_A},\mathbf{x_B},k)$ and $I_\pi(\mathbf{x_A},\mathbf{x_B},k)$, defined in equations (3.7.7) and (3.7.10) respectively, is in a form suitable to be approximated by the stationary phase method. The approximation to the integral $I(\mathbf{x_A},\mathbf{x_B},k)$ will comprise of the sum of the approximations to each of the integrals on the right hand side of equation (3.7.11).

The stationary phase approximation to $I_0(\mathbf{x_A},\mathbf{x_B},k)$ is considered first, corresponding to the stationary point of the phase at $t=0$ (i.e. $\mathbf{x}'(0)=[r,0]$), noting that $2I_0(\mathbf{x_A},\mathbf{x_B},k)$ corresponds to integrating along the half boundary from $t=-\pi/2$ to $t=\pi/2$. Revisiting the conditions (i)-(viii) laid out in Section 3.2, we note that $a=0$ is a minimum. Furthermore, $b=\frac{\pi}{2}$ and using equation (3.5.11) yields

$$\phi'(b) = \phi'\left(\tfrac{\pi}{2}\right) = \frac{2\,rd}{\sqrt{r^2+d^2}} \neq 0\,.$$

so that the functions $P_m(t)$ given by equation (3.2.7) are well defined. Furthermore, we have by equation (3.5.11) and the argument under equation (3.5.12) that $\phi'(t) > 0$ for $t \in (0,b)$ (as $\sin(t) > 0$ in this interval) and hence $\phi(t)$ is strictly increasing in this open interval as required. Finally, as per the earlier analysis, the arguments of the radicals in expression (3.5.7) for $\phi(t)$ are bounded away from zero, so that each radical function is infinitely differentiable. Hence a series expansion for $\phi(t)$ as defined by (3.5.7) may be taken around $t=0$.

Hence, using equation (B.1.1) and definitions (3.2.3) to (3.2.10) , as well as the formula for the gamma function with positive half-integer argument (see for example Section 8.339

in Gradshteyn and Ryzhik (2014))

$$\Gamma\left(\tfrac{n}{2}\right) = \frac{\sqrt{\pi}}{2^{\frac{n-1}{2}}}(n-2)!!\,,$$

where $(\cdot)!!$ denotes the double factorial, the $n^{\text{th}}$ order stationary phase approximation of $I_{0^+}(\mathbf{x_A}, \mathbf{x_B}, k)$ is given by

$$I_0(\mathbf{x_A}, \mathbf{x_B}, k) = A_n(k) - B_m(k) + \delta_{mn}(k) - \epsilon_{mn}(k)$$

with the stationary phase approximation given by

$$I_0(\mathbf{x_A}, \mathbf{x_B}, k) \approx A_n(k) - B_m(k)\,, \tag{3.7.12}$$

with

$$A_n(k) = e^{-2d\,ik}\sqrt{\pi}\sum_{j=0}^{n-\nu} e^{(j+1)\frac{\pi}{4}i}\,\frac{(j-1)!!}{\sqrt{2^j k^{j+1}}}\,a_j\,, \tag{3.7.13}$$

and

$$B_m(k) = e^{ik}\sum_{j=0}^{m-1} P_j\left(\tfrac{\pi}{2}\right)\left(\frac{i}{k}\right)^{j+1}, \tag{3.7.14}$$

where $\phi\left(\frac{\pi}{2}\right) = 0$ has been used, and the error terms are given by

$$\delta_{mn}(k) = \left(\frac{i}{k}\right)^m \int_0^{\pi/2} e^{ik\phi(t)} Q'_{mn}(t)\,dt \tag{3.7.15}$$

and

$$\epsilon_{mn}(k) = e^{-2dik}\sum_{j=0}^{n-1} e^{(j+1)\frac{\pi}{4}i}\,\frac{\Gamma\left(\frac{j+1}{2}\right)}{\Gamma\left(\frac{j+1}{2}-m\right)}\Gamma\left(\tfrac{j+1}{2}-m,\,-2d\,ik\right)\frac{a_j}{k^{\frac{j+1}{2}}}\,, \tag{3.7.16}$$

with $\phi(t)$ given by (3.5.7), $2m-1 \le n < 2(m+1)$ according to (3.2.5), and $\nu = 1$ unless $n = 2m-1$, in which case $\nu = 0$ (see (3.2.6)). The total error is given using the triangle inequality as

$$|\delta_{mn}(k) - \epsilon_{mn}(k)| \le |\delta_{mn}(k)| + |\epsilon_{mn}(k)| \tag{3.7.17}$$

Consider now the approximation for $n = 1$ and $m = 1$ (noting that for this choice of $n$ and

$m$ we have $\nu = 0$ according to the restriction given in (3.2.5)) and $b = \pi/2$. Then we have

$$\begin{aligned} A_1(k) &= \sqrt{\frac{\pi}{4kd}} e^{i\left(\frac{\pi}{4}-2kd\right)}\,, \\ B_1(k) &= \frac{i}{2d\,k}\,, \\ \delta_{11}(k) &= \frac{i}{k}\int_0^{\pi/2} e^{ik\phi(t)} Q_{11}'(t)\,dt\,, \\ \epsilon_{11}(k) &= \frac{1}{4\sqrt{kd}}\, e^{i\left(\frac{\pi}{4}-2kd\right)} \Gamma\left(-\frac{1}{2},\, -2kdi\right)\,, \end{aligned} \tag{3.7.18}$$

where the function $Q_{11}'(t)$ is the derivative of $Q_{11}(t)$ with respect to $t$, and $Q_{11}(t)$ is defined according to equation (3.2.11) as

$$Q_{11}(t) = \frac{f(t)}{\phi'(t)} - \frac{1}{2\sqrt{d(\phi(t)+2d)}}\,, \tag{3.7.19}$$

with $f(t)/\phi'(t)$ given explicitly by

$$\frac{f(t)}{\phi'(t)} = \frac{\{\,(r^2+d^2)^2 - 4r^2d^2\cos^2(t)\,\}^{\frac{1}{4}}}{d\sin(t)\left(\sqrt{r^2-2\,rd\cos(t)+d^2}+\sqrt{r^2+2\,rd\cos(t)+d^2}\right)}\,. \tag{3.7.20}$$

Hence, we have the following exact decomposition,

$$I_0(\mathbf{x_A}, \mathbf{x_B}, k) = A_1(k) - B_1(k) + \delta_{11}(k) - \epsilon_{11}(k)\,.$$

Therefore the stationary phase approximation to the interferometric integral (3.7.7) is given by the difference

$$I_0(\mathbf{x_A}, \mathbf{x_B}, k) \approx A_1(k) - B_1(k) = \frac{1}{\sqrt{k}}\sqrt{\frac{\pi}{4d}} e^{i\left(\frac{\pi}{4}-2kd\right)} - \frac{i}{2d\,k}\,. \tag{3.7.21}$$

Moreover, the error bounds for this approximation are given by (B.1.14) and (B.1.12), yield-

ing for the case at hand

$$|\delta_{11}(k)| \leq \frac{1}{k} \int_0^{\frac{\pi}{2}} |Q'_{11}(t)|\, dt \tag{3.7.22}$$

and

$$|\epsilon_{11}(k)| \leq \frac{1}{4\sqrt{2}\, d^2\, k^2}\,, \tag{3.7.23}$$

Note that all terms depend on the inter-receiver distance $2d$ (in the case of $\delta_{11}(k)$, this dependence is implicit through the function $Q_{11}(t)$ defined in (3.7.19)). This dependence is not made explicit in the notation for simplicity's sake, and the dependence on the inter-receiver distance is introduced explicitly again once the final error bounds have been derived. The bound for the error term $\epsilon_{11}(k)$ given is given explicitly in (3.7.23). It decreases with $k^2$, which agrees with the physical intuition that the stationary phase approximation is better at higher frequencies. It also decreases with the square of the inter-receiver distance $4d^2 = |\mathbf{x_A} - \mathbf{x_B}|^2$. On the other hand, the bound for the error term $\delta_{11}(k)$ given in (3.7.22) decreases with $k$, in continued agreement with the physical intuition that the stationary phase approximation improves at higher frequencies. However, this bound is not explicit, and as previously discussed the $\delta_{11}(k)$ term itself is difficult to calculate numerically as the integrand is highly oscillatory. Hence, we aim to derive an explicit expression for this bound. In order to to this consider the the sign of $Q'_{11}(t)$ on the interval $(0, \frac{\pi}{2})$. Taking a derivative of equation (3.7.19) results in

$$Q'_{11}(t) = \frac{f'(t)\phi'(t) - f(t)\phi''(t)}{\phi'(t)^2} + \frac{d\phi'(t)}{4\sqrt{d^3(\phi(t) + 2d)^3}}\,,$$

and direct evaluation shows that this derivative is non negative on the interval $t \in (0, \frac{\pi}{2})$. Therefore $|Q'_{11}(t)| = Q'_{11}(t)$ and integrating over $t \in (0, \frac{\pi}{2})$ we have

$$\int_0^{\pi/2} |Q'_{11}(t)|\, dt = \int_0^{\pi/2} Q'_{11}(t)\, dt = Q_{11}(\pi/2) - Q_{11}(0)\,. \tag{3.7.24}$$

To show that $Q_{11}(t)$ is well-defined at $t = 0$, consider the expansion of $h(t) = f(t)/\phi'(t)$ around $a = 0$ given in (3.3.6), together with (3.3.7). We have for small $t$

$$h(t) \approx \frac{\sqrt{r^2 - d^2}}{2\, rd}\frac{1}{t} + \frac{r^4 + d^2r^2 + 4d^4}{12\, rd\sqrt{(r^2 - d^2)^3}}\, t + O(t^3)\,.$$

On the other hand, by equation (3.5.25) and using the previously derived value for $\phi_2$ we

have for small $t$

$$\phi(t) + 2d \approx \frac{r^2 d}{r^2 - d^2}\, t^2 - r^2 d\, \frac{r^4 + 7\, r^2 d^2 + 4\, d^4}{12(r^2 - d^2)^3}\, t^4 + O(t^6)\,,$$

so that taking the composition of this approximation to $\phi(t) + 2d$ and the series expansion for $(1 - t^2)^{-\frac{1}{2}}$ the following approximation is derived

$$\frac{1}{2\sqrt{d(\phi(t) + 2d)}} \approx \frac{\sqrt{r^2 - d^2}}{2\, rd}\, \frac{1}{t} + \frac{r^4 + 7r^2 d^2 + 4d^4}{48 rd \sqrt{(r^2 - d^2)^3}}\, t + O(t^3)$$

Substituting these approximations into the right-hand side of (3.7.19) and simplifying we have

$$Q_{11}(t) \approx \frac{r^4 - r^2 d^2 + 4d^4}{16 rd \sqrt{(r^2 - d^2)^3}}\, t + O(t^3)\,, \qquad t \ll 1\,. \tag{3.7.25}$$

Figure 3.20 shows a an example of the function $Q_{11}(t)$ for a source boundary radius of $r = 1000$ m and an inter-receiver distance of 200 m (i.e. $d = 100$), and the linear term in the right hand side of the approximation of $Q_{11}(t)$ for small $t$ given in (3.7.25). Furthermore, a high order approximation to $Q_{11}(t)$ using the asymptotic coefficient formula derived in Section 3.3 is depicted with yellow dashes, exhibiting excellent agreement. This approximation was used in the numerical implementation of the bound for the error term $\delta_{11}(k)$, given in (3.7.22) and used to verify the explicit bound calculated below in (3.7.26). Nineteen coefficients calculated with formula (3.3.2) were taken to ensure the integral in (3.7.22) could be numerically estimated with sufficient accuracy.

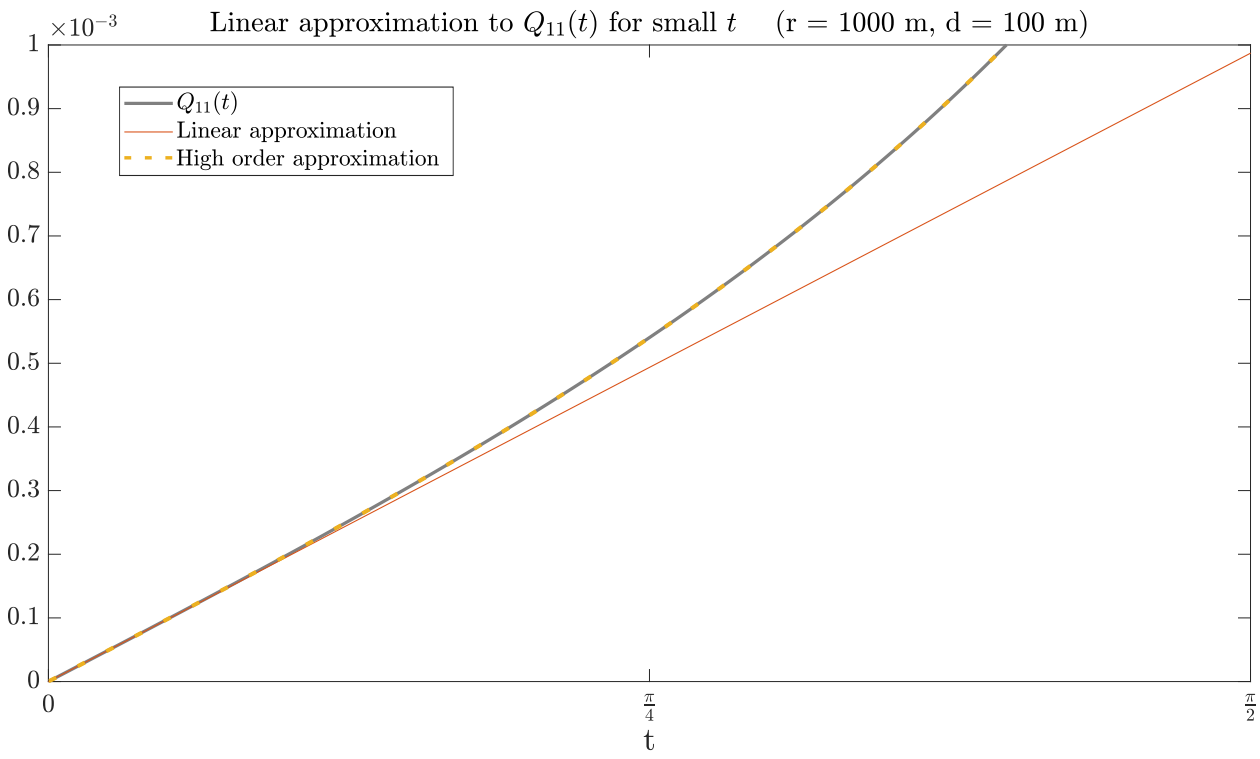


**Figure 3.20:** Comparison of $Q_{11}(t)$ in grey, its linear approximation (3.7.25) in orange, and the high order approximation used in the numerical implementation, using the coefficients derived in Section 3.3, for $r = 1000$ m and $d = 100$ m.

The approximation given in (3.7.25) allows us to conclude that

$$Q_{11}(t) \underset{t \to 0^+}{\longrightarrow} 0\,,$$

and this behaviour can be plainly appreciated in Figure 3.20. Hence, using equations (3.7.24) and (3.7.19) , noting that direct evaluation shows that

$$Q_{11}(\pi/2) = \frac{\sqrt{2}-1}{2\sqrt{2}\,d}$$

the bound for the error term $\delta_{11}^0(k)$ can be given explicitly by

$$|\delta_{11}(k)| \leq \frac{\sqrt{2}-1}{2\sqrt{2}d\,k}\,. \tag{3.7.26}$$

In conclusion, the stationary phase approximation to $I_0(\mathbf{x_A}, \mathbf{x_B}, k)$ is

$$I_0(\mathbf{x_A}, \mathbf{x_B}, k) \approx A_1(k) - B_1(k) = \frac{1}{\sqrt{k}}\sqrt{\frac{\pi}{4d}}e^{i\left(\frac{\pi}{4}-2kd\right)} - \frac{i}{2d\,k}\,,$$

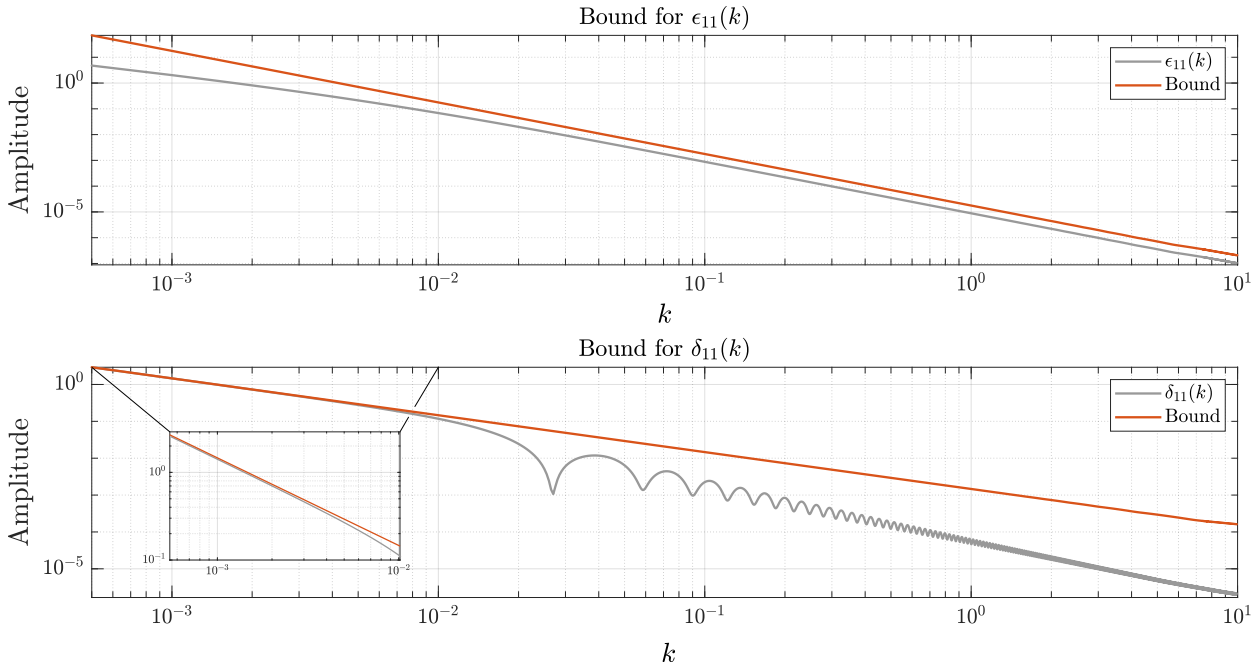


**Figure 3.21:** Comparison of the numerically calculated $\epsilon_{11}(k)$ in grey to the bound (3.7.23) in orange (**top**), and the numerically calculated $\delta_{11}(k)$ in grey to the bound (3.7.26) in orange (**top**) for an inter-receiver distance of 200 m (i.e. $d = 100$). The inset in the bottom panel shows the the bound in detail for low values of $k$

and noting that $2d = |\mathbf{x_A} - \mathbf{x_B}|$ we have

$$I_0(\mathbf{x_A}, \mathbf{x_B}, k) \approx \frac{1}{\sqrt{k}} \sqrt{\frac{\pi}{2|\mathbf{x_A} - \mathbf{x_B}|}} e^{i\left(\frac{\pi}{4} - |\mathbf{x_A} - \mathbf{x_B}|k\right)} - \frac{i}{k\,|\mathbf{x_A} - \mathbf{x_B}|}\,, \tag{3.7.27}$$

Figure 3.22 illustrates the approximation (3.7.27) for an inter-receiver distance of $|\mathbf{x_A} - \mathbf{x_B}| = 50$ m as a function of the wavenumber $k$ in the range $0 < k \leq 10$. The integral $I_0(\mathbf{x_A}, \mathbf{x_B}, k)$ given by (3.7.7) was numerically calculated for reference, and the approximation (3.7.21) was calculated directly. In this Figure, a logarithmic scale is used in the horizontal axis to illustrate the behaviour of the approximation across different scales of $k$. As expected, the error is visible for lower values of $k$, ranging from $10^{-3}$ to approximately $0.5 \times 10^{-3}$. On the approximation is very good for larger values of $k$. The particular cut-off value of $k$ that ensures a good approximation depends on the inter-receiver distance, and this is explored more carefully in equation (3.7.30) below, as well as the accompanying remarks.

Note that the integral $I_0(\mathbf{x_A}, \mathbf{x_B}, k)$ is highly oscillatory and therefore challenging to a calculate numerically with accuracy. To address this, a trapezoidal rule was implemented with increasingly fine partitions of the domain while monitoring the error to avoid introducing numerical instability due to a too-fine partition. On the other hand, the value of the

wavenumber $k$ ranged from $10^{-3}$ to $10^{1}$, which is realistic for applications while avoiding a frequency regime so high that numerical integration of $I_0(\mathbf{x_A}, \mathbf{x_B}, k)$ became unfeasible.

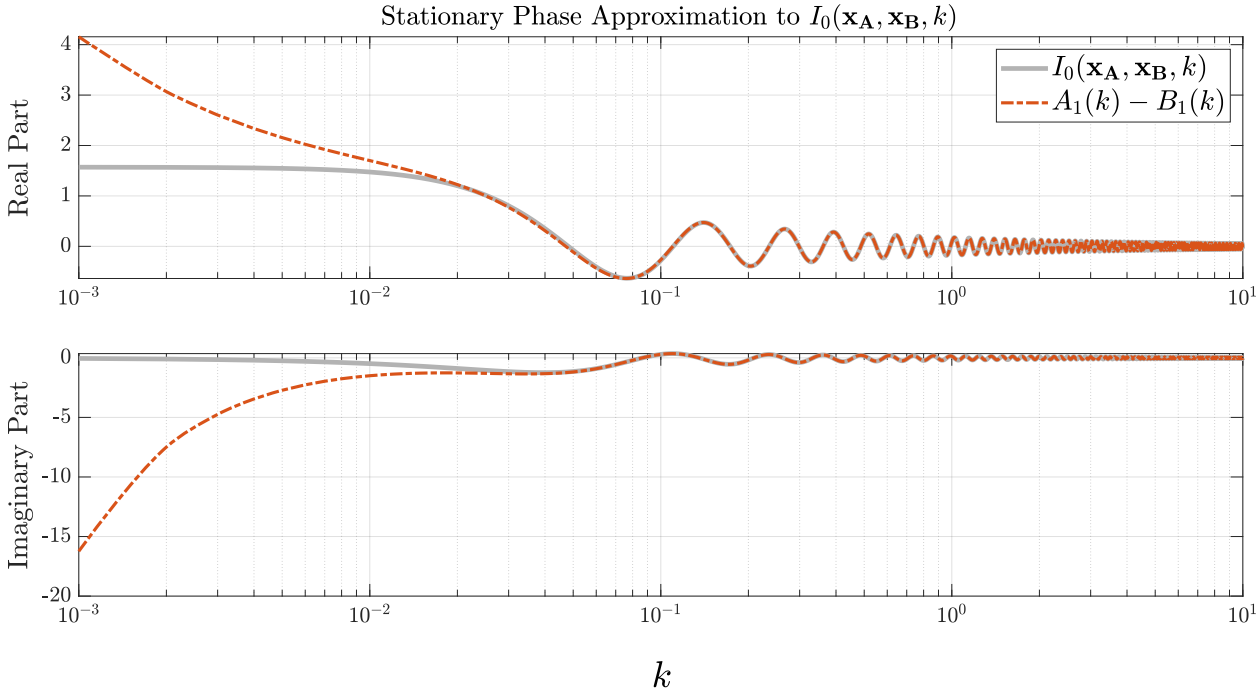


**Figure 3.22:** Comparison of the real (**top**) and imaginary (**bottom**) parts of the numerically calculated value of $I_0(\mathbf{x_A}, \mathbf{x_B}, k)$ in grey, and the stationary phase approximation given in (3.7.27) in orange dashes, as a function of the wavenumber $k$. An inter-receiver distance of $|\mathbf{x_A} - \mathbf{x_B}| = 50$ m was used. Logarithmic scale is used in the horizontal $k$-axis. The approximation was calculated for $0 < k \leq 10$.

Figure 3.23 illustrates the same approximation and parameters for the amplitude and the phase of $I_0(\mathbf{x_A}, \mathbf{x_B}, k)$ compared to the amplitude and phase of the stationary phase approximation (3.7.27). A logarithmic scale is used in both axes to illustrate the behaviour of the stationary phase approximation across different scales of the wavenumber $k$. Note that the approximation to the phase becomes accurate very rapidly The bounds given in (3.7.22) and (3.7.23) are used to define the total error bound for the stationary phase approximation to the interferometric integral $I_0(\mathbf{x_A}, \mathbf{x_B}, k)$ as

$$| I_0(\mathbf{x_A}, \mathbf{x_B}, k) - (A_1(k) - B_1(k)) | \leq E_0(\mathbf{x_A}, \mathbf{x_B}, k) \tag{3.7.28}$$

where the bound on the right hand side is given by (3.7.17) as the sum of the bounds (3.7.23) and (3.7.26)

$$E_0(\mathbf{x_A}, \mathbf{x_B}, k) = \frac{1}{\sqrt{2}} \left( \frac{\sqrt{2} - 1}{k\,|\mathbf{x_A} - \mathbf{x_B}|} + \frac{1}{k^2\,|\,\mathbf{x_A} - \mathbf{x_B}|^2} \right), \tag{3.7.29}$$

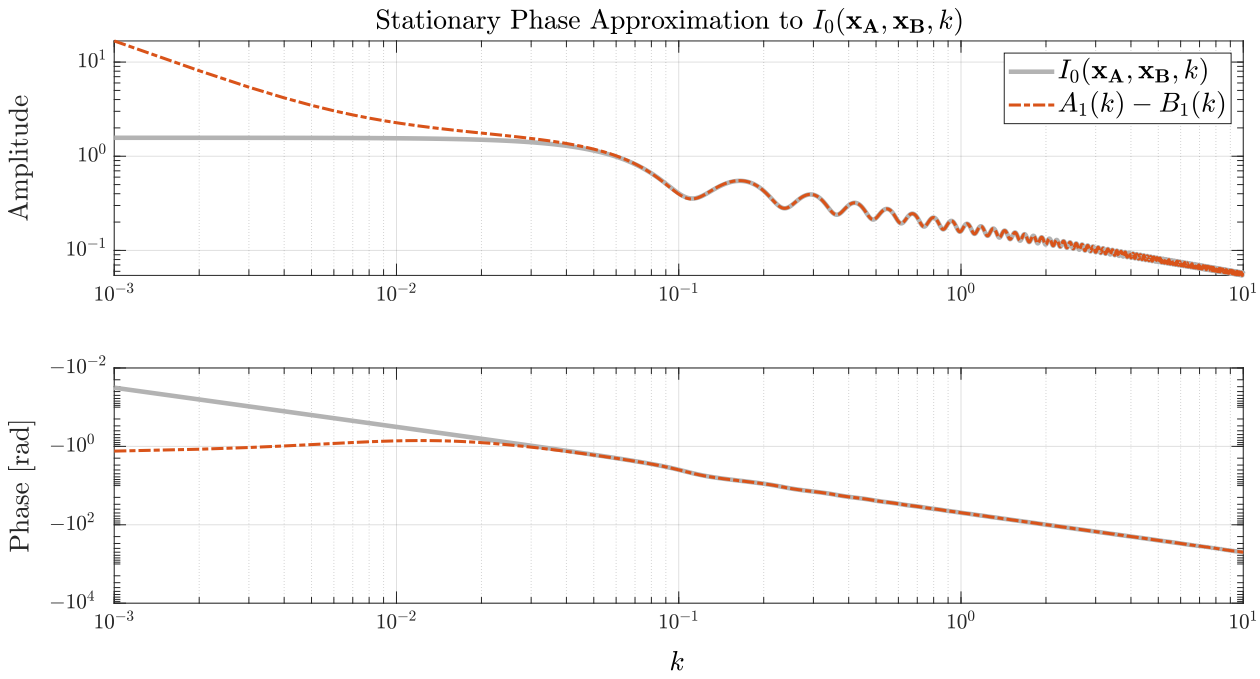


**Figure 3.23:** Comparison of the amplitude (**top**) and phase (**bottom**) of the numerically calculated value of $I_0(\mathbf{x_A}, \mathbf{x_B}, k)$ in grey, and the stationary phase approximation given in (3.7.27) in orange dashes, as a function of the wavenumber $k$. An inter-receiver distance of $|\mathbf{x_A} - \mathbf{x_B}| = 50$ m was used. Logarithmic scale is used in both axes. The approximation was calculated for $0 < k \leq 10$.

noting that $2d = |\mathbf{x_A} - \mathbf{x_B}|$ has been used. Figure 3.24 compares the direct error calculated directly from the right hand side of (3.7.28) with the direct implementation of the error bound $E_0(\mathbf{x_A}, \mathbf{x_B}, k)$ given by (3.7.29). The direct error and the bound were calculated as a function of the wavenumber $k$, for $0 < k \leq 10$, and a fixed inter-receiver distance of $|\mathbf{x_A} - \mathbf{x_B}| = 50$ m. A logarithmic scale has been used in both axes to illustrate the behaviour of the error and its bound across different scales of the wavenumber $k$. Using the error bound $E_0(\mathbf{x_A}, \mathbf{x_B}, k)$ given in equation (3.7.29) we find that for a wavenumber $k$ and $n > 0$, the inter-receiver distance

$$|\mathbf{x_A} - \mathbf{x_B}| = \frac{\sqrt{3 + (2^{n+2} - 1)\sqrt{2}} + \sqrt{2} - 1}{2^{n+1}\sqrt{2}\, k} \tag{3.7.30}$$

ensures that the error in the stationary phase approximation to $I_0(\mathbf{x_A}, \mathbf{x_B}, k)$ satisfies

$$| I_0(\mathbf{x_A}, \mathbf{x_B}, k) - (A_1(k) - B_1(k)) | \leq 2^n .$$

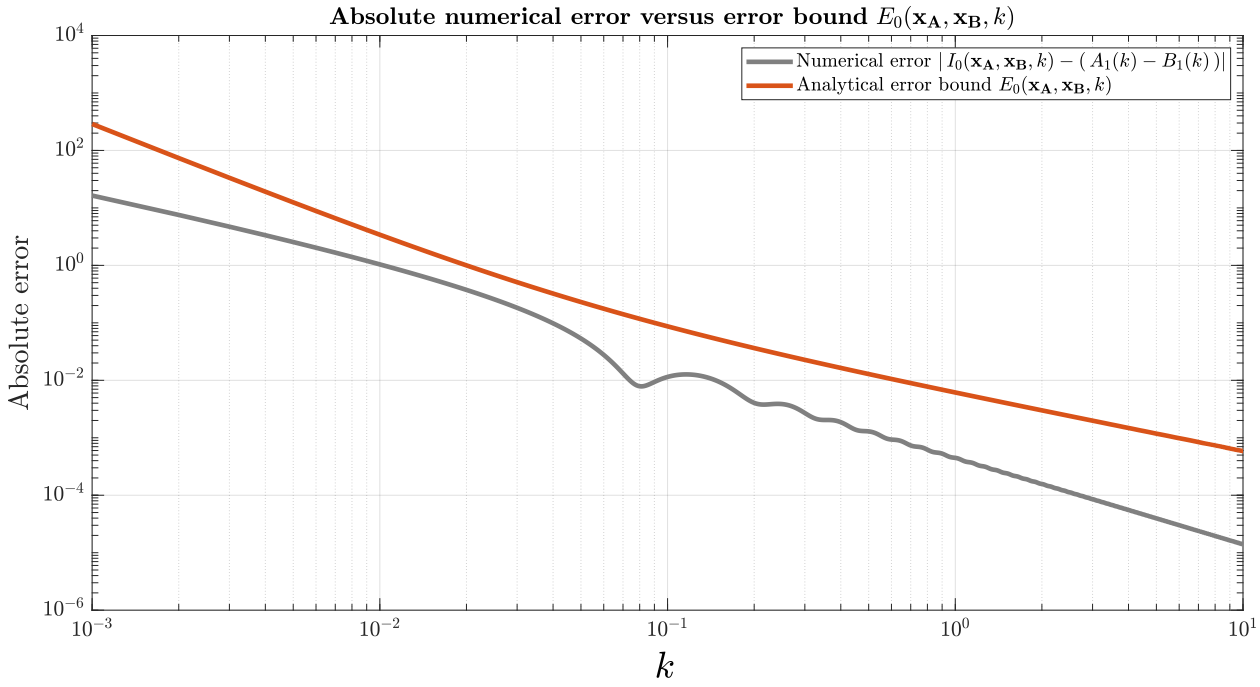


**Figure 3.24:** Comparison of the direct error $\left| I_0(\mathbf{x_A}, \mathbf{x_B}, k) - \left(A_1^0(k) - B_1^0(k)\right) \right|$ in grey with the bound $E_0(\mathbf{x_A}, \mathbf{x_B}, k)$ given in equation (3.7.29) on orange, as a function of the wavenumber $k$ for $0 < k \leq 10$ and a fixed inter-receiver distance of $|\mathbf{x_A} - \mathbf{x_B}| = 50$ m.

For small values of $n$ the distance (3.7.30) can be estimated by

$$|\mathbf{x_A} - \mathbf{x_B}| = (\, 1 + Cn\,)\,\frac{1}{k} \tag{3.7.31}$$

where $C = (\sqrt{2} - 2)\log(2)$. This approximation was derived by taking a Taylor series expansion of (3.7.30) in terms of $n$ around $n = 0$, with the Lagrange form of the remainder no larger than $n^2/4$, so that the error incurred by using the approximate distance (3.7.31) instead of the exact expression (3.7.30) is no larger than $n^2/4$, ensuring that the total error of the stationary phase approximation will be no larger than $2^n$ for small $n$.

We now consider the stationary phase approximation to the integral $I_\pi(\mathbf{x_A}, \mathbf{x_B}, k)$, with the same amplitude function $f(t)$ as defined in (3.7.6) but phase function $\phi^-(t) = -\phi(t)$, where $\phi(t)$ is given by (3.5.7). Recall the definition of $I_\pi(\mathbf{x_A}, \mathbf{x_B}, k)$ given in (3.7.10), and

consider the change of variable $t = \eta - \pi$, then

$$\begin{aligned} I_\pi(\mathbf{x_A}, \mathbf{x_B}, k) &= \int_\pi^{3\pi/2} f(t) e^{ik\phi^-(t)}\, dt \\ &= \int_0^{\pi/2} f(\eta - \pi) e^{ik\phi^-(\eta-\pi)} d\eta \\ &= \int_0^{\pi/2} f(\eta) e^{ik\phi^-(\eta-\pi)} d\eta\,, \end{aligned}$$

where the $\pi$-periodicity of $f(t)$ has been used. Moreover, using the property $\cos(t) = -\cos(t-\pi)$ we have

$$\begin{aligned} \phi^-(\eta - \pi) &= -\phi(\eta - \pi) \\ &= -\left(\sqrt{r^2 - 2\,rd\cos(\eta-\pi) + d^2} - \sqrt{r^2 + 2\,rd\cos(\eta-\pi) + d^2}\right) \\ &= -\sqrt{r^2 + 2\,rd\cos(\eta) + d^2} + \sqrt{r^2 - 2\,rd\cos(\eta) + d^2} \\ &= \phi(\eta)\,. \end{aligned}$$

Therefore

$$I_\pi(\mathbf{x_A}, \mathbf{x_B}, k) = \int_0^{\pi/2} f(\eta) e^{ik\phi(\eta)} d\eta = I_0(\mathbf{x_A}, \mathbf{x_B}, k)\,,$$

so that using equation (3.7.11) we have

$$\begin{aligned} I(\mathbf{x_A}, \mathbf{x_B}, k) &= 2\, I_0(\mathbf{x_A}, \mathbf{x_B}, k) + 2\, I_\pi^*(\mathbf{x_A}, \mathbf{x_B}, k) \\ &= 2\left(I_0(\mathbf{x_A}, \mathbf{x_B}, k) + I_0^*(\mathbf{x_A}, \mathbf{x_B}, k)\right) \\ &= 4\mathrm{Re}\left\{I_0(\mathbf{x_A}, \mathbf{x_B}, k)\right\}\,, \end{aligned}$$

where $\mathrm{Re}\{\cdot\}$ denotes the real part of the argument. Hence, using equation (3.7.12) the

stationary phase approximation to the integral $I(\mathbf{x_A}, \mathbf{x_B}, k)$ is given by

$$I(\mathbf{x_A}, \mathbf{x_B}, k) \approx 4\mathrm{Re}\left\{ e^{-2d\,ik}\sqrt{\pi}\sum_{j=0}^{n-\nu} e^{(j+1)\frac{\pi}{4}i}\,\frac{(j-1)!!}{\sqrt{2^j k^{j+1}}}\,a_j - \right. \\ \left. - e^{ik}\sum_{j=0}^{m-1} P_j\left(\frac{\pi}{2}\right)\left(\frac{i}{k}\right)^{j+1}\right\} \tag{3.7.32}$$

with the error given using equations (3.7.15) and (3.7.16) by

$$4\mathrm{Re}\left\{\delta_{mn}(k)\ -\epsilon_{mn}(k)\right\} = 4\mathrm{Re}\left\{\left(\frac{i}{k}\right)^m \int_0^{\pi/2} e^{ik\phi(t)} Q'_{mn}(t)\,dt - \right. \\ \left. - e^{-2d\,ik}\sum_{j=0}^{n-1} e^{(j+1)\frac{\pi}{4}i}\frac{\Gamma\left(\frac{j+1}{2}\right)}{\Gamma\left(\frac{j+1}{2}-m\right)}\Gamma\left(\frac{j+1}{2}-m, -ik(2d)\right)\frac{a_j}{k^{\frac{j+1}{2}}}\right\}.$$

An error bound for this approximation can be derived directly from the bounds given in (B.1.12) (B.1.14), and using the triangle inequality to derive

$$|4\mathrm{Re}\left\{\delta_{mn}(k) - \epsilon_{mn}(k)\right\}| \le \frac{8}{k^{m+1}}\sum_{j=0}^{n-1}\frac{\Gamma\left(\frac{j+1}{2}\right)}{\left|\Gamma\left(\frac{j+1}{2}-m\right)\right|}\frac{|a_j|}{|\mathbf{x_A}-\mathbf{x_B}|^{(m+1)-(j+1)/2}} \\ + \frac{4}{k^m}\int_0^{\pi/2}|Q'_{mn}(t)|\,dt\,.$$

A tighter bound can be derived for the approximation derived for $n = m = 1$, noting that in that case the term $B_1(k)$ given in (3.7.18) is purely imaginary and hence disappears when the real part is taken, so that using equation (3.7.21)

$$\begin{aligned} I(\mathbf{x_A}, \mathbf{x_B}, k) &\approx 4\mathrm{Re}\left\{A_1(k) - B_1(k)\right\} \\ &= 4\mathrm{Re}\left\{\frac{1}{\sqrt{k}}\sqrt{\frac{\pi}{4d}}e^{i\left(\frac{\pi}{4}-2kd\right)} - \frac{i}{2d\,k}\right\} \\ &= 4\mathrm{Re}\left\{\frac{1}{\sqrt{k}}\sqrt{\frac{\pi}{4d}}e^{i\left(\frac{\pi}{4}-2kd\right)}\right\} \end{aligned} \tag{3.7.33}$$

with the total error given by

$$4\mathrm{Re}\left\{\delta_{11}(k) - \epsilon_{11}(k)\right\}$$

and therefore, using the triangle inequality and the bound (3.7.29) for $|\delta^0_{11}(k)| + |\epsilon^0_{11}(k)|$ we

have the bound

$$|4\mathrm{Re}\left\{\delta_{11}(k) - \epsilon_{11}(k)\right\}| \leq 4\, E_0(\mathbf{x_A}, \mathbf{x_B}, k)\,. \tag{3.7.34}$$

Figure 3.25 illustrates the approximation (3.7.33) as a function of the wavenumber $k$ in the range $0 < k \leq 10$. The integral $I_0(\mathbf{x_A}, \mathbf{x_B}, k)$ given by (3.7.7) was numerically calculated for reference, and the approximation (3.7.33) was implemented directly. A logarithmic scale is used in the horizontal axis to illustrate the behaviour of the approximation across different scales of $k$. As expected, the approximation is accurate for large values of $k$.

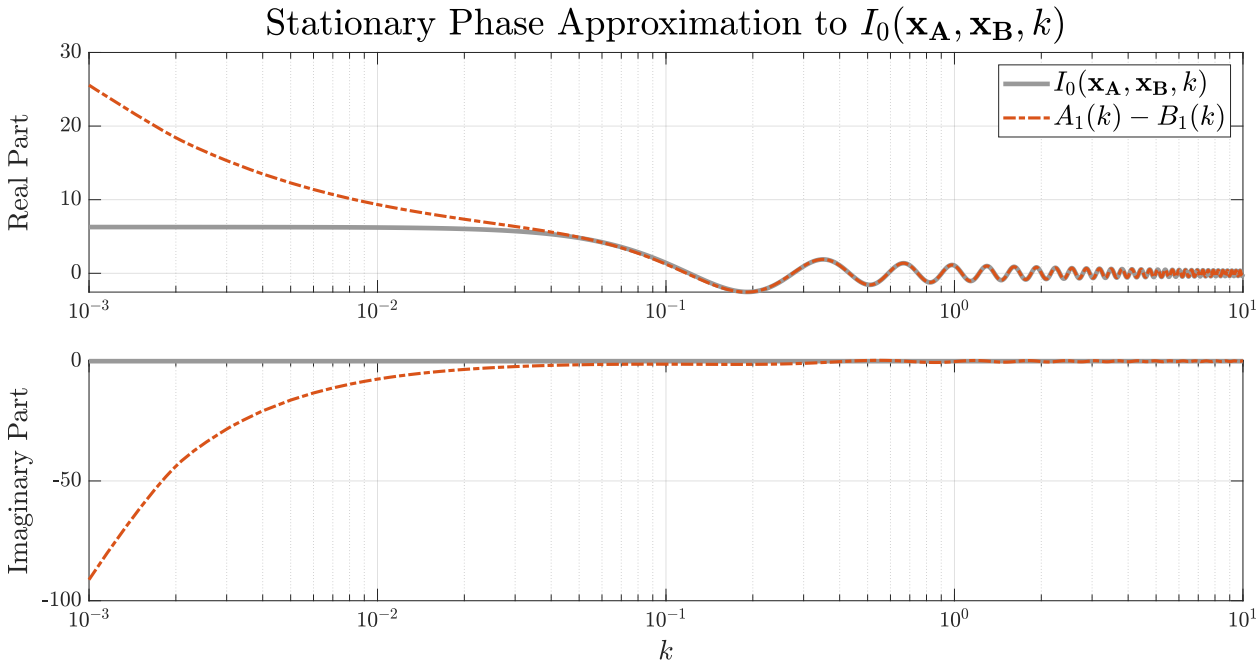


**Figure 3.25:** Comparison of the real (**top**) and imaginary (**bottom**) parts of $I(\mathbf{x_A}, \mathbf{x_B}, k)$ in grey, and the stationary phase approximation (3.7.33) in orange dashes, as a function of the wavenumber $k \in (0, 10)$. An inter-receiver distance of $|\mathbf{x_A} - \mathbf{x_B}| = 50$ m was used. Logarithmic scale is used in the horizontal $k$-axis.

Figure 3.26 illustrates the same approximation and parameters for the amplitude and the phase of $I_0(\mathbf{x_A}, \mathbf{x_B}, k)$ compared to the amplitude and phase of the stationary phase approximation (3.7.33). A logarithmic scale is used in both axes to illustrate the behaviour of the stationary phase approximation across different scales of the wavenumber $k$. Note that the approximation to the phase becomes accurate very rapidly

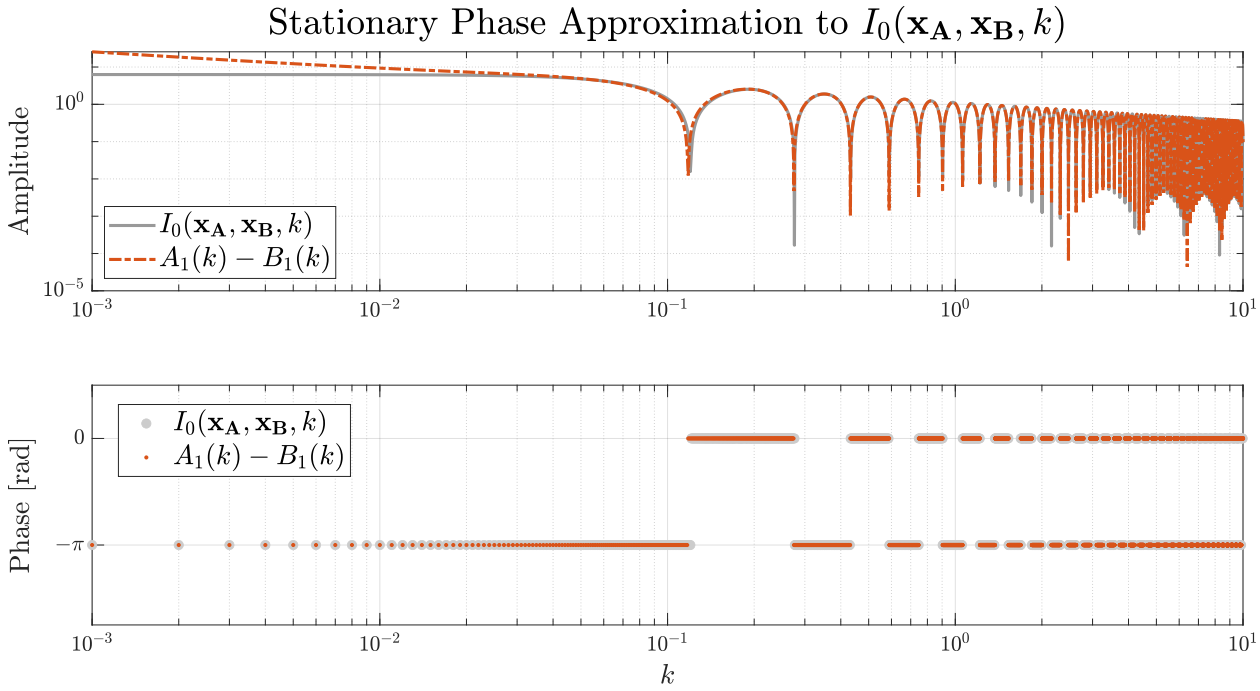


**Figure 3.26:** Comparison of the amplitude (**top**) and phase (**bottom**) of the numerically calculated value of $I(\mathbf{x_A}, \mathbf{x_B}, k)$ in grey, and the stationary phase approximation given in (3.7.33) in orange dashes, as a function of the wavenumber $k$. An inter-receiver distance of $|\mathbf{x_A} - \mathbf{x_B}| = 50$ m was used. Logarithmic scale is used in both axes. The approximation was calculated for $0 < k \leq 10$.

Figure 3.27 compares the error calculated directly from the right hand side of (3.7.28) with the numerical implementation of the error bound $E_0(\mathbf{x_A}, \mathbf{x_B}, k)$ given by (3.7.29). The direct error and the bound were calculated as a function of the wavenumber $k$, for $0 < k \leq 10$, and a fixed inter-receiver distance of $|\mathbf{x_A} - \mathbf{x_B}| = 50$ m. A logarithmic scale has been used in both axes to illustrate the behaviour of the error and its bound across different scales of the wavenumber $k$.

Regarding the relevance of the results presented in Figure 3.27 in realistic applications, recall Remark 2.2.1, where it is established that in common practical applications of active source interferometry, frequency regimes can vary for example from 5 Hz to 50 Hz. For medium speeds ranging from $c = 500$ m/s t0 $c = 5000$ m/s this results in a range of wavenumber values ranging from $k = 0.0063$ to $k = 0.6283$. This example illustrates, firstly, that the range of values taken for $k$ in this study (ranging from $10^{-3}$ to 10) encompasses realistic applications well; and secondly, that the amplitude error of order 10 observed in the top panel of Figure 3.27 for low values of $k$ is indeed relevant for these practical applications. On the other hand, the bottom panel of this Figure illustrates how well the interferometric estimate predicts the inter-receiver phase, even in low wavenumber regimes. This is consistent with the analytically derived stationary phase approximation (3.7.32), where examination

of the exponential term reveals a phase of $2dk = \omega|\mathbf{x_A} - \mathbf{x_B}|/c$, i.e. the inter-receiver travel time.

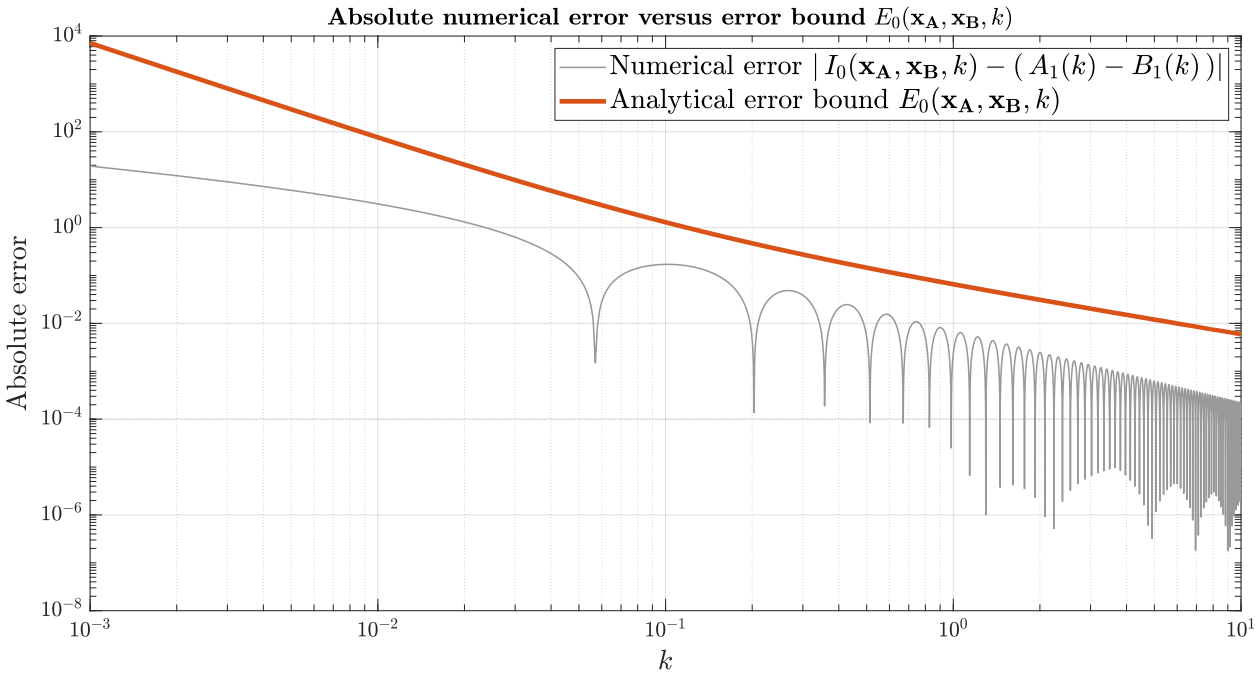


**Figure 3.27:** Comparison of the numerically calculated error $\left| \hat{I}(\mathbf{x_A}, \mathbf{x_B}, k) - 4\left(\hat{A}_1^0(k) - \hat{B}_1^0(k)\right) \right|$ in grey with the bound $4\,E_0(\mathbf{x_A}, \mathbf{x_B}, k)$ given in equation (3.7.34) on orange, as a function of the wavenumber $k$ for $0 < k \leq 10$ and a fixed inter-receiver distance of $|\mathbf{x_A} - \mathbf{x_B}| = 50$ m.

Finally, Figure 3.28 shows the waveforms $A_1(t)$ and $B_1(t)$ associated to the components $\hat{A}_1(k)$ and $\hat{B}_1(k)$ in the stationary phase approximation (3.7.33), obtained by numerical inverse Fourier transform. As discussed in Remark 3.2.1, the term $B_1(t)$, (or $\hat{B}_1(k)$ in the frequency domain) corresponds to the contribution from the endpoint $t = \pi/2$ of the interval of integration. In the parametrisation of the source boundary $S$ this source location corresponds to the point where the $y$-axis intersects the upper half of $S$, which is equidistant to each of the receivers $\mathbf{x_A}$ and $\mathbf{x_B}$ (see Figure 3.5), and hence the travel time from this source location to each of the receivers is the same. Recalling that the cross-correlation of these traces in the interferometric integrand yields the travel-time difference of the signal emitted from a source location to each receiver, we have that the endpoint contribution from the source location corresponding to $t = \pi/2$ is an arrival at time $t = 0$, which can be appreciated in the top and bottom panels of Figure 3.28, albeit with an almost negligible amplitude compared to the main inter-receiver arrival at $t = |\mathbf{x_A} - \mathbf{x_B}|/c$. This figure further illustrates that the stationary phase method approximates the phase of the inter-receiver Green's function well, but the amplitude is not accurately retrieved as shown by the insets in the top panel that compares the stationary phase approximation $A_1(t) - B_1(t)$ to

the true integral $I_0(\mathbf{x_A}, \mathbf{x_B}, t)$.

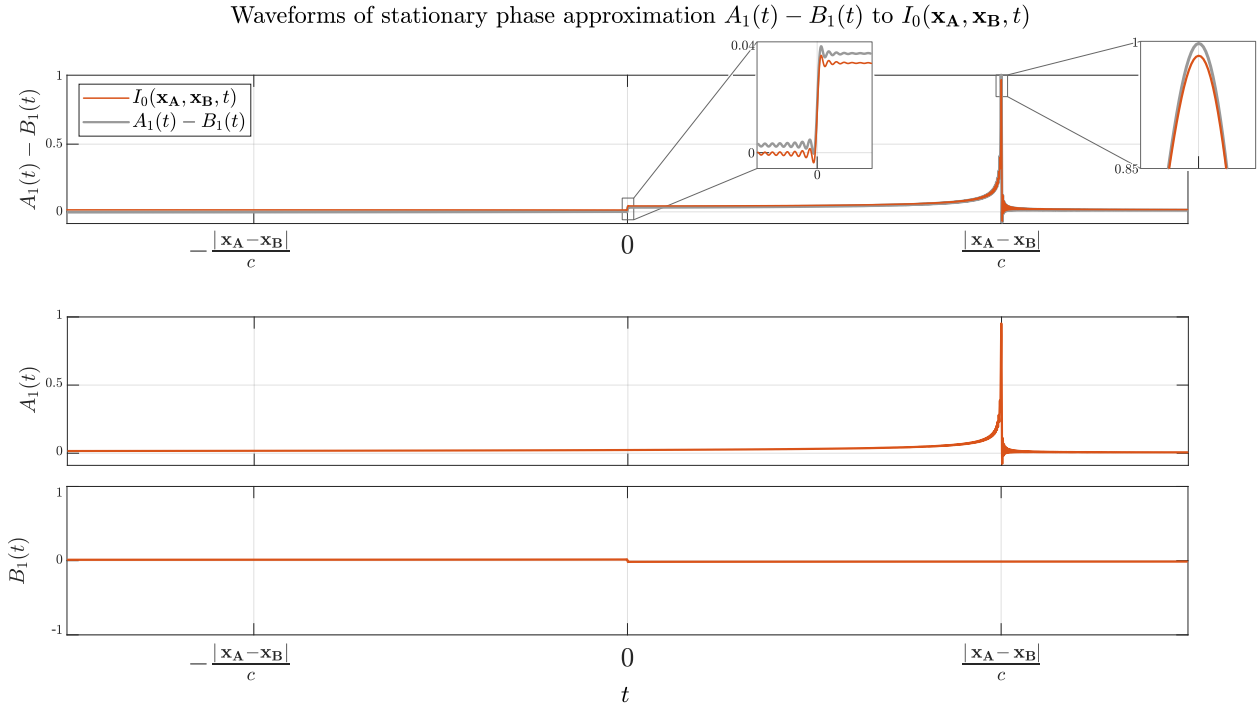


**Figure 3.28:** Illustration of the waveform associated with the monopole interferometric retrieval, given by the right hand side of equation (3.7.2) in grey and the stationary phase approximation given by (3.7.33) in orange. The horizontal axis corresponds ti time and the inter-receiver arrival time is labelled as $|\mathbf{x_A} - \mathbf{x_B}|/c$. The amplitude is normalised with respect to the amplitude of (3.7.2). The insets show detail at the main arrival and the endpoint effect corresponding to the term $B_1(t)$.

## 3.8 Discussion

The numerical and analytical results presented in this Chapter contribute a series of tools to quantify error and uncertainty introduced through the stationary phase approximation in wavefield interferometry.

The explicit formula derived in Section 3.3 for the asymptotic coefficients in the stationary phase approximation allow for accurate numerical implementation of the method and are indispensable for higher order approximations. In practical settings, the stationary phase approximation is applied by taking a neighbourhood of the source boundaries around the sources. The radius of this neighbourhood is linked to the aperture of the the Fresnel zones of the receiver array (van Kampen, 1958; Southwell, 1981), and potentially restricted by data availability and other practical concerns. As discussed in Section 3.2, the radius encompassed by the stationary phase approximation depends on the order $m$ of the approx-

imation, which is in turn directly limited by the differentiability of the amplitude of the cross-correlation integrand (see Figure 3.9 and accompanying Remark). Hence when the azimuthal inhomogeneities of source intensity along neighbourhoods of the stationary points on the boundary $S$ do not vary slowly, the stationary phase approximation is not appropriate and likely to introduce errors in the retrieval. Hence the accuracy of the stationary phase approximation is linked to the smoothness of the noise-field surrounding the receivers, modelled in this Chapter by the random field $\alpha$. When the Matérn covariance model is used, the smoothness parameter could therefore be used to estimate the reliability of the stationary phase approximate. This becomes apparent in the numerical study presented in Section 3.6.1. While the error $e_{\text{ph}}(\mathbf{x_A}, \mathbf{x_B}, k; \alpha)$ was proven to be of mean zero, we found its probability distribution oscillated between symmetric unimodal and bimodal behaviours, consistent with our findings in Chapter 2. The bimodal behaviour is striking in the sense that while the stationary phase estimator is unbiased, there are regimes of noise smoothness and correlation where a zero error is the least likely (namely low smoothness $\nu_\alpha$ and low correlation length $\rho_\alpha$), and where convergence to this mean would be slow. We showed that the variance of the noise needs to be very small to overcome the bimodality effect. While taking a full boundary integration could benefit from a very rough (noisy) field, if the integral over $S$ is interpreter as a spatial average, the stationary phase approximation loses that advantage through the restriction of the integral to the two stationary point locations. However, it continues to benefit from very large correlation lengths and very large smoothness, as in this case the difference between the values of the random field $\alpha$ at the stationary points is more likely to be small, so that appropriate phase cancellation occurs and one is more likely to be left with a purely (or nearly so) imaginary quantity, consistent with the homogeneous Green's function one expects to retrieve. The numerical study shows that the transition between unimodal and bimodal regimes happens at a critical value of the variance of the phase error (Figures 3.15 and 3.14). This error variance is encoded in the more general variance studied in Sections 3.5.2 and 3.6.3. The error variance is itself a predictor of uncertainty in the estimate, and for the Matérn-correlated log-normal scenario studied in Section 3.6.3 an explicit expression was given in terms of the Matérn covariance function defined in (2.4.4), which is in turn defined in terms of a modified Bessel function of the second kind, whose asymptotic behaviour with respect to the argument (which is inversely proportional to $\rho_\alpha$) and the smoothness parameter $\nu_\alpha$ is well known. For example, for $\nu_\alpha \gg 1$ we have[5]

$$K_{\nu_\alpha}(x) \sim \sqrt{\frac{\pi}{2\nu_\alpha}} \left( \frac{ex}{2\nu_\alpha} \right)^{\nu_\alpha}, \tag{3.8.1}$$

[5]This is a standard asymptotic result for the modified Bessel function of the second kind. See for example Section 10.41 of the Digital Library of Mathematical Functions.

so that the Matérn covariance function becomes

$$M(d;\,\rho_\alpha,\nu_\alpha) \sim \frac{2^{1-\nu_\alpha/2}}{\Gamma(\nu_\alpha)}\, e^{-\nu_\alpha}\sqrt{\pi}{\nu_\alpha}^{\nu_\alpha}\left(\frac{2r}{\rho_\alpha}\right)^{\nu_\alpha-1}.$$

As $\rho_\alpha \to \infty$, the Matérn covariance function grows unbounded (see Figure 3.29).

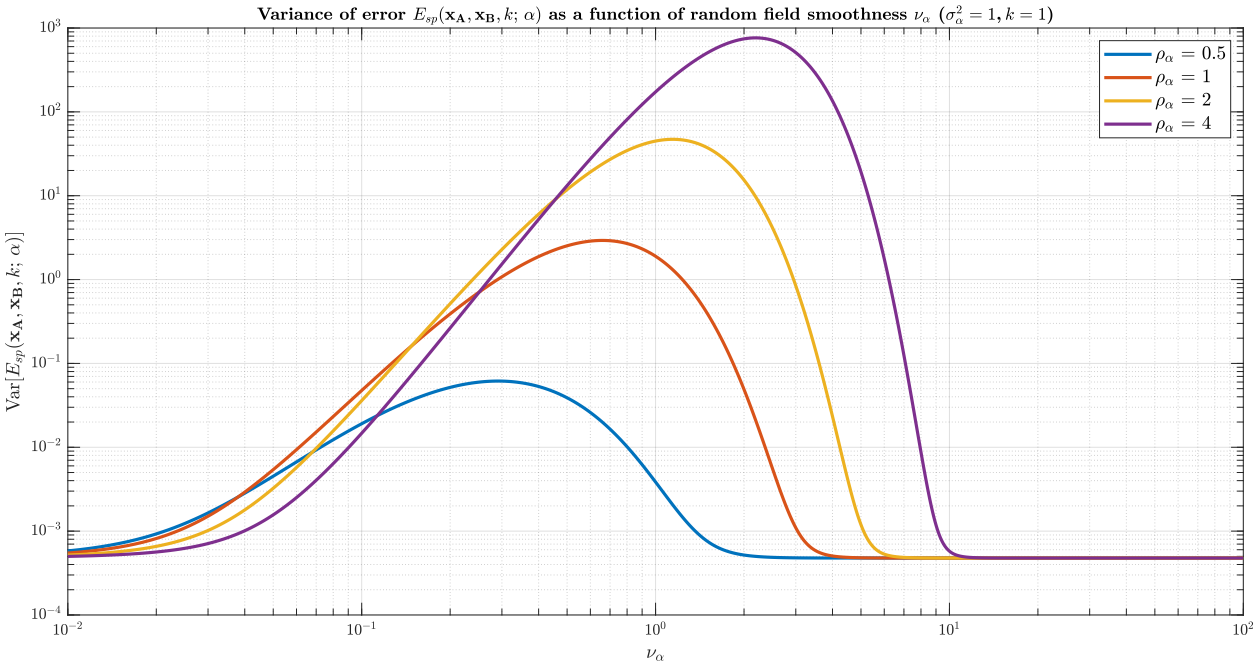


**Figure 3.29:** Variance of the error in the stationary phase approximation in the presence of a log-distributed, Matérn-correlated perturbing random field, implemented directly from equation (2.4.4), for $k = 1$, field variance $\sigma_\alpha = 1$ and field mean $\mu_\alpha = 1$. The variance is shown as a function of the local smoothness of the field, $\nu_\alpha$, for four increasing values of the correlation length $\rho_\alpha$.

Considering that it enters the variance of the stationary phase error with a fourth power (see equation (3.6.6)), the variance of the error becomes unbounded, even if the original field $\alpha$ has bounded moments. While the phase can conceivably still be retrieved in such a scenario, a very smooth highly correlated would result by this argument in amplitude errors of very large variance. Similar analyses can be performed using other asymptotic approximations of the modified Bessel function. Moreover, this variance was used to give a probabilistic bound for the error which, while rough due to the nature of the Chebyshev inequality, has the advantage of being very general, requiring only that the first and second moments of the noise field be finite. Figure 3.19 shows examples of the Chebyshev bound for a high wavenumber $k = 10$ but also for a lower wavenumber $k = 1$. In realistic practical applications, the range of wavenumbers may be quite low, making the Chebyshev boundary

relevant ad the error would be larger. For example, in a medium with a realistic speed of $c = 500$ m/s, a signal at 40 Hz (which is significantly high for some applications, ocean noise for example produces frequencies in a range lower than 0.5 Hz, but reasonable for example for some types of urban noise), results in a wavenumber of $k \approx 0.5$, so that the error bounds in this Chapter are relevant for applications where the wavenumber regime may be low but the stationary phase approximation is nonetheless performed.

For such practical applications the mean, variance, smoothness and correlation length parameters could be empirically estimated in a variety of contexts. For example, in the case of ocean noise the work of Ardhuin et al. (2011) on models of ocean noise could be combined with the approach presented in this Chapter to yield practical applications. Finally, in a setting where there is less randomness, like a controlled-source experiment, the bound (3.1.7) can be used directly to estimate a bound on the error incurred by the stationary phase approximation in terms of the estimated wavenumber and the inter-receiver distance.

## 3.9 Conclusions

In this Chapter, we presented a formal derivation of the stationary phase approximation in two-dimensional wavefield interferometry, applying the results of Olver (1974). We expanded upon that work by deriving an explicit closed formula for the asymptotic expansion of Fourier integrals with a random amplitude.

We further developed expressions for the error incurred in the spectrum, the phase and the amplitude when making use of the stationary phase approximation. The expected value and variance of some of these expressions were calculated. We also showed that the estimated amplitude is always biased. On the other hand, we gave sufficient conditions to ensure that the stationary phase approximation is an unbiased estimator of the phase of the interferometric inter-receiver Green's function, in terms of the statistical properties of the perturbations in source intensity along the source boundary. In this way we have addressed the commonplace assumption that sources of seismic energy impart equal energy upon the medium, and quantified the effect that violating this assumption has on the stationary phase approximate. For the sake of concreteness we implemented the analytical results using a Matérn-correlated random field with a log-normal distribution, in order to investigate the effect that source correlation and smoothness have on the stationary phase approximation. We concluded that this approximation benefits from smoothly varying perturbations along the source boundary, and from longer range source correlations as this helps mitigate spurious effects due to anisotropy.

Furthermore, we derived the corresponding expressions for the stationary phase approx-

imation when the sources are of equal intensity (that is, the perturbing random field is constant and normalised to 1 for simplicity). In this case error expressions and bounds were given applying the results of Olver (1974), explicitly linking the effectiveness of the stationary phase approximation to the wavenumber and the inter-receiver distance. A derivation was also given for the stationary phase approximation when the source boundary is a straight line, which is relevant for Chapter 4.

Chapter 4

# Error quantification in ambient noise interferometry from correlated noise sources

This thesis is concerned with quantifying errors associated with the use of interferometric equations of the type (1.2.13), when they are used for the estimation inter-receiver Green's functions. Furthermore, we propose methods to mitigate these errors in some cases. So far we have considered scenarios where individual recordings are at least roughly available for each source location $\mathbf{x}$ on a source boundary $S$, and the ambient noise has been successfully filtered out of the recordings (i.e $\beta \equiv 0$ in the framework developed in Chapter 2).

As discussed in Section 1.4 of Chapter 1, the theoretical assumptions that underpin many interferometric methods include that recorded energy comes from sources that are distributed isotropically in space around the receivers, and that the time series emitted by the sources are statistically uncorrelated between pairs of sources. The latter assumption precludes sources that are spatio-temporally correlated. However, it is often necessary or even desirable to rely on noise sources that are already present in the environment. This is especially true in areas of the Earth where environmental constraints preclude the use of active artificial seismic source, or when we wish to illuminate large volumes of the Earth that require more powerful sources than can be generated artificially. Sources of freely available ambient noise abound in the Earth and interferometry has been successfully performed by cross-correlating earthquake codas (the long tail of energy that is recorded after the initial impulses from first-arriving seismic waves) which are assumed to act as an approximately diffuse, reverberating wavefield approaching receivers from all directions (Campillo and Paul, 2003), or by using recorded wavefields assumed to come from isotropic noise fields (Curtis et al., 2006; Wapenaar and Fokkema, 2006; Bensen et al., 2007; Wapenaar et al., 2011; Nicolson et al., 2012). Many known physical noise sources that contribute to ambient noise are in motion, e.g. storm

sources, ocean waves or wind (Ardhuin et al., 2019, 2011), and man-made activities such as shipping (Sabra et al., 2005a) or noise from traffic. Recently it has been recognised that highway and/or railway traffic can comprise a dominant component of the ambient noise field, and interferometry has been applied to highway traffic noise (Halliday et al., 2008a; Nakata et al., 2011; Behm and Snieder, 2013), railway noise (Quiros et al., 2016; Zhang et al., 2019; Brenguier et al., 2019; Dales et al., 2020; Pinzon-Rincon et al., 2021; Liu et al., 2021), and noise generated from waves breaking along coastlines (Gerstoft et al., 2006), as illustrated in Figure 4.1. However, all of these sources of ambient noise are inherently correlated in space and time, which is in direct contradiction to the theoretical assumptions outlined above. Importantly, the extent of the error in the interferometric estimates of the Green's function due to the assumption of uncorrelated noise sources has so far not been quantified, and no general methods to reduce these errors have been published[1].

In this Chapter, we present a unified theory of inter-receiver wavefield interferometry that encompasses correlated and uncorrelated noise sources in both the near and far fields, including the case of moving sources. The theoretical framework allows us to develop a novel workflow that mitigates the spurious effects arising from the use of correlated noise sources, leading to the retrieval of the Green's function from a short-time recording of a single statistically correlated moving noise source. Moreover, our framework provides a systematic insight into the mechanisms through which the correlation in the sources induces errors in the estimates of the Green's function and its phase. We quantify these errors and show that they have a significant effect for commonly used noise sources, with spurious effects that obscure the estimates of phase (and hence of wave travel times). We also mitigate them using our novel method, which is based on an appropriate randomisation of the recorded traces and allows for an accurate interferometric retrieval even from a single moving energy source. Furthermore, our analysis explains why stacking multiple traces may reduce errors due to noise correlation in the interferometric estimates, but also highlights limitations of this approach, and identifies potentially commonly-occurring circumstances in which it will fail. This unified methodology is applicable to both correlated and uncorrelated ambient noise, and is particularly useful in cases where stacking does not improve the signal to noise ratio in the retrieval.

In what follows we begin by briefly presenting the theoretical principles of standard wavefield interferometry for the case when individual recordings from static impulsive sources are available, as well as for an ambient noise scenario. Subsequently, we highlight the challenges in retrieving the interferometric inter-receiver Green's function from ambient noise. The important case of performing interferometric retrieval from wavefields generated by correlated

[1]We have published such a method in Ayala-Garcia et al. (2021).

moving sources is considered next, and the corrupting effect due to the Doppler spread on the quality of the interferometric retrieval is discussed. We then review the standard ensemble average approach in ambient noise interferometry, which is referred to as *stacking*. Potential pitfalls of the retrieval through the stacking average are discussed in terms of the correlation structure of the source signature. Moreover, an analytical decomposition of the ambient noise retrieval is derived which, based on the characteristic correlation length of the source signature, separates the retrieval into a term comprising predominantly coherent contributions that correctly approximate the inter-receiver phase, and the cross-talk term associated with spurious incoherent contributions. These analytical findings motivate the development of a novel and versatile technique, referred to as the *random windowing* approach. In contrast to the standard stacking average, the random-windowing average does not rely on spatial localisation of the correlation structure of the source signature, and it can be used for interferometric phase retrieval from short recordings of a correlated noise signal. We conclude by outlining an algorithm for carrying out the random-windowing retrieval and present an example with the resulting phases retrieved successfully from both correlated and uncorrelated ambient noise.

In practice, recordings for individual active source locations are often not available. Hence, it becomes necessary and even desirable to rely on noise that is already present in the environment, commonly referred to as "ambient noise". In order to successfully estimate inter-receiver Green's function from ambient noise recordings, there is a theoretical requirement that the noise sources be uncorrelated in time. Indeed, many applications of ambient noise interferometry explicitly make this assumption (see e.g. Lobkis and Weaver (2001); Wapenaar (2004); Snieder et al. (2009); Wapenaar et al. (2010a); Sabra (2010); Nakata et al. (2011)). However, many real-world noise sources such as trains, highway traffic and ocean waves are inherently correlated in space and time, in direct contradiction to the these theoretical foundations. Applying standard interferometric techniques to recordings from correlated energy sources makes the Green's function estimate liable to errors that so far have not been fully accounted for theoretically nor in practice.

This Chapter is organised as follows: Section 4.1 contrasts the equations for active and ambient noise interferometry, highlighting the technical differences and the consequences of the Doppler effect. Next, our analysis in Section 4.2 explains why standard stacking may reduce the phase errors, but also shows that in commonly encountered circumstances this widely used technique will not remediate the problem. This analytical insight allowed us to develop a novel workflow in Section 4.3 that significantly mitigates effects arising from the use of correlated noise sources. The methodology presented can be used in conjunction with already existing approaches, and improves results from both correlated and uncorrelated

ambient noise, shown in Section 4.3.5. Hence, we expect it to be widely applicable in ambient noise interferometry studies. Results from this Chapter have been published in Ayala-Garcia et al. (2021).

In the framework set out in Chapter 2, the situation where individual active source recordings are not available corresponds to $\alpha \equiv 0$ in equation (2.2.8), so that the retrieval relies entirely on the recorded ambient noise terms $\beta$, and equation (2.2.8) reduces to

$$\hat{g}(\mathbf{x_A}, \mathbf{x_B}, k; 0, \beta) \propto \hat{\beta}(\mathbf{x_A}, k)\hat{\beta}^*(\mathbf{x_B}, k)\ell(S)\,, \tag{4.0.1}$$

where $\ell(S)$ is interpreted as the arc-length of an implicit source boundary, and a proportionality symbol is used for consistency with the framework set out in Wapenaar and Fokkema (2006), where volume injection sources are used instead of volume injection rate sources, as discussed in Chapter 1. Equation (4.0.1) above represents the standard formulation of ambient noise retrieval for uncorrelated noise sources.

## 4.1 Introduction

It is a well-established principle that cross-correlating seismic observations recorded at different receiver locations yields seismic responses that under certain conditions, provide useful estimates of the inter-receiver Green's function of linear wave equations. This principle has been expressed in a variety of ways, often via the acoustic or elastic representation theorems, and using either the convolution, deconvolution or cross-correlation of recorded seismic traces. For our purposes, a cross-correlational Green's function representation theorem is used in line with Wapenaar and Fokkema (2006) and Schuster (2009), in a regime of volume-injection rate impulsive sources.

Consider a medium of density $\rho$ and sound speed $c$, and let $\hat{G}(\mathbf{x}, \mathbf{x}', \omega)$ denote the frequency-domain response of the medium to an impulsive source located at $\mathbf{x}'$ and recorded at location $\mathbf{x}$. Throughout, $\hat{\cdot}$ denotes quantities in the frequency domain, and $\cdot^*$ denotes complex conjugation. Given a pair of receiver locations $\mathbf{x_A}$ and $\mathbf{x_B}$ we assume an empirical estimate $\hat{g}(\mathbf{x_A}, \mathbf{x_B}, \omega)$ of the inter-receiver Green's function $\hat{G}(\mathbf{x_A}, \mathbf{x_B}, \omega)$ can be represented as

$$\hat{g}(\mathbf{x_A}, \mathbf{x_B}, \omega) = \frac{2}{\rho c}\int_S \hat{G}^*(\mathbf{x_A}, \mathbf{x}', \omega)\hat{G}(\mathbf{x_B}, \mathbf{x}', \omega)d\mathbf{x}'\,, \tag{4.1.1}$$

where each $\mathbf{x}'$ is an impulsive source location along the boundary $S$ (see leftmost panel in Figure 4.1). The integrand in equation (4.1.1) is equivalent to the convolution of the time-reversed trace recorded at $\mathbf{x_A}$ with the trace recorded at $\mathbf{x_B}$, and this operation corre-

sponds to a cross-correlation in the time domain. This statement holds exactly for recordings $G(\mathbf{x}, \mathbf{x}', t)$ defined for all time. Please note that $\hat{g}$ in equation (4.1.1) is proportional to the spatial average of the integrand in the right-hand side of equation (4.1.1) over $S$; this interpretation will be helpful below.

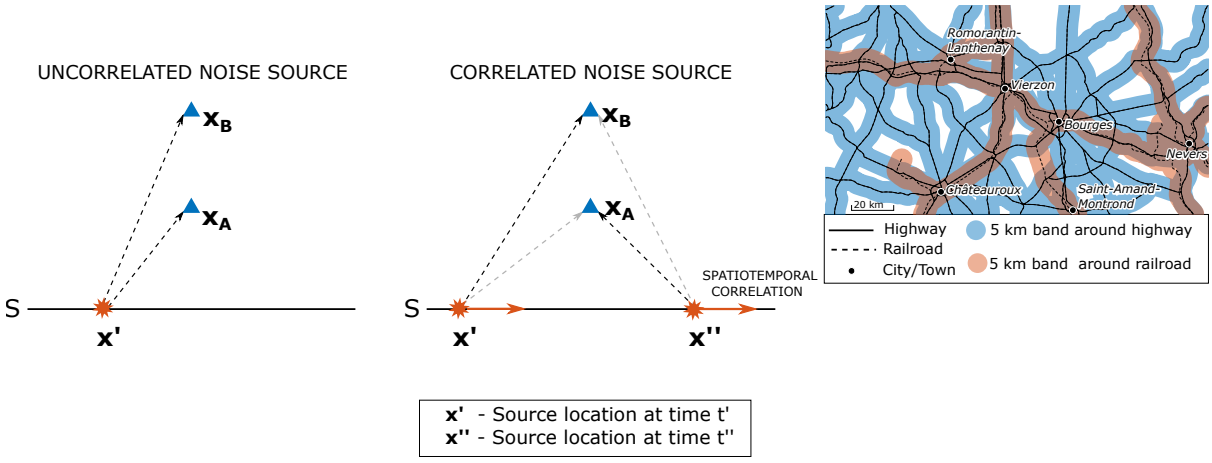


**Figure 4.1:** Geometry of a boundary $S$ of uncorrelated, impulsive sources (see equation (4.1.1)) versus a time-ordered train of impulsive sources (see equation (4.1.4)). Blue triangles denote receivers and source locations are represented by orange stars. Orange arrows in the source boundary indicate the presence of a spatiotemporal correlation of sources along the boundary. The top right panel shows the main roads (solid black) and railways (black dashes) within an area of about 9000 km$^2$ around Bourges, France. A zone of 5 km on either side of each road (blue) and railway (orange) highlights the prevalence of near-field traffic noise. The bottom panel shows oblique waves breaking against the coast of Skeleton Bay, Namibia. These are common examples of correlated noise sources.

The main theoretical requirements for equation (4.1.1) to provide a good estimate of the inter-receiver Green's function are: (i) that the medium is lossless, (ii) that the source boundary $S$ encloses the receivers and that energy is emitted equally from all directions, (iii) that $S$ is sufficiently far from the receivers for the recorded energy flux to be emitted approximately perpendicular to the boundary, and (iv) that individual recordings are acquired independently for each impulsive source location $\mathbf{x}'$ within $S$. Under these idealized conditions, the empirical estimate $\hat{g}(\mathbf{x_A}, \mathbf{x_B}, \omega)$ provides a good approximation to the homogeneous inter-receiver Green's function (Wapenaar and Fokkema, 2006), i.e., $\hat{g}(\mathbf{x_A}, \mathbf{x_B}, \omega) = \hat{G}(\mathbf{x_A}, \mathbf{x_B}, \omega) - \hat{G}^*(\mathbf{x_A}, \mathbf{x_B}, \omega)$ or, equivalently $g(\mathbf{x_A}, \mathbf{x_B}, t) = G(\mathbf{x_A}, \mathbf{x_B}, t) - G(\mathbf{x_A}, \mathbf{x_B}, -t)$ in the time domain. Wapenaar et al. (2011) discuss spurious effects that are introduced when the above theoretical assumptions are violated. However, in practice artefacts due to the violation of these theoretical assumptions are usually assumed to be sufficiently weak to allow for retrieval of useful empirical estimates of the Green's function. In particular, wavefield

interferometry has been shown empirically to be applicable in regimes where the medium illumination is one-sided (Halliday and Curtis, 2008b; Wapenaar et al., 2011; Mehta et al., 2007b; Snieder, 2004). Hence, while the boundary $S$ in equation (4.1.1) is typically assumed to be a closed contour which is sufficiently distant from the receivers, we assume $S$ to be a straight source-line as depicted in the left insets of Figure 4.1. It is worth noting that while the amplitudes of empirical Green's function estimates are acknowledged to be unreliable, the phases of the Green's function recovered through such a procedure are assumed to be well approximated (see for example, Wapenaar and Fokkema (2006); Thorbecke and Wapenaar (2008), and remarks under equation (4.2.4) below).

The main practical obstacle in the context of ambient noise interferometry stems from the fact that the medium's response to impulsive sources is not readily available. Hence, the information required for constructing the integrand in equation (4.1.1) cannot be obtained directly. Instead, Wapenaar and Fokkema (2006) propose the ambient noise interferometric relationship defined as

$$\hat{h}(\mathbf{x_A}, \mathbf{x_B}, \omega) := \frac{2}{\rho c}\, \hat{p}^*(\mathbf{x_A}, \omega)\, \hat{p}(\mathbf{x_B}, \omega)\,, \tag{4.1.2}$$

where $\hat{p}(\mathbf{x}, \omega)$ denotes ambient noise recorded at a receiver location $\mathbf{x}$ for frequency $\omega$. It is useful (and theoretically appropriate) to consider each recording $\hat{p}(\mathbf{x}, \omega)$ as a random field which is obtained via the Fourier transform of a realization of a stochastic process $p(\mathbf{x}, t)$ (these statements hold for $t, \omega \in \mathbb{R}$, we do not delve into the accuracy of finite-time approximations of the Fourier transform). In such a framework source locations $\mathbf{x}' \in S$ are no longer required to be known explicitly. Instead, the source characteristics are implicitly present in the ambient noise representation in equation (4.1.2) and they are accounted for, in principle, in the ambient noise recordings represented via

$$\hat{\beta}(\mathbf{x}, \omega) = \int_S \hat{F}(\mathbf{x}', \omega) \hat{G}(\mathbf{x}, \mathbf{x}', \omega) d\mathbf{x}'\,, \tag{4.1.3}$$

where $\hat{F}(\mathbf{x}, \omega)$ characterizes the unknown *source signature*. Wapenaar and Fokkema (2006) showed that provided that $\hat{\beta}(\mathbf{x_A}, \omega)$ and $\hat{\beta}(\mathbf{x_B}, \omega)$ are obtained from recordings of uncorrelated noise sources, taking the empirical average over a large number ($N \gg 1$) of realizations of $\hat{h}(\mathbf{x_A}, \mathbf{x_B}, \omega)$ in equation (4.1.2), referred to hereafter as *stacking*, leads to a good approximation of the phase of the inter-receiver Green's function $\hat{G}(\mathbf{x_A}, \mathbf{x_B}, \omega)$. Such an approximation is increasingly accurate for $N, t \to \infty$ provided that $h(\mathbf{x_A}, \mathbf{x_B}, t)$ is ergodic, which

seems to be a reasonable assumption in practice[2]. However, as discussed in the subsequent sections, the stacking average is likely to produce unsatisfactory results in the presence of correlated noise sources even when long-time recordings are available.

In this Section, we delve deeper into the relationship between the estimates $\hat{g}(\mathbf{x_A}, \mathbf{x_B}, \omega)$ and $\hat{h}(\mathbf{x_A}, \mathbf{x_B}, \omega)$ in order to identify conditions under which the ambient noise retrieval based on equation (4.1.2) provides a satisfactory approximation of the retrieval equation (4.1.1), and to develop techniques that allow us to achieve this for both uncorrelated and correlated noise sources.

To understand the need for statistical averaging over multiple realizations of the ambient noise recordings in the retrieval (4.1.2) for some fixed boundary $S$, substitute the integral expression (4.1.3) for the noise recordings at receivers $\mathbf{x_A}$ and $\mathbf{x_B}$ into equation (4.1.2) to obtain

$$\hat{h}(\mathbf{x_A}, \mathbf{x_B}, \omega) = \frac{2}{\rho c} \int_S \int_S \hat{F}^*(\mathbf{x}', \omega) \hat{F}(\mathbf{x}'', \omega)\, \hat{G}^*(\mathbf{x_A}, \mathbf{x}', \omega) \hat{G}(\mathbf{x_B}, \mathbf{x}'', \omega) d\mathbf{x}''\, d\mathbf{x}' \,. \tag{4.1.4}$$

Please note that the above formula represents a product of two independent integrals which are re-written in a form suitable for the subsequent analysis; to simplify notation, we skip the explicit dependence of $\hat{F}$ in equation (4.1.4) on the particular recording of ambient noise, but this remains implicit. The geometry corresponding to the retrieval based on, respectively, equations (4.1.1) and (4.1.4) is sketched on the left side of Figure 4.1. In contrast to $\hat{g}(\mathbf{x_A}, \mathbf{x_B}, \omega)$ in equation (4.1.1), where averaging over the source locations $\mathbf{x}' \in S$ leads to the cancellation of all phases except for the inter-receiver phase, the ambient noise retrieval $\hat{h}(\mathbf{x_A}, \mathbf{x_B}, \omega)$ in equation (4.1.4) does not represent a spatial average over $S$. Consequently, the retrieval in equation (4.1.4) is dominated by acausal and spurious information contained in the integrand for $\mathbf{x}' \neq \mathbf{x}''$ (see middle panel of Figure 4.1).

It turns out that a reliable phase retrieval of the inter-receiver Green's function from equation (4.1.4) relies on an appropriate statistical average which couples the source characteristics $\hat{F}(\mathbf{x}', \omega)$ and $\hat{F}(\mathbf{x}'', \omega)$ for all $\mathbf{x}', \mathbf{x}'' \in S$ to generate an integral kernel which is localized in the neighborhood of $\mathbf{x}' = \mathbf{x}''$. As discussed in subsequent sections, the suitable statistical average depends on the nature of the noise. In particular, for correlated noise sources the (stacking) average over multiple realizations of equation (4.1.2) is largely unsatisfactory regardless of the amount of available data, and a more versatile averaging approach must be used. Please note that while a constant medium density and propagation

[2]See for example Weaver and Lobkis (2001), Shapiro and Campillo (2004), Sabra et al. (2005b), Snieder (2004) or Curtis et al. (2006) for representative literature examples where ergodicity is implicitly assumed and and wavefield interferometry is then successfully applied

speed have been assumed, the analysis presented still holds when these two quantities are space-dependent.

In light of the above discussion, it is clear that the non-averaged relationship in equation (4.1.4) is dominated by contributions from incongruous source locations, and these may lead to spurious contributions that completely obscure the phase of the inter-receiver Green's function. Consider, for example, the interferometric retrieval from a simulated sequence of sources which generate seismic impulses in a time-ordered fashion; hereafter, we refer to such a sequence as a *train of sources*. The train of sources is not to be confused with a *set of impulsive sources* recorded individually and used to calculate the retrieval equation (4.1.1); these two cases will be compared in what follows. In both cases we assume that the signal is recorded by a pair of receivers deployed in the vicinity of the source-line $S$. To simulate the wavefield generated by trains of sources, we derived an analytical two-dimensional model which is described in Section 4.1.1.

### 4.1.1 Analytical derivation of a moving point source model

In this Section, the wavefield generated by a band-limited point source in motion is calculated in order to provide synthetic data that helps illustrate the theory and methods presented in the latter Sections. We begin by assuming a monochromatic point source, emitting sound at a constant angular frequency $\tilde{\omega}$, that moves with constant speed $\mathbf{v}$ in a two-dimensional homogeneous medium. This wavefield is denoted by $p_{\tilde{\omega}}(t, \mathbf{x}, \mathbf{v})$ when measured at time a $t$ and at a receiver location $\mathbf{x}$. We may also refer to the constant source frequency as $\tilde{f}$ when we wish to express it in Hertz, so that $\tilde{\omega} = 2\pi\tilde{f}$. The moving point source is characterised through the function

$$s_{\tilde{\omega}}(t, \mathbf{x}, \mathbf{v}) = e^{-i\tilde{\omega}t}\delta(\mathbf{x} - \mathbf{v}t)\,. \tag{4.1.5}$$

It is assumed without loss of generality that at time $t = 0$ the monochromatic source is located at the origin of the coordinate system. It is further assumed that the medium density $\rho$ and sound speed $c$ are constant. Then we have that the wavefield, denoted by $p_{\tilde{\omega}}$, satisfies the linear wave equation

$$\frac{1}{c^2}\frac{\partial^2 p_{\tilde{\omega}}}{\partial t^2} - \nabla^2 p_{\tilde{\omega}} = \rho\,\frac{\partial s_{\tilde{\omega}}}{\partial t} \tag{4.1.6}$$

where we restrict ourselves to real solutions. In order to solve equation (4.1.6) we introduce the abstract complex potential $\phi^{\mathcal{C}}_{\tilde{\omega}}(t, \mathbf{x}, \mathbf{v})$ of the particle velocity, so that

$$p_{\tilde{\omega}} = \rho\,\Re\left\{\frac{\partial \phi^{\mathcal{C}}_{\tilde{\omega}}}{\partial t}\right\}\,. \tag{4.1.7}$$

This potential satisfies the wave equation

$$\frac{1}{c^2}\frac{\partial^2 \phi^{\mathcal{C}}_{\tilde{\omega}}}{\partial t^2} - \nabla^2 \phi^{\mathcal{C}}_{\tilde{\omega}} = s_{\tilde{\omega}}\,, \tag{4.1.8}$$

which can be derived directly from (4.1.6) by integrating once with respect to time and cancelling a factor of $\rho$. Note that if $\phi^{\mathcal{C}}_{\tilde{\omega}}$ is a solution to equation (4.1.8), then $p_{\tilde{\omega}}$ as defined by equation (4.1.7) will satisfy equation (4.1.6).

A solution to (4.1.8) can be immediately written down by convolving the source term (4.1.5) with the outgoing Green's function of the wave equation in time and space for a volume injection source. This Green's function is given by

$$G(t,\mathbf{x}) = \frac{\Theta\left(t - \frac{|\mathbf{x}|}{c}\right)}{2\pi\sqrt{t^2 - \frac{|\mathbf{x}|^2}{c^2}}}\,, \tag{4.1.9}$$

where $\Theta$ denotes the Heaviside function. Hence, the complex potential $\phi^{\mathcal{C}}_{\tilde{\omega}}(t,\mathbf{x},\mathbf{v})$ can be expressed in integral form as

$$\phi^{\mathcal{C}}_{\tilde{\omega}}(t,\mathbf{x},\mathbf{v}) = \frac{1}{2\pi}\int_{-\infty}^{\infty}\int_{\mathbb{R}^2} e^{-i\tilde{\omega}t'}\delta(\mathbf{x}' - \mathbf{v}t')\frac{\Theta\left(t - t' - \frac{|\mathbf{x}-\mathbf{x}'|}{c}\right)}{\sqrt{(t-t')^2 - \frac{|\mathbf{x}-\mathbf{x}'|^2}{c^2}}}d\mathbf{x}'dt'\,. \tag{4.1.10}$$

Performing the integral in space is straightforward owing to the sifting property of the delta distribution, yielding

$$\phi^{\mathcal{C}}_{\tilde{\omega}}(t,\mathbf{x},\mathbf{v}) = \frac{1}{2\pi}\int_{-\infty}^{\infty} e^{-i\tilde{\omega}t'}\frac{\Theta\left(t - t' - \frac{|\mathbf{x}-\mathbf{v}t'|}{c}\right)}{\sqrt{(t-t')^2 - \frac{|\mathbf{x}-\mathbf{v}t'|^2}{c^2}}}dt'\,. \tag{4.1.11}$$

In order to perform the time integral in equation (4.1.11), define the auxiliary functions

$$q_1(t,\mathbf{x},\mathbf{v}) = \frac{c^2 t - \mathbf{x}\cdot\mathbf{v}}{c^2 - |\mathbf{v}|^2}\,, \tag{4.1.12}$$

and

$$q_2(t,\mathbf{x},\mathbf{v}) = q_1(t,\mathbf{x},\mathbf{v})^2 - \frac{c^2t^2 - |\mathbf{x}|^2}{c^2 - |\mathbf{v}|^2}\,, \tag{4.1.13}$$

noting that we assume a subsonic source throughout this work, i.e. $\mathbf{v} < c$. Then, by the

definition of the Heaviside function, we have

$$\Theta\left(t - t' - \frac{|\mathbf{x} - \mathbf{v}t'|}{c}\right) = \begin{cases} 1 & \text{if } t' \leq \mathring{t}\,, \\ 0 & \text{if } t' > \mathring{t}\,, \end{cases} \tag{4.1.14}$$

where

$$\mathring{t} = q_1(t, \mathbf{x}, \mathbf{v}) - \sqrt{q_2(t, \mathbf{x}, \mathbf{v})}\,. \tag{4.1.15}$$

It is useful highlight the physical interpretation of time $\mathring{t}$. This value is such that the argument of the Heaviside function in the left hand side becomes zero or, equivalently,

$$c(t - \mathring{t}) = |\mathbf{x} - \mathbf{v}\mathring{t}|\,.$$

Note that $t - \mathring{t}$ is the time it takes for energy to travel from the location of the source at time $\mathring{t}$ (given by $\mathbf{v}\mathring{t}$) to the receiver location $\mathbf{x}$. In other words, $\mathring{t}$ represents the time at which the wave arriving at time $t$ and location $\mathbf{x}$ was emitted. Equation (4.1.15), scaled by the source speed $\mathbf{v}$, is useful later on in Section 4.3 to calculate the location of the spatial window induced by a time window in Section 4.3.

Next, performing the time integral in equation (4.1.11) yields the following solution for the potential:

$$\phi^{\mathcal{C}}_{\tilde{\omega}}(t, \mathbf{x}, \mathbf{v}) = \frac{ie^{-i\tilde{\omega}\, q_1(t,\mathbf{x},\mathbf{v})}}{4c\sqrt{c^2 - |\mathbf{v}|^2}} \mathcal{H}^{(1)}_0\left(\tilde{\omega}\sqrt{q_2(t, \mathbf{x}, \mathbf{v})}\right)\,, \tag{4.1.16}$$

where $\mathcal{H}^{(1)}_0$ denotes the first-kind Hankel function of order zero, and $q_1$ and $q_2$ are defined by equations (4.1.12) and (4.1.13). In order to simplify our expressions, we define the non-dimensional parameter $M = \frac{|\mathbf{v}|}{c}$ i.e. the Mach number, which quantifies the ratio of the source speed with respect to the speed in the medium and is in this work always assumed to be smaller than one. This parameter simplifies our analysis when considering the Doppler effect below. Further, we place the origin of our reference system at the instantaneous location where the source is collinear with the perpendicular receiver pair. Hence we assume the receiver to be of the form $\mathbf{x} = [\,0\,,\, x_y\,]$, and that the source speed can be written as $\mathbf{v} = [\,v\,,\, 0\,]$. Finally, we define for simplicity

$$t_{\mathbf{x}} = \frac{|\mathbf{x}|}{c}\,, \tag{4.1.17}$$

that is, the travel time from the reference origin described above to the receiver location $\mathbf{x}$. Under these assumptions we can write the wavefield generated by a monochromatic moving

point source as

$$p_{\tilde{\omega}}(t,\mathbf{x},M) = \Re\left\{-\frac{i\rho\,\tilde{\omega}}{4c^2(1-M^2)^{\frac{3}{2}}}\exp\left\{-i\,\frac{\tilde{\omega}}{1-M^2}\,t\right\}\right.$$
$$\times\left[\frac{M^2\,t}{\sqrt{M^2t^2+(1-M^2)\,t_{\mathbf{x}}^2}}\mathcal{H}_1^{(1)}\left(\frac{\tilde{\omega}}{1-M^2}\,\sqrt{M^2t^2+(1-M^2)\,t_{\mathbf{x}}^2}\right)\right.$$
$$\left.\left.+\;iH_0^{(1)}\left(\frac{\tilde{\omega}}{1-M^2}\,\sqrt{M^2t^2+(1-M^2)\,t_{\mathbf{x}}^2}\right)\right]\right\}. \tag{4.1.18}$$

Expressing the wavefield in this way allows us to see how its behaviour depends on the source speed $|\mathbf{v}|$ and the distance to the road $|\mathbf{x}|$, albeit always scaled by the medium speed $c$. It also allows us to see how the distance from the receiver to the source boundary $S$ affects the wavefield's behaviour. See Figure 4.2 for a direct implementation of this equation in the time domain, as well as its numerically calculated frequency spectrum. In order to obtain a frequency-domain expression for the interferometric retrieval, we derive an analytical expression for the spectrum of equation (4.1.18). Consider the following Fourier transform of the real part of the potential (4.1.16)

$$\hat{\phi}_{\tilde{\omega}}(\omega,\mathbf{x},\mathbf{v}) = \int_{-\infty}^{\infty} e^{-i\omega t}\mathrm{Re}\left\{\,\phi_{\tilde{\omega}}^{\mathcal{C}}(t,\mathbf{x},\mathbf{v})\,\right\}dt\,. \tag{4.1.19}$$

To perform this integration, we start by taking an integral representation for the spectrum of the potential by taking the real part of the integral representation (4.1.11), where only the spatial integration has been performed, yielding

$$\mathrm{Re}\left\{\,\phi_{\tilde{\omega}}^{\mathcal{C}}(t,\mathbf{x},\mathbf{v})\,\right\} = \int_{-\infty}^{\infty}\cos(\tilde{\omega}t')\frac{\Theta\left(t-t'-\frac{|\mathbf{x}-\mathbf{v}t'|}{c}\right)}{\sqrt{(t-t')^2-\frac{|\mathbf{x}-\mathbf{v}t'|^2}{c^2}}}dt' \tag{4.1.20}$$

Substituting equation (4.1.20) into equation (4.1.19) results after a few manipulations in the

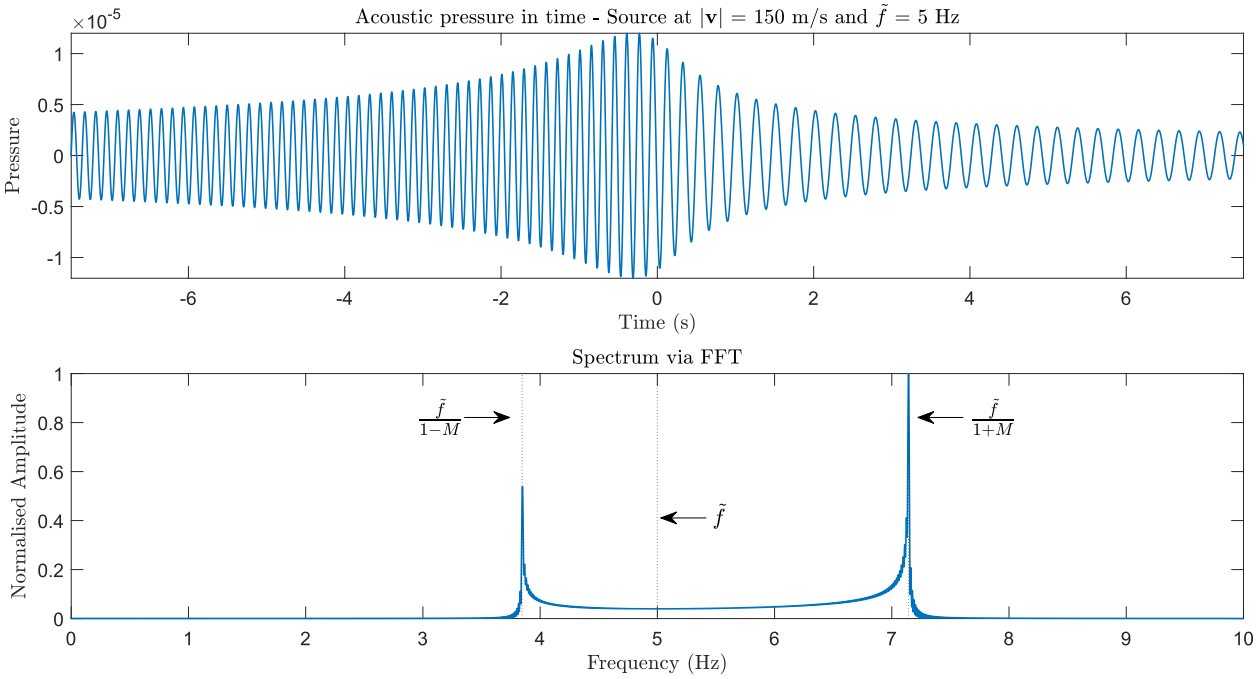


**Figure 4.2:** Example of simulated monochromatic wavefield $p_{\tilde{\omega}}$. Medium speed is $c = 500\,m/s$ and medium density is set to $\rho = 1$. The receiver location is $\mathbf{x} = (\,0\,\text{m}\,, 100\,\text{m}\,)$. The monochromatic source travels with speed $|\mathbf{v}| = 150$ m/s along the positive direction of the $x$-axis, emitting sound at $\tilde{f} = 5$ Hz. It crosses the origin at time $t = 0$ according to our parametrisation. For illustration purposes, source parameters were chosen so that the Doppler effect could be plainly appreciated in the waveform (low emitting frequency $\tilde{f}$, relatively high value of $M$ at 0.3). The top panel shows the waveform in the time domain directly implemented from equation (4.1.18). We can see how the perceived frequency increases or decreases when the source is moving towards or away from the receiver, respectively. The bottom panel shows the spectrum of this source, calculated numerically via fast Fourier transform in MATLAB. The spectrum spreads between the frequency values predicted by the standard Doppler formula, $\frac{\tilde{f}}{1\pm M}$, highlighted in grey dotted lines.

following expression for the spectrum of the wavefield generated by a moving point source

$$\hat{\phi}_{\tilde{\omega}}(\omega, \mathbf{x}, \mathbf{v}) = -\frac{i}{4}\int_{-\infty}^{\infty} e^{-i\omega t'} \cos(\tilde{\omega}t')\mathcal{H}_0^{(2)}\left(\frac{\omega}{c}\,|\mathbf{x} - \mathbf{v}t'|\right) dt'\,. \tag{4.1.21}$$

where $H_0^{(2)}$ denotes the second-kind Hankel function of order zero. Finally, to derive the spectrum of the wavefield $p_{\tilde{\omega}}$ equation (4.1.7) is Fourier transformed so that (4.1.21) is simply multiplied by the corresponding frequency factor $i\omega$ that corresponds to a differentiation in the time domain, that is

$$\hat{p}_{\tilde{\omega}}(\omega, \mathbf{x}, \mathbf{v}) = \frac{\omega\rho}{4}\int_{-\infty}^{\infty} e^{-i\omega t'} \cos(\tilde{\omega}t')\,\mathcal{H}_0^{(2)}\left(\frac{\omega}{c}\,|\mathbf{x} - \mathbf{v}t'|\right) dt'\,. \tag{4.1.22}$$

Numerical implementation of the integral (4.1.22) agrees with the spectrum of the time domain wavefield (4.1.18) calculated using the fast Fourier transform algorithm. Moreover, the spectrum (4.1.22) can be written in the standard form of a recording given by equation (4.1.3), or more generally equation (2.1.5) in the time domain, where the source boundary $S$ is parametrised by $t'$ (via $\mathbf{x}'(t') = t'\mathbf{v}$) and the source kernel is given explicitly by

$$\hat{F}(\mathbf{x}'(t'), \omega) = e^{-i\omega t'} \cos(\tilde{\omega} t')$$

and the Green's function is indeed the Green's function of the Helmholtz operator for a volume injection rate source, given by

$$\hat{G}(\mathbf{x}, \mathbf{x}'(t'), \omega) = \frac{\omega\rho}{4} \mathcal{H}_0^{(2)} \left( \frac{\omega}{c} |\mathbf{x} - \mathbf{x}'(t')| \right) .$$

### 4.1.2 The Doppler effect

With frequency-domain analytical expressions available, the instantaneous frequency of the model can be evaluated. The complex model will be used. An analytical expression is derived for the instantaneous phase of the recorded source and then a derivative is taken to find the instantaneous frequency.

Consider the asymptotic approximation of the Hankel function for a large argument $x$ (see e.g. Goldstein and Thaler (1958) or Appendix A of Galetti et al. (2013)),

$$\mathcal{H}_0^{(2)}(x) \sim e^{-i(x - \frac{\pi}{4})} \sqrt{\frac{2}{\pi x}} . \tag{4.1.23}$$

The frequency regime and the source-receiver distance are already required to be sufficiently large for the monopole interferometry equation to be applied, which makes approximation (4.1.23) reasonable. Using this approximation, the spectrum of the theoretical complex wavefield $\hat{p}^{\mathcal{C}}_{\tilde{\omega}}(\omega, \mathbf{x}, \mathbf{v})$ (which is derived in a manner analogous to equation (4.1.22), taking the full complex potential) can be expressed as

$$\hat{p}^{\mathcal{C}}_{\tilde{\omega}}(\omega, \mathbf{x}, \mathbf{v}) \sim \frac{\omega\rho}{4} \int_{-\infty}^{\infty} e^{-i\left\{(\omega+\tilde{\omega})t' + \frac{\omega}{c}|\mathbf{x} - \mathbf{v}t'| - \frac{\pi}{4}\right\}} \sqrt{\frac{2c}{\pi\omega|\mathbf{x} - \mathbf{v}t'|}} \, dt' . \tag{4.1.24}$$

The instantaneous phase recorded at a receiver location $\mathbf{x}$ will be denoted by $\mathrm{ph}_{\mathbf{x}}(t')$ and given by

$$\mathrm{ph}_{\mathbf{x}}(t') = (\omega + \tilde{\omega})t' + \frac{\omega}{c}|\mathbf{x} - \mathbf{v}t'| - \frac{\pi}{4} , \tag{4.1.25}$$

and differentiating once in time yields

$$\frac{d}{dt'}\mathrm{ph}_{\mathbf{x}}(t') = \omega + \tilde{\omega} - \frac{\omega}{c}\left(\frac{\mathbf{x}-\mathbf{v}t'}{|\mathbf{x}-\mathbf{v}t'|}\right)\cdot\mathbf{v}\,. \tag{4.1.26}$$

The integral (4.1.24) is highly oscillatory and in accordance to the stationary phase approximation the main contributions correspond stationary points of the phase (4.1.25). The spectrum will be otherwise negligibly small by the Riemann-Lebesgue lemma. Hence the spectrum will be largely negligible except at the zeros of (4.1.26). Solving the resulting equation and using the fact that $\mathbf{x}-\mathbf{v}t'$ is the position of the source with respect to the receiver at time $t'$ results in the following expression for the instantaneous frequency recorded at location $\mathbf{x}$ and time $t'$

$$\breve{\omega}(\mathbf{x},t') = \frac{\tilde{\omega}}{1-\frac{|\mathbf{v}|}{c}\cos\theta_{\mathbf{x}}(t')}\,. \tag{4.1.27}$$

The instantaneous recorded frequency (4.1.27) exhibits the Doppler shift induced by the movement of the source with respect to the receiver. Note that for any time $t'$ the relative position angle $\cos\theta_{\mathbf{x}}(t')$ is bounded between $-\pi$ (when the source is infinitely far to the left of the receiver) and $\pi$ (when the source is infinitely far to the right), corresponding to the frequencies $\tilde{\omega}/(1\pm M)$ where $M = |\mathbf{v}|/c$. Equation (4.1.27) agrees with the well known expressions for the recorded frequency when the receiver is directly in the path of the source, and is more general as the instantaneous frequency can be calculated for an arbitrary recording location $\mathbf{x}$. Moreover, it is straightforward to show that (4.1.27) is larger than $\tilde{\omega}$ when the source is moving towards the receiver and smaller when the source is moving away, with the true emitted frequency $\tilde{\omega}$ recorded the moment the source-receiver ray-path is perpendicular to the source boundary.

### 4.1.3 Broadband moving source model

We construct a broadband source emitting noise on a discrete frequency domain $\tilde{\omega}\in\tilde{\Omega}$ by applying the principle of superposition to the monochromatic wavefields (4.1.22), and imposing a random phase shift for each emitted frequency. That is, we define the broadband wavefield

$$\hat{p}(\mathbf{x},\omega) = \sum_{\tilde{\omega}\in\tilde{\Omega}} c_{\tilde{\omega}}\hat{p}_{\tilde{\omega}}(\mathbf{x},\omega)\,, \tag{4.1.28}$$

where $c_{\tilde{\omega}}$ is an appropriate scaling coefficient that depends on how the spectrum $\tilde{\Omega}$ is constructed, and the dependence on the source speed $\mathbf{v}$ is left implicit. In this work, it is

assumed that the source spectrum can be represented in the form (4.1.28). A more general representation can be achieved by taking the Fourier transform of a wavefield of the form

$$p(\mathbf{x},t) = \sum_{\tilde{\omega}\in\tilde{\Omega}} c_{\tilde{\omega}}(t) p_{\tilde{\omega}}(\mathbf{x},t)\,,$$

where the coefficients $c_{\tilde{\omega}}(t)$ and time dependent and random with their own correlation structure. While we do not deal with this case in detail here, we point out such a setup would be necessary to derive a kernel that becomes localised for the case of a monochromatic source, as remarked under equation (4.2.9).

Assuming that the source spectrum can be represented in the form (4.1.28), we have

$$\hat{p}(\mathbf{x},\omega) = \frac{\omega\rho}{4} \sum_{\tilde{\omega}\in\tilde{\Omega}} c_{\tilde{\omega}} \int_{-\infty}^{\infty} e^{-i\omega t'} \cos(\tilde{\omega}t' + \theta_{\tilde{\omega}})\, \mathcal{H}_0^{(2)}\left(\omega \frac{|\,\mathbf{x}-\mathbf{v}t'\,|}{c}\right) dt'\,, \tag{4.1.29}$$

where $\theta_{\tilde{\omega}}$ are a collection of random variables indexed by $\tilde{\omega}$. The random quantity

$$F(t';\theta_{\tilde{\Omega}}) = \sum_{\tilde{\omega}\in\tilde{\Omega}} c_{\tilde{\omega}} \cos(\tilde{\omega}t' + \theta_{\tilde{\omega}}) \tag{4.1.30}$$

characterises the spectrum emitted by the source, as well as how the component frequencies interact with each other depending on the distribution of $\theta_{\tilde{\omega}}$ and their correlation structure. Equation (4.1.29) can then be written more compactly as

$$\hat{p}(\mathbf{x},\omega) = \frac{\omega\rho}{4} \int_{-\infty}^{\infty} F(t';\theta_{\tilde{\Omega}})\, e^{-i\omega t'}\, \mathcal{H}_0^{(2)}\left(\omega \frac{|\,\mathbf{x}-\mathbf{v}t'\,|}{c}\right) dt'\,, \tag{4.1.31}$$

where it becomes apparent that $\hat{p}$ is itself a random quantity.

### 4.1.4 Analytical kernel for a band-limited source train with random-phase emitted frequency components

The stacking average interferometric retrieval from the recordings of the form (4.1.31) at a receiver pair $\mathbf{x_A}$ and $\mathbf{x_B}$ can be written for a source travelling at speed $\mathbf{v}$ as

$$\begin{aligned}\mathbb{E}[\,\hat{h}(\mathbf{x_A},\mathbf{x_B},\mathbf{v},\omega)\,] &= \frac{2}{\rho c}\,\mathbb{E}[\,\hat{p}^*(\mathbf{x_A},\omega)\hat{p}(\mathbf{x_B},\omega)\,] \\ &= \frac{\omega^2\rho}{8c}\int_{-\infty}^{\infty}\int_{-\infty}^{\infty}\mathbb{E}[\,F(t';\theta_{\tilde{\Omega}})F(t'';\theta_{\tilde{\Omega}})\,]\,e^{-i\omega(t''-t')} \\ &\qquad\times\,\mathcal{H}_0^{(1)}\left(\omega\,\frac{|\,\mathbf{x_A}-\mathbf{v}t'\,|}{c}\right)\mathcal{H}_0^{(2)}\left(\omega\,\frac{|\,\mathbf{x_B}-\mathbf{v}t''\,|}{c}\right)dt'dt''\end{aligned} \tag{4.1.32}$$

For an arbitrary discrete source spectrum $\tilde{\Omega}$ and associated source signature in the form of (4.1.30), the generalised average source kernel in an ambient noise interferometric retrieval is given by

$$\begin{aligned}\mathbb{E}[\,F(t';\theta_{\tilde{\Omega}})F(t'';\theta_{\tilde{\Omega}})\,] = \sum_{\tilde{\omega}\in\tilde{\Omega}} c_{\tilde{\omega}}^2\Big(&\cos(\tilde{\omega}t')\cos(\tilde{\omega}t'')\;\mathbb{E}[\,\cos^2(\theta_{\tilde{\omega}})\,] \\ &-\sin(\tilde{\omega}(t'+t''))\;\mathbb{E}[\,\cos(\theta_{\tilde{\omega}})\sin(\theta_{\tilde{\omega}})\,] \\ &+\sin(\tilde{\omega}t')\sin(\tilde{\omega}t'')\;\mathbb{E}[\,\sin^2(\theta_{\tilde{\omega}})\,]\Big) \\ +\sum_{\tilde{\omega}\in\tilde{\Omega}}\sum_{\substack{\tilde{\omega}'\in\tilde{\Omega}\\ \tilde{\omega}\neq\tilde{\omega}'}} c_{\tilde{\omega}}c_{\tilde{\omega}'}\Big(&\cos(\tilde{\omega}t')\cos(\tilde{\omega}'t'')\;\mathbb{E}[\,\cos(\theta_{\tilde{\omega}})\cos(\theta_{\tilde{\omega}'})\,] \\ &-\cos(\tilde{\omega}t')\sin(\tilde{\omega}'t'')\;\mathbb{E}[\,\cos(\theta_{\tilde{\omega}})\sin(\theta_{\tilde{\omega}'})\,] \\ &-\sin(\tilde{\omega}t')\cos(\tilde{\omega}'t'')\;\mathbb{E}[\,\sin(\theta_{\tilde{\omega}})\cos(\theta_{\tilde{\omega}'})\,] \\ &+\sin(\tilde{\omega}t')\sin(\tilde{\omega}'t'')\;\mathbb{E}[\,\sin(\theta_{\tilde{\omega}})\sin(\theta_{\tilde{\omega}'})\,]\Big),\end{aligned} \tag{4.1.33}$$

where the double summation is split into diagonal terms and cross-terms $\tilde{\omega}\neq\tilde{\omega}'$. Equation (4.1.33) shows that the standard ensemble average operator depends on the phases of the emitted frequency components of the source, as well as their correlation.

For example, consider the case when the source spectrum is a regular partition of a

bounded interval, that is $\tilde{\Omega} = \{\tilde{\omega}_j\}_{j=1}^{|\tilde{\Omega}|}$ for some finite spacing $\triangle\tilde{\omega} = \tilde{\omega}_{j+1} - \tilde{\omega}_j$, and associated random phase shifts $\theta_j$ for each frequency $\tilde{\omega}_j$. Moreover, assume that the random shifts are such that $\theta_j \sim \text{Unif}(0, 2\pi)$ for all $j \in \{1, \ldots, |\tilde{\Omega}|\}$. Further, assume that the phase shifts $\theta_j$ and $\theta_k$ are independent whenever $\tilde{\omega}_j \neq \tilde{\omega}_k$. These assumptions result in the following probability distributions for the random variables in (4.1.33)

$$\sin(\theta)\,, \cos(\theta) \sim \text{ArcSin}(-1, 1)\,,$$

$$\sin(\theta)\cos(\theta) \sim \text{ArcSin}\left(-\tfrac{1}{2}, \tfrac{1}{2}\right)\,,$$

and

$$\sin(\theta)^2\,,\ \cos^2(\theta) \sim \text{ArcSin}(0, 1)\,,$$

where $\text{ArcSin}(a, b)$ denotes the arcsine probability distribution over the bounded support $(a, b)$. Moreover, assume that the coefficients $c_{\tilde{\omega}}$ in (4.1.30) do not depend on the individual frequencies $\tilde{\omega}$, and let this coefficient be denoted henceforth simply as $c_{\tilde{\Omega}}$. Then the random source kernel (4.1.33) reduces to the deterministic expression

$$\mathbb{E}\,[\,F(t';\theta_{\tilde{\Omega}})F(t'';\theta_{\tilde{\Omega}})\,] = c_{\tilde{\Omega}}^2 \frac{1}{|\tilde{\Omega}|} \sum_{j=0}^{|\tilde{\Omega}|} \cos(\,\tilde{\omega}_j(t'' - t')\,). \tag{4.1.34}$$

Next, one can deduce in a standard fashion Rudin (1976) that

$$\mathbb{E}\,[\,F(t';\theta_{\tilde{\Omega}})F(t'';\theta_{\tilde{\Omega}})\,] \underset{\substack{\triangle_{\tilde{\omega}}\to 0 \\ |\tilde{\Omega}|\triangle_{\tilde{\omega}} = const.}}{\longrightarrow} \frac{c_{\tilde{\Omega}}^2}{\tilde{\omega}_{\max} - \tilde{\omega}_{\min}} \int_{\tilde{\omega}_{\min}}^{\tilde{\omega}_{\max}} \cos(\tilde{\omega}(t'' - t'))d\tilde{\omega}\,,$$

where $\triangle_{\tilde{\omega}} = \tilde{\omega}_{j+1} - \tilde{\omega}_j$ and $\tilde{\omega}_{\max} - \tilde{\omega}_{\min} = |\tilde{\Omega}|\triangle_{\tilde{\omega}}$, which leads to

$$\mathbb{E}\,[\,F(t';\theta_{\tilde{\Omega}})F(t'';\theta_{\tilde{\Omega}})\,] \approx\ c_{\tilde{\Omega}}^2\, \frac{\sin(\,\tilde{\omega}_{\max}(t'' - t)\,) - \sin(\,\tilde{\omega}_{\min}(t'' - t)\,)}{(\tilde{\omega}_{\max} - \tilde{\omega}_{\min})(t'' - t')}\,. \tag{4.1.35}$$

Finally, the right hand side of equation (4.1.35) can be expanded using well-known trigonometric identities to derive

$$\mathbb{E}\,[\,F(t';\theta_{\tilde{\Omega}})F(t'';\theta_{\tilde{\Omega}})\,] \approx c_{\tilde{\omega}}^2 \cos\left(\frac{(\tilde{\omega}_{\max} + \tilde{\omega}_{\min})}{2}\,(t'' - t')\right) \text{sinc}\left(\frac{(\tilde{\omega}_{\max} - \tilde{\omega}_{\min})}{2}\,(t'' - t')\right) \tag{4.1.36}$$

The kernel equation (4.1.36) is parametrised in time. Under the assumption that the source is in motion, that is $\mathbf{v} \neq 0$, equation (4.1.36) leads to expression (4.2.9). To see this, let $\mathbf{x}'$

be the source location at time $t'$, and $\mathbf{x}''$ the source location at time $t''$, so that $\mathbf{x}' = [\,|\mathbf{v}|t',\, 0\,]$ and $\mathbf{x}'' = [\,|\mathbf{v}|t'',\, 0\,]$. Hence

$$|t'' - t'| = \frac{||\mathbf{v}|t'' - |\mathbf{v}|t'|}{|\mathbf{v}|} = \frac{|\mathbf{x}'' - \mathbf{x}'|}{|\mathbf{v}|}\,. \tag{4.1.37}$$

Combining equations (4.1.36) and (4.1.37) yields an expression proportional to equation (4.2.9).

Figure 4.3 illustrates the situation where the interferometric trace retrieved via equation (4.1.4) from a train of sources differs significantly from the retrieval obtained from individually recorded impulsive sources, according to equation (4.1.1). Both retrievals are based on sources on the same boundary $S$ and recorded over the same time interval, except that the impulses in the train of sources are generated in a time-ordered sequence of physical locations which span $S$. When the sources are individually recorded (bottom of Figure 4.3)

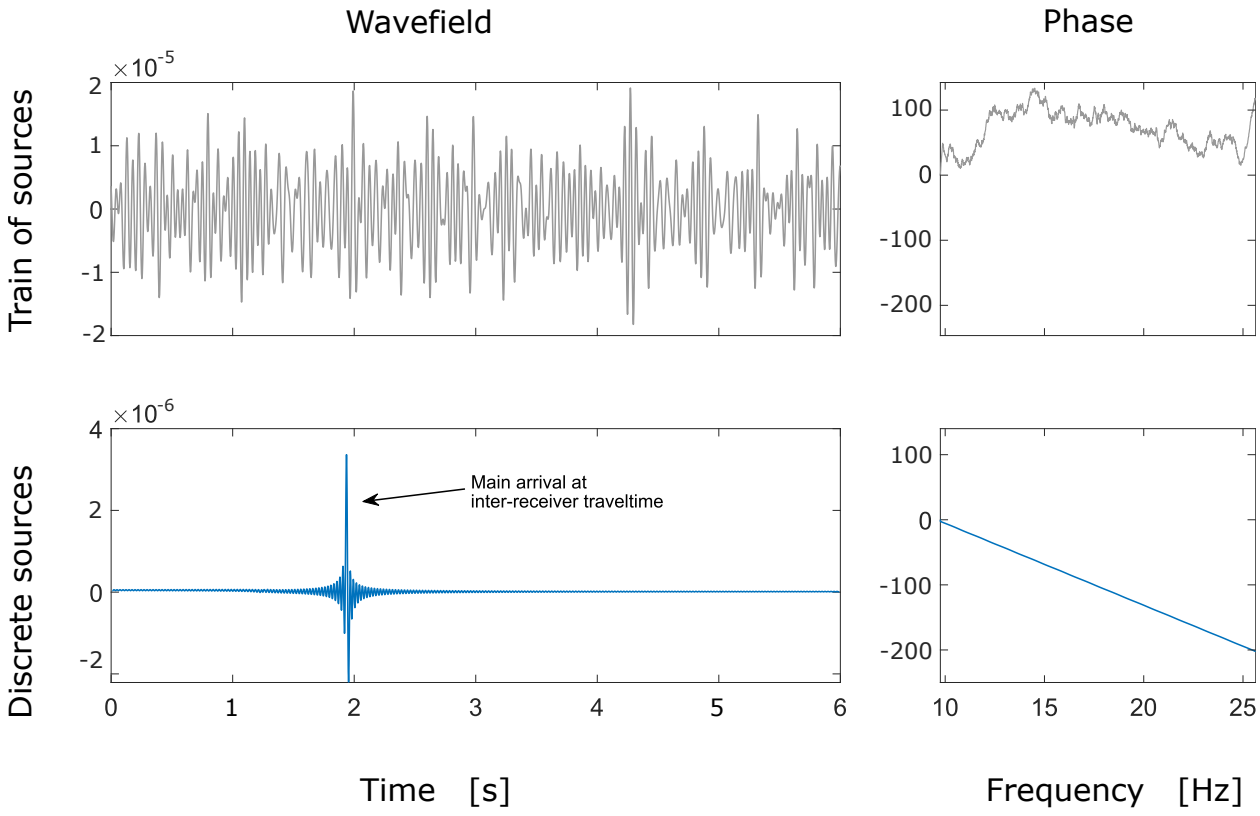


**Figure 4.3:** Comparison of the interferometric estimate of the Green's function from a simulated train of sources as per equation (4.1.4) (**top**), versus the estimate from a boundary of static point sources (**bottom**) recorded individually, according to equation (4.1.1). The left side panels show the waveforms in time, while the panels to the right show the corresponding estimated phases (unwrapped). The source train moves along the boundary line at 25 m/s (90 km/h) and emits sound in a frequency range between 10 and 25 Hertz. The receiver pair is oriented perpendicularly to the source boundary and 2000 m away from each other. Sound speed in the medium was set at 1000 m/s. The receiver closest to the source boundary was 400 m away.

the inter-receiver Green's function is retrieved accurately with the main arrival found around 2 s, which corresponds to the inter-receiver travel time. In the top panels, the inter-receiver arrival is completely obscured by spurious arrivals, and the phase does not reproduce the reference estimate in the bottom panels.

In addition to the above issues, if the noise source is in motion, one must take into account both the spatiotemporal correlations of the noise sources, as well as the Doppler effect which shifts the energy emitted by the source at each frequency to a range of other recorded frequencies, even if the source is monochromatic. The instantaneous frequency $\breve{\omega}(\mathbf{x}, t')$ of the train of sources recorded at location $\mathbf{x}$ and time $t'$ can be derived analytically from equation (4.1.3) when it is used to represent a continuously moving source, resulting in the following expression (see the derivation of equation (4.1.27) in Appendix 4.1.1)

$$\breve{\omega}(\mathbf{x}, t') = \frac{\tilde{\omega}}{1 - \frac{|\mathbf{v}|}{c} \cos\theta_{\mathbf{x}}(t')}, \tag{4.1.38}$$

where $\tilde{\omega}$ is the frequency emitted by the source, and $\theta_{\mathbf{x}}(t')$ is the angle between the line from the instantaneous source location at time $t'$ to the receiver location $\mathbf{x}$, and the source-line $S$. Equation (4.1.38) agrees with the well-known expressions for the Doppler shift for the instantaneous frequency when the source is moving directly towards, or away from, the receiver. However, it is more general in that it quantifies the Doppler spread in the recorded frequency in terms of the relative source-receiver position angle $\theta_{\mathbf{x}}(t')$, when the source has an azimuthal velocity component. It is clear from equation (4.1.38) that for a pair of distinct receivers $\mathbf{x_A}$ and $\mathbf{x_B}$, the corresponding relative position angles of the source $\theta_{\mathbf{x_A}}(t')$ and $\theta_{\mathbf{x_B}}(t')$ will be different; this means that the same source emitting the single frequency $\tilde{\omega}$ will be recorded with a different frequency at each location. Figure 4.4 illustrates the relationship between the instantaneous location of a moving noise source and the recorded frequency $\breve{\omega}$ at each receiver $\mathbf{x_A}$ and $\mathbf{x_B}$. As expected, the recorded frequency is higher when the source is moving towards the receivers, and lower as it moves away. Clearly, as can be deduced from equation (4.1.38) and observed in Figure 4.4, the only (instantaneous) location of the source that will lead to recording the true emitted frequency occurs when the source is collinear with the pair of receivers, and the line through $\mathbf{x_A}$ and $\mathbf{x_B}$ is perpendicular to the boundary $S$; depending on the geometry of the problem, such a location need not exist. Thus, in general, the frequency emitted by a moving noise source and recorded at the receivers will differ from the true frequency $\tilde{\omega}$, and the frequency bias will be different at $\mathbf{x_A}$ and $\mathbf{x_B}$ at all instantaneous locations except when the source is collinear with the receiver pair.

This has important implications for wavefield interferometry, since recordings at any particular frequency will usually have been emitted at different source locations. For example, in

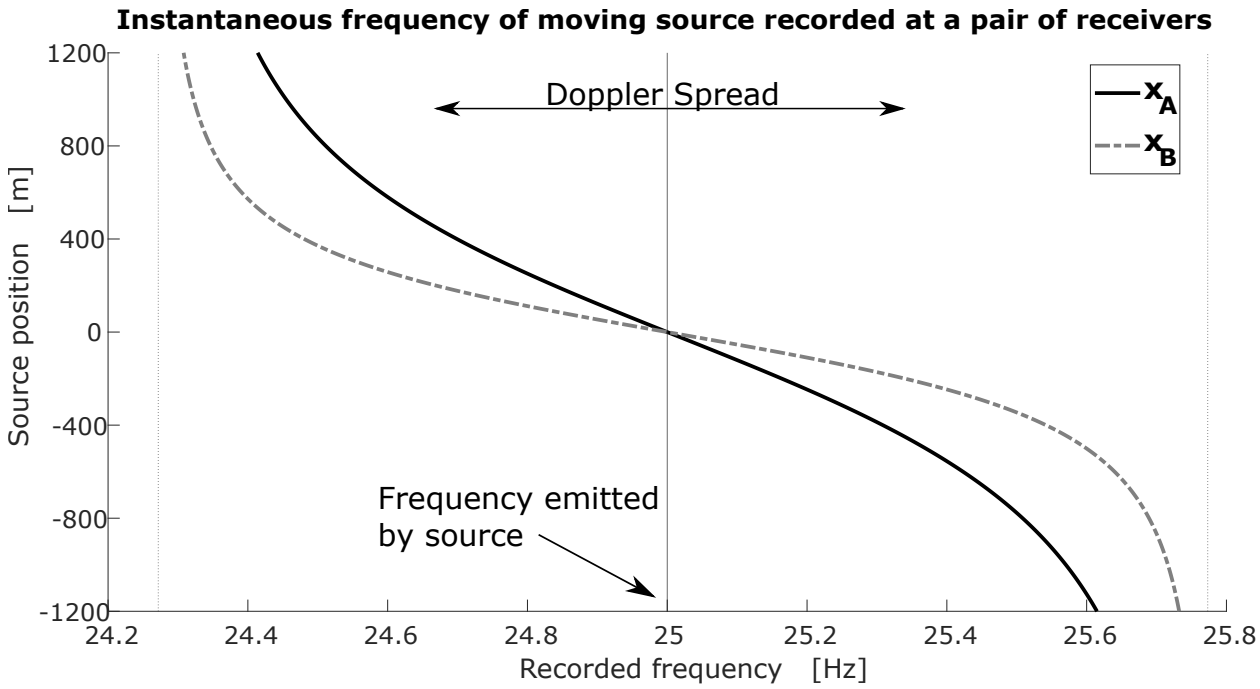


**Figure 4.4:** Relationship between source location and instantaneous frequency recorded at two different receiver locations $\mathbf{x_A}$, and $\mathbf{x_B}$. The simulated source was travelling at 30 m/s (108 km/h) and the medium speed was set at 1000 m/s. For illustration purposes the source was set to be monochromatic, emitting noise at a fixed frequency of 25 Hz. The limiting values for the Doppler spread, given by $25/(1 \pm |\mathbf{v}|/c)$ Hz, are marked with vertical dotted lines.

Figure 4.4 the spectrum value recorded at 24.5 Hz would have been emitted by a source that was 800 m along the boundary for receiver $\mathbf{x_A}$, but only 400 m for receiver $\mathbf{x_B}$. Given that interferometry is performed frequency by frequency, this inconsistency in the recorded frequency is conceptually equivalent to introducing further spurious contributions from spatially incongruous source locations. Moreover, in the case of a more realistic broadband source the spread and consequent interaction among different frequencies becomes compounded, with multiple source locations along the boundary $S$ introducing spatially incongruous contributions for every recorded frequency. Hence, the Doppler shift associated with moving noise sources further compounds the spurious effects inherent to ambient noise interferometry if we use the retrieval (4.1.2).

Equation (4.1.38) shows that the Doppler shift is amplified for higher frequencies, as well as increasing source train speeds. In addition, larger inter-receiver distances, as well as near-field recordings, will increase the discrepancies in frequencies recorded $\mathbf{x_A}$ and $\mathbf{x_B}$, resulting in further deterioration of the interferometric retrieval. Figure 4.5 illustrates the deterioration of the interferometric retrieval $h(t)$ as the source speed $\mathbf{v}$ increases. To produce this figure, the receiver pair was placed perpendicularly oriented with respect to the source line, and

the inter-receiver distance was set at 2000 m. The medium speed was $c = 1000$ m/s and the train of sources was simulated at increasing speeds from 10 m/s to 100 m/s, emitting noise at a frequency range between 10 Hz and 25 Hz. In order to produce comparable estimates, the recording time was adjusted for each value of the source speed to ensure the source traversed the exact same spatial boundary $S$ in all cases. In Figure 4.5 one can see that at the slowest source speed (10 m/s, bottom of the Figure), the inter-receiver arrival emerges clearly at about two seconds, whereas at higher source speeds acausal arrivals become more prevalent, and the inter-receiver arrival finally becomes indistinguishable from the surrounding noise when the source is travelling at 100 m/s (top of the Figure). Because the spatial coverage of the source is the same in all traces shown in Figure 4.5, the increased prevalence of spurious arrivals can be attributed directly to the increase in source speed and subsequent increase in the differential Doppler spread (see Figure 4.4).

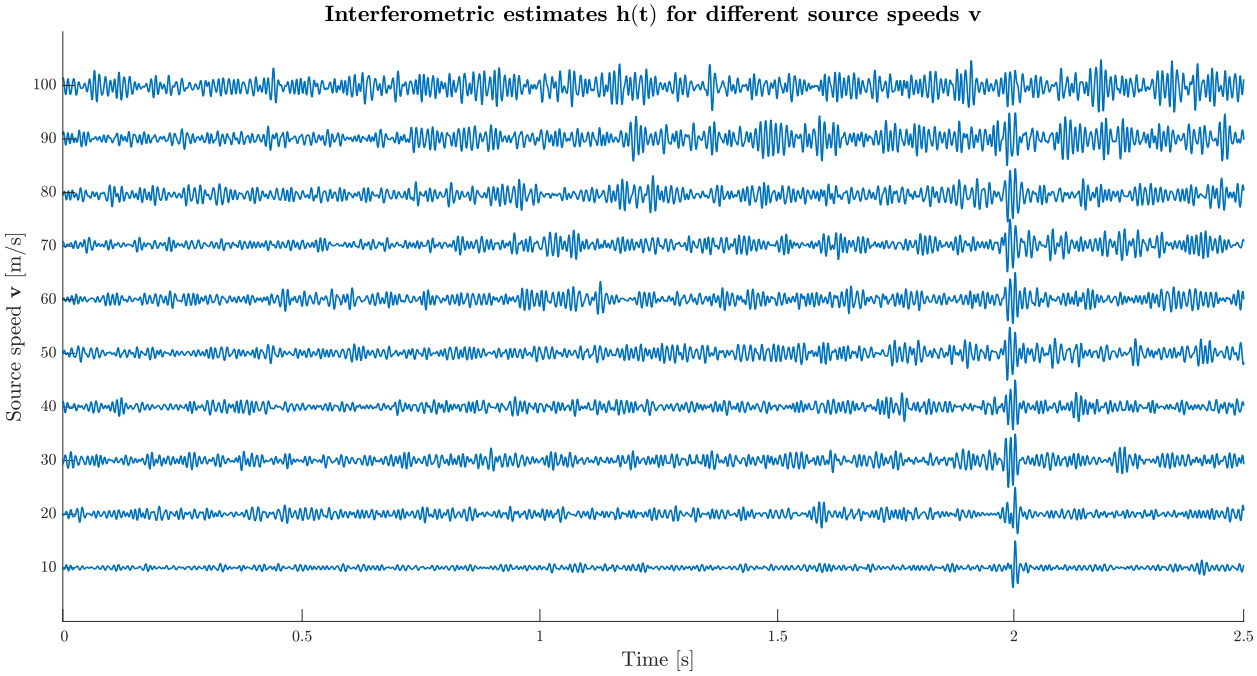


**Figure 4.5:** Waveforms of the ambient noise retrieval $h(t)$ obtained from a recorded train of sources travelling at increasing speeds $\mathbf{v}$. The medium speed was set at $c = 1000$ m/s and the train of sources moved at a range of speeds varying from 36 km/h to 360 km/h (10 m/s to 100 m/s) and emitted noise in the frequency range of 10 Hz to 25 Hz. The recording time for each source speed was adjusted to ensure the source traversed the same spatial boundary $S$ in every case. The inter-receiver distance was of 2000 m. The amplitudes have been normalised.

Similarly, Figure 4.6 shows the deterioration of the estimated inter-receiver signal $h(t)$ when the inter-receiver distance increases (left panel), and when the distance from the receivers to the source line increases (right panel).

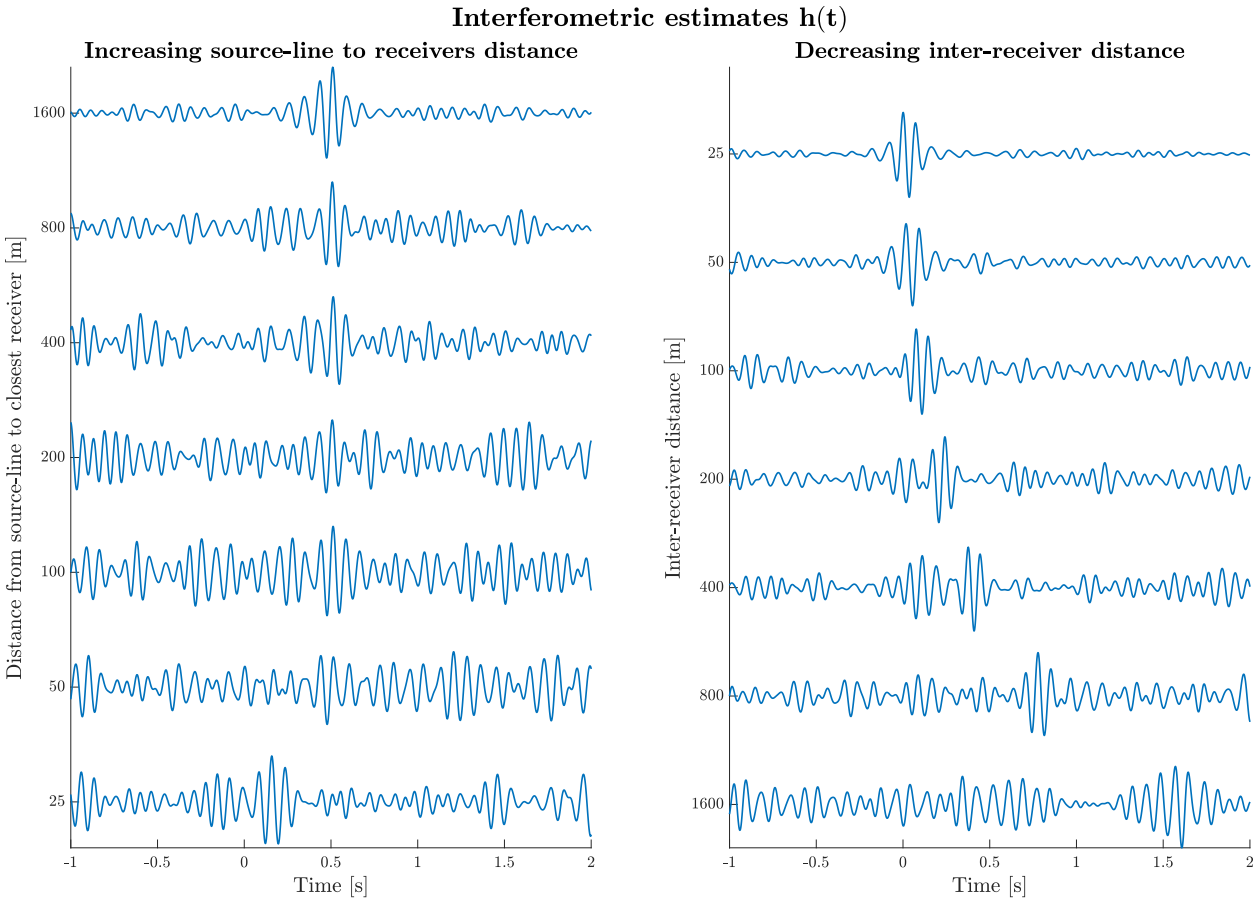


**Figure 4.6:** Waveforms of the ambient noise retrieval $h(t)$ obtained from a recorded train of sources for decreasing inter-receiver distances (**right**) and increasing source-line to receiver distances (**left**). The medium speed was set at $c = 1000$ m/s, and the train of sources moved at a fixed speed of 90 km/h (25 m/s), emitting noise in the frequency range of 10 Hz to 25 Hz. The recording time was 300 s in all cases. The receiver pairs were always oriented perpendicularly to the source line. In the left panel, the inter-receiver distance was fixed at 500 m and the distance to the source line was varied from 25 m to 1600 m. In the right panel, the distance to the source line was fixed at 500 m, and the inter-receiver distance ranges from 25 m to 1600 m. A portion of the acausal negative-time axis is included for illustration purposes. All amplitudes have been normalised.

Some of the potential obstacles for retrieving inter-receiver Green's functions from sources in motion have been considered theoretically by Sabra (2010), where the inconsistency induced by the differential Doppler effect at the receivers is mitigated via a stationary phase approximation, consistent with the discussion above, but under the assumption that the ambient noise sources are statistically uncorrelated in time. More recent work by Liu et al. (2021), applies standard ambient noise interferometry (4.1.2) to an expression for the wavefield generated by a train, and the potential retrievable wave types are discussed using intuitive ray-path arguments which are then tested on train recordings. However, the explicit role of the source speed in the retrieval, and systematic methods for mitigating these effects

have not been addressed (and the Doppler effect is not considered in the latter study).

In summary, the crosstalk terms associated with the integrand in equation (4.1.2) for $\mathbf{x}' \neq \mathbf{x}''$ emerge naturally in systematic ambient noise interferometry analysis but their effects are commonly removed from considerations by imposing the assumption that the ambient noise field is uncorrelated. Such an assumption greatly simplifies the theoretical retrieval procedure, but it is often unrealistic. This is the case, for example, when performing traffic or railway noise interferometry. Moreover, ambient noise interferometry (4.1.2) using moving point sources must contend with the Doppler effect, in addition to the unavoidable correlations between the noise sources.

We discuss consequences of these issues in detail in the following Section, where we point out that the delta-correlated assumption is unnecessarily restrictive, and that excluding near-diagonal terms reduces uncertainty in the retrieved amplitudes. We show in detail how the success of the standard stacking procedure depends on the properties of the source signature and on the source speed in cases where the noise sources are in motion. Moreover, we show how this standard stacking technique may fail, and propose an alternative workflow in Section 4.3 which proves to be successful at isolating terms from the incongruous crosstalk terms, leading to the extraction of the underlying inter-receiver phase regardless of the presence of correlation in the ambient noise field. Finally, for the scenario where the presence of correlation is caused by motion of the source, the workflow presented implicitly mitigates spurious contributions due the Doppler spread as explained above.

## 4.2 Standard stacking technique

A commonly used averaging procedure in ambient noise interferometry (stacking), relies on the arithmetic average over several interferometric retrievals $\hat{h}(\mathbf{x_A}, \mathbf{x_B}, \omega)$ in equation (4.1.2))—e.g., Wapenaar and Fokkema (2006). Here, we define *stacking* more formally as the operation consisting of taking the statistical average of functions evaluated on an ensemble of recordings of the ambient noise field over some time interval; we denote such an ensemble average by $\mathbb{E}[\,\cdot\,]$. Below, we formally link the interferometric retrieval (4.1.2) to the retrieval (4.1.1) and determine conditions leading to the likely failure of the stacking average retrieval when the ambient noise field is correlated.

Application of the stacking average operator to the ambient noise retrieval represented via equation (4.1.4) leads to

$$\mathbb{E}[\,\hat{h}(\mathbf{x_A}, \mathbf{x_B}, \omega)\,] = \frac{2}{\rho c} \int_S \int_S \mathbb{E}[\,\hat{F}^* \hat{F}\,](\mathbf{x}', \mathbf{x}'', \omega)\, \hat{G}^*(\mathbf{x_A}, \mathbf{x}', \omega) \hat{G}(\mathbf{x_B}, \mathbf{x}'', \omega) d\mathbf{x}'\, d\mathbf{x}''\,, \quad (4.2.1)$$

where

$$\mathbb{E}[\,\hat{F}^*\hat{F}\,](\mathbf{x}',\mathbf{x}'',\omega) := \mathbb{E}\left[\,\hat{F}^*(\mathbf{x}',\omega)\hat{F}(\mathbf{x}'',\omega)\,\right] \tag{4.2.2}$$

is referred to as the *kernel of the stacking average* or simply as the *stacking average kernel*. This is determined by the correlation structure of the noise source characteristics $\hat{F}$.Recall that for brevity of notation we consistently skip the explicit dependence of $\hat{F}$ in equation (4.2.1) on the particular recording of ambient noise, and that for any fixed $\mathbf{x}$ and $\omega$, the source signature $\hat{F}(\mathbf{x},\omega)$ should be thought of as a random variable, since it is associated with the Fourier transform of the ambient noise recording $p(\mathbf{x},t)$. The stacking average $\langle\,\cdot\,\rangle$ is linear by construction and we assume that the order of integration is irrelevant (Fubini's theorem is satisfied). Please note that the averaging in $\mathbb{E}[\,\hat{h}(\mathbf{x_A},\mathbf{x_B},\omega)\,]$ effectively couples the two integrals which contribute to the single-recording ambient noise retrieval $\hat{h}(\mathbf{x_A},\mathbf{x_B},\omega)$ in equation (4.1.4). The formula in equation (4.2.1) formally highlights the link between $\hat{g}(\mathbf{x_A},\mathbf{x_B},\omega)$ in equation (4.1.1), the stacked ambient noise retrieval $\mathbb{E}[\,\hat{h}(\mathbf{x_A},\mathbf{x_B},\omega)\,]$, and the properties of the stacking average kernel $\mathbb{E}[\,\hat{F}^*\hat{F}\,]$. Clearly, the properties of the kernel of the stacking average control the discrepancy between $\mathbb{E}[\,\hat{h}(\mathbf{x_A},\mathbf{x_B},\omega)\,]$ and $\hat{g}(\mathbf{x_A},\mathbf{x_B},\omega)$, which one is interested in minimizing.

In particular, the common interferometric assumption that the ambient noise field is uncorrelated leads to the stacking average kernel in equation (4.2.1) of the form

$$\mathbb{E}[\,\hat{F}^*\hat{F}\,](\mathbf{x}',\mathbf{x}'',\omega) \propto \delta(\mathbf{x}'-\mathbf{x}'')|\hat{s}(\omega)|^2\,, \tag{4.2.3}$$

where $\hat{s}(\omega)$ is the power spectrum of the ambient noise source. There is a further implicit assumption in equation (4.2.3) that the power spectrum of the source does not depend on the spatial variables. Clearly, if equation (4.2.3) holds, evaluating the integrals in equation (4.2.1) leads to

$$\mathbb{E}[\,\hat{h}(\mathbf{x_A},\mathbf{x_B},\omega)\,] \propto \hat{g}(\mathbf{x_A},\mathbf{x_B},\omega)|\hat{s}(\omega)|^2\,, \tag{4.2.4}$$

where $\hat{g}(\mathbf{x_A},\mathbf{x_B},\omega)$ represents the retrieval from individually recorded discrete sources defined by equation (4.1.1). The result in equation (4.2.4) implies that even in the idealized scenario when equation (4.2.3) holds, ambient noise interferometry does not generally allow for accurate retrieval of the amplitude of the Green's function due to the presence of the noise power spectrum $|\hat{s}(\omega)|^2$, and the lack of individual source recordings which could allow for a source-specific spectrum correction. On the other hand, the estimated phase remains unaffected by the presence of the real factor $|\hat{s}(\omega)|^2$ in equation (4.2.4). Note also that in practice, one has to consider empirical averages in equations (4.2.1)–(4.2.3) based on a finite number of ambient noise recordings instead of the abstract stacking in terms of the statistical

average over an 'infinite' number of recordings implied by the operator $\langle \cdot \rangle$. In such a case, if the relationship in equation (4.2.3) holds in the limit of averaging over several samples tending to infinity, it can be shown that the acausal contributions from off-diagonal, incongruent source locations (i.e., when $\mathbf{x}' \neq \mathbf{x}''$) decay with the number of samples and equation (4.2.4) holds asymptotically. A related derivation of a bound on the signal-to-noise ratio can be found in Appendix B of van Manen et al. (2006), and Weaver and Lobkis (2005) discuss the rate of convergence for a statistically uncorrelated model using the signal-to-noise ratio.

The requirement that ambient noise be delta-correlated in space is restrictive and it is often unrealistic to assume in applications. As pointed out in van Dalen et al. (2014), most sources in practice are, unsurprisingly, neither fully correlated nor fully uncorrelated, with source correlation slowing down convergence to the inter-receiver Green's function (Kimman and Trampert, 2010). Although some advances have been made in the context of simultaneously acting sources (Wapenaar et al., 2012; van Dalen et al., 2015) based on deconvolution techniques to tackle the resulting underdetermined systems, further investigation of such deconvolution techniques is required. Nevertheless, the relationship in equations (4.2.3) and (4.2.4) is desirable, as it allows for the retrieval of correct phases of the associated Green's functions from equation (4.2.1). Therefore, in what follows we consider approaches which resemble the relationship in equation (4.2.3) but without the requirement for the spatially uncorrelated noise sources. The remainder of this Section is devoted to the analysis of the stacking average through the properties of the stacking average kernel $\mathbb{E}[\,\hat{F}^*\hat{F}\,]$ in equation (4.2.2). A new approach, which exploits a different averaging kernel and applies to both correlated and uncorrelated noise sources, is proposed and analyzed in Section 4.3.

To gain a theoretical insight into the ambient noise retrieval, we decompose equation (4.1.4) as

$$\hat{h}(\mathbf{x_A}, \mathbf{x_B}, \omega) = \hat{g}_\epsilon(\mathbf{x_A}, \mathbf{x_B}, \omega) + \hat{x}_\epsilon(\mathbf{x_A}, \mathbf{x_B}, \omega)\,, \tag{4.2.5}$$

where $\epsilon \geqslant 0$ and

$$\hat{g}_\epsilon(\mathbf{x_A}, \mathbf{x_B}, \omega) = \frac{2}{\rho c} \int\limits_{\mathbf{x}' \in S} \int\limits_{\substack{\mathbf{x}'' \in S \\ |\mathbf{x}' - \mathbf{x}''| < \epsilon}} \hat{F}^*(\mathbf{x}', \omega) \hat{F}(\mathbf{x}'', \omega)\, \hat{G}^*(\mathbf{x_A}, \mathbf{x}', \omega) \hat{G}(\mathbf{x_B}, \mathbf{x}'', \omega)\, d\mathbf{x}''\, d\mathbf{x}'\,, \tag{4.2.6}$$

and

$$\hat{x}_\epsilon(\mathbf{x_A}, \mathbf{x_B}, \omega) = \frac{2}{\rho c} \int\limits_{\mathbf{x}' \in S} \int\limits_{\substack{\mathbf{x}'' \in S \\ |\mathbf{x}' - \mathbf{x}''| \geqslant \epsilon}} \hat{F}^*(\mathbf{x}', \omega) \hat{F}(\mathbf{x}'', \omega)\, \hat{G}^*(\mathbf{x_A}, \mathbf{x}', \omega) \hat{G}(\mathbf{x_B}, \mathbf{x}'', \omega)\, d\mathbf{x}''\, d\mathbf{x}'\,. \tag{4.2.7}$$

The term $\hat{g}_\epsilon(\mathbf{x_A}, \mathbf{x_B}, \omega)$, referred to hereafter as the *$\epsilon$-diagonal term*, accounts for the contributions from sources such that $|\mathbf{x}' - \mathbf{x}''| < \epsilon$, and one might consider sufficiently small $\epsilon \geqslant 0$, in order to minimize the contribution from acausal arrivals from incongruous source locations in $\hat{g}_\epsilon$. The decomposition in equation (4.2.5) holds for any choice of $\epsilon \geqslant 0$ but taking $\epsilon \to 0$ does not necessarily remove all acausal arrivals from $\hat{g}_\epsilon$ for moving noise sources, as explained in the discussion in Section 4.1. However, the aim of the above decomposition is to find an appropriate choice of the *spatial correlation length cut-off* $\epsilon$ so that $\hat{g}_\epsilon$ is dominated by the coherent terms, whereas $\hat{x}_\epsilon$ is dominated by the acausal contributions due to incongruous source locations. Please note that the decomposition in equation (4.2.5) could be applied to the integral with respect to $\mathbf{x}'$ instead of $\mathbf{x}''$ without loss of generality.

Finally, we consider the stacking average of the decomposition in equation (4.2.5) given by

$$\mathbb{E}[\,\hat{h}(\mathbf{x_A}, \mathbf{x_B}, \omega)\,] = \mathbb{E}[\,\hat{g}_\epsilon(\mathbf{x_A}, \mathbf{x_B}, \omega)\,] + \mathbb{E}[\,\hat{x}_\epsilon(\mathbf{x_A}, \mathbf{x_B}, \omega)\,] \tag{4.2.8}$$

with the aim of linking the characteristics of the stacking average kernel $\mathbb{E}[\,\hat{F}^*\hat{F}\,](\mathbf{x}', \mathbf{x}'', \omega)$ to the spatial correlation length cut-off $\epsilon$ in the above decomposition. Please note that in this Section no specific assumptions have been made about the source or its spectrum, as the representation (4.1.3) used to arrive at equations (4.2.5) and (4.2.8) is general.

## Interferometric retrieval from spatially correlated noise due to a source in motion

To show the usefulness of the $\epsilon$-diagonal decomposition (4.2.5) in interferometric analysis, we consider a specific but common example of a broadband source train travelling at speed $\mathbf{v} \neq 0$ and emitting sound within the frequency band $[\tilde{\omega}_{\min}, \tilde{\omega}_{\max}]$, such that the phases for different emitted frequencies are random and independent from each other (we address correlation of the phase across different frequencies below), i.e., for each frequency $\tilde{\omega}$ emitted by the source, there is a corresponding random phase shift $\theta_{\tilde{\omega}}$ uniformly distributed between 0 and $2\pi$, and we assume that the phase shifts $\theta_{\tilde{\omega}}$ and $\theta_{\tilde{\omega}'}$ are independent whenever $\tilde{\omega} \neq \tilde{\omega}'$. In such a case we find (see equation (4.1.36) for details) that the stacking average kernel in equation (4.2.2) is given by

$$\mathbb{E}[\,\hat{F}^*\hat{F}\,](\mathbf{x}', \mathbf{x}'', \omega) = \cos\left(\bar{\tilde{\omega}}\frac{|\mathbf{x}'' - \mathbf{x}'|}{|\mathbf{v}|}\right) \operatorname{sinc}\left(\tfrac{1}{2}\Delta_{\tilde{\omega}}\,\frac{|\mathbf{x}'' - \mathbf{x}'|}{|\mathbf{v}|}\right) |\hat{s}(\omega)|^2, \tag{4.2.9}$$

which depends on the train speed $\mathbf{v} \neq 0$, the mean emitted frequency $\bar{\tilde{\omega}} := \frac{1}{2}(\tilde{\omega}_{\max} + \tilde{\omega}_{\min})$ and the bandwidth $\Delta_{\tilde{\omega}} := \tilde{\omega}_{\max} - \tilde{\omega}_{\min}$, and where $\operatorname{sinc}(x) := \sin(x)/x$. The model and the resulting stacking average kernel (4.2.9) implicitly take account of the Doppler effect

(see model derivations in Appendix 4.1.1). Expression (4.2.9) for the kernel holds for non-monochromatic sources travelling at speeds $\mathbf{v} \neq 0$, and for sources whose spectrum can be represented in the form equation (4.1.30). In the limit of $\Delta_{\tilde{\omega}} \to 0$, i.e., when the source is monochromatic with frequency $\tilde{\omega}$, this kernel reduces to $\mathbb{E}[\,\hat{F}^*\hat{F}\,](\mathbf{x}', \mathbf{x}'', \omega) = \cos(\tilde{\omega}(|\mathbf{x}'' - \mathbf{x}'|)|\hat{s}(\omega)|^2)/|\mathbf{v}|$ which is no longer localized. See remarks under equation (4.1.28) in Appendix 4.1.1 concerning a more general model that allows for appropriate localization. For simplicity, we consider the parametrization of the straight boundary $S$ given by $\mathbf{x} = (\,x,\, 0\,)$, where $x = 0$ corresponds to the location where the line through the receiver pair intersects the boundary $S$, so that $\mathbf{x}' = (\,x',\, 0\,)$ and similarly $\mathbf{x}'' = (\,x'',\, 0\,)$. Using this parametrization we have that $|\mathbf{x}' - \mathbf{x}''| = |x' - x''|$ in equation (4.2.9). For further details see equation (4.1.37) and accompanying remarks in Appendix 4.1.4.

The movement of the noise source allows us to parameterize any locations $\mathbf{x}', \mathbf{x}'' \in S$ via the travel time so that $\mathbf{x}' = (\,|\mathbf{v}|t'\,,0\,)$ and $\mathbf{x}'' = (\,|\mathbf{v}|t'',\, 0\,)$. The analytical expression for the stacking average kernel associated with a broadband correlated train of sources allows one to identify the approximate correlation length beyond which the envelope of the kernel (4.2.9) decays rapidly. The unwanted long-range correlations contributing to the kernel away from the neighborhood of $\mathbf{x}' = \mathbf{x}''$, $\mathbf{x}', \mathbf{x}'' \in S$, represent the main contribution to $\left\langle \hat{h}(\mathbf{x_A}, \mathbf{x_B}, \omega) \right\rangle$ in equation (4.2.8) from the acausal arrivals. Based on equation (4.2.9), we set the spatial correlation length cut-off $\epsilon$ to twice the value of the first zero of the envelope of the stacking average kernel (see the bottom panel of Figure 4.7), which is given by

$$\epsilon = \frac{|\mathbf{v}|}{\tilde{\omega}_{\max} - \tilde{\omega}_{\min}}\,, \tag{4.2.10}$$

for non-monochromatic sources travelling at speeds $\mathbf{v} \neq 0$. Figure 4.7 shows the numerically approximated stacking average kernel $\mathbb{E}[\,\hat{F}^*\hat{F}\,](\mathbf{x}', \mathbf{x}'', \omega)$ and its exact form (4.2.9). The rate of decay of the source kernel in terms of the spatial discrepancy $|\mathbf{x}' - \mathbf{x}''|$ is controlled by the envelope of the $\mathrm{sinc}(x)$ factor in equation (4.2.9). As noted before, the spatial discrepancy can be represented in terms of the travel times so that $|\mathbf{x}' - \mathbf{x}''| = |t' - t''||\mathbf{v}|$, where $\mathbf{v}$ is the train speed.

Although the choice of the spatial correlation cut-off length $\epsilon$ has so far been somewhat arbitrary, the main principle in its determination is to use the structure of the stacking average kernel $\mathbb{E}[\,\hat{F}^*\hat{F}\,]$ in order to approximately identify the correlation length beyond which the crosstalk terms dominate the correlation structure represented by $\mathbb{E}[\,\hat{F}^*\hat{F}\,]$. In the ideal case of statistically uncorrelated ambient noise, the interferometric phase estimate is robust in the sense that it converges to the inter-receiver phase under stacking (see equation (4.2.2)). In later sections it will be seen that this is not the case when the sources are

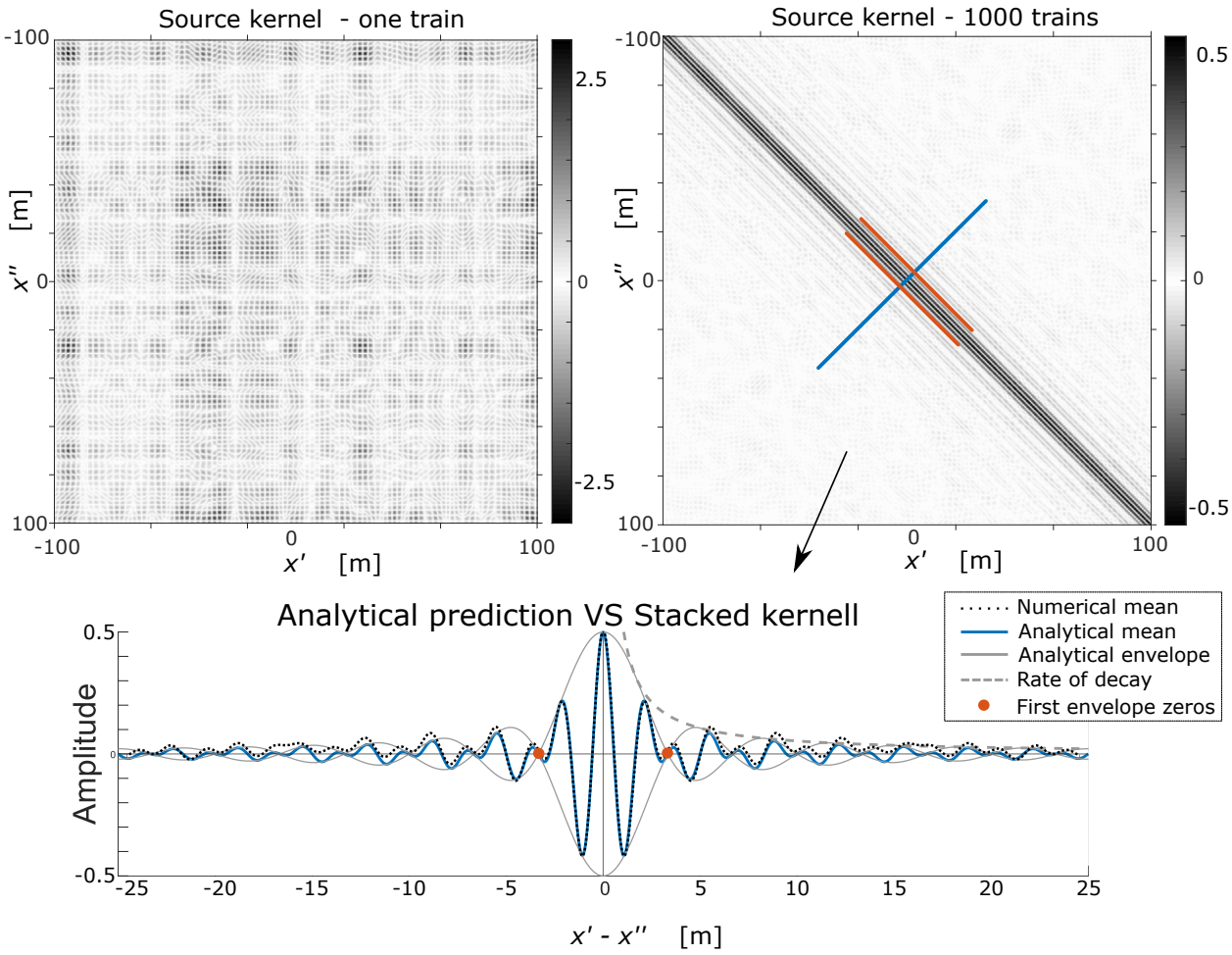


**Figure 4.7:** Example of the structure of the source kernel $\hat{F}^*(\mathbf{x}', \omega)\hat{F}(\mathbf{x}'', \omega)$ and the stacking average kernel $\mathbb{E}\left[\hat{F}^*\hat{F}\right](\mathbf{x}', \mathbf{x}'', \omega)$ derived in equation (4.2.9). Top left panel shows the spatial part of the source kernel (4.2.9) (i.e., without including the frequency-dependent term $|\hat{s}(\omega)|^2$) as a function of the location of a single train of sources recorded at each receiver. The simulated train travels at 90 km/h and its spectrum ranges from 10 Hz to 25 Hz. The top-right panel shows the kernel after stacking 1000 source train recordings, each five minutes long. The bottom panel compares the numerical anti-diagonal Section in black dashes, extracted from the numerical mean in the top-right panel, with the prediction given by equation (4.2.9) in blue, as well as its analytical envelope in solid grey and the rate of decay in dashed grey, in terms of the signed spatial discrepancy $x' - x''$, where the parametrization $\mathbf{x}' = (x', 0)$, $\mathbf{x}'' = (x'', 0)$ has been used. The rate of decay is derived from the envelope of the sinc factor in equation (4.2.9). The orange dots highlight the first pair of zeros of the analytical envelope, capturing the energy around the mean. The radius $\epsilon$ will be taken to be the distance between these zeros.

statistically correlated, and the choice of an appropriate cut-off length is critical in these non-ideal circumstances.

Please note that while the decomposition (4.2.5) and its stacking average equation (4.2.8) are given in the frequency domain to highlight the interaction between incongruous source

locations, the corresponding stacking average decomposition in the time domain is given by

$$h(\mathbf{x_A}, \mathbf{x_B}, t) = g_\epsilon(\mathbf{x_A}, \mathbf{x_B}, t) + x_\epsilon(\mathbf{x_A}, \mathbf{x_B}, t)\,, \tag{4.2.11}$$

and its stacking average is given by

$$\mathbb{E}[\,h(\mathbf{x_A}, \mathbf{x_B}, t)\,] = \mathbb{E}[\,g_\epsilon(\mathbf{x_A}, \mathbf{x_B}, t)\,] + \mathbb{E}[\,x_\epsilon(\mathbf{x_A}, \mathbf{x_B}, t)\,]\,. \tag{4.2.12}$$

The above time-domain decompositions hold due to the linearity of the inverse Fourier transform; as is standard in the interferometric literature, we assume throughout that $h$ is square-integrable in $t \in \mathbb{R}$ (so that the Fourier transform is well-defined on $h \in L^2(\mathbb{R})$) and that $\hat{F}$ and $\hat{G}$ are such that Fubini's theorem holds throughout. Thus, the diagonal band decompositions of $h$ and $\hat{h}$ are dual to each other and they can be considered interchangeably.

The formulation of the $\epsilon$-diagonal decomposition in the time domain (i.e., representation (4.2.11)) lends itself directly to the analysis based on time series recordings provided that a suitable spatial correlation length cut-off $\epsilon$ can be determined. When the noise source is in motion, as in the case considered here, the spatial correlation length cut-off $\epsilon$ has a temporal counterpart $T_\epsilon = \epsilon/|\mathbf{v}|$ for $\mathbf{v} \neq 0$. In Section 4.3, we will focus on a procedure for recovering the $\epsilon$-diagonal band structure, analogous to that in $\langle g_\epsilon \rangle$ in equation (4.2.12), from a single short recording when the value of the spatial correlation length cut-off $\epsilon$ cannot be estimated from the stacking average kernel. First, however, we outline the general properties of the stacking average and its potential pitfalls when retrieving the inter-receiver interferometric Green's function. To this end we consider two different classes of noise sources, and we compare the standard stacked retrieval $h(\mathbf{x_A}, \mathbf{x_B}, t)$ and its stacking average $\mathbb{E}[\,h(\mathbf{x_A}, \mathbf{x_B}, t)\,]$ with retrievals based on isolating the $\epsilon$-diagonal band terms $g_\epsilon(\mathbf{x_A}, \mathbf{x_B}, t)$ and $\mathbb{E}[\,g_\epsilon(\mathbf{x_A}, \mathbf{x_B}, t)\,]$ in the decomposition equations (4.2.11) and (4.2.12), respectively, using an 'informed' choice of the spatial correlation length cut-off $\epsilon$ given by equation (4.2.10).

In Figure 4.8 we use the spatial cut-off radius $\epsilon$ determined in equation (4.2.10) and apply the $\epsilon$-diagonal decomposition procedure laid out in equation (4.2.11). First, we assume that individual recordings are statistically independent. In particular, for a noise source with a broadband spectrum this constraint translates to the requirement that the frequencies associated with the random source signature $\hat{F}$ be independent. To generate this figure, a train of sources travelling at 90 km/h along a straight boundary and emitting sound between 10 Hz and 25 Hz was simulated to generate the ambient noise recordings $p(\mathbf{x_A}, t)$ and $p(\mathbf{x_B}, t)$. The receiver pair was oriented perpendicularly to the source-line, with an inter-receiver distance of 2000 m and the closest receiver 400 m from the source-line. The medium speed was set to 1000 m/s. The ambient noise recordings were transformed to the

frequency domain and $\hat{h}(\mathbf{x_A}, \mathbf{x_B}, \omega)$ was computed according to equation (4.1.2). Then the $\epsilon$-decomposition was calculated for a single run to generate the insets in the top row. The frequency-domain data were used to extract the phase in the top-right panel of Figure 4.8, as well as transformed back to the time domain to generate the time series $h(\mathbf{x_A}, \mathbf{x_B}, t)$, $g_\epsilon(\mathbf{x_A}, \mathbf{x_B}, t)$, and $x_\epsilon(\mathbf{x_A}, \mathbf{x_B}, t)$ in the top left panel of the same Figure. This procedure was repeated 1000 times and averaged to calculate $\langle \hat{h}(\mathbf{x_A}, \mathbf{x_B}, \omega) \rangle$, as well as its $\epsilon$-decomposition with the associated phases (**right**) and waveforms (**left**) in the bottom row of this figure.

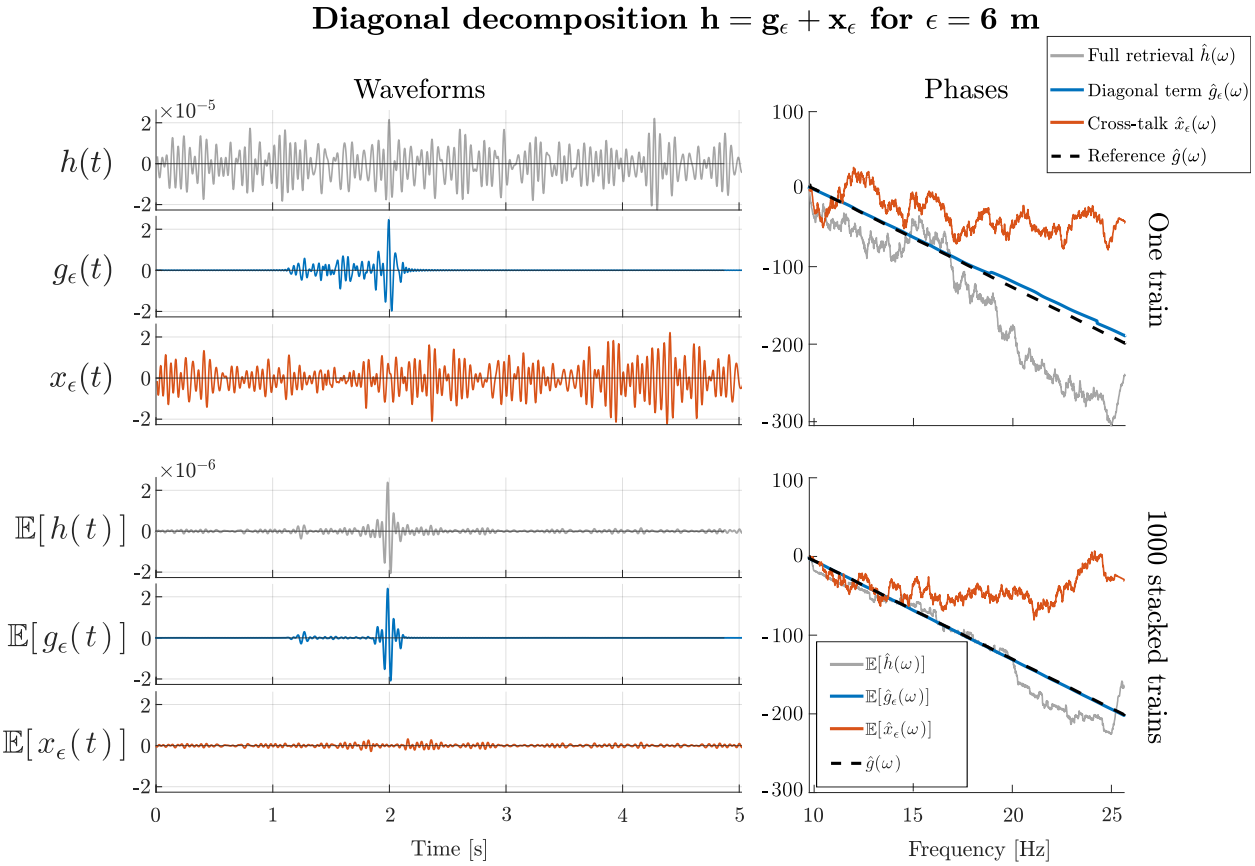


**Figure 4.8:** Example of the $\epsilon$-diagonal decomposition procedure (see equation (4.2.11)) and its stacking average version (equation (4.2.12)) for a train travelling at 90 km/h with the emitted spectrum between 10 Hz and 25 Hz. The receiver pair was perpendicularly oriented to the road, with an inter-receiver distance of 2000 m and a distance of 400 m from the source-line to the closest receiver. The medium speed was set at 1000 m/s. The value of $\epsilon = 6\,\text{m}$ ($T_\epsilon = 0.25$ s) is determined from equation (4.2.10)) for a single five-minute recorded source train (**top**) and for a stacked retrieval over 1000 five-minute train source recordings (**bottom**). The left panels show the waveforms of the components equations (4.2.11)) and (4.2.12)), and the right panels show the corresponding phases in the frequency domain obtained from the frequency representation of the retrieval given by equations (4.2.5) and (4.2.8). The retrieval $h(t)$ and its stacking average $\mathbb{E}[\,h(t)\,]$ are shown in grey, and their components $g_\epsilon(t)$, $\mathbb{E}[\,g_\epsilon(t)\,]$, and $x_\epsilon(t)$, $\mathbb{E}[\,x_\epsilon(t)\,]$, are shown in blue and orange, respectively. The phase plots include the phase of the inter-receiver Green's function (dashed black) estimated from discrete sources, as prescribed by equation (4.1.1) as a reference.

In this setup, and given the stacking average kernel in equation (4.2.9), the retrieval of the inter-receiver Green's function is shown in grey in both the temporal and the spatial domains, with the $\epsilon$-diagonal terms $g_\epsilon$, $\hat{g}_\epsilon$ in blue and the crosstalk $x_\epsilon$, $\hat{x}_\epsilon$ shown in orange. According to equation (4.2.10), we chose $\epsilon = 6$ m which corresponds to a time window length $T_\epsilon \approx 0.25$ s. The resulting spectra were transformed to the temporal domain via inverse Fourier transform to show the effect of the decomposition on the retrieved waveforms; the components of equation (4.2.11) are shown in the left panels of Figure 4.8. The decomposition was applied to a single five-minute recording of a source train (**top**), and to the averaged waveform resulting from stacking 1000 such recordings (**bottom**). The phases corresponding to each waveform are shown in the panels to the right in Figure 4.8.

This illustrates the improvement in the retrieval using the decomposition (4.2.5) which satisfactorily separates the causal contributions to the inter-receiver phase from the spurious crosstalk.

Note that the phase of $\mathbb{E}\left[\hat{h}(\omega)\right]$ in the bottom right panel of Figure 4.8 (in blue) typifies the phase retrieved from the standard ambient noise interferometry approach, which relies on averaging over stacked independent recordings of ambient noise of the form (4.1.2). Although stacking can clearly improve the quality of the retrieved phase of the inter-receiver Green's function, significant discrepancies remain. This is especially in the higher frequency range of the spectrum due to the increased influence of the Doppler shift, even for many stacked recordings. It should be noted that sources travelling at different speeds and overlapping with each other may help improve the rate of convergence of the standard stacking to the correct phase. On the other hand, the phase of the $\epsilon$-diagonal term $\hat{g}_\epsilon(\omega)$ shows a much better agreement with the uncorrelated reference estimate even for a single short recording (blue phase in top-right panel of Figure 4.8). Application of the stacking average to the $\epsilon$-diagonal term $\mathbb{E}\left[\,\hat{g}_\epsilon(\omega)\,\right]$ leads to a further but slight improvement over the standard stacking applied directly to $\hat{h}$ which is evident in the higher frequency range of the spectrum. This increased uncertainty for higher frequencies is to be expected given the presence of the Doppler shift.

Please further note that at this point the decomposition is solely theoretical, and not yet directly applicable, as this would require thorough knowledge of the source locations and signatures. A method to implement this decomposition in practice is presented in Section 4.3.

The above experiment indicates that although there is some flexibility in the choice of the spatial correlation length cut-off $\epsilon$, it is possible to carry out the $\epsilon$-diagonal decomposition (4.2.5) in a way which on average, largely separates the desired contributions from coherent sources and the crosstalk between incongruous source locations into two distinct terms $\hat{g}_\epsilon(t)$ and $\hat{x}_\epsilon(t)$ respectively. In the case of correlated moving noise sources, a sufficiently small correlation length cut-off $\epsilon$ results in attributing a significant proportion of

the coherent noise contributions which should be captured by $\hat{g}_\epsilon$ relative to the 'crosstalk' term $\hat{x}_\epsilon$; the situation is reversed for a sufficiently large $\epsilon$. If we were to evaluate these integrals explicitly in order to estimate the true phase, the challenge lies in determining an optimal value of the spatial correlation length cut-off $\epsilon$ that minimizes the error in the phase retrieval in the absence of knowledge of the spatial correlation structure contained in the stacking average kernel $\left\langle \hat{F}^* \hat{F} \right\rangle (\mathbf{x}', \mathbf{x}'', \omega)$ in equation (4.2.2).

It is worth noting that a successful phase retrieval of the inter-receiver Green's function based on the empirical average of stacked recordings fundamentally relies, via the law of large numbers, on the statistical independence of the individual recordings. In particular, for a noise source with a broadband spectrum this constraint translates to the requirement that the frequencies associated with the random source signature $\hat{F}$ are independent; otherwise, the empirical average of the stacked retrieval $\frac{1}{N} \sum_{n=1}^{N} \hat{h}^{(n)}(\mathbf{x_A}, \mathbf{x_B}, \omega)$ might still converge as $N \to \infty$ but there are no guarantees that the resulting limit $\left\langle \hat{h}(\mathbf{x_A}, \mathbf{x_B}, \omega) \right\rangle$ will lead to the recovery of the true inter-receiver phase. Figure 4.9 shows one such example, where the setup and parameters are identical to those in Figure 4.8, except that the phases of the frequencies emitted by the sources are no longer uncorrelated. Such a scenario would be likely to occur, for example, due to an interaction between sleepers on a rail track and the wheels of the train (Brenguier et al., 2019). Specifically, for each frequency $\tilde{\omega}$ emitted by the source, the random phases associated with each emitted frequency are such that for a pair of emitted frequencies $\tilde{\omega}$ and $\tilde{\omega}'$, $|\tilde{\omega} - \tilde{\omega}'| \ll 1$, the phase shifts satisfy $\theta_{\tilde{\omega}} = \theta'_{\tilde{\omega}} + r$, where $r$ is uniformly distributed between 0 and $2\pi$, so that the phase shifts $\theta_{\tilde{\omega}}$ and $\theta_{\tilde{\omega}'}$ are no longer uncorrelated.

The grey trace in the middle panel of Figure 4.9 shows the averaged waveform in the time domain obtained by stacking 1000 five-minute long recordings. In contrast to the result of the equivalent procedure shown in Figure 4.8 (bottom left), stacking the recordings does not converge (or does not converge sufficiently quickly) to the correct inter-receiver arrival, and the crosstalk term (orange) in the middle panel does not decay. The corresponding phases are shown in the right panel of Figure 4.9 with the phase estimated from stationary discrete sources (see equation (4.1.1) in dashed black as a reference. However, the phase of the inter-receiver signal is still successfully isolated by the $\epsilon$-diagonal decomposition (4.2.5), as indicated by the blue line, showing a good agreement with the phase of the inter-receiver Green's function estimated from discrete sources, as per equation (4.1.1).

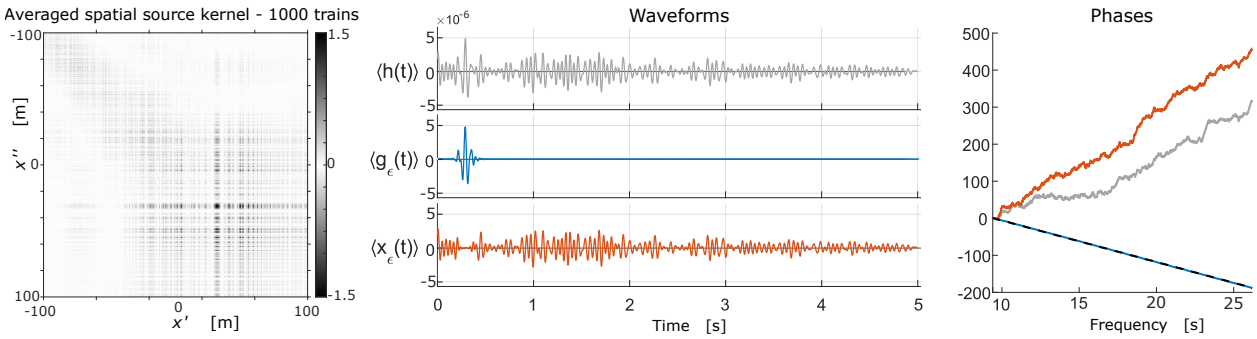


**Figure 4.9:** Example of a source signature from which the interferometric Green's function estimate cannot be retrieved by stacking. The left panel shows the numerical/empirical approximation of the stacking average kernel $\langle \hat{F}^* \hat{F} \rangle(\mathbf{x}', \mathbf{x}'', \omega)$ in equation (4.2.2) estimated by stacking 1000 trains of sources travelling at 90 km/h with an emitted spectrum between 10 Hz and 25 Hz. The receivers were placed perpendicularly to the source-line, with an inter-receiver distance of 200 m and the receiver closest to the source-line at a distance of 400 m. Away from the diagonal, non-zero elements persist. The middle panel shows the stacked waveform $\mathbb{E}[\, h(t) \,]$ and its $\epsilon$-diagonal decomposition into $\mathbb{E}[\, g_\epsilon(t) \,]$ and $\mathbb{E}[\, x_\epsilon(t) \,]$. The right panel shows the corresponding unwrapped phases for the full term $\mathbb{E}[\, \hat{h}(\omega) \,]$ (grey) and its decomposition into the $\epsilon$-diagonal term $\mathbb{E}[\, \hat{g}_\epsilon(\omega) \,]$ (blue) and the crosstalk term and $\mathbb{E}[\, \hat{x}_\epsilon(\omega) \,]$ (orange), as well as the phase of the inter-receiver Green's function (dashed black) estimated from discrete sources as per equation (4.1.1) as a reference. In this case, the stacking average kernel $\langle \hat{F}^* \hat{F} \rangle(\mathbf{x}', \mathbf{x}'', \omega)$ in equation (4.2.2) is not localized and the value of the correlation length cut-off $\epsilon$ was chosen according to the approach described in Section 4.3. The phase retrieval from $\mathbb{E}[\, \hat{g}_\epsilon(\omega) \,]$ and $\hat{g}_\epsilon(\omega)$ is similar and not shown.

Clearly, in most real-world applications it is not possible to gauge the retrieval against some reference benchmark, which leaves the retrieved results and the convergence trends open to subjective interpretation. Moreover, even if enough recorded data are available to allow for stacked averaging but the stacking average kernel $\langle \hat{F}^* \hat{F} \rangle(\mathbf{x}', \mathbf{x}'', \omega)$ in equation (4.2.2) is not spatially localized, there is no a priori criteria for estimating the appropriate value for the spatial correlation length cut-off $\epsilon$ needed in the decomposition (4.2.5) (compare the example in Figure 4.9 with that illustrated in Figures 4.7 and 4.8). The key point of these considerations is that in principle it remains possible to estimate the correct phase of the underlying Green's function from a single short recording of a correlated ambient noise source, and that the cause of the noise correlation is not relevant in such considerations.

In summary, in this Section we discussed a constructive example of the interferometric retrieval of the inter-receiver Green's function which was based on an abstract decomposition of the retrieval (4.1.2) as $\hat{h} = \hat{g}_\epsilon + \hat{x}_\epsilon$, as in equations (4.2.5) or (4.2.11), and based on an 'informed' choice of the spatial correlation length cut-off $\epsilon$ so that the undesirable crosstalk terms are largely contained in the $\hat{x}_\epsilon$ term. This construct, driven by analytical insight and illustrated in Figures 4.7–4.9, suggests that it should be possible to carry out such a decomposition and subsequently obtain the phase estimate of the inter-receiver Green's

function if a suitable correlation cut-off length $\epsilon$ can be estimated. Importantly, this approach would allow one to sidestep the classical stacking average approach and avoid its potential pitfalls. In the following Section we propose a workflow that facilitates the extraction of the interferometric phase estimate from a single short recording of a passing train (i.e., an instance of a moving correlated noise source). In fact, the choice of the correlation length cut-off $\epsilon$ in the example in Figure 4.9 was determined via a procedure described in the next Section, since in the setup of Figure 4.9 the stacking average kernel $\mathbb{E}[\,\hat{F}^*\hat{F}\,](\mathbf{x}', \mathbf{x}'', \omega)$ was not spatially localized due to implicit correlations between the noise sources.

## 4.3 The random windowing technique

Based on the analytical insight outlined in the previous sections, we consider the problem of estimating the phase of the inter-receiver Green's function from a single short recording of a train of sources, without resorting to the standard averaging over a stacked ensemble of recordings. Nevertheless, the retrieval based on this procedure effectively results in the extraction of the $\epsilon$-diagonal term in the decomposition $\hat{h}(\mathbf{x_A}, \mathbf{x_B}, \omega) = \hat{g}_\epsilon(\mathbf{x_A}, \mathbf{x_B}, \omega) + \hat{x}_\epsilon(\mathbf{x_A}, \mathbf{x_B}, \omega)$ introduced in equation (4.2.5), where $\epsilon$ is determined without the explicit knowledge of the stacking average kernel $\mathbb{E}[\,\hat{F}^*\hat{F}\,](\mathbf{x}', \mathbf{x}'', \omega)$ and the need for it to be localized. Importantly, the technique applies to both correlated and uncorrelated noise sources.

Consider a single time-domain recording of a train of sources at a receiver pair $\mathbf{x_A}$ and $\mathbf{x_B}$ and denote these recordings by, respectively, $p(\mathbf{x_A}, t)$ and $p(\mathbf{x_B}, t)$ whose Fourier transform leads to the retrieval $\hat{h}(\mathbf{x_A}, \mathbf{x_B}, \omega) = \hat{p}^*(\mathbf{x_A}, \omega)\hat{p}(\mathbf{x_B}, \omega)$ in equation (4.1.2), representing the interferometric approximation of the inter-receiver Green's function $\hat{G}(\mathbf{x_A}, \mathbf{x_B}, \omega)$. In the previous Section the correlation length cut-off $\epsilon$ had to be estimated from the stacking average kernel $\mathbb{E}[\,\hat{F}^*\hat{F}\,](\mathbf{x}', \mathbf{x}'', \omega)$ in equation (4.2.1), assuming that the stacking average had a localized kernel (e.g., Figure 4.7) which is not always the case for correlated noise sources (e.g., Figure 4.9). We now determine an optimal spatial/temporal window size that minimizes the effect of acausal arrivals in the interferometric retrieval from a single short recording. The approach relies on the use of an appropriate randomization technique, termed *random windowing*, in order to introduce incoherence into the acausal part of the phase in the retrieval $\hat{h}(\mathbf{x_A}, \mathbf{x_B}, \omega)$ in the available recording and mitigate the influence of the crosstalk terms, largely contained in $\hat{x}_\epsilon(\mathbf{x_A}, \mathbf{x_B}, \omega)$ of the $\epsilon$-diagonal decomposition of $\hat{h}(\mathbf{x_A}, \mathbf{x_B}, \omega)$, which hinder the accurate retrieval of the Green's function $\hat{G}(\mathbf{x_A}, \mathbf{x_B}, \omega)$.

### 4.3.1 General setup

First, consider the interferometric retrieval $h(\mathbf{x_A}, \mathbf{x_B}, t)$ in equation (4.1.2) obtained from recorded time series data within an interval/window of duration $T > 0$ and centered at some randomly drawn time $t_n$. For a pair of receiver locations $\mathbf{x_A}$ and $\mathbf{x_B}$ restrict the recorded time series $p(\mathbf{x_A}, t)$ and $p(\mathbf{x_B}, t)$ to that temporal window (see Figure 4.10). The random windowing method introduced below can be applied to recorded time series generated by arbitrary noise sources. However, in what follows we consider correlated noise generated by a source moving with speed $\mathbf{v} \neq 0$. This setup is relevant in applications, and it also aids understanding of the theoretical underpinning of the random windowing method, since it allows one to link the windowing of the time series to the corresponding spatial windowing, as illustrated in Figure 4.10.

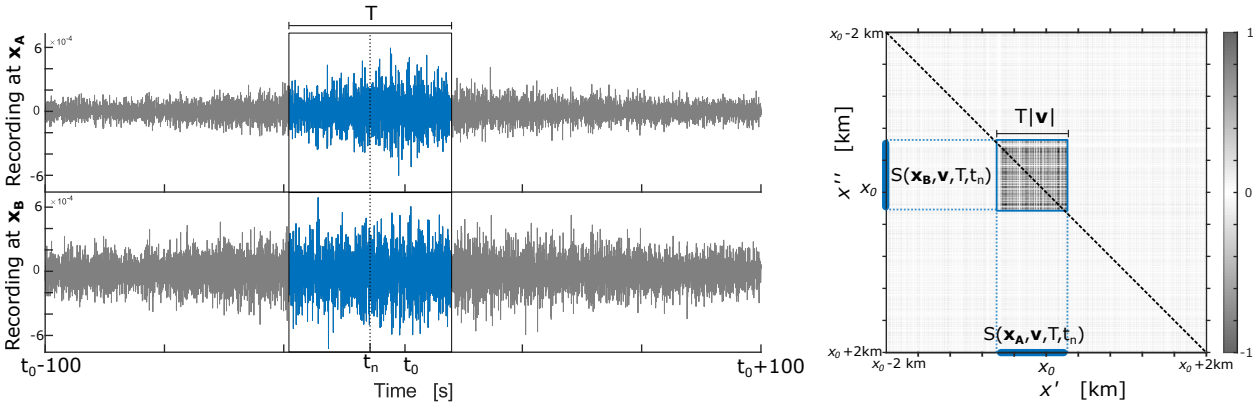


**Figure 4.10:** Illustration of the random windowing procedure for a single realization of a window of size $T$ in the temporal domain (**left**), and the corresponding window of length $T|\mathbf{v}|$ in the spatial domain (**right**) for $\mathbf{v} \neq 0$. The panels on the left show the waveforms recorded at a pair of receivers generated by a moving noise source. The approximate time at which the moving source is collinear with the receiver pair is denoted by $t_0$, and the location of a window of duration $T$ (blue) is centered around the randomly drawn time $t_n$. The background in the inset on the right shows the spatial part of the source kernel $\langle \hat{F}^*(\mathbf{x}', \omega)\hat{F}(\mathbf{x}'', \omega)\rangle$ in equation (4.2.1), where $\mathbf{x}_0$ corresponds to the spatial location of the moving source at time $t_0$. The boundary of the spatial window, centered at a random location $\mathbf{x}_n = t_n|\mathbf{v}|$, and its projections are highlighted in blue and denoted by $S(\mathbf{x}, \mathbf{v}, T, t_n)$ for each receiver; the resulting square window (of size $T|\mathbf{v}|$) is slightly off the diagonal. The parts of the source kernel excluded from this random window are greyed out.

For time series generated by arbitrary noise sources, $\mathbf{v}$ does not correspond to a physical velocity, and stands for an abstract parameter that allows for the space time transformation. Next, for a given average source velocity, the window of duration $T$ is linked to a spatial window which we define for a receiver location $\mathbf{x}$ as

$$S(\mathbf{x}, \mathbf{v}, T, t_n) = \Big\{\mathbf{x}' \in S : \mathbf{x}' = \mathbf{v}t' \text{ for } |t' - t_n| < \tfrac{1}{2}T\Big\}, \tag{4.3.1}$$

and which corresponds to the segment of the (spatial) source boundary traversed by the source moving at speed $\mathbf{v}$ from the origin at time zero, and recorded at a receiver location $\mathbf{x}$ within the time window of duration $T$ centered at $t_n$. As illustrated in the right panel of Figure 4.10, these boundary segments will differ for each receiver, depending on the inter-receiver distance, the distance to the source-line, and the speed of the source. The theoretical spatial location of $S(\mathbf{x}, \mathbf{v}, T, t_n)$ for each receiver can be calculated explicitly using equation (4.1.15) and scaling by the source speed (or by its estimated mean), as described in Section 4.1.1. The frequency-domain representation of the time-windowed data at each receiver can be expressed as

$$\begin{aligned} \hat{p}(\mathbf{x_A}, \omega\,;\, T, t_n) &= \int\limits_{S(\mathbf{x_A}, \mathbf{v}, T, t_n)} \hat{F}(\mathbf{x}', \omega)\hat{G}(\mathbf{x_A}, \mathbf{x}', \omega) d\mathbf{x}'\,, \\ \hat{p}(\mathbf{x_B}, \omega\,;\, T, t_n) &= \int\limits_{S(\mathbf{x_B}, \mathbf{v}, T, t_n)} \hat{F}(\mathbf{x}', \omega)\hat{G}(\mathbf{x_B}, \mathbf{x}', \omega) d\mathbf{x}'\,, \end{aligned} \tag{4.3.2}$$

where $S(\mathbf{x}, \mathbf{v}, T, t_n)$ is given by equation (4.3.1). Please note that explicit knowledge of the signals integrated along boundary sections is not required in practice, as the windowing procedure is performed directly on the full recorded time series. A source travelling at speed $|\mathbf{v}|$ will span a distance no greater than $|\mathbf{v}|T$ during a time window of duration $T$, so that for any random time window location $t_n$ the corresponding spatial location $\mathbf{x}_n = |\mathbf{v}|t_n$ satisfies $|\mathbf{x}' - \mathbf{x}_n| \leqslant |\mathbf{v}|T$. Restricting the time window size to $T$ will implicitly restrict the spatial locations contributing to the cross-correlation terms, and it will limit the crosstalk between incongruous source locations. Choosing the set of source locations $\mathbf{x}'$ such that $|\mathbf{x}' - \mathbf{x}_n| \leqslant |\mathbf{v}|T$ allows us to write a recording equation (4.3.2) in a manner consistent with representation (4.1.3); namely

$$\hat{p}(\mathbf{x}, \omega\,;\, T, t_n) := \int\limits_{S} \hat{F}(\mathbf{x}', \omega)\hat{G}(\mathbf{x}, \mathbf{x}', \omega)\, \chi_{\{|\mathbf{x}' - \mathbf{x}_n| \leq T|\mathbf{v}|\}}(\mathbf{x}')\, d\mathbf{x}'\,, \tag{4.3.3}$$

where $\chi_A(\mathbf{x})$ is the indicator function of a set $A$; i.e., $\chi_A(\mathbf{x}) = 1$ if $\mathbf{x} \in A$ and $\chi_A(\mathbf{x}) = 0$ if $\mathbf{x} \notin A$. Then, applying the ambient noise retrieval equation (4.1.2) to the time-windowed recordings (see Figure 4.10) for a window of duration $T$ centered at $t_n$ results in the windowed retrieval.

$$\hat{h}(\mathbf{x_A}, \mathbf{x_B}, \omega\,;\, T, t_n) := \frac{2}{\rho c}\, \hat{p}^*(\mathbf{x_A}, \omega\,;\, T, t_n)\, \hat{p}(\mathbf{x_B}, \omega\,;\, T, t_n)$$

$$= \frac{2}{\rho c} \int_S \int_S \hat{F}^*(\mathbf{x}', \omega) \hat{F}(\mathbf{x}'', \omega) \hat{G}^*(\mathbf{x}, \mathbf{x}', \omega) \hat{G}(\mathbf{x}, \mathbf{x}'', \omega)$$

$$\times \chi_{\{|\mathbf{x}'-\mathbf{x}_n| \le T|\mathbf{v}|\}}(\mathbf{x}') \, \chi_{\{|\mathbf{x}''-\mathbf{x}_n| \le T|\mathbf{v}|\}}(\mathbf{x}'') \, d\mathbf{x}' d\mathbf{x}'', \tag{4.3.4}$$

where the second equality is derived by substituting equation (4.3.3) for each recording, and recasting the resulting product of integrals in a manner consistent with the form of equation (4.1.4). Please note that as in equation (4.1.4), the term $\hat{F}^*(\mathbf{x}', \omega)\hat{F}(\mathbf{x}'', \omega)$ is still present in equation (4.3.4), and one could consider applying the standard stacking to equation (4.3.4). However, if the resulting stacked source kernel $\mathbb{E}[\, \hat{F}^*(\mathbf{x}', \omega)\hat{F}(\mathbf{x}'', \omega)\,]$ is not sufficiently localized (as discussed in Section 4.2), there are no guarantees that we will retrieve the correct inter-receiver phase. Instead, we consider a new averaging operator which relies on averaging over randomized window locations $t_n$. We denote this operator by $\mathbb{E}_T[\,\cdot\,]$ and define it for a scalar function $\gamma : \mathbb{R} \to \mathbb{R}$ as

$$\mathbb{E}_T\,[\,\gamma\,] := \int_{\mathbb{R}} \gamma(\tau) f_T(\tau) d\tau, \tag{4.3.5}$$

where $f_T$ is the probability density function associated with the choice of locations $t_n$ which is parameterized by $T$ and assumed to be non-zero only on a bounded interval, and the function $\gamma$ is integrable with respect to $f_T$. Next, we define the *averaged retrieval for a time window of duration* $T$ as

$$\begin{aligned} \hat{h}_T(\mathbf{x_A}, \mathbf{x_B}, \omega) &:= \mathbb{E}[\, \hat{h}(\mathbf{x_A}, \mathbf{x_B}, \omega\,;\, T,\, \cdot\,)\,]_T \\ &= \frac{2}{\rho c} \int_S \int_S \mathbb{E}_T[\chi\chi](\mathbf{x}', \mathbf{x}'') \hat{F}^*(\mathbf{x}', \omega) \hat{F}(\mathbf{x}'', \omega) \hat{G}^*(\mathbf{x}, \mathbf{x}', \omega) \hat{G}(\mathbf{x}, \mathbf{x}'', \omega) d\mathbf{x}' d\mathbf{x}\,, \end{aligned} \tag{4.3.6}$$

where we assume that Fubini's theorem is satisfied and the *random windowing averaging kernel* is defined as

$$\mathbb{E}_T\,[\,\chi\chi\,]\,(\mathbf{x}', \mathbf{x}'') := \mathbb{E}_T\,\left[\, \chi_{\{|\mathbf{x}'-\mathbf{x}_n| \le T|\mathbf{v}|\}}(\mathbf{x}')\, \chi_{\{|\mathbf{x}''-\mathbf{x}_n| \le T|\mathbf{v}|\}}(\mathbf{x}'')\right]. \tag{4.3.7}$$

Please note that given the above formulation and the $\epsilon$-diagonal decomposition (4.2.5), we have

$$\hat{h}_T(\mathbf{x_A}, \mathbf{x_B}, \omega) \propto \hat{g}_\epsilon(\mathbf{x_A}, \mathbf{x_B}, \omega), \qquad \epsilon = 2T|\mathbf{v}|. \tag{4.3.8}$$

Furthermore, similarly to standard averaging via the stacking of recordings as in equa-

tion (4.2.1), the structure of the random windowing averaging kernel determines the quality of the retrieval of the interferometric phase estimate from $\hat{h}_T(\mathbf{x_A}, \mathbf{x_B}, \omega)$. Note, in particular, that the random windowing averaging kernel $\mathbb{E}_T[\,\chi\chi\,](\mathbf{x}', \mathbf{x}'')$ is a symmetric function of the locations $\mathbf{x}', \mathbf{x}'' \in S$, and is concentrated in the neighborhood of $\mathbf{x}' = \mathbf{x}''$. Note also that the source speed $|\mathbf{v}|$ affects the properties of the random windowing averaging kernel. As suggested by the results illustrated in Figure 4.10 and confirmed by analytical estimates for a typical setup in Section 4.3.2, the random windowing procedure has an analogous effect to the $\epsilon$-localization procedure in decomposition (4.2.8) in the sense that interactions between incongruous source locations are implicitly restricted to within the time/space window of the recordings before cross-correlating. Hence, the contribution of the acausal crosstalk is mitigated. Moreover, if sufficient data are available, one can additionally apply the standard stacking operation to $\hat{h}_T(\mathbf{x_A}, \mathbf{x_B}, \omega)$ which yields the general retrieval

$$\mathbb{E}[\,\hat{h}_T(\mathbf{x_A}, \mathbf{x_B}, \omega)\,] = \frac{2}{\rho c} \int_S \int_S \mathbb{E}[\,\hat{F}^*(\mathbf{x}', \omega)\hat{F}(\mathbf{x}'', \omega)\,]\,\mathbb{E}[\,\chi_{\{|\mathbf{x}'-\mathbf{x}_n|\le T|\mathbf{v}|\}}(\mathbf{x}')\,\chi_{\{|\mathbf{x}''-\mathbf{x}_n|\le T|\mathbf{v}|\}}(\mathbf{x}'')\,]_T \times \hat{G}^*(\mathbf{x}, \mathbf{x}', \omega)\hat{G}(\mathbf{x}, \mathbf{x}'', \omega)\, d\mathbf{x}' d\mathbf{x}'', \tag{4.3.9}$$

since the standard stacking operator $\mathbb{E}\,[\,\cdot\,]$ and the window randomization operator $\mathbb{E}_T[\cdot]$ are independent by design, and therefore they commute. Importantly, the form of (4.3.9) implies that the random window average and the stacking average play, in principle, a similar role in the elimination of the crosstalk contributions in the ambient noise retrieval, in the spirit of the $\epsilon$-diagonal decomposition (4.2.5). For $T \ll 1$ the random windowing kernel $\langle \chi\chi \rangle_T$ will concentrate the integrand in (4.3.9) to within the $\mathcal{O}(T|\mathbf{v}|)$ neighborhood of $\mathbf{x}' = \mathbf{x}''$. A similar effect is achieved if enough data are available, and the noise sources are such that the stacking average kernel $\langle \hat{F}^* \hat{F} \rangle$ localizes around $\mathbf{x}' = \mathbf{x}''$ (see Section 4.2 and Figure 4.7). In principle, both operations can be applied concurrently. However, in contrast to the stacking average, the use of random windowing averaging relies on a single recording provided that a suitable value $T$ of the time window can be determined; derivation of such a procedure described in Sections 4.3.3 and 4.3.4 is preceded by an example which is aimed at elucidating the main properties of the random windowing average.

### 4.3.2 Example: Uniformly distributed window locations

Consider a default situation in which the temporal window location $t_n$ is uniformly distributed within the interval $D = \big[t_0 - T,\ t_0 + T\big]$. We then have

$$f_T(t_n) = \frac{1}{2T}, \qquad \big\langle t_n \big\rangle_T = t_0, \qquad \mathrm{Var}(t_n) = \big\langle (t_n - t_0)^2 \big\rangle_T = T^2/3.$$

Then, if we define the spatial source location at time $t_n$ as $\mathbf{x}_n = t_n \mathbf{v}$, we have $\big\langle \mathbf{x}_n \big\rangle_T = \mathbf{v} t_0 = \mathbf{x}_0$. Applying the operator $\mathbb{E}_T[\,\cdot\,]$ with the uniform density $f_T$ to the product of the indicator functions in equation (4.3.7) corresponds to the convolution of two boxcar functions of constant height one and width $T|\mathbf{v}|$, parameterized in terms of the source location discrepancy $|\mathbf{x}' - \mathbf{x}''|$, $\mathbf{x}', \mathbf{x}'' \in S$.

A standard calculation shows that applying operator $\mathbb{E}_T[\,\cdot\,]$ to the product of indicator functions in equation (4.3.9) yields a symmetric kernel in the random windowing averaging of the form

$$\begin{aligned} \mathbb{E}\big[\, \chi_{\{|\mathbf{x}' - \mathbf{x}_n| \leq T|\mathbf{v}|\}}(\mathbf{x}')\, \chi_{\{|\mathbf{x}'' - \mathbf{x}_n| \leq T|\mathbf{v}|\}}(\mathbf{x}'') \,\big]_T &= \big( |\mathbf{x}' - \mathbf{x}''| + T|\mathbf{v}| \big)\, \Theta\big( |\mathbf{x}' - \mathbf{x}''| + T|\mathbf{v}| \big) \\ &\quad + \big( |\mathbf{x}' - \mathbf{x}''| - T|\mathbf{v}| \big)\, \Theta\big( |\mathbf{x}' - \mathbf{x}''| - T|\mathbf{v}| \big) \\ &\quad - 2|\mathbf{x}' - \mathbf{x}''|\, \Theta\big( |\mathbf{x}' - \mathbf{x}''| \big)\,, \end{aligned} \tag{4.3.10}$$

which represents the tent map supported on the interval $-2T|\mathbf{v}| \leqslant \mathbf{x}' - \mathbf{x}'' \leqslant 2T|\mathbf{v}|$ and centered at $\mathbf{x}' - \mathbf{x}'' = 0$, where $\Theta$ denotes the Heaviside function. An example of equation (4.3.10) is plotted in the right inset in Figure 4.11, where the kernel (4.3.10) is plotted in blue, and its approximation obtained via direct simulations is indicated by the dotted black line.

It is informative to compare the kernel $\big\langle \chi\chi \big\rangle_T$ of the random windowing average in equation (4.3.10) illustrated in Figure 4.11 with the stacking average kernel $\big\langle \hat{F}^* \hat{F} \big\rangle$ in equation (4.2.2) which is illustrated in Figure 4.7. Recall that both these kernels are present in the retrieval (4.3.9) and that they play, in principle, a similar role aimed at reducing the contribution from the off-diagonal, crosstalk terms into the retrieval. One can see that the random windowing procedure is akin to extraction of the $\epsilon$-diagonal term $\hat{g}_\epsilon$ in the decomposition (4.2.5), in the sense that for any pair of sources such that $|\mathbf{x}' - \mathbf{x}''| > 2T|\mathbf{v}|$ the random windowing kernel mutes the corresponding acausal contributions. For uniformly distributed locations of the random windows around $t_0$, only the contributions satisfying $|\mathbf{x}' - \mathbf{x}''| \leqslant 2T|\mathbf{v}|$ are included in the resulting retrieval (4.3.9). Moreover, the analytical expression (4.3.10) implies that the width of the diagonal band induced by the random windowing procedure

is directly proportional to the source speed $|\mathbf{v}|$. This suggests that a progressively shorter time window size $T$ should be chosen for increasing train speeds to mitigate acausal arrivals associated with the crosstalk terms in the ambient noise retrieval (4.2.5).

### 4.3.3 Estimation of the retrieval $\hat{h}_T(\mathbf{x_A}, \mathbf{x_B}, \omega)$

In this Section, we describe a procedure for the estimation of the random windowing average $\mathbb{E}_T[\,\cdot\,]$ with some fixed time window length $T > 0$. A systematic way of choosing the optimal time window size $T_{opt}$ for any given single recording by means of estimating the acausal energy present in each averaged retrieval $\hat{h}_T(\mathbf{x_A}, \mathbf{x_B}, \omega)$ in equation (4.3.6) is discussed in Section 4.3.4.

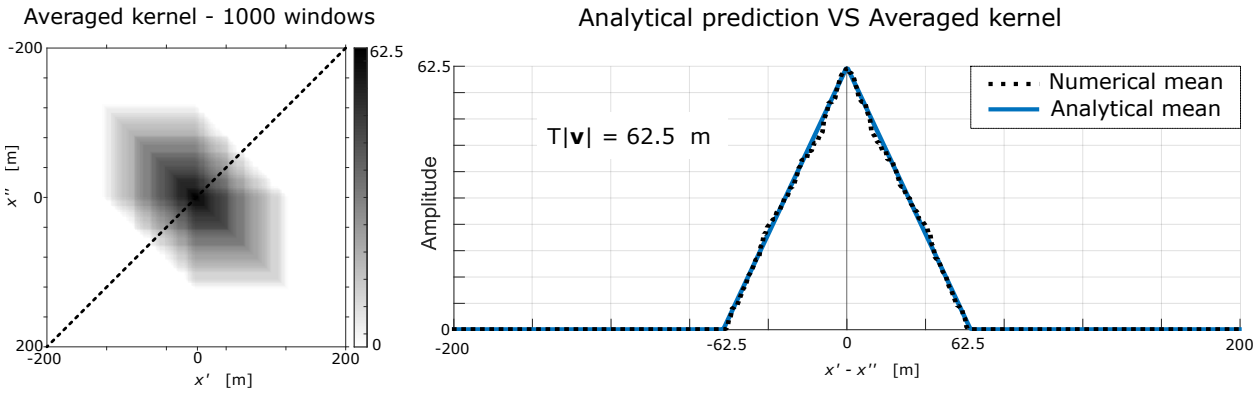


**Figure 4.11:** The structure of the kernel $\langle \chi\chi \rangle_T$ in equation (4.3.7) of random windowing averaging (4.3.6) based on the uniform distribution of window locations. The kernel is given by a tent map (4.3.10) with height $T|\mathbf{v}|$ and width $2T|\mathbf{v}|$, centered at $\mathbf{x}' = \mathbf{x}''$. The right panel shows the kernel parameterized in terms of the distance from the source locations $x'$ (for receiver $\mathbf{x_A}$) and $x''$ (for receiver $\mathbf{x_B}$) to the location of the source boundary with the receiver line (see the parametrization used in Figure 4.7); the analytical solution (4.3.10) is shown in blue and its approximation within the anti-diagonal section of the random windowing kernel (see the left panel) obtained via direct simulations is indicated by the dotted black line. The left panel shows the numerical approximation of the random window kernel based on 1000 windows for a single source train recording travelling at speed $|\mathbf{v}| = 25$ m/s (90 km/h), with $T = 2.5$ s. Compare the structure of the above random windowing kernel $\langle \chi\chi \rangle_T$ with the stacking average kernel $\langle \hat{F}^* \hat{F} \rangle$ illustrated in Figure 4.7. Both kernels are present in the general retrieval (4.3.9).

As outlined in Section 4.3.1 and illustrated in Section 4.3.2, the random windowing procedure will lead to an improved phase retrieval through damping the contributions from the cross-correlation terms in equation (4.3.9) provided that a suitable temporal window length $T > 0$ is identified, so that the random windowing kernel $\big\langle \chi\chi \big\rangle_T$ in equation (4.3.6) effectively enforces the recovery of the diagonal band term $\hat{g}_\epsilon$ in the decomposition (4.2.5). In the case of standard stacking the choice of the spatial correlation length cut-off $\epsilon$ can be inferred from the form of stacking average kernel $\langle \hat{F}^* \hat{F} \rangle$ in equation (4.2.2), assuming

that the kernel is sufficiently localized. Clearly, the structure of the stacking average kernel cannot be determined from a single short recording or in situations when the stacking average kernel can be estimated but it is not sufficiently localized (e.g., as in the example presented in Figure 4.9). On the other hand, the random windowing average with an appropriately chosen $T$ can be applied to obtain the retrieval $\hat{h}_T(\mathbf{x_A}, \mathbf{x_B}, \omega)$ in the most challenging case where only a single (possibly short) recording of a source train is available. Moreover, as mentioned earlier and expressed via equation (4.3.9), if enough recorded data are available, one can combine both averaging techniques to recover $\mathbb{E}[\,\hat{h}_T(\mathbf{x_A}, \mathbf{x_B}, \omega)\,]$. It is clear that the use of such a doubly averaged approach is more versatile than using only standard stacking in the absence of knowledge about the structure of the noise sources, and it will lead to an improved retrieval, as long as at least one of the kernels is sufficiently concentrated around the set $\mathbf{x}' = \mathbf{x}''$, $\mathbf{x}', \mathbf{x}'' \in S$.

The first step in the procedure for the empirical approximation of the random windowing average $\mathbb{E}_T[\,\cdot\,]$ with some fixed time window length $T$ is to identify the approximate time in the recorded traces when the source train is collinear with the receiver pair (see for instance Dales et al. (2020) for one example of a method that achieves this using plane-wave beamforming). We chose a configuration in which the line through the receiver pair is perpendicular to the source boundary, as depicted in Figure 2. In such a geometry the Fresnel zone of the receiver pair is symmetric about the stationary phase point (see van Dalen et al. (2015)) on the source boundary but this is not essential to the random windowing method. To see this note that when the instantaneous source location is collinear with the receiver pair the signal recorded at the two receivers is generated at $\mathbf{x}' = \mathbf{x}''$, and the frequency recorded at each receiver, as well as the Doppler bias, are the same ($\theta_{\mathbf{x_A}}(t') = \theta_{\mathbf{x_B}}(t')$ in equation (4.1.38)). Thus, in this instantaneous configuration the effect of spurious contributions to the retrieval is minimized. Finally, note that regardless of whether or not the noise source is in motion, the source location contained in the line through the receiver pair coincides with the stationary phase point (on the source boundary) which is always contained in the Fresnel zone of the receiver pair, unless the line through the receivers is parallel to the source boundary.

The time tag at which the source is collinear with the receivers is denoted by $t_0$ (see left panels of Figure 4.10) and the corresponding source location is denoted by $\mathbf{x}_0 = \mathbf{v}t_0$. Please note that while $t_0$ is a known time tag, explicit knowledge of $\mathbf{x}_0$ is not necessary in practice. However, this notation will be useful when describing our method in the steps below. We note further that $\mathbf{x}_0$ will by construction be in the middle of the Fresnel zone of the receiver pair. Note also that for a given recording of a single source moving in one direction, the time tag $t_0$ remains fixed throughout the procedure.

To estimate $\hat{h}_T(\mathbf{x_A}, \mathbf{x_B}, \omega)$ consider the sequence $n = 1, \ldots, N$, $N \gg 1$, and perform the following steps for the given pair of recordings $p(\mathbf{x_A}, t)$ and $p(\mathbf{x_B}, t)$:

(i) *Generate a set of random window locations* $\{t_n\}_{n=1}^N$ of a fixed duration $T$ by sampling from the distribution associated with $f_T$ in equation (4.3.5), and such that $|t_n - t_0| < T$. There is flexibility in the choice of the probability distribution $f_T$ of $t_n$ provided that $\langle t_{(\cdot)} \rangle_T = t_0$ and that $f_T$ is non-zero only on a bounded interval.

(ii) *For each* $t_n$ *extract the windowed recordings* $p(\mathbf{x_A}, t; T, t_n)$ *and* $p(\mathbf{x_B}, t; T, t_n)$ *of duration* $T$ *and centered at* $t_n$ *from* $p(\mathbf{x_A}, t)$ *and* $p(\mathbf{x_B}, t)$. This procedure is illustrated in the left panels of Figure 4.10 and is performed on the recorded time series for each receiver.

(iii) *Perform interferometry using the windowed data* in order to derive one realization of $\hat{h}(\mathbf{x_A}, \mathbf{x_B}, \omega\,;\, T, t_n)$ according to equation (4.3.6), using the Fourier transforms of the windowed recordings from (ii).

(iv) *Repeat Steps (i)–(iii) for a large number* $N$ *of random window locations* $t_n$ and take the arithmetic mean of $\{\hat{h}(\mathbf{x_A}, \mathbf{x_B}, \omega\,;\, T, t_n)\}_{n=1}^N$ in order to approximate the random windowing kernel $\langle \chi\chi \rangle_T$ given by equation (4.3.7), and to obtain the ambient noise retrieval $\hat{h}_T(\mathbf{x_A}, \mathbf{x_B}, \omega)$ in equation (4.3.6).

Due to the law of large numbers, one has

$$\frac{1}{N} \sum_{n=1}^{N} \hat{h}(\mathbf{x_A}, \mathbf{x_B}, \omega\,;\, T, t_n) \underset{N \to \infty}{\longrightarrow} \hat{h}_T(\mathbf{x_A}, \mathbf{x_B}, \omega), \tag{4.3.11}$$

and the empirical mean of the sample $\{\hat{h}(\mathbf{x_A}, \mathbf{x_B}, \omega\,;\, T, t_n)\}_{n=1}^N$ converges, in the limit of $N \to \infty$, to the expectation of $\hat{h}(\mathbf{x_A}, \mathbf{x_B}, \omega\,;\, T, \tau)$ as in equation (4.3.5) provided that $\tau$ has a finite variance (i.e., $\int_{\mathbb{R}} \tau^2 f_T(\tau) d\tau < \infty$) and the locations $\{t_n\}_{n=1}^N$ are sampled independently from $f_T$. Finally, note that the steps outlined above do not require knowledge of the source speed $\mathbf{v}$, or for the source to be in motion, as long as it is possible to identify a suitable recorded time $t_0$ corresponding to the emission of energy from a source location collinear with the receiver pair.

### 4.3.4 Optimal time window size $T_{\mathbf{opt}}$ in $\hat{h}_{T_{\mathbf{opt}}}(\mathbf{x_A}, \mathbf{x_B}, \omega)$

The procedure described in the previous Section can be applied to any time window of size $0 < T < \infty$. However, similarly to the general $\epsilon$-diagonal decomposition defined in equation (4.2.5), a successful approximation of the phase of the inter-receiver Green's function

depends on the choice of an optimal support of the random windowing kernel $\mathbb{E}[\chi\chi]_T$ in equation (4.3.7). The steps outlined below provide a systematic way to choose an optimal time window size $T_{opt}$ for any given single recording by estimating the acausal energy present in each averaged retrieval $\hat{h}_T(\mathbf{x_A}, \mathbf{x_B}, \omega)$ in equation (4.3.6).

To determine $T_{opt}$ for a given pair of recordings $p(\mathbf{x_A}, t)$ and $p(\mathbf{x_B}, t)$, consider first a sufficiently large range of test values $T \in (T_{\min}, T_{\max})$; this range will necessarily be limited by the length of the recordings available. Steps to find the optimal window size $T_{\text{opt}}$ for any fixed pair of recordings $p(\mathbf{x_A}, t)$ and $p(\mathbf{x_B}, t)$ are:

(1) Choose an ordered collection of time window sizes $\{T^{(j)}\}_{j=1}^{J}$ contained in the test range $T \in (T_{\min}, T_{\max})$.

(2) Estimate the averaged retrieval $\hat{h}_{T^{(j)}}(\mathbf{x_A}, \mathbf{x_B}, \omega)$ for each time window size $\{T^{(j)}\}_{j=1}^{J}$ using the procedure described in Section 4.3.3.

(3) Transform each estimate $\left\{\hat{h}_{T^{(j)}}(\mathbf{x_A}, \mathbf{x_B}, \omega)\right\}_{j=1}^{J}$ to the time domain to obtain the corresponding waveforms $\left\{h_{T^{(j)}}(\mathbf{x_A}, \mathbf{x_B}, t)\right\}_{j=1}^{J}$.

(4) Order the waveforms $h_{T^{(j)}}(\mathbf{x_A}, \mathbf{x_B}, t)$ according to the time window size $T^{(j)}$ (see bottom panel of Figure 4.12).

(5) Use the ordered family of waveforms $h_{T^{(j)}}(\mathbf{x_A}, \mathbf{x_B}, t)$ to identify the time tag of the *feature of interest*, which is normally the first-arriving dominant wave, denoted by $t_I$. In Figure 4.12, $t_I = 0.4$ s and is highlighted in orange.

(6) Calculate the waveform energy of each trace $h_{T^{(j)}}(\mathbf{x_A}, \mathbf{x_B}, t)$ from time $t = 0$ to a time slightly before $t_I$. This calculation quantifies the acausal energy present in each of the traces as a function of $T^{(j)}$. (In Figure 4.12 the waveform energy is calculated for each trace between $t = 0$ and $t = 0.3\,$s. Please note that this curve would be different for different recordings.)

(7) Compute the spurious waveform energy calculated in equation (4) as a function of the time window sizes $T^{(j)}$ (see the top panel of Figure 4.12).

(8) Minimize the spurious energy with respect to $T^{(j)}$; the minimizer is denoted by $T_{opt}$.

(9) Use the optimal window size $T_{opt}$ determined in equation (8) for the interferometric retrieval by following the steps described in Section 4.3.3. Compute the final/optimal ambient noise retrieval of the inter-receiver Greens function $\hat{h}_{T_{\text{opt}}}(\mathbf{x_A}, \mathbf{x_B}, \omega)$ given by equation (4.3.6)) or its time-domain counterpart $h_{T_{\text{opt}}}(\mathbf{x_A}, \mathbf{x_B}, t)$.

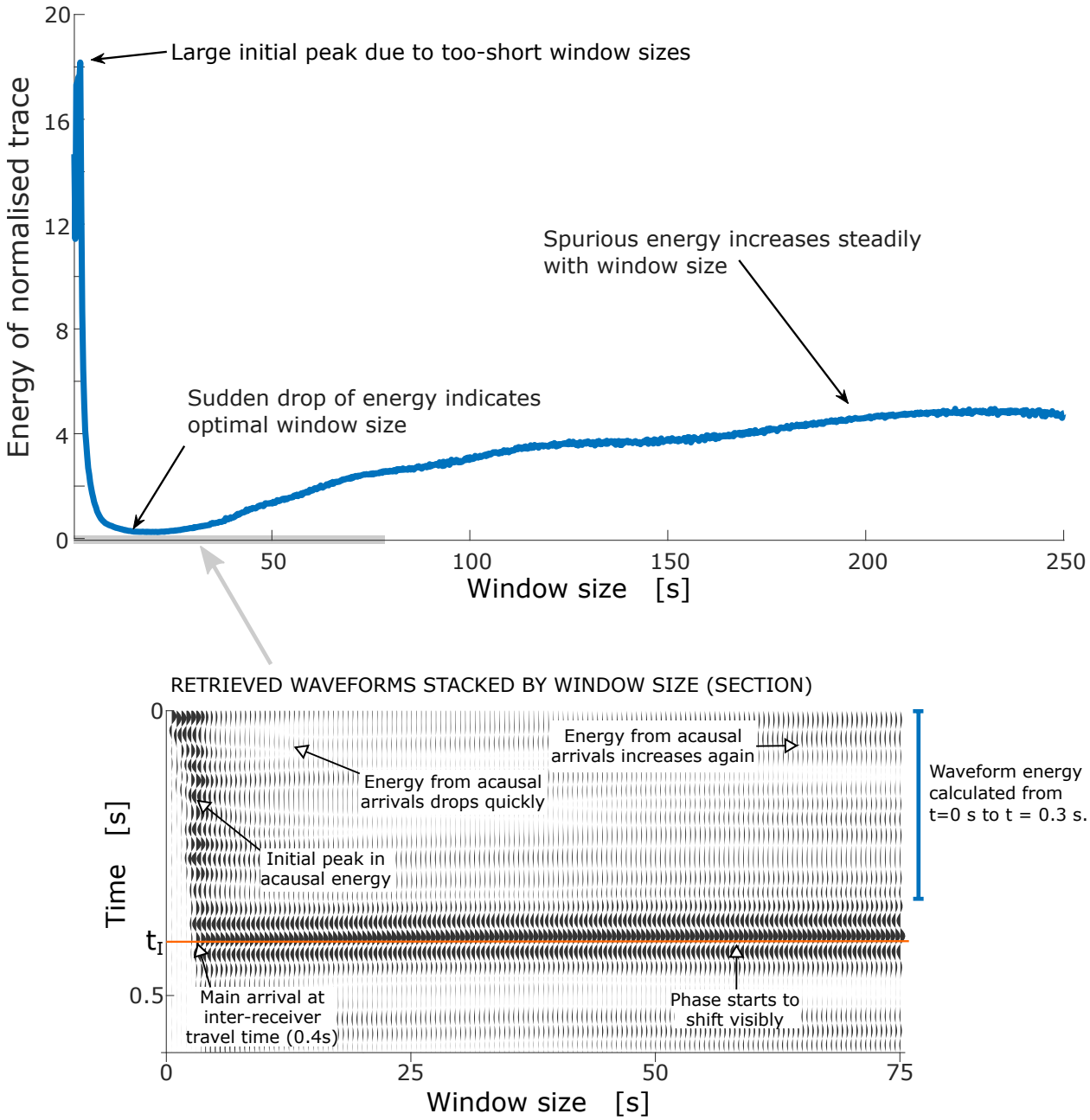


**Figure 4.12:** Calculation of acausal energy curve for a recording of a single moving source. Values of $T$ tested ranged between 0.25 s and 250 s. The bottom panel shows the waveforms corresponding to the average random window retrieval for $T$ only in the range between 0.25 s and 75 s, for clarity. The waveforms are arranged by window size $T$. The arrival of interest is highlighted in orange at time $t_I = 0.4$ s. The top panel shows the acausal energy curve in blue. The waveform energy was calculated for each waveform in the range from t = 0 to t = 0.3 s. The acausal energy curve exhibits a clear initial peak for small values of $T$, followed by a sharp drop and then a slow increase with $T$. The minimum is achieved at $T_{\text{opt}} \approx 15$ s.

Please note that the above procedure can easily be automated. For multiple source train recordings Steps (1)–(8) can be performed for each recording, noting that the optimal window

size $T_{\text{opt}}$ will, in general, be different for each recording. Then, the standard stacking average can be applied to estimate $\mathbb{E}\left[\hat{h}_{T_{\text{opt}}}(\mathbf{x_A}, \mathbf{x_B}, \omega)\right]$ and thus potentially improve the retrieval even further.

### 4.3.5 Results

We now present some examples of the interferometric retrieval obtained via the random windowing method described in Section 4.3.3 which is carried out for the optimal time window size $T_{opt}$ determined according to the procedure described in Section 4.3.4. We present results for a receiver pair that is perpendicularly oriented with respect to the source-line, as well as results for a receiver pair that is oriented at 30 degrees with respect to the source-line. The results are of essentially identical quality. The distribution of the window locations is chosen to be uniform, as in the example of Section 4.3.2. The random windowing method was applied to the two configurations discussed in Section 4.2. These configurations corresponded to, first, the case where the stacking average kernel $\mathbb{E}[\,\hat{F}^*\hat{F}\,]$ of the ambient noise is localized, as in Figure 4.8 (left panels of Figure 4.13), and second, the challenging scenario when $\mathbb{E}[\,\hat{F}^*\hat{F}\,]$ is not localized and the spurious crosstalk arrivals do not decay (right panels of Figure 4.13). The random windowing method leading to $\hat{h}_{T_{opt}}(\mathbf{x_A}, \mathbf{x_B}, \omega)$ is applied in all cases to a single short recording of a train of sources, and the stacking average is not applied to $\hat{h}_{T_{opt}}(\mathbf{x_A}, \mathbf{x_B}, \omega)$ unless otherwise stated. Figure 4.13 shows phase estimates produced by the random windowing average in blue and the phase estimate based on $\hat{h}(\mathbf{x_A}, \mathbf{x_B}, \omega)$ in light grey for comparison. Receivers oriented perpendicularly with respect to the source-line were used in the top row, whereas the bottom row of Figure 4.13 shows the results for a receiver pair oriented at 30 degrees with respect to the source-line. The phase estimated from individually recorded sources, which allows us to calculate the reference retrieval using equation (4.1.1), is indicated in dashed black. We also show the phase of the inter-receiver Green's function retrieved through the standard stacking average over six source train recordings restricted to a one-minute-long window in a similar fashion to Pinzon-Rincon et al. (2021). To generate the blue random windowing estimates in this Figure, a single five-minute recording was used, and exhibit a significant improvement over traditional approaches. In particular, the standard approach in light grey, which also made use of five minutes of data, is shown to be very poor when such short recordings are used. When 30 minutes of recorded noise is taken, as in the dark grey estimate which uses six five-minute recordings, the estimate is only accurate when the sources and their phases are statistically uncorrelated (top left panel). On the other hand, the random windowing method produces a significantly more accurate phase in all cases, even with a drastically short five-minute

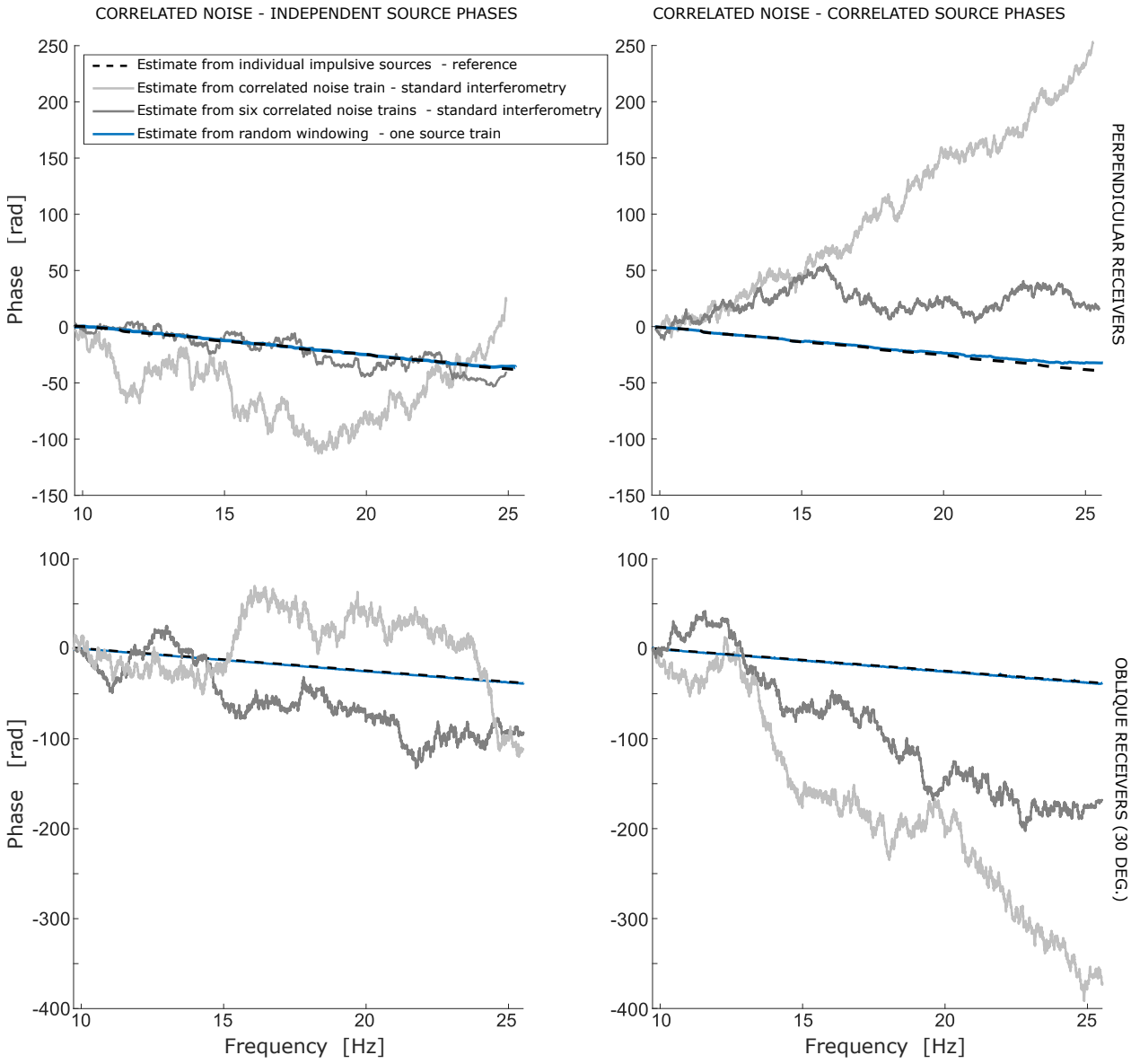


**Figure 4.13:** Phase estimates obtained from the random windowing scheme applied to a short (5 min) recording of a single source using receivers that are perpendicularly oriented with respect to the source-line (**top**) and oriented at 30 degrees with respect to the source-line (**bottom**). The left column shows the results for correlated noise where source phases at different frequencies are independent (as in Figure 4.7). The phase estimated from discrete sources, in black dashes, is used for reference. The phases produced by the random windowing scheme are shown in blue and exhibit very good agreement with the reference phase. The phase of the retrieval using the standard method and no stacking is shown in light grey, and the phase of six stacked sources is shown in dark grey for comparison. The same phase estimates are shown in the right column for correlated noise with correlated source phases (as shown in Figure 4.9). The phase estimates from the random windowing scheme, in blue, are better than the retrieval obtained using the standard method, with slightly reduced accuracy at higher frequencies.

recording.

For illustration, Figure 4.14 shows the waveforms corresponding to the phases depicted in the top-right panel of Figure 4.13 (i.e., a correlated noise source with correlated phases, and perpendicularly oriented receivers) with normalized amplitudes. As expected, the waveform corresponding to the random windowing estimate (in blue) exhibits the best agreement with the reference waveform (in black dashes). The phases estimated from the random windowing scheme agree well with the reference phase in all cases, showing that our method is effective in mitigating the undesired effects of correlation in the noise sources in ambient noise interferometry, especially where moving sources such as trains or traffic on a highway are concerned.

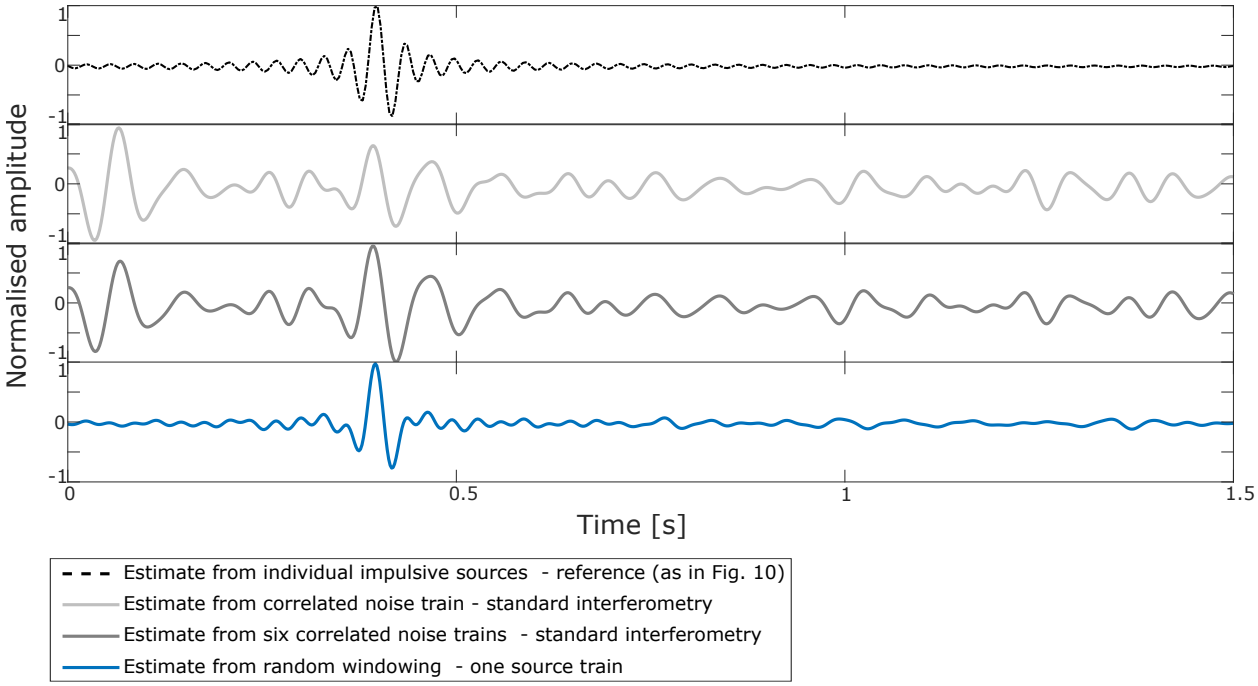


**Figure 4.14:** Waveforms corresponding to the estimated phases shown in the top-right panel of Figure 4.13, for correlated noise with source phases recorded at a perpendicularly oriented pair of receivers 400 m apart, with the medium speed set at 1000 m/s. For reference, the estimate calculated from individual point sources is depicted in black dashes (**top**), exhibiting the inter-receiver arrival at 0.4 s. The estimate produced by standard interferometry without stacking is shown in light grey (**second from top**). The waveform resulting from standard stacking of six estimates is depicted in dark grey (**third from top**). The estimate obtained from the random windowing method applied to a short recording of a single source is shown in blue (**bottom**).

To further illustrate the utility of the random windowing approach, Figure 4.15 shows an example of the waveforms (**right**) and phases (**left**) estimated from a single realisation of a window centred at $t_0$, of length $T_{\text{opt}}$, precisely when the source is aligned with the receiver pair. While noise in the single-window signal is reduced by the spatial restriction induced

by the data windowing, which helps reduce the cross-talk, in the example presented there is a strong acausal component and the phase estimated from a single window is incorrect (see reference in black dashes for comparison). Using the random windowing method minimises acausal energy in the retrieval, and the correct phase is sucessfully estimated (see data in blue).

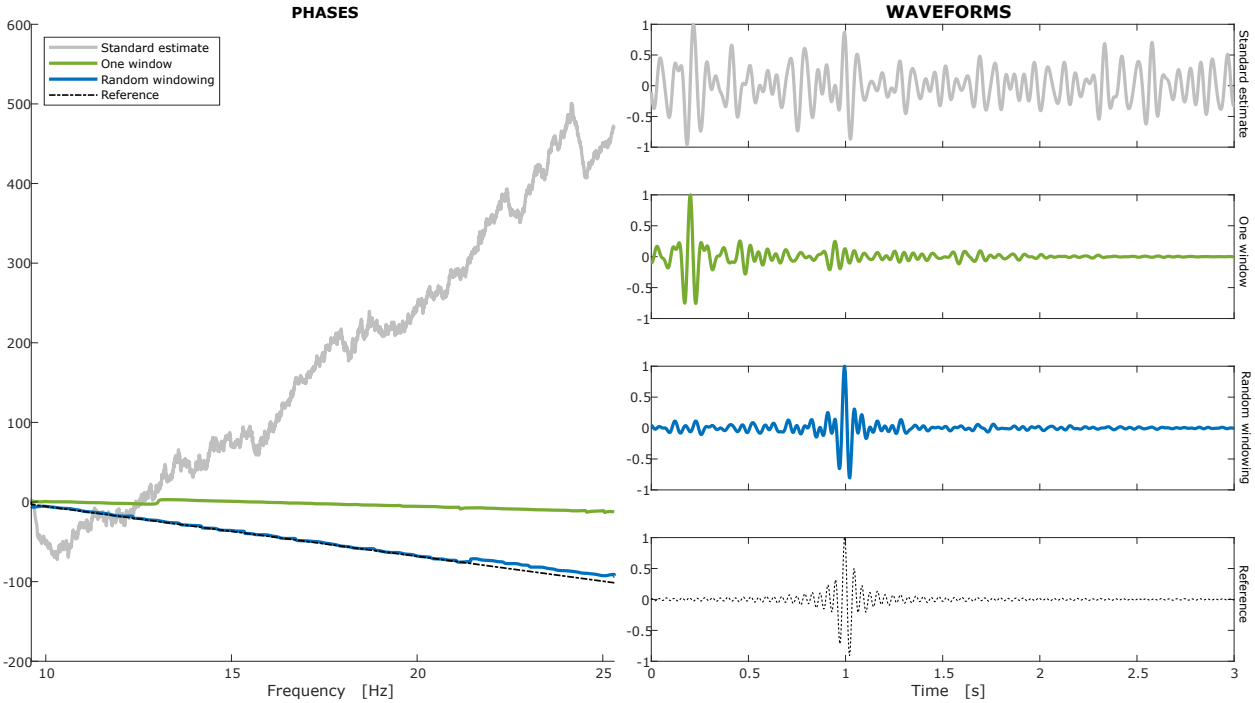


**Figure 4.15:** Comparison of the phase estimate resulting from using a single windowed retrieval in green, and using the full random windowing procedure in blue. Phase estimates are shown to the right and normalised waveforms to the left. For reference, we include the original retrieval $\hat{h}$ in grey, and the reference estimate from individually recorded point sources in black dashes. The receivers were perpendicularly oriented, with an inter-receiver distance of 1000 m in a medium with propagation speed of 1000 m/s. The receiver closest to the source line was 400 m away. The source was set to travel at 108 km/h (30 m/s) and emit sound between 10 Hz and 25 Hz.

We note that the workflow outlined in Section 4.3.4 and illustrated above is not restricted to ambient noise interferometry from correlated noise. In fact, this methodology can be applied to short recordings of uncorrelated noise to find an optimal window size that minimizes spurious arrivals. In this scenario, the choice of $t_0$ as described in Section 4.3.3 is more flexible as the source no longer exhibits coherent spatiotemporal correlation or a Doppler spread differential, as would be the case for a source in motion. Therefore, the choice of time tag $t_0$ may be arbitrary and the random windowing method can still be applied as described in Section 4.3.4. Figure 4.16 shows the phase estimated by the random windowing method when the ambient noise recording is uncorrelated. The random windowing method

was applied to a short (five-minute) recording of uncorrelated ambient noise, producing satisfactory results. These numerical results illustrate that the random windowing approach has the potential to retrieve the inter-receiver phase from recordings that are to short for traditional interferometry to be feasible (see the degraded phases in Figure 4.13 when one applies traditional interferometric methods to a five-minute recording of strongly correlated noise). Significantly less data is required to estimate the inter-receiver phase with accuracy. Hence, the approach presented here has the potential to speed up convergence to the inter-receiver phase when applied to uncorrelated ambient noise.

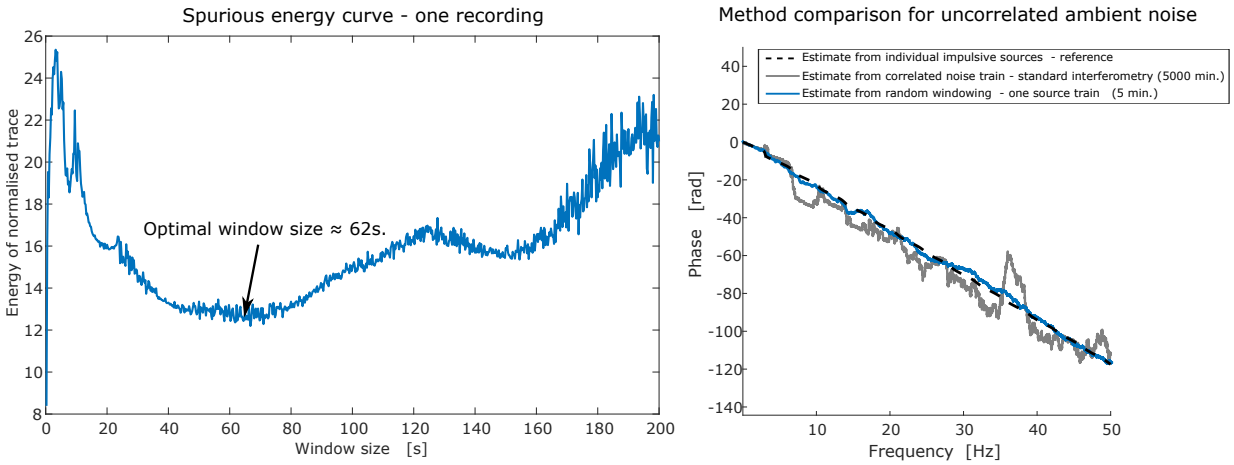


**Figure 4.16:** Random windowing method applied to uncorrelated ambient noise. The left panel shows the acausal energy curve estimated from one ambient noise recording. The right panel shows the resulting estimated phase in blue, which matches the reference phase in black dashes well. For comparison, the phase estimated from stacking 1000 simulated recordings of ambient noise five minutes long is shown in dark grey. We can see the stacking in this case will converge to the correct phase estimate as expected for truly uncorrelated ambient noise, but only after a very large number of ambient noise recordings are processed and stacked.

Finally, Figure 4.17 shows the mean optimal window sizes $T_{\text{opt}}$ as a function of the distance from the closest receiver to the source-line; in the illustrated case the inter-receiver distance is 400 m, and three different source speeds are considered.

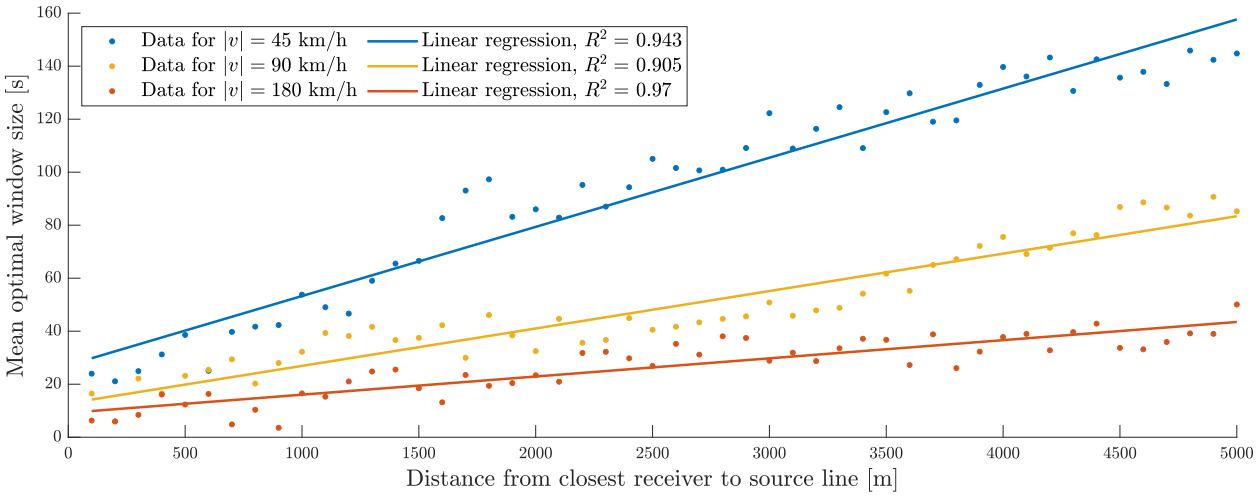


**Figure 4.17:** Estimated optimal window size for the random windowing scheme, calculated for trains travelling at 45 km/ (in blue), 90 km/h (in red) and 180 km/h (in orange), in terms of the distance between the receivers and the road (using the closest receiver as reference) and averaged over 30 samples each. The receivers were 400 m apart from each other. The average optimal window sizes are shown as coloured circles. For each speed, linear regression was performed to estimate the best linear fit, which is shown as a solid line. The statistic $R^2$ for each linear fit is stated in the legend.

Recall that optimal window sizes $T_{\text{opt}}$ are, to some extent, recording-dependent due to the randomness in recorded signals, so their value will vary for different recordings even if the receiver geometry remains fixed; hence, 30 samples for each considered closest receiver distance and velocity were calculated and averaged to produce the linear fits in Figure 4.17; the fluctuations in the data diminish with the number of samples used. Linear regression was performed to estimate the line of best fit for each speed, which is shown as solid lines in the Figure. The $R^2$ statistic is stated for each estimated line, as a measure of goodness-of-fit. This statistic is a classical measure of goodness-of fit in linear regression, defined as

$$R^2 = \frac{\sum_{j=1}^{n}(y_j - \hat{y}_j)^2}{\sum_{j=1}^{n}(y_j - \bar{y})^2},$$

where $n$ is the number of data points, $\{y_j\}_{j=1}^n$ denote the original data, $\{\hat{y}_j\}_{j=1}^n$ denote the fitted values and $\bar{y}$ denotes the mean of the original data. This statistic takes values between 0 and 1, and values closer to 1 indicate a better fit. The relationship illustrated in Figure 4.17 indicates that for a fixed source speed and a fixed inter-receiver distance, the optimal window size decreases with the distance of the receivers to the source boundary. Moreover, the optimal window size decreases for increasing source speeds, which agrees with physical intuition and with the form of the random windowing average kernel (4.3.10) illustrated in Figure 4.11. Furthermore, as can be deduced from equations (4.1.38) and (4.1.15),

the spatial discrepancy of the implicit source locations (i.e., the difference $x' - x''$) will be smaller for decreasing inter-receiver distances. Consequently, the error due to the presence of the residual crosstalk terms in the retrieval decreases with decreasing inter-receiver distance, while larger inter-receiver distances require smaller values of the time window size $T_{\text{opt}}$ to mitigate this error.

## 4.4 Discussion

The ambient noise interferometric retrieval based on the random windowing average (Sections 4.3.3 and 4.3.4) is capable of accurately estimating the phase of the inter-receiver Green's function based on a short pair of recordings of a correlated noise source (Section 4.3.5). As pointed out in equation (4.3.8), the random windowing average allows one to extract the $\epsilon$-diagonal term in decomposition (4.2.5) of the ambient noise retrieval $\hat{h}(\mathbf{x_A}, \mathbf{x_B}, \omega)$ without the explicit knowledge of the stacking average kernel $\mathbb{E}[\hat{F}^* \hat{F}]$ which need not be localized. For a given pair of recordings this new technique requires one to pre-process the spurious energy to determine the optimal time window size $T_{opt}$; then, the optimal spatial window length can be used in decomposition (4.2.5) to retrieve $\hat{g}_\epsilon$ with the optimal cut-off length $\epsilon = T_{opt}|\mathbf{v}|$. This procedure, illustrated in Figure 4.12, can be automated in practical applications. Based on the derivations and the discussion in Sections 4.2 and 4.3, the optimal value $T_{opt}$ of the temporal window size decreases with the inter-receiver distance and with the distance between the source-line and the receiver pair, since the Doppler shift and the spatial incongruence become increasingly important. Moreover, the optimal value of the temporal window size decreases for increasing speeds of the moving noise source, as indicated in equation (4.3.10). These trends are consistent with physical intuition, as faster source speeds have the compound effect of increasing the spatial coverage (and hence the prevalence of the crosstalk contributions to the ambient noise retrieval), and increasing the importance of the Doppler shift for the retrieval.

The random windowing approach can be used in conjunction with the standard stacking average procedure as discussed in Section 4.3. This is especially tractable when estimating inter-receiver Green's functions from a small ensemble of source train recordings, where the random windowing procedure can be applied to each individual train recording before performing standard stacking to optimize the extraction of causal information. In Pinzon-Rincon et al. (2021), the distance from the receiver array to the rail track on which trains provide source energy is of the order of 5–10 km. This large distance combined with the stationary phase zone approach likely mitigates spurious effects arising from the Doppler effect induced by the trains' motion, since such a receiver array configuration and their

localization methodology implicitly restrict the recordings to regions of the source boundary on which the train is roughly collinear with the receiver pairs. In fact, the choice of the optimal time window size in Pinzon-Rincon et al. (2021) in the stacked retrieval is consistent with our findings. Incorporating our methodology in such a setup could allow for the retrieval of inter-receiver estimates from near-field recordings (closer to the rail tracks) maintaining the optimality of extraction of coherent information from each recorded trace.

Sabra (2010) concludes that under some circumstances the Doppler effect does not have a significant effect on the interferometric estimate of the inter-receiver Green's function. However, that work explicitly assumes that the ambient noise field is uncorrelated in time. To achieve this the sources considered were randomly, statistically independent, and uniformly distributed in space around the receiver pair. The situation where the ambient noise field is statistically correlated is not considered. Moreover, to mitigate the differential Doppler effect, a stationary phase approximation is performed throughout, and the far-field assumption is made. These approaches are consistent with the findings presented in this Chapter, as well as with the random windowing method presented in Section 4.3.

In interferometric studies from traffic noise, such as the one performed by Behm and Snieder (2013), wave velocities are retrieved from a linear array of receivers which crosses the main road perpendicularly. In this setup, the choice of the time window sizes could be further informed by our proposed framework, possibly using consistently shorter time windows for receiver pairs which are closer to the road. This interesting study points out that longer observation periods do not necessarily lead to better results, which indicates that correlations in the underlying ambient noise are too significant for the stacked-averaged retrieval to be appropriate, analogously to the case illustrated in Figure 4.9. Thus, integrating the random windowing approach could be beneficial by providing an informed method for selecting temporal window sizes so that the effect of spurious arrivals is minimized, or even averaging over different time window sizes. Liu et al. (2021) conclude, using physically motivated ray-path arguments, that the crosstalk can be negligible when performing interferometry using seismic noise generated by high-speed trains in the case of direct, scattered and refraction waves. Our approach to interferometry from correlated noise sources links the quality of the retrieved phase of the inter-receiver Green's function from direct waves explicitly to the correlation structure of the noise source, as well as the receiver array geometry (inter-receiver distance and distance to the source-line) while further providing a methodology to mitigate the spurious effects induced by any of these causes. In the common case of sources in motion, we established a link between the spurious energy in the retrieved trace and the speed of the source, and the proposed methodology has the potential to mitigate spurious effects induced by the Doppler spread for this type of source. We further note that

the receivers in Liu et al. (2021) are very close to the location of the source train, confirming that correlated noise interferometry is applicable in the near-field of seismic noise generated by road traffic and trains.

We constrained our study to estimating the direct wave arrivals in two dimensions, which loosely resembles the case of surface waves in the three-dimensional setup. Similar derivations could be carried out for body waves that have been critically refracted in three dimensions along horizontal interfaces in the subsurface and then refract back up to the surface. Our methodology could be used to image and monitor the subsurface using these non-physical refracted arrivals, as suggested by King and Curtis (2011a) and Brenguier et al. (2019), respectively.

Finally, our method is optimized when the location of the source in motion can be identified from a location tracker or from the acquired data. The latter approach has been shown to be possible for example in Yin et al. (2018); Brenguier et al. (2019); Pinzon-Rincon et al. (2021), but may not be feasible in an urban environment with a more complicated road network and multiple simultaneous sources. In those situations, one could apply directional decomposition of the wavefield into constituent energy from its different individual sources prior to using these methods, similarly to the methods employed by Maranò et al. (2012). Although we have focused on the application of interferometry from noise sources in motion, representative of most known physical sources that contribute to ambient noise, the random windowing method can be used regardless of the underlying cause of statistical correlation in the ambient noise field.

## 4.5 Conclusions

A novel and robust procedure was developed for the accurate retrieval of the phase of the inter-receiver Green's function from a short recording of a single source of ambient noise, without the need to rely on the commonly used stacking average method, and thus avoiding the potential pitfalls of standard ambient noise interferometry. The random windowing approach provides a versatile framework for ambient noise interferometry, and it should prove useful either as a stand-alone technique when only short recordings of correlated noise are available or in situations where the standard stacking operation fails to resolve the inter-receiver Green's function phase due to significant correlations in the recorded signal, or insufficiently long recordings of the seismic noise. The random windowing method mitigates the spurious crosstalk effects introduced by the presence of statistical correlations in the ambient noise, regardless of the cause of this correlation. It includes the common case of correlation caused by a spatially migrating train of sources, and in that case it also

potentially mitigates the bias introduced by the Doppler effect. This approach is general in the sense that it improves the quality of the phase of the inter-receiver Green's function without detriment to the retrieval obtained using the standard stacking average methodology, and it applies to both correlated and uncorrelated ambient noise in both near and far-field configurations. Thus, this unified framework offers a novel workflow that can be deployed for robust estimation of inter-receiver phases from ambient noise interferometry, regardless of the statistical characteristics of the ambient noise and, in general, using less data than are required for standard interferometry that uses the stacking average approach.

Chapter 5

# Conclusions

Wavefield recordings carry information about the medium that allow geoscientists to infer the properties and structure of the Earth's subsurface. In the last two decades, wavefield interferometry has emerged as a powerful technique to extract useful medium information that ambient and active noise recording carry within them. A classical and widely used form of wavefield interferometry is implemented by cross-correlating recordings made at a pair of receivers, which yields an approximate of the inter-receiver Green's function. These estimates can be used at a later stage to image the subsurface structures.

The theoretical foundations of wavefield interferometry are comprised of Green's functions representation theorems that by necessity impose a number of assumptions on the medium and the way energy arrives at the receiver. Moreover, in practical settings these idealised mathematical formulations undergo a number of further assumptions and approximations that make them more amenable for applications. Some of the most important assumptions include that the wavefields recorded at the receivers arrive from sources that are statistically uncorrelated and that illuminate the medium around the receiver pair isotropically. If variations in these illumination are allowed, they are required to do so slowly and smoothly. In this thesis, we considered the interesting effects of violating this assumption while carrying wavefield interferometry through.

In Chapter 1, we briefly summarised the theoretical foundations of seismic interferometry, highlighting both implicit and explicit assumptions as well as the derivations required to take the representation theorem of the correlation type to the cross-correlation form of wavefield interferometry. These assumptions and their interplay were discussed and compared, highlighting current approaches to mitigate, quantify, and generally address them. We found the assumption of uncorrelated sources an area of interest due to its persistence in theoretical and practical studies, and the need to investigate, quantify and mitigate the

errors introduced to the interferometric estimate when violating this assumption.

In Chapter 2, we derived from first principles a unified error quantification framework that can be applied to active source and passive noise interferometry. We found conditions for the phase estimate to be unbiased and that the amplitude estimate is generally biased. We prioritised studying the phase, as this part of the Green's function estimate is the most relevant for imaging applications. We performed a preliminary numerical exploration of these errors by implementing a geostatistical model that accounts both for long-range statistical spatial correlations in the source, as well as local-range correlations. The local-range correlation parameter can also be interpreted as the smoothness of the random field in a mean square differentiability sense. We generally found a non-trivial the interplay between the correlations at the large and local scale, as well as with the frequency of the wave. Counter-intuitively, we found that a rougher field is beneficial to the retrieval interferometry is interpreted as s spatial averaging over the source locations. We explored a multi-contour approach to mitigate errors in the phase.

In Chapter 3 we considered the interplay of these long and short range correlations with the stationary phase approximation. Finding that, as opposed to taking a full boundary as in Chapter 2, a rougher field has negative effects on the stationary phase estimate that are difficult to mitigate, even if the estimate is unbiased. We found this is due to the theoretical requirements of the stationary phase approximation, which imposes smoothness requirements on the source amplitude on the neighbourhood of the stationary points. We extended existing frameworks to quantify error in the stationary phase approximation and derived bounds for the errors in terms of the statistical parameters of the random field, as well as error bounds in ideal conditions when randomness is absent.

Finally, we addressed source correlations in ambient noise interferometry in Chapter 4. We theoretically addressed this assumption in general, and considered the important case of correlation induced by motion of the source. We found that the statistical structure of the source phase is critical for the success of traditional ambient noise interferometry and we discussed the interplay between interferometry and the Doppler effect. Finally, we developed a novel and robust methodology to significantly mitigate spurious effects in interferometric traces due to source correlations, and tested it on synthetic data, showing significant improvement in the phase retrieved.

Appendix A

# Framework for uncertainty quantification in source-receiver interferometry

In this Appendix, we outline a mathematical framework that would allow the implementation of the multi-contour technique explored in Section 2.5 and inspired by the work of Curtis and Halliday (2010a), where an array of receivers can be used to assemble boundaries of virtual sources. When a relatively dense array of receivers is available, one can envision the construction of multiple virtual source boundaries to which the averaging multi-contour technique illustrated in this thesis could be applied, in order to reduce the uncertainty in the phase retrieved. This application would require the integration of the uncertainty quantification framework presented in Chapter 2 with the source-receiver interferometry formulas introduced by Curtis and Halliday. This derivation is presented below.

## A.1 Uncertainty in source-receiver interferometry with active sources

Curtis and Halliday (2010a) propose a more general interferometric formula that integrates both the cross-correlation and the convolution representation theorems. This formula is given for a specific canonical configuration of an active source boundary $S$ and a receiver boundary $R$ by

$$G_{\text{emp}}(\mathbf{x_A}, \mathbf{x_B}) = \oint_S \oint_R \hat{G}(\mathbf{r}, \mathbf{x_A}) \hat{G}^*(\mathbf{r}, \mathbf{x}') \hat{G}(\mathbf{x_B}, \mathbf{x}')\, d\mathbf{r}\, d\mathbf{x}' \,, \tag{A.1.1}$$

where $\mathbf{x_A}$ is a source and $\mathbf{x_B}$ is a receiver. The empirical Green's function approach may be applied to equation (A.1.1) by substituting each of the Green's functions $G$ on the right hand side by its corresponding empirical version $g_{\alpha\beta}$ as defined by equation (2.1.11).

If we were interested, for example, in studying source-generated error we would apply the same approach as before to define

$$\begin{aligned} G_{\text{emp}}(\mathbf{x_A},\mathbf{x_B},k;\alpha,\beta) = &\oint_S \oint_R \alpha(\mathbf{x_A})|\alpha(\mathbf{x}')|^2 G(\mathbf{r},\mathbf{x_A},k)\hat{G}^*(\mathbf{r},\mathbf{x}',k)\hat{G}(\mathbf{x_B},\mathbf{x}',k)\,d\mathbf{r}\,d\mathbf{x}' \\ &+ \beta \oint_S \oint_R \alpha(\mathbf{x_A})\alpha^*(\mathbf{x}')\hat{G}(\mathbf{r},\mathbf{x_A},k)\hat{G}^*(\mathbf{r},\mathbf{x}',k) + |\alpha(\mathbf{x}')|^2 G^*(\mathbf{r},\mathbf{x}',k)\hat{G}(\mathbf{x_B},\mathbf{x}',k)d\mathbf{r}\,d\mathbf{x}' \\ &+ \beta^* \oint_S \oint_R \alpha(\mathbf{x_A})\alpha(\mathbf{x}')\hat{G}(\mathbf{r},\mathbf{x_A},k)\hat{G}(\mathbf{x_B},\mathbf{x}',k)\,d\mathbf{r}\,d\mathbf{x}' \\ &+ \beta^2 \oint_S \oint_R \alpha(\mathbf{x_A})\alpha^*(\mathbf{x}')\hat{G}^*(\mathbf{r},\mathbf{x}',k)\,d\mathbf{r}\,d\mathbf{x}'\,. \end{aligned} \tag{A.1.2}$$

from this point onwards we would quantify the error exactly as in the previous scenarios via definition (2.3.1). A multi-contour approach on $S$ would be used as described in Section 2.5. On the other hand, receiver-generated error could be studied by applying the source-receiver reciprocity relation to the Green's functions in the right hand side of equation (A.1.1), and proceeding a completely analogous manner.

## A.2 Uncertainty in a receiver-generated noise scenario

Now we are interested in quantifying the uncertainty introduced by faults in the receiver equipment, in an active source scenario. We assume that a dense grid of receivers is available to record signals within the contour $S$. One could in principle construct a number of different contours of receivers and use each of these in turn to retrieve the interferometric Green's function, as illustrated in Figure A.2. These receivers $\mathbf{r}_j$, for $j \in \{1,\ldots,N\}$, could be placed arbitrarily within $S$ with the only restriction that they contain both $\mathbf{x_A}$ and $\mathbf{x_B}$ (other layouts could be considered). Then we could use one of the many available interferometric formulas to estimate the Green's function between $\mathbf{x_A}$ and $\mathbf{x_B}$ (as illustrated by Figure A.2) using the Green's functions between each of $\mathbf{x_A}$, $\mathbf{x_B}$ and the surrounding receivers $r \in \mathbf{r}_j$.

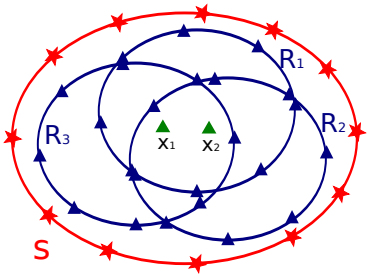


**Figure A.1:** Construction of multiple contours of receivers in blue, within an active source contour $S$ in red. All contours contain both points of interest $\mathbf{x_A}$ and $\mathbf{x_B}$, which are themselves receivers represented by green triangles.

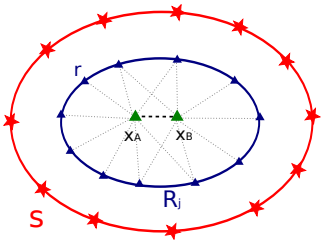


**Figure A.2:** Illustration of the retrieval of $\hat{G}(\mathbf{x_A}, \mathbf{x_B})$ (thick black dashes) via cross-correlation of Green's functions between these receivers and those on the blue receiver contour $\mathbf{r}_j$ (grey dotted lines).

Now we ask how the latter Green's functions may be retrieved in the first place (i.e. $\hat{G}(\mathbf{r}_j, x_i)$ for $\mathbf{r}_j \in \mathbf{r}_j$ and $i \in \{A, B\}$. We can simply use the interferometric formula of our choice again, this time using the active source contour $S$ as illustrated in Figure A.3.

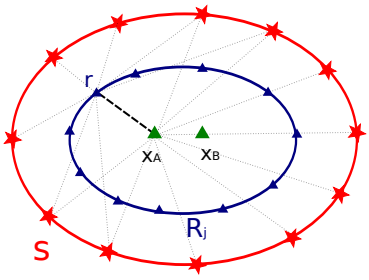


**Figure A.3:** Illustration of the retrieval of $\hat{G}(\mathbf{x_A}, \mathbf{x_B})$ (thick black dashes) via cross-correlation of Green's functions between these receivers and those on the blue receiver contour $\mathbf{r}_j$ (grey dotted lines).

To express source-receiver interferometry in a more compact way, we define the bilinear

operator $\underset{S}{\otimes}$ as

$$\hat{G}[\mathbf{x_A}] \underset{S}{\otimes} G[\mathbf{x_B}](k) = \oint_S G^*(\mathbf{x}, \mathbf{x_B}, k)\partial\mathbf{n_x}\hat{G}(\mathbf{x_A}, \mathbf{x}, k) - \hat{G}(\mathbf{x_A}, \mathbf{x}, k)\partial\mathbf{n_x}\hat{G}^*(\mathbf{x}, \mathbf{x_B}, k)\, d\mathbf{x}\,, \tag{A.2.1}$$

for a pair of receiver locations $\mathbf{x_A}$ and $\mathbf{x_B}$ enclosed by a boundary $S$. Furthermore, in the presence of the random field $\alpha$ we define

$$\begin{aligned}\hat{G}[\mathbf{x_A}] \overset{\alpha}{\underset{S}{\otimes}} G[\mathbf{x_B}](k) = \oint_S &\alpha^*(\mathbf{x})G^*(\mathbf{x}, \mathbf{x_B}, k)\partial\mathbf{n_x}\alpha(\mathbf{x})\hat{G}(\mathbf{x_A}, \mathbf{x}, k) \\ &- \alpha(\mathbf{x})\hat{G}(\mathbf{x_A}, \mathbf{x}, k)\partial\mathbf{n_x}\alpha^*(\mathbf{x})\hat{G}^*(\mathbf{x}, \mathbf{x_B}, k)\, d\mathbf{x}\,.\end{aligned} \tag{A.2.2}$$

Hence, we can express the retrieved homogeneous Green's function between $\mathbf{x_A}$ and $\mathbf{x_B}$ as

$$G_{\text{emp}}(\mathbf{x_A}, \mathbf{x_B}, k) = \left(G[\mathbf{r}] \underset{S}{\otimes} G[\mathbf{x_A}]\right) \underset{R}{\otimes} \left(G[\mathbf{r}] \underset{S}{\otimes} G[\mathbf{x_B}]\right)(k)\,, \tag{A.2.3}$$

where for illustration purposes the bilinear operator $\otimes$ is defined again by equation (A.2.1) (i.e. we have chosen a cross-correlational form of interferometry). In Section 2.5 it was seen that for an array of boundaries, we would have a corresponding collection of different recovered Green's functions $G_{\text{emp}}(\mathbf{x_A}, \mathbf{x_B})$. These functions can be interpreted as particular realisations of some appropriately constructed random variable. One could then hope to improve the retrieval of the Green's function and study the behaviour of the error by taking the average of these realisations.

Following a procedure analogous to the one presented in Section 2.2, we argue that the Green's function in the right hand side of (A.2.3) is more accurately described by the empirical expression given by equation (2.1.11). Then we would have

$$G_{\text{emp}}(\mathbf{x_A}, \mathbf{x_B}, k; \alpha, \beta) = \left(g_{\alpha\beta}[\mathbf{r}] \underset{S}{\otimes} g_{\alpha\beta}[\mathbf{x_A}]\right) \underset{R}{\otimes} \left(g_{\alpha\beta}[\mathbf{r}] \underset{S}{\otimes} g_{\alpha\beta}[\mathbf{x_B}]\right)(k)\,, \tag{A.2.4}$$

for a contour of active sources $S$, a given contour of receivers $R$ and a wavenumber $k$.

Expression (A.2.4) captures how the uncertainty in the measured Green's function (described by $\alpha$ and $\beta$) propagates through the interferometric reconstruction given by our choice of bilinear operator $\otimes$.

Using definition (A.2.2) for the operator $\overset{\alpha}{\otimes}$, we expand equation (A.2.4) as shown below

$$G_{\text{emp}}(\mathbf{x_A}, \mathbf{x_B}, k; \alpha, \beta) = \alpha^*(\mathbf{x_A})\alpha(\mathbf{x_B}) \left(G[\mathbf{x_A}] \overset{\alpha}{\underset{R}{\otimes}} G[\mathbf{x_B}]\,(k)\right)$$

$$+\beta\alpha^*(\mathbf{x_A})\left(G[\mathbf{x_A}]\overset{\alpha}{\underset{R}{\otimes}}\mathcal{S}_\partial(\mathbf{r})+\alpha(\mathbf{x_B})\mathcal{S}^*_\partial(\mathbf{x_A})\oint\limits_R\partial\mathbf{n}_r\left\{\alpha(\mathbf{r})\hat{G}(\mathbf{r},\mathbf{x_B})\right\}^*d\mathbf{r}\right)$$

$$+\beta^*\alpha(\mathbf{x_B})\left(\mathcal{S}_\partial(\mathbf{r})\overset{\alpha}{\underset{R}{\otimes}}G[\mathbf{x_B}]-\alpha^*(\mathbf{x_A})\mathcal{S}_\partial(\mathbf{x_B})\oint\limits_R\partial\mathbf{n}_r\left\{\alpha(\mathbf{r})\hat{G}(\mathbf{r},\mathbf{x_A})\right\}d\mathbf{r}\right) \tag{A.2.5}$$

$$+|\beta|^2\left(\mathcal{S}_\partial(\mathbf{r})\overset{\alpha}{\underset{R}{\otimes}}\mathcal{S}_\partial(\mathbf{r})\right)$$

$$+\beta^2\alpha^*(\mathbf{x_A})\mathcal{S}^*_\partial(\mathbf{x_A})\oint\limits_R\partial\mathbf{n}_r\left\{\alpha(\mathbf{r})\mathcal{S}_\partial(\mathbf{r})\right\}^*d\mathbf{r} \tag{A.2.6}$$

$$-\beta^{*2}\alpha(\mathbf{x_B})\mathcal{S}_\partial(\mathbf{x_B})\oint\limits_R\partial\mathbf{n}_r\left\{\alpha(\mathbf{r})\mathcal{S}_\partial(\mathbf{r},k)\right\}d\mathbf{r}\ ,$$

where

$$\mathcal{S}_\partial(\mathbf{r},k)=\oint\limits_S\partial\mathbf{n_s}\hat{G}(\mathbf{x}',\mathbf{r},k)\,d\mathbf{x}'\,, \tag{A.2.7}$$

Note as before that when operator notation is used there is always an implicit dependency on the integration variable $r\in R$. This dependency has been made explicit in some cases for clarity's sake.

Since the ideal recovery of the Green's function happens again when $\alpha\equiv 1$ and $\beta\equiv 0$, we define the error exactly as in equation (2.3.1), reproduced below as reference.

$$\epsilon(\mathbf{x_A},\mathbf{x_B},k;\alpha,\beta)=G_{\text{emp}}(\mathbf{x_A},\mathbf{x_B},k;1,0)-G_{\text{emp}}(\mathbf{x_A},\mathbf{x_B},k;\alpha,\beta)\,. \tag{A.2.8}$$

Substituting the expression (A.2.5) into the error given by equation (A.2.8) we obtain

$$\epsilon(\mathbf{x_A},\mathbf{x_B},k;\alpha,\beta)=G[\mathbf{x_A}]\underset{R}{\otimes}G[\mathbf{x_B}]-G[\mathbf{x_A}]\overset{\alpha}{\underset{R}{\otimes}}G[\mathbf{x_B}]$$

$$
\begin{aligned}
&+ \beta\alpha^*(\mathbf{x_A}) \left( G[\mathbf{x_A}] \underset{R}{\overset{\alpha}{\otimes}} \mathcal{S}_\partial(\mathbf{r}) + \alpha(\mathbf{x_B})\mathcal{S}^*_\partial(\mathbf{x_A}) \oint_R \partial\mathbf{n}_r \left\{ \alpha(\mathbf{r})\hat{G}(\mathbf{r},\mathbf{x_B}) \right\}^* d\mathbf{r} \right) \\
&+ \beta^*\alpha(\mathbf{x_B}) \left( \mathcal{S}_\partial(\mathbf{r}) \underset{R}{\overset{\alpha}{\otimes}} G[\mathbf{x_B}] - \alpha^*(\mathbf{x_A})\mathcal{S}_\partial(\mathbf{x_B}) \oint_R \partial\mathbf{n}_r \left\{ \alpha(\mathbf{r})\hat{G}(\mathbf{r},\mathbf{x_A}) \right\} d\mathbf{r} \right) \\
&+ |\beta|^2 \left( \mathcal{S}_\partial(\mathbf{r}) \underset{R}{\overset{\alpha}{\otimes}} \mathcal{S}_\partial(\mathbf{r}) \right) \qquad \text{(A.2.9)} \\
&+ \beta^2\alpha^*(\mathbf{x_A})\mathcal{S}^*_\partial(\mathbf{x_A}) \oint_R \partial\mathbf{n}_r \left\{ \alpha(\mathbf{r})\mathcal{S}_\partial(\mathbf{r}) \right\}^* d\mathbf{r} \\
&- \beta^{*2}\alpha(\mathbf{x_B})\mathcal{S}_\partial(\mathbf{x_B}) \oint_R \partial\mathbf{n}_r \left\{ \alpha(\mathbf{r})\mathcal{S}_\partial(\mathbf{r}) \right\} d\mathbf{r} \,.
\end{aligned}
$$

(A.2.10)

and we note as before that

$$
G[\mathbf{x_A}] \underset{R_j}{\overset{1}{\otimes}} G[\mathbf{x_B}] = G[\mathbf{x_A}] \underset{R_j}{\otimes} G[\mathbf{x_B}] \,.
$$

As previously discussed, we wish to simplify the error expression given by equation (A.2.9) so that it requires only monopole sources. To this end we apply the Sommerfeld condition (see Section 1.2.2), as well as the specific condition for $\alpha$ described by equation (2.2.12) to the error expression (A.2.9). We obtain the following simplified error formula

$$
\begin{aligned}
\epsilon_{\alpha\beta}(\mathbf{x_A},\mathbf{x_B},k) &= 2ik \oint_R \left( 1 - \alpha^*(\mathbf{x_A})\alpha(\mathbf{x_B})|\alpha(\mathbf{r})|^2 \right) G^*(\mathbf{r},\mathbf{x_B})\hat{G}(\mathbf{r},\mathbf{x_A}) d\mathbf{r} \\
&+ k^2\beta\alpha^*(\mathbf{x_A}) \left( 2 \oint_R |\alpha(\mathbf{r})|^2 \hat{G}(\mathbf{r},\mathbf{x_A})\mathcal{S}^*(\mathbf{r})\, d\mathbf{r} + \alpha(\mathbf{x_B})\mathcal{S}^*(\mathbf{x_A}) \oint_R \alpha(\mathbf{r})^* \hat{G}(\mathbf{r},\mathbf{x_B})^* d\mathbf{r} \right)
\end{aligned}
$$

$$+ k^2\beta^*\alpha(\mathbf{x_B}) \left( 2 \oint_R |\alpha(\mathbf{r})|^2 \hat{G}^*(\mathbf{r},\mathbf{x_B})\mathcal{S}(\mathbf{r})\, d\mathbf{r} - \alpha^*(\mathbf{x_A})\mathcal{S}(\mathbf{x_B}) \oint_R \alpha(\mathbf{r})\hat{G}(\mathbf{r},\mathbf{x_A}) d\mathbf{r} \right)$$

$$- 2ik^3|\beta|^2 \oint_R |\alpha(\mathbf{r})|^2 |\mathcal{S}(\mathbf{r})|^2 dr \tag{A.2.11}$$

$$- ik^3\beta^2\alpha^*(\mathbf{x_A})\mathcal{S}^*(\mathbf{x_A}) \oint_R \alpha^*(\mathbf{r})\mathcal{S}^*(\mathbf{r})\, d\mathbf{r}$$

$$- ik^3\beta^{*2}\alpha(\mathbf{x_B})\mathcal{S}(\mathbf{x_B}) \oint_R \alpha(\mathbf{r})\mathcal{S}(\mathbf{r})\, d\mathbf{r}\,,$$

It is interesting to note that in this scenario the modulating factor $\alpha$ will only affect the phase of the measured Green's functions when $\beta$ is not zero. This is a direct consequence of having chosen a cross-correlational form of interferometry (as it introduces products of the form $\alpha\alpha^*$, which in turn enter the retrieval as a real squared modulus). If we were to construct these expressions via convolutions, this would not be the case.

# Appendix B

# Numerical validation and calculations for the stationary phase approximation

## B.1 Summary of the derivation of the stationary phase approximation and the bounds on its error

A justification of Proposition 3.2.1 is now briefly summarised here for the reader, following Olver (1974). In order to establish the validity of this Proposition, three preliminary results regarding convergence of certain integrals are necessary. For brevity, the proofs of these auxiliary statements are only outlined. They can be established from the results found in Hardy (1903, 1908) and Olver (1974).

**Lemma B.1.1.**

*(a) For $k > 0$ and $x > 0$,*

$$\lim_{\xi \to 0^+} \int_0^\infty e^{(ik-\xi)v} v^{x-1}\, dv = e^{ix\frac{\pi}{2}} \frac{\Gamma(x)}{k^x}\,.$$

*(b) If $\phi(v)$ is piecewise continuous on $(0,\infty)$ and $\int_0^\infty \phi(v)dv$ converges, then $\int_0^\infty e^{-\xi v}\phi(v)dv$ converges for every $\xi > 0$, and furthermore*

$$\int_0^\infty e^{-\xi v}\phi(v)dv \underset{\xi\to 0^+}{\longrightarrow} \int_0^\infty \phi(v)dv\,.$$

*(c) For $k > 0$ and $y > 0$,*

$$\lim_{\xi \to 0^+} \int_y^\infty e^{(ik-\xi)v} v^{x-1}\, dv = \frac{e^{ix\frac{\pi}{2}}}{k^x} \Gamma(x, -iky)\,.$$

*Proof.* Part (a) of this Lemma may be established by rotation of the path of integration to coincide with the ray $\arg(v) = \operatorname{atan}(x/\eta)$, performing an appropriate change of variable and taking the limit. It is in fact a particular case of part (b), which is a result established by Hardy (1903). Part (c) can be proven in a manner similar to part (a). For details see Hardy (1903, 1908) and Olver (1974). □

The main result is now stated.

**Proposition B.1.1.** *Under the assumptions (i) - (vii) set out in Section 3.2.2, the integral (3.2.1) can be expressed for $k \gg 1$ as*

$$\int_a^b f(t) e^{ik\phi(t)} = A_n(k) - B_m(k) + \delta_{mn}(k) - \epsilon_{mn}(k)\,, \tag{B.1.1}$$

*where the terms in the right hand side have been defined in (3.2.3), (3.2.4), (3.2.9) and (3.2.10), respectively.*

*Proof.* To establish the validity of the result given in (B.1.1), begin by making the change of variable $v = \phi(t) - \phi(a)$ in in (3.2.1). This change of variable is well-defined by the monotonicity of $\phi(t)$ on $(a, b)$ (assumption *(vi)*). In terms of $v$, the integral $I(k)$ in (3.2.1) becomes

$$I(k) = e^{ik\phi(a)} \int_0^{\phi(b)-\phi(a)} e^{ikv} h(v) dv\,,$$

where the function $h(v)$ is defined as

$$h(v) = h(\phi(t) - \phi(a)) \coloneqq \frac{f(t)}{\phi'(t)}\,.$$

Next, $h(v)$ and $t - a$ are expanded for small $v$ in the asymptotic series

$$t - a \sim \sum_{j=0}^{\infty} c_j v^{j/\mu}\,,$$

and

$$h(v) \sim \sum_{j=0}^{\infty} a_j v^{(j+\lambda-\mu)/\mu} \,. \tag{B.1.2}$$

Note that the coefficients $a_j$ in (B.1.2) are explicitly required in order to determine the terms $A_n(k)$ and $\epsilon_{mn}(k)$ in (B.1.1) (see equations (3.7.13) and (3.2.10)). These coefficients can calculated in terms of $\phi_j$ and $f_j$ in (3.2.13) and (3.2.12), normally by series inversion techniques. Later on, in Section 3.3, a general formula for the coefficients $a_j$ is derived, so that manual series inversion is no longer necessary.

Let $y = \phi(b) - \phi(a)$, and for $n \in \mathbb{N}$ define the functions $\theta_n(v)$ as

$$\theta_n(v) = h(v) - \sum_{j=0}^{n-1} a_j v^{\frac{j+\lambda}{\mu}-1}$$

for $0 < v < y$, so that using (B.1.2) we have $\theta_n(v) \sim a_n v^{\frac{n+\lambda}{\mu}-1} + a_{n+1} v^{\frac{n+1+\lambda}{\mu}-1} + \dots$, as $v \to 0^+$, and the $\ell^{\text{th}}$ derivative of $\theta_n(v)$ is given by

$$\theta_n^{(\ell)}(v) = h^{(l)}(v) - \sum_{j=0}^{n-1} \frac{\Gamma\left(\frac{j+\lambda}{\mu}\right)}{\Gamma\left(\frac{j+\lambda}{\mu} - \ell\right)} a_j v^{\frac{j+\lambda}{\mu}-(\ell+1)} \,, \tag{B.1.3}$$

for $\ell \in \{0, \dots, m\}$. Note that $h^{(\ell)}(v) = P_\ell(t)$, and that the functions $h(v)$, $\theta_n(v)$ and their first $m$ derivatives are continuous for $v \in (0, y]$ under the assumptions made in this Section. Next, for any $\xi > 0$ we have

$$\int_0^y e^{(ik-\xi)v} h(v)\, dv = \sum_{j=0}^{n-1} a_j \int_0^\infty e^{(ik-\xi)v} v^{\frac{j+\lambda}{\mu}-1}\, dv + E_n(\xi, k) - F_n(\xi, k) \,, \tag{B.1.4}$$

where

$$E_n(\xi, k) = \int_0^y e^{-\xi v} e^{ikv} \theta_n(v)\, dv \,, \tag{B.1.5}$$

and

$$F_n(\xi, k) = \sum_{j=0}^{n-1} a_j \int_y^\infty e^{-\xi v} e^{ikv} v^{\frac{j+\lambda}{\mu}-1}\, dv \,. \tag{B.1.6}$$

Taking the limit as $\xi \to 0$ and applying parts (a) and (b) of Lemma B.1.1 yields

$$\int_0^y e^{ikv} h(v) dv = \sum_{j=0}^{n-1} e^{i\pi \frac{j+\lambda}{2\mu}} \Gamma\left(\tfrac{j+\lambda}{\mu}\right) \frac{a_j}{k^{\frac{j+\lambda}{\mu}}} + E_n(k) - F_n(k)\,,$$

where $E_n(k) = \lim_{\xi\to 0} E_n(\xi, k)$ and $F_n(k) = \lim_{\xi\to 0} F_n(\xi, k)$. To determine $E_n(k)$, repeated integration by parts is applied to expression (B.1.5) $m-1$ times. The next step is to note that condition (3.2.5) results in all the necessary derivatives of $\theta_n(v)$ vanishing at $v = 0$, except maybe the $(m-1)^{\text{th}}$ derivative. Taking the limit as $\xi \to 0$ and applying part (b) of Lemma B.1.1 finally yields

$$E_n(k) = \left(\frac{i}{k}\right)^m \theta_n^{(m-1)}(0) e^{iky} \sum_{j=0}^{m-1} \theta_n^{(j)}(y) \left(\tfrac{i}{k}\right)^{j+1} + \left(\tfrac{i}{k}\right)^m \int_0^y e^{ikv} \theta_n^{(m)}(v)\, dv\,. \tag{B.1.7}$$

Similarly, to determine the corresponding expression for $F_n(k)$ part (c) of B.1.1 is applied to (B.1.6). Integration by parts is performed on the incomplete Gamma function term $m-1$ times, finally yielding

$$F_n(k) = e^{iky} \sum_{j=0}^{n-1} \sum_{\ell=0}^{m-1} a_j \frac{\Gamma\left(\frac{j+\lambda}{\mu}\right)}{\Gamma\left(\frac{j+\lambda}{\mu} - \ell\right)} \left(\tfrac{i}{k}\right)^{l+1} y^{\frac{j+\lambda}{\mu} - (1+\ell)} + e^{-ik\phi(a)} + \epsilon_{mn}(k)\,, \tag{B.1.8}$$

where $\epsilon_{mn}(k)$ is defined in (3.2.10). Finally, substituting the expression for $\theta_n^{(l)}(v)$ given in (B.1.3) into (B.1.7) and subtracting the result from (B.1.8) cancels out the double sum, so that the remaining expression is

$$E_n(k) - F_n(k) = -e^{iky} \sum_{j=0}^{m-1} h^{(j)}(y) \left(\tfrac{i}{k}\right)^{j+1} + \left(\tfrac{i}{k}\right)^m \theta_n^{m-1}(0) + e^{ik\phi(a)} \left( \delta_{mn}(k) - \epsilon_{mn}(k) \right)\,, \tag{B.1.9}$$

where

$$\delta_{mn}(k) = e^{ik\phi(a)} \left(\tfrac{i}{k}\right)^m \int_0^y e^{ikv} \theta_n^{(m)}(v)\, dv\,. \tag{B.1.10}$$

It can be directly verified that $\theta_n^{(m)}(v) = Q'_{mn}(t)/\phi'(t)$, and thus (B.1.10) is in agreement with (3.2.9). On the other hand, the restriction set out in (3.2.5) ensures that $\theta_n^{m-1}(0)$ vanishes except when $n = m\mu - \lambda$, in which case it is equal to $(m-1)! a_n$. These assertions, together with (B.1.4) and (B.1.9), establish the result set out in (B.1.1). □

**Proposition B.1.2** (Olver (1974)). *The total error* (3.2.8) *is bounded above by*

$$|E_{mn}(k)| \leq \frac{1}{k^m} \int_a^b |Q'_{mn}(t)|\, dt + \frac{2}{k^{m+1}} \sum_{j=0}^{n-1} \frac{\Gamma\left(\frac{j+\lambda}{\mu}\right)}{\left|\Gamma\left(\frac{j+\lambda}{\mu} - m\right)\right|} \frac{|a_j|}{(\,\phi(b) - \phi(a)\,)^{m+1-\frac{j+\lambda}{\mu}}}\,. \quad \text{(B.1.11)}$$

*Proof.* It can be established directly from (3.2.9) that

$$|\delta_{mn}(k)| \leq \frac{1}{k^m} \int_a^b |Q'_{mn}(t)|\, dt\,, \quad \text{(B.1.12)}$$

where the integral in the right hand side corresponds to the arc-length of $Q_{mn}(t)$ over the interval of integration $(a,\, b)$ (i.e. the total variation of $Q_{mn}(t)$ over the interval of integration). Note that as discussed in Remark 3.2.2, numerical calculation of this bound may be challenging due to cancellation errors. This issue can be circumvented by either finding a closed form for the integral in (B.1.12) or deriving high-order series approximations to $Q_{mn}(t)$ that can be integrated exactly and provide an accurate estimate of the bound. A higher order bound can be given by partial integration of (3.2.9), yielding

$$|\delta_{mn}(k)| \leq \frac{1}{k^{m+1}} \left( |Q_{m+1\,n}(a)| + |Q_{m+1\,n}(b)| + \int_0^\pi Q'_{m+1\,n}(t) dt \right)\,, \quad \text{(B.1.13)}$$

when the right hand side is finite. The finiteness of the bound (B.1.12) is guaranteed by assumptions *(i)* - *(viii)*, however this may not suffice in the case of bound (B.1.13).

For the remaining error term, $\epsilon_{mn}(k)$, the auxiliary inequality[1]

$$|\Gamma(x, \pm iy)| \leq 2y^{x-1}$$

for $x < 1$ and $y > 0$ is used directly to establish

$$|\epsilon_{mn}(k)| \leq \frac{2}{k^{m+1}} \sum_{j=0}^{n-1} \frac{\Gamma\left(\frac{j+\lambda}{\mu}\right)}{\left|\Gamma\left(\frac{j+\lambda}{\mu} - m\right)\right|} \frac{|a_j|}{(\,\phi(b) - \phi(a)\,)^{m+1-\frac{j+\lambda}{\mu}}}\,. \quad \text{(B.1.14)}$$

Finally, using the triangle inequality and combining (B.1.12) and (B.1.14) yields (3.2.14) directly. □

[1] To establish this bound, the path of integration in the incomplete Gamma function may be deformed into the imaginary axis. Then integration by parts is applied.

## B.2 Numerical validations of the explicit formula for asymptotic coefficients in the stationary phase approximation

The analytical expression for the coefficients $a_s$ given in (3.3.25) was implemented in MATLAB and in Mathematica for several test cases. Test functions were chosen to produce different values of $\mu$ and to result in $\tilde{h}(v)$ relatively straightforward to expand in Puiseaux series form, in order to have an exact reference to compare the coefficients produced by (3.3.25). The expansion points $a$ were always chosen to be minima of the phase $\phi$, in accordance with the default theoretical framework. The coefficient produced by (3.3.25) were tested up to index $s = 50$, and in all cases they produce a satisfactory result. In the following Figures the reference coefficients, extracted from the series expansion of $\tilde{h}(v)$, are plotted as blue circles, whereas the coefficients calculated from equation (3.3.25) are depicted as orange crosses. Results are presented below.

**Test 1**

- $\phi(t) = \cos(t)$
- $f(t) = \sin^2(t)$
- $\tilde{h}(v) = \sqrt{-v^2 + 2v}$
- $a = \pi$
- $\lambda = 3$
- $\mu = 2$

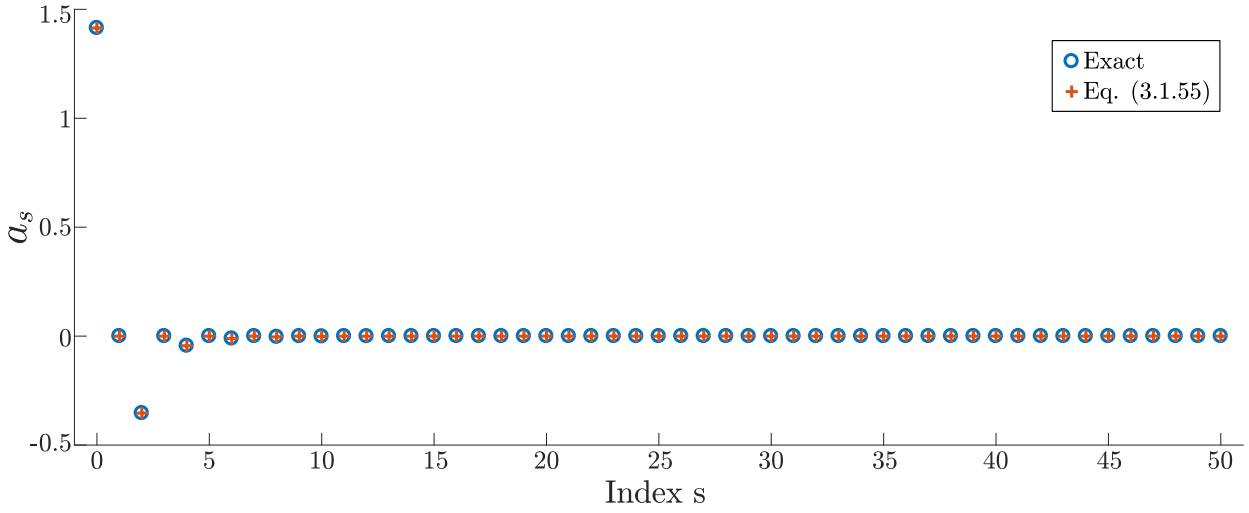


**Figure B.1:** Comparison of the first 50 coefficients calculated from (3.3.25) (blue circles) and those extracted directly from the Puiseaux series expansion of $\tilde{h}$ (orange crosses). Coefficients match up very well.

**Test 2**

- $\phi(t) = \sin(t)$
- $f(t) = \frac{1}{t}$
- $\tilde{h}(v) = -\frac{1}{\arcsin(1-v)\sqrt{-v^2+2v}}$
- $a = -\frac{\pi}{2}$
- $\lambda = 1$
- $\mu = 2$

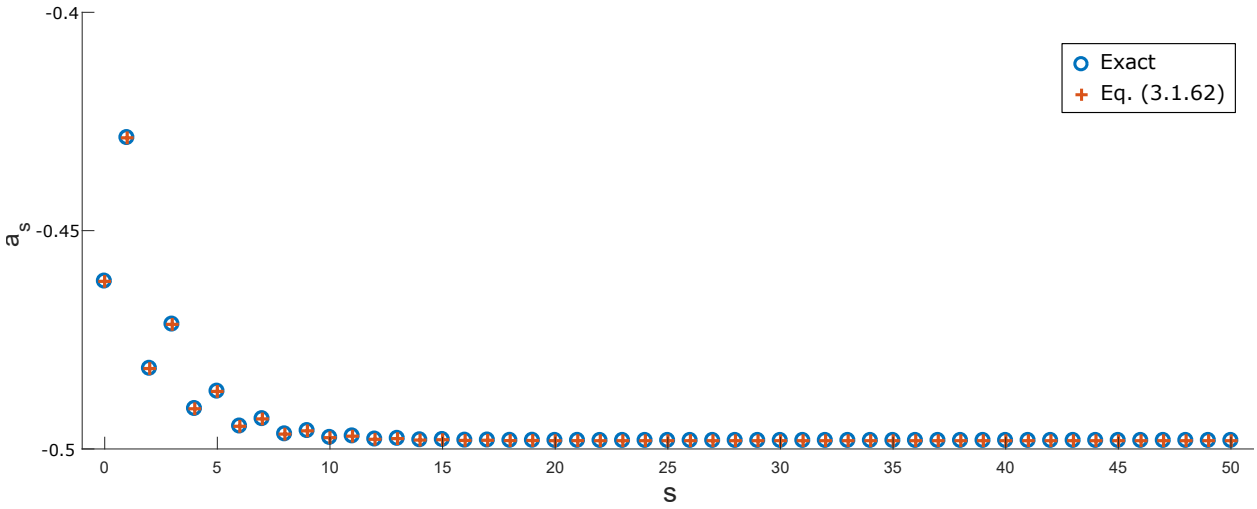


**Figure B.2:** Comparison of the first 50 coefficients calculated from (3.3.25) (blue circles) and those extracted directly from the Puiseaux series expansion of $\tilde{h}$ (orange crosses). Coefficients match up very well.

**Test 3**

- $\phi(t) = t^2 - 2t$
- $f(t) = \frac{1}{t}$
- $\tilde{h}(v) = \frac{1}{2v+2\sqrt{v}}$
- $a = 1$
- $\lambda = 1$
- $\mu = 2$

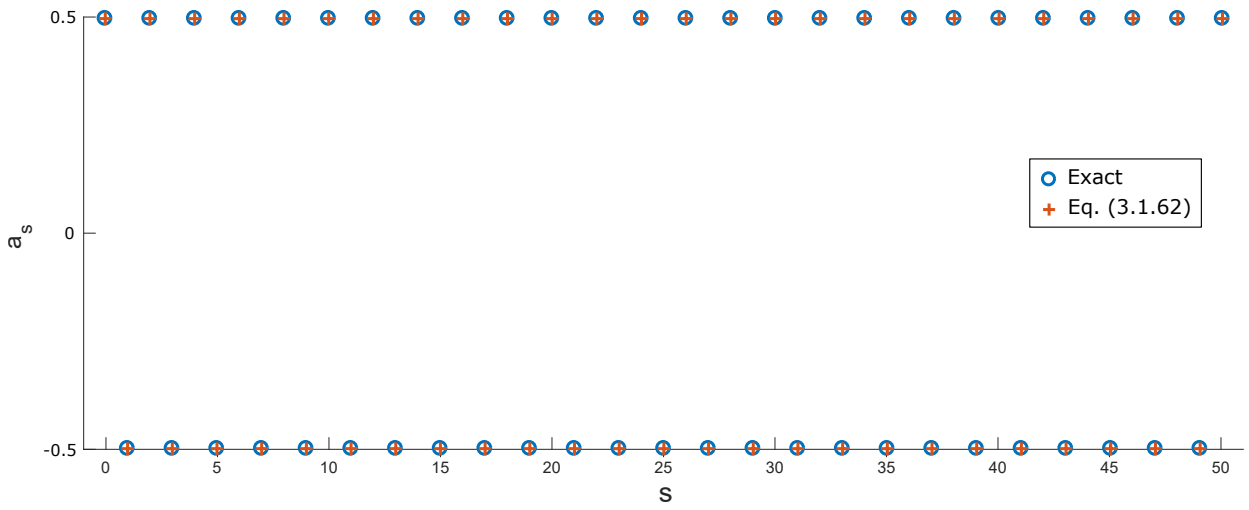


**Figure B.3:** Comparison of the first 50 coefficients calculated from (3.3.25) (blue circles) and those extracted directly from the Puiseaux series expansion of $\tilde{h}$ (orange crosses). Coefficients match up very well.

**Test 4**

- $\phi(t) = t^3$
- $f(t) = \frac{1}{t+1}$
- $\tilde{h}(v) = -\frac{1}{3(v+v^{2/3})}$
- $a = 0$
- $\lambda = 1$
- $\mu = 3$

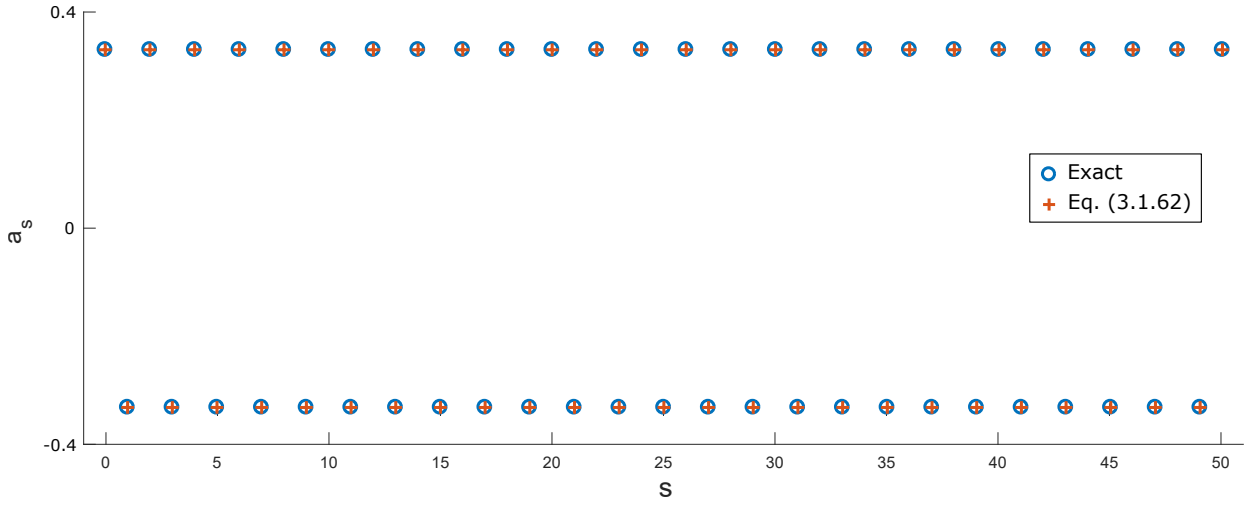


**Figure B.4:** Comparison of the first 50 coefficients calculated from (3.3.25) (blue circles) and those extracted directly from the Puiseaux series expansion of $\tilde{h}$ (orange crosses). Coefficients match up very well.

## B.3 Calculation of stationary phase approximation in wavefield interferometry

We now move on to performing this analysis for the integral $I^{\alpha,0^-}(\mathbf{x_A},\mathbf{x_B},k)$ which corresponds to the interval of integration $t\in(-\frac{\pi}{2},0)$, as defined in (3.5.21). In order to bring this integral to a form that satisfies the requirements set out in Section 3.2.2, specifically that the stationary point $t=0$ be the lower limit of integration, and that the phase $\phi(t)$ be increasing over the interval of integration, the following manipulations are performed,

$$\begin{aligned} I^{\alpha,0^-}(\mathbf{x_A},\mathbf{x_B},k) &= \int_{-\pi/2}^{0} f^{\alpha}(t)e^{ik\phi(t)}\,dt \\ &= -\int_{0}^{-\pi/2} f^{\alpha}(t)e^{ik\phi(t)}\,dt \\ &= \int_{0}^{\pi/2} f^{\alpha}(-t)e^{ik\phi(-t)}\,dt \\ &= \int_{0}^{\pi/2} |\alpha(-t)|^2 f(t)e^{ik\phi(t)}\,dt \end{aligned} \tag{B.3.1}$$

where the change of variable $t\to -t$ has been performed in the third equality, and the properties (3.5.14) and (3.5.16) have been used in the last. The representation (B.3.1) for $I^{\alpha,0^-}(\mathbf{x_A},\mathbf{x_B},k)$ satisfies the conditions set out in Section 3.2.2 for the application of the stationary phase method. Moreover, in this representation the phase of the integrand in $I^{\alpha,0^-}(\mathbf{x_A},\mathbf{x_B},k)$ the same as the phase of $I^{\alpha,0^+}(\mathbf{x_A},\mathbf{x_B},k)$. The random amplitude however is in general different, as it involves evaluation of the random field at locations parametrised by $-t$ rather than $t$. On the other hand the expansions continue to be taken around $t=0$, so that

$$\alpha(-t)=\alpha(t) \qquad \text{for } t=0\,,$$

and hence, using the chain rule and formulas (3.5.31) and (3.5.32) the coefficients of the expansion of $f^{\alpha}(-t)$ around $t=0$ are given in general by

$$f_j^{\alpha,0^-} = (-1)^j f_j^{\alpha,0^+}\,,$$

where the coefficients $f_j^{\alpha,0^-}$ are those given in (3.5.33), or explicitly

$$\begin{aligned}
f_0^{\alpha,0^-} &= \left(\alpha_0^0\right)^2 \frac{r}{\sqrt{r^2-d^2}}\,,\\
f_1^{\alpha,0^-} &= -\,\alpha_0^0\alpha_1^0 \frac{2\,r}{\sqrt{r^2-d^2}}\,,\\
f_2^{\alpha,0^-} &= \left(\,\alpha_0^0\alpha_2^0 + \left(\alpha_1^0\right)^2\,\right)\frac{2\,r}{\sqrt{r^2-d^2}} - \left(\alpha_0^0\right)^2 \frac{r^3 d^2}{\sqrt{(r^2-d^2)^5}}\,,\\
f_3^{\alpha,0^-} &= -\left(\,\alpha_0^0\alpha_3^0 + 3\,\alpha_1^0\alpha_2^0\,\right)\frac{2\,r}{\sqrt{r^2-d^2}} - \alpha_0^0\alpha_1^0 \frac{6\,r^3 d^2}{\sqrt{(r^2-d^2)^5}}\,,
\end{aligned} \tag{B.3.2}$$

and so on. Hence, using formula (3.3.25) the coefficients $a_j^{\alpha,0^-}$ are determined to be

$$a_j^{\alpha,0^-} = (-1)^j a_j^{\alpha,0^+}\,,$$

where the coefficients $a_j^{\alpha,0^-}$ have been given in (3.5.34), explicitly

$$\begin{aligned}
a_0^{\alpha,0^-} &= \frac{\left(\alpha_0^0\right)^2}{2\sqrt{d}}\,,\\
a_1^{\alpha,0^-} &= -\,\alpha_0^0\alpha_1^0 \frac{\sqrt{r^2-d^2}}{rd}\,,\\
a_2^{\alpha,0^-} &= \left(\,\left(\alpha_1^0\right)^2 + \alpha_0^0\alpha_2^0\,\right)\frac{r^2-d^2}{2\,r^2\sqrt{d^3}} + \left(\alpha_0^0\right)^2 \frac{r^4 - r^2d^2 + 4d^4}{16\,r^2\,(r^2-d^2)\,\sqrt{d^3}}\,,\\
a_3^{\alpha,0^-} &= -\left(\alpha_0^0\alpha_3^0 + 3\,\alpha_1^0\alpha_2^0\right)\frac{\sqrt{(r^2-d^2)^3}}{6\,r^3d^2} + \alpha_0^0\alpha_1^0\,\frac{r^4 + r^2d^2 + 4d^4}{6\,r^3d^2\sqrt{r^2-d^2}}
\end{aligned} \tag{B.3.3}$$

and so on. Next we define the auxiliary functions $Q_{mn}^{\alpha,0^-}(t)$ and $P_m^{\alpha,0^-}$ as

$$P_m^{\alpha,0^-}(t) = \left\{\frac{1}{\phi'(t)}\frac{d}{dt}\right\}^m \frac{f^\alpha(-t)}{\phi'(t)}\,, \tag{B.3.4}$$

and using the fact that $\phi'(t)$ is an odd function (which is determined by direct evaluation in (3.5.11)) and the linearity of the differentiation operation, we have

$$\begin{aligned} P^{\alpha}_{m,\,0^-}(-t) &= \left\{ \frac{1}{\phi'(-t)} \frac{d}{dt} \right\}^m \frac{f^{\alpha}(t)}{\phi'(-t)} \\ &= (-1)^{m+1} \left\{ \frac{1}{\phi'(t)} \frac{d}{dt} \right\}^m \frac{f^{\alpha}(t)}{\phi'(t)} \\ &= (-1)^{m+1} P^{\alpha}_{m,\,0^+}(t) \end{aligned} \tag{B.3.5}$$

a property that will not be used just yet but comes in useful later on. We further define

$$Q^{\alpha,\,0^-}_{mn}(t) = P^{\alpha,\,0^-}_{m-1} - \sum_{j=0}^{n-1} \frac{\Gamma\left(\frac{j+1}{2}\right)}{\Gamma\left(\frac{j+1}{2}+1-m\right)} \frac{a_j^{\alpha,\,0^-}}{(\,\phi(t)+2d\,)^{m-\frac{j+1}{2}}}\,, \tag{B.3.6}$$

Hence, applying (B.1.1) to $I^{\alpha,\,0^-}(\mathbf{x_A}, \mathbf{x_B}, k)$ results in the exact equation

$$I^{\alpha,\,0^-}(\mathbf{x_A}, \mathbf{x_B}, k) = A^{\alpha,\,0^-}_n(k) - B^{\alpha,\,0^-}_m(k) + \delta^{\alpha,\,0^-}_{mn}(k) - \epsilon^{\alpha,\,0^-}_{mn}(k)\,, \tag{B.3.7}$$

where

$$A^{\alpha,\,0^-}_n(k) = e^{-2d\,ik}\sqrt{\pi} \sum_{j=0}^{n-\nu} e^{(j+1)\frac{\pi}{4}i}\, \frac{(j-1)!!}{\sqrt{2^j k^{j+1}}}\, a_j^{\alpha,\,0^-}\,, \tag{B.3.8}$$

$$B^{\alpha,\,0^-}_m(k) = \sum_{j=0}^{m-1} P^{\alpha,\,0^-}_j\left(\tfrac{\pi}{2}\right) \left(\frac{i}{k}\right)^{j+1}\,, \tag{B.3.9}$$

$$\delta^{\alpha,\,0^-}_{mn}(k) = \left(\frac{i}{k}\right)^m \int_0^{\pi/2} e^{ik\phi(t)} Q^{\alpha,\,0^-\,\prime}_{mn}(t)\, dt \tag{B.3.10}$$

and

$$\epsilon^{\alpha,\,0^-}_{mn}(k) = e^{-2dik} \sum_{j=0}^{n-1} e^{(j+1)\frac{\pi}{4}i} \frac{\Gamma\left(\frac{j+1}{2}\right)}{\Gamma\left(\frac{j+1}{2}-m\right)} \Gamma\left(\tfrac{j+1}{2}-m,\, -2d\,ik\right) \frac{a_j^{\alpha,\,0^-}}{k^{\frac{j+1}{2}}}\,. \tag{B.3.11}$$

Similarly to (3.5.41), the error incurred in the approximation (B.3.7) is given by

$$E^{\alpha,\,0^-}_{mn}(k) = \delta^{\alpha,\,0^-}_{mn}(k) - \epsilon^{\alpha,\,0^-}_{mn}(k),\,, \tag{B.3.12}$$

with

$$\delta_{mn}^{\alpha,0^-}(k) = \left(\frac{i}{k}\right)^m \int_0^{\pi/2} e^{ik\phi(t)} Q_{mn}^{\alpha,0^-\prime}(t)\, dt \tag{B.3.13}$$

and

$$\epsilon_{mn}^{\alpha,0^-}(k) = e^{-2dik} \sum_{j=0}^{n-1} e^{(j+1)\frac{\pi}{4}i} \frac{\Gamma\left(\frac{j+1}{2}\right)}{\Gamma\left(\frac{j+1}{2}-m\right)} \Gamma\left(\tfrac{j+1}{2}-m,\, -2d\, ik\right) \frac{a_j^{\alpha,0^-}}{k^{\frac{j+1}{2}}}\,, \tag{B.3.14}$$

As before, bounds for each of these error terms are determined using (B.1.12) and (B.1.14), yielding

$$|\delta_{mn}^{\alpha,0^-}(k)| \le \left(\frac{1}{k}\right)^m \int_0^{\pi/2} |Q_{mn}^{\alpha,0^-\prime}(t)|\, dt \tag{B.3.15}$$

and

$$|\epsilon_{mn}^{\alpha,0^-}(k)| \le \frac{2}{k^{m+1}} \sum_{j=0}^{n-1} \frac{\Gamma\left(\frac{j+1}{2}\right)}{\left|\Gamma\left(\frac{j+1}{2}-m\right)\right|} \frac{|a_j^{\alpha,0}|}{(\,2d\,)^{m+1-\frac{j+1}{2}}}\,, \tag{B.3.16}$$

Finally, the bound for the total error $E_{mn}^{\alpha,0^-}(k)$ defined in (B.3.12) is given by

$$|E_{mn}^{\alpha,0^-}(k)| \le \left(\frac{1}{k}\right)^m \int_0^{\pi/2} |Q_{mn}^{\alpha,0^-\prime}(t)|\, dt \;+\; \frac{2}{k^{m+1}} \sum_{j=0}^{n-1} \frac{\Gamma\left(\frac{j+1}{2}\right)}{\left|\Gamma\left(\frac{j+1}{2}-m\right)\right|} \frac{|a_j^{\alpha,0}|}{(\,2d\,)^{m+1-\frac{j+1}{2}}}\,. \tag{B.3.17}$$

Approximations (3.5.37) and (B.3.7) together capture the contribution of the stationary point $t = 0$ to the original integral (3.5.6), so that

$$\begin{aligned} \int_{-\pi/2}^{\pi/2} f^\alpha(t) e^{ik\phi(t)}\, dt &= I^{\alpha,0^-}(\mathbf{x_A}, \mathbf{x_B}, k) + I^{\alpha,0^+}(\mathbf{x_A}, \mathbf{x_B}, k) \\ &= A_n^{\alpha,0^+}(k) + A_n^{\alpha,0^-}(k) - \left(B_m^{\alpha,0^-}(k) + B_m^{\alpha,0^+}(k)\right) + \\ &\quad + \delta_{mn}^{\alpha,0^-}(k) + \delta_{mn}^{\alpha,0^+}(k) - \left(\epsilon_{mn}^{\alpha,0^+}(k) + \epsilon_{mn}^{\alpha,0^-}(k)\right)\,. \end{aligned} \tag{B.3.18}$$

Hence the stationary phase contribution from the stationary point corresponding to $t = 0$ is given by the approximation

$$\int_{-\pi/2}^{\pi/2} f^{\alpha}(t)e^{ik\phi(t)}\,dt \approx A_n^{\alpha,0^+}(k) + A_n^{\alpha,0^-}(k) - \left(B_m^{\alpha,0^-}(k) + B_m^{\alpha,0^+}(k)\right), \tag{B.3.19}$$

and the error incurred is given by the term

$$E_{mn}^{\alpha,0}(k) = \delta_{mn}^{\alpha,0^-}(k) + \delta_{mn}^{\alpha,0^+}(k) - \left(\epsilon_{mn}^{\alpha,0^+}(k) + \epsilon_{mn}^{\alpha,0^-}(k)\right). \tag{B.3.20}$$

Now we proceed to capturing the approximation at the stationary point corresponding to $t = \pi$, starting with the integral $I^{\alpha,\pi^+}(\mathbf{x_A}, \mathbf{x_B}, k)$ defined in (3.5.24), corresponding to the interval $t \in (\pi, \frac{3\pi}{2})$. Note that this stationary point is a maximum rather than a minimum of the phase $\phi(t)$, so the integral needs to be manipulated as follows

$$\begin{aligned} I^{\alpha,\pi^+}(\mathbf{x_A}, \mathbf{x_B}, k) &= \int_{\pi}^{3\pi/2} f^{\alpha}(t)e^{ik\phi(t)}\,dt \\ &= \left(\int_{\pi}^{3\pi/2} f^{\alpha}(t)e^{-ik\phi(t)}\,dt\right)^* \\ &= \left(\int_{0}^{\pi/2} f^{\alpha}(\pi+t)e^{-ik\phi(\pi+t)}\,dt\right)^* \end{aligned}$$

where the change of variable $t \to \pi + t$ has been used on the third equality and the $\pi$-periodicity of $f(t)$ as stated in (3.5.13) has been used. Finally, using the property (3.5.15) for $-\phi(\pi + t)$ we have

$$I^{\alpha,\pi^+}(\mathbf{x_A}, \mathbf{x_B}, k) = \left(\int_{0}^{\pi/2} f^{\alpha}(\pi+t)e^{ik\phi(t)}\,dt\right)^*, \tag{B.3.21}$$

where the integral inside the brackets satisfies the necessary conditions in Section 3.2.2 for the application of the stationary phase approximation. Moreover, by virtue of these manipulations the expansion of the phase $\phi(t)$ is taken again around $t = 0$, so that the coefficients

calculated in (3.5.26) may be used again. On the other hand, the random amplitude of the integrand is no longer evaluated around zero, but rather at $t = \pi$, which is appropriate as the stationary point at hand is $t = \pi$. Then $f^\alpha(\pi + t)$ can be expanded around $t = 0$ as

$$f^\alpha(t) \approx f_0^{\alpha,\,\pi^+} + f_1^{\alpha,\,\pi^+} t + f_2^{\alpha,\,\pi^+} t^2 + \dots$$

where the coefficients $f_j^{\alpha,\,\pi^+}$ are defined as

$$f_j^{\alpha,\,\pi^+} = \left\{ \alpha(\pi + t)^2 f(t) \right\}^{(j)} \Big|_{t=0} .$$

Moreover, for simplicity let $\alpha_j^\pi$ denote the $j^{\text{th}}$ derivative of $\alpha(\pi + t)$ at $t = 0$, i.e.

$$\alpha_j^\pi = \{\alpha(\pi + t)\}^{(j)} \Big|_{t=0} ,$$

where the superindex $(\cdot)^\pi$ has been used to highlight the fact that these coefficients correspond to the values of $\alpha(t)$ and it derivatives at the stationary point $t = \pi$ (that corresponds to location $\mathbf{x}_\pi$ on $S$), and distinguish them from the coefficients resulting from the corresponding expansion around the other stationary point, namely $t = \pi$, that will be taken later on. Then using (3.5.31) and the coefficients $f_j$ given for the homogeneous amplitude function $f(t)$ in (3.5.30), the first few coefficients $f_j^{\alpha,\,\pi^+}$ are given explicitly by

$$\begin{aligned}
f_0^{\alpha,\,\pi^+} &= (\alpha_0^\pi)^2 \, \frac{r}{\sqrt{r^2 - d^2}} \,, \\[2ex]
f_1^{\alpha,\,\pi^+} &= \alpha_0^\pi \alpha_1^\pi \frac{2\,r}{\sqrt{r^2 - d^2}} \,, \\[2ex]
f_2^{\alpha,\,\pi^+} &= \left( \alpha_0^\pi \alpha_2^\pi + (\alpha_1^\pi)^2 \right) \frac{2\,r}{\sqrt{r^2 - d^2}} - (\alpha_0^\pi)^2 \, \frac{r^3 d^2}{\sqrt{(r^2 - d^2)^5}} \,, \\[2ex]
f_3^{\alpha,\,\pi^+} &= \left( \alpha_0^\pi \alpha_3^\pi + 3\,\alpha_1^\pi \alpha_2^\pi \right) \frac{2\,r}{\sqrt{r^2 - d^2}} - \alpha_0^\pi \alpha_1^\pi \frac{6\,r^3 d^2}{\sqrt{(r^2 - d^2)^5}}
\end{aligned} \tag{B.3.22}$$

Nevertheless, the deterministic part of the amplitude of the integrand, namely $f(t)$ is the same as in our earlier derivations, and therefore for small $t$ we take

$$f^\alpha(\pi + t) \approx |\alpha(\pi)|^2 f(t) \,,$$

where the $\pi$-periodicity of $f(t)$ has been used again. Hence, the coefficients necessary for the stationary phase approximation of $I^{\alpha,\pi^+}(\mathbf{x_A},\mathbf{x_B},k)$ are given explicitly by

$$\begin{aligned}
a_0^{\alpha,\pi^+} &= \frac{(\alpha_0^\pi)^2}{2\sqrt{d}}\,,\\[2ex]
a_1^{\alpha,\pi^+} &= \alpha_0^\pi\alpha_1^\pi\frac{\sqrt{r^2-d^2}}{rd}\,,\\[2ex]
a_2^{\alpha,\pi^+} &= \left((\alpha_1^\pi)^2+\alpha_0^\pi\alpha_2^\pi\right)\frac{r^2-d^2}{2\,r^2\sqrt{d^3}}+(\alpha_0^\pi)^2\,\frac{r^4-r^2d^2+4d^4}{16\,r^2\,(r^2-d^2)\,\sqrt{d^3}}\,,\\[2ex]
a_3^{\alpha,\pi^+} &= (\alpha_0^\pi\alpha_3^\pi+3\,\alpha_1^\pi\alpha_2^\pi)\,\frac{\sqrt{(r^2-d^2)^3}}{6\,r^3d^2}+\alpha_0^\pi\alpha_1^\pi\,\frac{r^4+r^2d^2+4d^4}{6\,r^3d^2\sqrt{r^2-d^2}}
\end{aligned}\tag{B.3.23}$$

and so on. Finally, the auxiliary functions $P_m^{\alpha,\pi^+}(t)$ and $Q^{\alpha}_{mn\,\pi^+}(t)$ are defined as

$$P_m^{\alpha,\pi^+}(t)=\left\{\frac{1}{\phi'(t)}\frac{d}{dt}\right\}^m\frac{f^\alpha(\pi+t)}{\phi'(t)}\,,\tag{B.3.24}$$

and

$$Q_{mn}^{\alpha,\pi^+}(t)=P_{m-1}^{\alpha,\pi^+}(t)-\sum_{j=0}^{n-1}\frac{\Gamma\left(\frac{j+1}{2}\right)}{\Gamma\left(\frac{j+1}{2}+1-m\right)}\frac{a_j^{\alpha,\pi^+}}{(\,\phi(t)+2d\,)^{m-\frac{j+1}{2}}}\,,\tag{B.3.25}$$

for $t\in\left(0,\frac{\pi}{2}\right)$. Therefore applying equation (B.1.1) to the integral within the brackets in the right hand side of (B.3.21), the integral $I^{\alpha,\pi^+}(\mathbf{x_A},\mathbf{x_B},k)$ can be written exactly as

$$I^{\alpha,\pi^+}(\mathbf{x_A},\mathbf{x_B},k)=\left(A_n^{\alpha,\pi^+}(k)\right)^*-\left(B_m^{\alpha,\pi^+}(k)\right)^*+\left(\delta_{mn}^{\alpha,\pi^+}(k)\right)^*-\left(\epsilon_{mn}^{\alpha,\pi^+}(k)\right)^*\tag{B.3.26}$$

with stationary phase approximation given by

$$I^{\alpha,\pi^+}(\mathbf{x_A},\mathbf{x_B},k)\approx\left(A_n^{\alpha,\pi^+}(k)\right)^*-\left(B_m^{\alpha,\pi^+}(k)\right)^*\tag{B.3.27}$$

where

$$A_n^{\alpha,\pi^+}(k)=e^{-2d\,ik}\sqrt{\pi}\sum_{j=0}^{n-\nu}e^{(j+1)\frac{\pi}{4}i}\,\frac{(j-1)!!}{\sqrt{2^j}\,k^{j+1}}\,a_j^{\alpha,\pi^+}\,,\tag{B.3.28}$$

and

$$B_m^{\alpha,\,\pi^+}(k) = \sum_{j=0}^{m-1} P_j^{\alpha,\,\pi^+}\left(\tfrac{\pi}{2}\right)\left(\frac{i}{k}\right)^{j+1}, \tag{B.3.29}$$

and the error incurred in the approximation (B.3.27) is given by the terms

$$E_{mn}^{\alpha,\,\pi^+}(k) = \left(\delta_{mn}^{\alpha,\,\pi^+}(k)\right)^* - \left(\epsilon_{mn}^{\alpha,\,\pi^+}(k)\right)^*, \tag{B.3.30}$$

with

$$\delta_{mn}^{\alpha,\,\pi^+}(k) = \left(\frac{i}{k}\right)^m \int_0^{\pi/2} e^{ik\phi(t)} Q_{mn}^{\alpha,\,\pi^+\,\prime}(t)\,dt \tag{B.3.31}$$

and

$$\epsilon_{mn,\,\pi^+}^{\alpha}(k) = e^{-2dik}\sum_{j=0}^{n-1} e^{(j+1)\frac{\pi}{4}i}\frac{\Gamma\left(\frac{j+1}{2}\right)}{\Gamma\left(\frac{j+1}{2}-m\right)}\Gamma\left(\tfrac{j+1}{2}-m,\,-2d\,ik\right)\frac{a_j^{\alpha,\,\pi^+}}{k^{\frac{j+1}{2}}}. \tag{B.3.32}$$

noting that the complex conjugation taken does not affect the bound. As before, bounds for each of these error terms are determined using (B.1.12) and (B.1.14), yielding

$$\left|\left(\delta_{mn}^{\alpha,\,\pi^+}(k)\right)^*\right| \le \left(\frac{1}{k}\right)^m \int_0^{\pi/2} \left|Q_{mn}^{\alpha,\,\pi^+\,\prime}(t)\right| dt \tag{B.3.33}$$

and

$$\left|\left(\epsilon_{mn}^{\alpha,\,\pi^+}(k)\right)^*\right| \le \frac{2}{k^{m+1}}\sum_{j=0}^{n-1}\frac{\Gamma\left(\frac{j+1}{2}\right)}{\left|\Gamma\left(\frac{j+1}{2}-m\right)\right|}\frac{\left|a_j^{\alpha,\,\pi^+}\right|}{(\,2d\,)^{m+1-\frac{j+1}{2}}}, \tag{B.3.34}$$

Finally, the bound for the total error $E_{mn}^{\alpha,\,\pi^+}(k)$ defined in (B.3.30) is given by

$$\left|E_{mn}^{\alpha,\,\pi^+}(k)\right| \le \left(\frac{1}{k}\right)^m \int_0^{\pi/2} \left|Q_{mn}^{\alpha,\,\pi^+\,\prime}(t)\right| dt \;+\; \frac{2}{k^{m+1}}\sum_{j=0}^{n-1}\frac{\Gamma\left(\frac{j+1}{2}\right)}{\left|\Gamma\left(\frac{j+1}{2}-m\right)\right|}\frac{\left|a_j^{\alpha,\,\pi^+}\right|}{(\,2d\,)^{m+1-\frac{j+1}{2}}}. \tag{B.3.35}$$

The remaining portion of the boundary corresponds to the integral $I^{\alpha,\pi^-}(\mathbf{x_A},\mathbf{x_B},k)$. In a procedure entirely analogous to the preceding cases we note that

$$\begin{aligned} I^{\alpha,\pi^-}(\mathbf{x_A},\mathbf{x_B},k) &= \int_{\pi/2}^{\pi} f^{\alpha}(t)e^{ik\phi(t)}\,dt \\ &= \left(\int_{\pi/2}^{\pi} f^{\alpha}(t)e^{-ik\phi(t)}\,dt\right)^* \\ &= \left(-\int_{\pi}^{\pi/2} f^{\alpha}(t)e^{-ik\phi(t)}\,dt\right)^* \\ &= \left(\int_{0}^{\pi/2} f^{\alpha}(\pi-t)e^{-ik\phi(\pi-t)}\,dt\right)^* \end{aligned}$$

where the change of variable $t \to \pi - t$ has been performed to obtain the last equality. Finally, using property (3.5.15) for $-\phi(\pi-t)$ we derive

$$I^{\alpha,\pi^-}(\mathbf{x_A},\mathbf{x_B},k) = \left(\int_{0}^{\pi/2} f^{\alpha}(\pi-t)e^{ik\phi(t)}\,dt\right)^*, \tag{B.3.36}$$

where the integral inside the brackets is in an appropriate form for the application of the stationary phase method. As before, the expansions of the phase and the amplitude are taken around $t = 0$, with the coefficients for $\phi(t)$ remaining the same. In regards to the phase, we take for small $t$

$$f^{\alpha}(\pi-t) \approx |\alpha(\pi)|^2 f(\pi-t) = |\alpha(\pi)|^2 f(t)\,,$$

where (3.5.13) and (3.5.14) have been used in the last equality (that is the $\pi$-periodicity and evenness of $f(t)$). Hence, using the chain rule and formulas (3.5.31) and (3.5.32) the coefficients of the expansion of $f^{\alpha}(\pi-t)$ around $t=0$ are given in general by

$$f_j^{\alpha,\pi^-} = (-1)^j f_j^{\alpha,\pi^+}\,,$$

where the coefficients $f_j^{\alpha,\pi^-}$ are those given in (B.3.37), or explicitly

$$\begin{aligned}
f_0^{\alpha,\pi^-} &= (\alpha_0^\pi)^2 \frac{r}{\sqrt{r^2-d^2}}\,, \\
f_1^{\alpha,\pi^-} &= -\alpha_0^\pi \alpha_1^\pi \frac{2\,r}{\sqrt{r^2-d^2}}\,, \\
f_2^{\alpha,\pi^-} &= \big(\,\alpha_0^\pi \alpha_2^\pi + (\alpha_1^\pi)^2\,\big)\,\frac{2\,r}{\sqrt{r^2-d^2}} - (\alpha_0^\pi)^2 \frac{r^3 d^2}{\sqrt{(r^2-d^2)^5}}\,, \\
f_3^{\alpha,\pi^-} &= -\,\big(\,\alpha_0^\pi \alpha_3^\pi + 3\,\alpha_1^\pi \alpha_2^\pi\,\big)\,\frac{2\,r}{\sqrt{r^2-d^2}} - \alpha_0^\pi \alpha_1^\pi \frac{6\,r^3 d^2}{\sqrt{(r^2-d^2)^5}}\,,
\end{aligned} \tag{B.3.37}$$

Hence, using formula (3.3.25) the coefficients $a_j^{\alpha,0^-}$ are determined to be

$$a_j^{\alpha,\pi^-} = (-1)^j a_j^{\alpha,\pi^+}\,,$$

where the coefficients $a_j^{\alpha,0^-}$ have been given in (3.5.34), or explicitly

$$\begin{aligned}
a_0^{\alpha,\pi^-} &= \frac{(\alpha_0^\pi)^2}{2\sqrt{d}}\,, \\
a_1^{\alpha,\pi^-} &= -\,\alpha_0^\pi \alpha_1^\pi \frac{\sqrt{r^2-d^2}}{r d}\,, \\
a_2^{\alpha,\pi^-} &= \big(\,(\alpha_1^\pi)^2 + \alpha_0^\pi \alpha_2^\pi\,\big)\,\frac{r^2-d^2}{2\,r^2\sqrt{d^3}} + (\alpha_0^\pi)^2 \frac{r^4 - r^2 d^2 + 4d^4}{16\,r^2\,(r^2-d^2)\,\sqrt{d^3}}\,, \\
a_3^{\alpha,\pi^-} &= -\,(\alpha_0^\pi \alpha_3^\pi + 3\,\alpha_1^\pi \alpha_2^\pi)\,\frac{\sqrt{(r^2-d^2)^3}}{6\,r^3 d^2} + \alpha_0^\pi \alpha_1^\pi \frac{r^4 + r^2 d^2 + 4d^4}{6\,r^3 d^2 \sqrt{r^2-d^2}}
\end{aligned} \tag{B.3.38}$$

All that remains is to define the auxiliary functions $P_m^{\alpha,\pi^-}(t)$ and $Q_{mn}^{\alpha\,\pi^-}(t)$ are defined as

$$P_m^{\alpha,\pi^-}(t) = \left\{ \frac{1}{\phi'(t)} \frac{d}{dt} \right\}^m \frac{f^\alpha(\pi - t)}{\phi'(t)}\,, \tag{B.3.39}$$

and

$$Q_{mn}^{\alpha\,\pi^-}(t) = P_{m-1}^{\alpha,\pi^-}(t) - \sum_{j=0}^{n-1} \frac{\Gamma\left(\frac{j+1}{2}\right)}{\Gamma\left(\frac{j+1}{2}+1-m\right)} \frac{a_j^{\alpha,\pi^-}}{(\,\phi(t)+2d\,)^{m-\frac{j+1}{2}}}\,. \tag{B.3.40}$$

Therefore, applying equation (B.1.1) to the integral within the brackets in (B.3.36), the integral $I^{\alpha,\pi^-}(\mathbf{x_A},\mathbf{x_B},k)$ can be written as

$$I^{\alpha,\pi^-}(\mathbf{x_A},\mathbf{x_B},k) = \left(A_n^{\alpha,\pi^-}(k)\right)^* - \left(B_m^{\alpha,\pi^-}(k)\right)^* + \left(\delta_{mn}^{\alpha,\pi^-}(k)\right)^* - \left(\epsilon_{mn}^{\alpha,\pi^-}(k)\right)^* \tag{B.3.41}$$

where

$$A_n^{\alpha,\pi^-}(k) = e^{-2d\,ik}\sqrt{\pi}\sum_{j=0}^{n-\nu} e^{(j+1)\frac{\pi}{4}i}\,\frac{(j-1)!!}{\sqrt{2^j}\,k^{j+1}}\,a_j^{\alpha,\pi^-}\,, \tag{B.3.42}$$

$$B_m^{\alpha,\pi^-}(k) = \sum_{j=0}^{m-1} P_j^{\alpha,\pi^-}\left(\tfrac{\pi}{2}\right)\left(\frac{i}{k}\right)^{j+1}\,. \tag{B.3.43}$$

$$\delta_{mn}^{\alpha,\pi^-}(k) = \left(\frac{i}{k}\right)^m \int_0^{\pi/2} e^{ik\phi(t)} Q_{mn}^{\alpha,\pi^-\,\prime}(t)\,dt \tag{B.3.44}$$

and

$$\epsilon_{mn}^{\alpha,\pi^-}(k) = e^{-2dik}\sum_{j=0}^{n-1} e^{(j+1)\frac{\pi}{4}i}\frac{\Gamma\left(\frac{j+1}{2}\right)}{\Gamma\left(\frac{j+1}{2}-m\right)}\Gamma\left(\tfrac{j+1}{2}-m,\,-2d\,ik\right)\frac{a_j^{\alpha,\pi^-}}{k^{\frac{j+1}{2}}}\,. \tag{B.3.45}$$

The stationary phase approximation is given as

$$I^{\alpha,\pi^-}(\mathbf{x_A},\mathbf{x_B},k) \approx \left(A_n^{\alpha,\pi^-}(k)\right)^* - \left(B_m^{\alpha,\pi^-}(k)\right)^*$$

and the error incurred in this approximation is given by the terms

$$E_{mn}^{\alpha,\pi^-}(k) = \left(\delta_{mn}^{\alpha,\pi^-}(k)\right)^* - \left(\epsilon_{mn}^{\alpha,\pi^-}(k)\right)^*\,, \tag{B.3.46}$$

We have analogous bounds for these error terms given by

$$\left|\left(\delta_{mn}^{\alpha,\pi^-}(k)\right)^*\right| \le \left(\frac{1}{k}\right)^m \int_0^{\pi/2} |Q_{mn}^{\alpha,\pi^-\,\prime}(t)|\,dt \tag{B.3.47}$$

and

$$\left|\left(\epsilon_{mn}^{\alpha,\pi^-}(k)\right)^*\right| \le \frac{2}{k^{m+1}}\sum_{j=0}^{n-1}\frac{\Gamma\left(\frac{j+1}{2}\right)}{\left|\Gamma\left(\frac{j+1}{2}-m\right)\right|}\frac{|a_j^{\alpha,\pi^-}|}{(\,2d\,)^{m+1-\frac{j+1}{2}}}\,, \tag{B.3.48}$$

noting as before that the complex conjugation does not affect the bound for the modulus. Hence, the bound for the total error $E_{mn}^{\alpha,\pi^-}(k)$ defined in (B.3.46) is given by

$$|E_{mn}^{\alpha,\pi^-}(k)| \leq \left(\frac{1}{k}\right)^m \int_0^{\pi/2} |Q_{mn}^{\alpha,\pi^-\prime}(t)|\,dt + \frac{2}{k^{m+1}} \sum_{j=0}^{n-1} \frac{\Gamma\left(\frac{j+1}{2}\right)}{\left|\Gamma\left(\frac{j+1}{2}-m\right)\right|} \frac{|a_j^{\alpha,\pi^-}|}{(2d)^{m+1-\frac{j+1}{2}}}\,. \quad \text{(B.3.49)}$$

# Bibliography


M. Abramowitz, I. A. Stegun, and R. H. Romer. Handbook of mathematical functions with formulas, graphs, and mathematical tables, 1988.

K. Aki and P. G. Richards. *Quantitative seismology*. University Science Books, 2002.

F. Ardhuin, E. Stutzmann, M. Schimmel, and A. Mangeney. Ocean wave sources of seismic noise. *Journal of Geophysical Research: Oceans*, 116(C9), 2011.

F. Ardhuin, L. Gualtieri, E. Stutzmann, N. Nakata, and A. Fichtner. Physics of ambient noise generation by ocean waves. *Seismic Ambient Noise*, pages 69–108, 2019.

P. Arroucau, N. Rawlinson, and M. Sambridge. New insight into Cainozoic sedimentary basins and Palaeozoic suture zones in southeast Australia from ambient noise surface wave tomography. *Geophysical Research Letters*, 37(7), 2010.

K. B. Athreya and S. N. Lahiri. *Measure theory and probability theory*, volume 19. Springer, 2006.

D. Ayala-Garcia, A. Curtis, and M. Branicki. Seismic Interferometry from Correlated Noise Sources. *Remote Sensing*, 13(14), 2021. ISSN 2072-4292. doi: 10.3390/rs13142703.

A. Bakulin and R. Calvert. The virtual source method: Theory and case study. *Geophysics*, 71(4):SI139–SI150, 2006.

A. Bakulin, A. Mateeva, K. Mehta, P. Jorgensen, J. Ferrandis, I. S. Herhold, and J. Lopez. Virtual source applications to imaging and reservoir monitoring. *The Leading Edge*, 26 (6):732–740, 2007.

M. Behm and R. Snieder. Love waves from local traffic noise interferometry. *The Leading Edge*, 32(6):628–632, 2013.

C. M. Bender and S. A. Orszag. *Advanced mathematical methods for scientists and engineers I: Asymptotic methods and perturbation theory*. Springer Science & Business Media, 2013.

G. Bensen, M. Ritzwoller, M. Barmin, A. L. Levshin, F. Lin, M. Moschetti, N. Shapiro, and Y. Yang. Processing seismic ambient noise data to obtain reliable broad-band surface wave dispersion measurements. *Geophysical journal international*, 169(3):1239–1260, 2007.

N. Bleistein. *Mathematical methods for wave phenomena*. Academic Press, 2012.

N. Bleistein and R. A. Handelsman. *Asymptotic expansions of integrals*. Courier Corporation, 1986.

F. Brenguier, N. M. Shapiro, M. Campillo, V. Ferrazzini, Z. Duputel, O. Coutant, and A. Nercessian. Towards forecasting volcanic eruptions using seismic noise. *Nature Geoscience*, 1(2):126–130, 2008.

F. Brenguier, P. Boué, Y. Ben-Zion, F. Vernon, C. Johnson, A. Mordret, O. Coutant, P.-E. Share, E. Beaucé, D. Hollis, et al. Train traffic as a powerful noise source for monitoring active faults with seismic interferometry. *Geophysical Research Letters*, 46(16):9529–9536, 2019.

M. Campillo and A. Paul. Long-range correlations in the diffuse seismic coda. *Science*, 299 (5606):547–549, 2003.

W. L. Chapman, G. Brown, and D. Fair. The Vibroseis system: A high-frequency tool. *Geophysics*, 46(12):1657–1666, 1981.

Y. Chen and E. Saygin. Empirical Green's Function Retrieval Using Ambient Noise Source-Receiver Interferometry. *Journal of Geophysical Research: Solid Earth*, 125(2): e2019JB018261, 2020.

J.-P. Chiles and P. Delfiner. *Geostatistics: modeling spatial uncertainty*, volume 497. John Wiley & Sons, 2009.

G. Christakos. *Random field models in Earth Sciences*. Courier Corporation, 2012.

J. F. Claerbout. Synthesis of a layered medium from its acoustic transmission response. *Geophysics*, 33(2):264–269, 1968.

J. Cooke. Note on the principle of stationary phase. *IMA Journal of Applied Mathematics*, 22(3):297–297, 1978.

E. L. Crow and K. Shimizu. *Lognormal distributions: Theory and Practice*. Taylor and Francis, 2017.

A. Curtis and D. Halliday. Source-receiver wavefield interferometry. *Physical Review E*, 81 (4):046601, 2010a.

A. Curtis and D. Halliday. Directional balancing for seismic and general wavefield interferometry. *Geophysics*, 75(1):SA1–SA14, 2010b.

A. Curtis, P. Gerstoft, H. Sato, R. Snieder, and K. Wapenaar. Seismic interferometry—turning noise into signal. *The Leading Edge*, 25(9):1082–1092, 2006.

A. Curtis, H. Nicolson, D. Halliday, J. Trampert, and B. Baptie. Virtual seismometers in the subsurface of the Earth from seismic interferometry. *Nature Geoscience*, 2(10):700–704, 2009.

A. Curtis, Y. Behr, E. Entwistle, E. Galetti, J. Townend, and S. Bannister. The benefit of hindsight in observational science: Retrospective seismological observations. *Earth and Planetary Science Letters*, 345:212–220, 2012.

P. Dales, L. Pinzon-Ricon, F. Brenguier, P. Boué, N. Arndt, J. McBride, F. Lavoué, C. J. Bean, S. Beaupretre, R. Fayjaloun, et al. Virtual Sources of Body Waves from Noise Correlations in a Mineral Exploration Context. *Seismological Research Letters*, 2020.

A. Derode, E. Larose, M. Campillo, and M. Fink. How to estimate the Green's function of a heterogeneous medium between two passive sensors? Application to acoustic waves. *Applied Physics Letters*, 83(15):3054–3056, 2003.

M. Di Renzo, F. Graziosi, and F. Santucci. Approximating the linear combination of log-normal RVs via Pearson type IV distribution for UWB performance analysis. *IEEE transactions on communications*, 57(2):388–403, 2009.

D. Draganov, K. Wapenaar, and J. Thorbecke. Seismic interferometry: Reconstructing the Earth's reflection response. *Geophysics*, 71(4):SI61–SI70, 2006.

E. Entwistle, A. Curtis, E. Galetti, B. Baptie, and G. Meles. Constructing new seismograms from old earthquakes: Retrospective seismology at multiple length scales. *Journal of Geophysical Research: Solid Earth*, 120(4):2466–2490, 2015.

A. Erdélyi. Asymptotic representations of Fourier integrals and the method of stationary phase. *Journal of the Society for Industrial and Applied Mathematics*, 3(1):17–27, 1955.

A. Erdélyi. Asymptotic expansions of Fourier integrals involving logarithmic singularities. *Journal of the Society for Industrial and Applied Mathematics*, 4(1):38–47, 1956.

Y. Fan and R. Snieder. Required source distribution for interferometry of waves and diffusive fields. *Geophysical Journal International*, 179(2):1232–1244, 2009.

A. Fichtner, L. Stehly, L. Ermert, and C. Boehm. Generalised interferometry-I. Theory for inter-station correlations. *Geophysical Journal International*, page ggw420, 2016.

A. Fichtner, V. Tsai, N. Nakata, and L. Gualtieri. Theoretical foundations of noise interferometry. *Seismic ambient noise*, pages 109–143, 2019.

E. Galetti, D. Halliday, and A. Curtis. A simple and exact acoustic wavefield modeling code for data processing, imaging, and interferometry applications. *Geophysics*, 78(6):F17–F27, 2013.

M. G. Genton and W. Kleiber. Cross-covariance functions for multivariate geostatistics. *Statistical Science*, 30(2):147–163, 2015.

P. Gerstoft, K. G. Sabra, P. Roux, W. Kuperman, and M. C. Fehler. Green's functions extraction and surface-wave tomography from microseisms in southern California. *Geophysics*, 71(4):SI23–SI31, 2006.

M. Goldstein and R. Thaler. Bessel functions for large arguments. *Mathematics of Computation*, 12(61):18–26, 1958.

I. S. Gradshteyn and I. M. Ryzhik. *Table of integrals, series, and products*. Academic Press, 2014.

G. Grimmett and D. Welsh. *Probability: an introduction*. Oxford University Press, 2014.

P. Guttorp and T. Gneiting. Studies in the history of probability and statistics XLIX on the Matérn correlation family. *Biometrika*, 93(4):989–995, 2006.

D. Halliday and A. Curtis. Seismic interferometry, surface waves and source distribution. *Geophysical Journal International*, 175(3):1067–1087, 2008b.

D. Halliday and A. Curtis. Seismic interferometry of scattered surface waves in attenuative media. *Geophysical Journal International*, 178(1):419–446, 2009.

D. Halliday and A. Curtis. An interferometric theory of source-receiver scattering and imaging. *Geophysics*, 75(6):SA95–SA103, 2010.

D. Halliday, A. Curtis, and E. Kragh. Seismic surface waves in a suburban environment: Active and passive interferometric methods. *The Leading Edge*, 27(2):210–218, 2008a.

M. Handcock and M. Stein. A Bayesian analysis of kriging. *Technometrics*, 35(4):403–410, 1993.

M. Handcock and J. Wallis. An Approach to Statistical Spatial-Temporal Modeling of Meteorological Fields. *Journal of the American Statistical Association*, 89:368–378, 1994.

G. H. Hardy. Researches in the theory of divergent series and divergent integrals. *Quarterly Journal of Pure and Applied Mathematics*, 35:22–26, 1903.

G. H. Hardy. Further researches in the theory of divergent series and integrals. *Transactions of the Cambridge Philosophical Society*, 21:1–48, 1908.

N. Harmon, C. Rychert, and P. Gerstoft. Distribution of noise sources for seismic interferometry. *Geophysical Journal International*, 183(3):1470–1484, 2010.

J. A. Hoeting, R. A. Davis, A. A. Merton, and S. E. Thompson. Model selection for geostatistical models. *Ecological Applications*, 16(1):87–98, 2006.

T.-K. Hong and W. Menke. Tomographic investigation of the wear along the San Jacinto fault, southern California. *Physics of the Earth and Planetary Interiors*, 155(3-4):236–248, 2006.

D. Jones. Fourier transforms and the method of stationary phase. *IMA Journal of Applied Mathematics*, 2(2):197–222, 1966.

W. Kimman and J. Trampert. Approximations in seismic interferometry and their effects on surface waves. *Geophysical Journal International*, 182(1):461–476, 2010.

S. King and A. Curtis. Velocity analysis using both reflections and refractions in seismic interferometry. *Geophysics*, 76(5):SA83–SA96, 2011a.

S. King, A. Curtis, and T. L. Poole. Interferometric velocity analysis using physical and nonphysical energy. *Geophysics*, 76(1):SA35–SA49, 2011b.

C. Lantuéjoul. *Geostatistical simulation: models and algorithms*. Springer Science & Business Media, 2013.

F. Lavoué, O. Coutant, P. Boué, L. Pinzon-Rincon, F. Brenguier, R. Brossier, P. Dales, M. Rezaeifar, and C. J. Bean. Understanding Seismic Waves Generated by Train Traffic via Modeling: Implications for Seismic Imaging and Monitoring. *Seismological Research Letters*, 92(1):287–300, 2020.

Y. Liu, Y. Yue, Y. Li, and Y. Luo. On the Retrievability of Seismic Waves From High-Speed-Train-Induced Vibrations Using Seismic Interferometry. *IEEE Geoscience and Remote Sensing Letters*, 2021.

C.-F. Lo. The sum and difference of two lognormal random variables. *Journal of Applied Mathematics*, 2012, 2012.

C.-F. Lo. WKB approximation for the sum of two correlated lognormal random variables. *Applied Mathematical Sciences*, 7(128):6355–6367, 2013.

O. I. Lobkis and R. L. Weaver. On the emergence of the Green's function in the correlations of a diffuse field. *The Journal of the Acoustical Society of America*, 110(6):3011–3017, 2001.

K. Löer, N. Riahi, and E. H. Saenger. Three-component ambient noise beamforming in the parkfield area. *Geophysical Journal International*, 213(3):1478–1491, 2018.

R. K. Mallik. Solutions of linear difference equations with variable coefficients. *Journal of Mathematical Analysis and Applications*, 222(1):79–91, 1998.

S. Maranò, C. Reller, H.-A. Loeliger, and D. Fäh. Seismic waves estimation and wavefield decomposition: application to ambient vibrations. *Geophysical Journal International*, 191 (1):175–188, 2012.

B. Matérn. Spatial Variation, 1960.

K. Mehta, R. Snieder, and V. Graizer. Extraction of near-surface properties for a lossy layered medium using the propagator matrix. *Geophysical Journal International*, 169(1): 271–280, 2007a.

K. Mehta, A. Bakulin, J. Sheiman, R. Calvert, and R. Snieder. Improving the virtual source method by wavefield separation. *Geophysics*, 72, 2007b.

N. B. Mehta, A. F. Molisch, J. Wu, and J. Zhang. Approximating the sum of correlated lognormal or, lognormal-Rice random variables. In *2006 IEEE International Conference on Communications*, volume 4, pages 1605–1610. IEEE, 2006.

J. M. Mejía and I. Rodríguez-Iturbe. On the synthesis of random field sampling from the

spectrum: An application to the generation of hydrologic spatial processes. *Water Resources Research*, 10(4):705–711, 1974.

B. Minasny and A. B. McBratney. Spatial prediction of soil properties using EBLUP with the Matérn covariance function. *Geoderma*, 140(4):324–336, 2007.

N. Nakata, R. Snieder, T. Tsuji, K. Larner, and T. Matsuoka. Shear wave imaging from traffic noise using seismic interferometry by cross-coherence. *Geophysics*, 76(6):SA97–SA106, 2011.

H. Nicolson, A. Curtis, B. Baptie, and E. Galetti. Seismic interferometry and ambient noise tomography in the British Isles. *Proceedings of the Geologists' Association*, 123(1):74–86, 2012.

K. Nishida, H. Kawakatsu, and K. Obara. Three-dimensional crustal S wave velocity structure in Japan using microseismic data recorded by Hi-net tiltmeters. *Journal of Geophysical Research: Solid Earth*, 113(B10), 2008.

K. Nishida, J.-P. Montagner, and H. Kawakatsu. Global surface wave tomography using seismic hum. *Science*, 326(5949):112–112, 2009.

F. Olver. Why steepest descents? *SIAM Review*, 12(2):228–247, 1970.

F. Olver. Error bounds for stationary phase approximations. *SIAM Journal on Mathematical Analysis*, 5(1):19–29, 1974.

C. J. Paciorek and M. J. Schervish. Spatial modelling using a new class of nonstationary covariance functions. *Environmetrics: The official journal of the International Environmetrics Society*, 17(5):483–506, 2006.

S. M. Papalexiou. Unified theory for stochastic modelling of hydroclimatic processes: Preserving marginal distributions, correlation structures, and intermittency. *Advances in Water Resources*, 115:234–252, 2018.

M. Pilz and S. Parolai. Statistical properties of the seismic noise field: influence of soil heterogeneities. *Geophysical Journal International*, 199(1):430–440, 2014.

L. Pinzon-Rincon, F. Lavoué, A. Mordret, P. Boué, F. Brenguier, P. Dales, Y. Ben-Zion, F. Vernon, C. J. Bean, and D. Hollis. Humming Trains in Seismology: An Opportune Source for Probing the Shallow Crust. *Seismological Research Letters*, 2021.

S. Purves. Phase and the Hilbert transform. *The Leading Edge*, 33(10):1164–1166, 2014.

D. A. Quiros, L. D. Brown, and D. Kim. Seismic interferometry of railroad induced ground motions: Body and surface wave imaging. *Geophysical Supplements to the Monthly Notices of the Royal Astronomical Society*, 205(1):301–313, 2016.

M. Ravasi, G. Meles, A. Curtis, Z. Rawlinson, and L. Yikuo. Seismic interferometry by multidimensional deconvolution without wavefield separation. *Geophysical Journal International*, 202(1):1–16, 2015.

J. Rickett and J. Claerbout. Acoustic daylight imaging via spectral factorization: Helioseismology and reservoir monitoring. *The leading edge*, 18(8):957–960, 1999.

W. Rudin. *Principles of mathematical analysis*, volume 3. McGraw-hill New York, 1976.

E. Ruigrok, D. Draganov, and K. Wapenaar. Global-scale seismic interferometry: theory and numerical examples. *Geophysical Prospecting*, 56(3):395–417, 2008.

K. G. Sabra. Influence of the noise sources motion on the estimated Green's functions from ambient noise cross-correlations. *The Journal of the Acoustical Society of America*, 127 (6):3577–3589, 2010.

K. G. Sabra, P. Roux, and W. Kuperman. Arrival-time structure of the time-averaged ambient noise cross-correlation function in an oceanic waveguide. *The Journal of the Acoustical Society of America*, 117(1):164–174, 2005a.

K. G. Sabra, P. Gerstoft, P. Roux, W. Kuperman, and M. C. Fehler. Extracting time-domain Green's function estimates from ambient seismic noise. *Geophysical Research Letters*, 32 (3), 2005b.

F. J. Sánchez-Sesma, J. A. Pérez-Ruiz, M. Campillo, and F. Luzón. Elastodynamic 2D Green function retrieval from cross-correlation: Canonical inclusion problem. *Geophysical Research Letters*, 33(13), 2006.

D. D. Sarma. *Geostatistics with applications in earth sciences*. Springer Science & Business Media, 2010.

H. Sato, M. C. Fehler, and T. Maeda. *Seismic wave propagation and scattering in the heterogeneous earth*. Springer Science & Business Media, 2012.

G. Schuster. *Seismic Interferometry*. Cambridge University Press, 2009.

G. Schuster, J. Yu, J. Sheng, and J. Rickett. Interferometric/daylight seismic imaging. *Geophysical Journal International*, 157(2):838–852, 2004.

G. T. Schuster and J. Rickett. Daylight imaging in V(x, y, z) media. *Utah tomography and modeling-migration project midyear report and Stanford Exploration Project midyear reports*, pages 55–66, 2000.

N. M. Shapiro and M. Campillo. Emergence of broadband rayleigh waves from correlations of the ambient seismic noise. *Geophysical Research Letters*, 31(7), 2004.

N. M. Shapiro, M. Campillo, L. Stehly, and M. H. Ritzwoller. High-resolution surface-wave tomography from ambient seismic noise. *Science*, 307(5715):1615–1618, 2005.

S. Shapiro, R. Schwarz, and N. Gold. The effect of random isotropic inhomogeneities on the phase velocity of seismic waves. *Geophysical Journal International*, 127(3):783–794, 1996.

E. Slob and K. Wapenaar. Electromagnetic Green's functions retrieval by cross-correlation and cross-convolution in media with losses. *Geophysical Research Letters*, 34(5), 2007.

E. Slob, D. Draganov, and K. Wapenaar. Interferometric electromagnetic green's functions representations using propagation invariants. *Geophysical Journal International*, 169(1): 60–80, 2007.

R. Snieder. Extracting the Green's function from the correlation of coda waves: A derivation based on stationary phase. *Physical Review E*, 69(4):046610, 2004.

R. Snieder and C. Sens-Schönfelder. Seismic interferometry and stationary phase at caustics. *Journal of Geophysical Research: Solid Earth*, 120(6):4333–4343, 2015.

R. Snieder and K. Van Wijk. *A guided tour of mathematical methods for the physical sciences*. Cambridge University Press, 2015.

R. Snieder, K. Wapenaar, and K. Larner. Spurious multiples in seismic interferometry of primaries. *Geophysics*, 71(4):SI111–SI124, 2006.

R. Snieder, K. Van Wijk, M. Haney, and R. Calvert. Cancellation of spurious arrivals in Green's function extraction and the generalized optical theorem. *Physical Review E*, 78 (3):036606, 2008.

R. Snieder, M. Miyazawa, E. Slob, I. Vasconcelos, and K. Wapenaar. A comparison of strategies for seismic interferometry. *Surveys in Geophysics*, 30(4-5):503–523, 2009.

A. Sommerfeld. *Partial differential equations in physics*. Academic Press, 1949.

X. Song and T. H. Jordan. Stochastic representations of seismic anisotropy: transversely isotropic effective media models. *Geophysical Journal International*, 209(3):1831–1850, 2017.

W. Southwell. Validity of the Fresnel approximation in the near field. *JOSA*, 71(1):7–14, 1981.

M. L. Stein. Interpolation of Spatial Data: Some Theory for Kriging, 1999.

J. Thorbecke and K. Wapenaar. Analysis of spurious events in seismic interferometry. In *SEG Technical Program Expanded Abstracts 2008*, pages 1415–1420. Society of Exploration Geophysicists, 2008.

K. N. van Dalen, K. Wapenaar, and D. F. Halliday. Surface wave retrieval in layered media using seismic interferometry by multidimensional deconvolution. *Geophysical Journal International*, 196(1):230–242, 2014.

K. N. van Dalen, T. D. Mikesell, E. N. Ruigrok, and K. Wapenaar. Retrieving surface waves from ambient seismic noise using seismic interferometry by multidimensional deconvolution. *Journal of Geophysical Research: Solid Earth*, 120(2):944–961, 2015.

N. van Kampen. The method of stationary phase and the method of fresnel zones. *Physica*, 24(1-5):437–444, 1958.

D. van Manen, A. Curtis, and J. Robertsson. Interferometric modeling of wave propagation

in inhomogeneous elastic media using time reversal and reciprocity. *Geophysics*, 71:SI47–SI60, 2006.

K. Wapenaar. Retrieving the elastodynamic Green's function of an arbitrary inhomogeneous medium by cross correlation. *Physical Review Letters*, 93(25):254301, 2004.

K. Wapenaar and J. Fokkema. Green's function representations for seismic interferometry. *Geophysics*, 71(4):SI33–SI46, 2006.

K. Wapenaar, E. Slob, and R. Snieder. Seismic and electromagnetic controlled-source interferometry in dissipative media. *Geophysical Prospecting*, 56(3):419–434, 2008.

K. Wapenaar, D. Draganov, R. Snieder, X. Campman, and A. Verdel. Tutorial on seismic interferometry: Part 1—Basic principles and applications. *Geophysics*, 75(5):75A195–75A209, 2010a.

K. Wapenaar, E. Slob, R. Snieder, and A. Curtis. Tutorial on seismic interferometry: Part 2—Underlying theory and new advances. *Geophysics*, 75(5):75A211–75A227, 2010b.

K. Wapenaar, J. Van Der Neut, E. Ruigrok, D. Draganov, J. Hunziker, E. Slob, J. Thorbecke, and R. Snieder. Seismic interferometry by crosscorrelation and by multidimensional deconvolution: A systematic comparison. *Geophysical Journal International*, 185(3):1335–1364, 2011.

K. Wapenaar, J. van der Neut, and J. Thorbecke. On the relation between seismic interferometry and the simultaneous-source method. *Geophysical Prospecting*, 60(4-Simultaneous Source Methods for Seismic Data):802–823, 2012.

R. L. Weaver and O. I. Lobkis. Ultrasonics without a source: Thermal fluctuation correlations at MHz frequencies. *Physical Review Letters*, 87(13):134301, 2001.

R. L. Weaver and O. I. Lobkis. The mean and variance of diffuse field correlations in finite bodies. *The Journal of the Acoustical Society of America*, 118(6):3447–3456, 2005.

H. Yao and R. D. Van Der Hilst. Analysis of ambient noise energy distribution and phase velocity bias in ambient noise tomography, with application to SE Tibet. *Geophysical Journal International*, 179(2):1113–1132, 2009.

J. Yin, C. Xiong, and W. Wang. Acoustic localization for a moving source based on cross array azimuth. *Applied Sciences*, 8(8):1281, 2018.

H. Zhang, B. Wang, J. Ning, and Y. Li. Interferometry imaging using high-speed-train induced seismic waves. *Chinese Journal of Geophysics*, 62(6):2321–2327, 2019.

Y. Zheng, R.-S. Wu, Y. Liu, and M. C. Fehler. Seismic interferometry using non-far-field sources and removing the spurious arrival. *Bulletin of the Seismological Society of America*, 101(2):888–894, 2011.